JPL PUBLICATION 82-95

Space Shuttle Columbia Views the World With Imaging Radar: the SIR-A Experiment

J.P. Ford
J.B. Cimino
C. Elachi

January 1, 1983

National Aeronautics and
Space Administration

Jet Propulsion Laboratory
California Institute of Technology
Pasadena, California

Space Shuttle Columbia Views the World With Imaging Radar: the SIR-A Experiment

Overleaf: Coregistered SIR-A and Seasat SAR Images of the Santa Ynez Mountains, California, U.S.A.

This color image was made using SIR-A and Seasat SAR data to demonstrate the effects of different incidence angles on radar backscatter. The area of common coverage is the oblique swath that was formed through coregistration of the SIR-A and Seasat SAR data sets. The SIR-A data were used for the background image to produce color; the Seasat SAR data were used to modulate intensity in the swath. Variations in color relate to small-scale roughness; variations in intensity relate to topography. The combination of small-scale surface roughness and topographic information permits better discrimination of lithologic units. The images used to produce this scene are discussed more fully under Scene 3.

ORIGINAL PAGE
COLOR PHOTOGRAPH

JPL PUBLICATION 82-95

Space Shuttle Columbia Views the World With Imaging Radar: the SIR-A Experiment

J.P. Ford
J.B. Cimino
C. Elachi

January 1, 1983

National Aeronautics and
Space Administration

Jet Propulsion Laboratory
California Institute of Technology
Pasadena, California

The research described in this publication was carried out by the Jet Propulsion Laboratory, California Institute of Technology, under contract with the National Aeronautics and Space Administration.

Foreword

NASA has historically conducted pioneering research in Earth and planetary exploration. Spacecraft equipped with a wide array of sensors have provided the first close-up views of other planetary bodies such as Mercury, Mars, Jupiter, and Saturn. Spacecraft have also provided the first global view of the Earth, and they have enabled us to study remote portions of our own planet in much greater detail.

Analyses of spacecraft data acquired during the past two decades have resulted in major discoveries concerning the structure and composition of neighboring planetary bodies, and have revolutionized our understanding of the processes that governed their evolution. In contrast, the Earth has been studied in considerable detail for hundreds of years by each generation of its inhabitants. We know much more about the Earth than other planets. However, our accumulated knowledge of the Earth has raised many more questions about its history, evolution, and day-to-day functioning than can presently be answered. Space technology provides new and fundamentally different ways of looking at our planet and studying its behavior on a global basis. Remote sensing techniques, in particular, allow us to extend our observational capabilities beyond the range of our human senses and to explore the Earth in ways that have not been possible in the past.

The Shuttle Imaging Radar (SIR-A) Experiment conducted in November, 1981, is a good example of the successful application of space techniques to the study of the Earth. SIR-A was launched into space on the second test flight of Space Shuttle Columbia. SIR-A possessed many of the same characteristics as the synthetic-aperture radar (SAR) system that operated onboard the Seasat spacecraft in 1978. The principal difference between these two radars was that SIR-A illuminated the Earth's surface at a larger angle of incidence than Seasat SAR.

SIR-A obtained over 10 million square kilometers of surface imagery. It acquired radar images of many tropical, arid, and mountainous regions for the first time. A variety of fascinating features have been detected in the SIR-A data collection. Many of these features can be related to local variations in surface slope and roughness, or the intrinsic dielectric properties of surficial materials. However, other features are enigmatic and are currently the object of intense study. SIR-A data are also being compared with imagery obtained with Seasat SAR, Landsat, and the Heat Capacity Mapping Mission (HCMM). In many instances, features apparent in one data set are absent in others. Researchers are currently trying to understand why this is so, and what it reveals about the surface characteristics of the Earth.

I invite you to share in the adventure of SIR-A data analysis through the use of this Atlas. Each SIR-A image presented here encompasses an area of about five thousand square kilometers. Considered together, the 60 scenes presented in the Atlas represent about 3 % of the SIR-A data collection. Each SIR-A image is accompanied by a Landsat, Seasat SAR, or HCMM image of the same area, or by a sketch map or photograph. These illustrations demonstrate the unique imaging capabilities of the SIR-A system and the potential utility of radar remote sensing techniques for a wide range of terrestrial studies.

Jesse W. Moore
Director
Earth and Planetary Exploration Division
Office of Space Science and Applications, NASA

Acknowledgment

The authors are indebted to numerous people at JPL who have contributed to the SIR-A experiment and to the preparation of this atlas. Thanks are particularly expressed to J. Granger and G. Sisk who led the engineering team that successfully implemented the SIR-A experiment. Data and contributions to the atlas provided by R. G. Blom, M. L. Bryan, T. H. Dixon, D. L. Evans, T. Farr, D. Harrison, and A. Holmes of the Imaging Radar Geology Group B. N. Rock and A. Gillespie of the Geology Remote Sensing Group, L. L. Fu and B. Holt of the Oceanography Group, and Ph. Rebillard (NRC Resident Research Associate) are gratefully acknowledged. Particular thanks are expressed to D. E. Fulton who edited the atlas, and to J. W. Kempton, M. F. Buehler, and R. T. Chandler of the Documentation Section, R. W. Post of the Photo-Duplicating Section, and B. Trinh, W. Fiechter, and M. Furuyama of the Radar Processing Group, each of whom cooperated closely with the authors throughout the different phases of its preparation. Thanks and appreciation are expressed for the support offered by J. V. Taranik (Program Scientist on OSTA-1), M. Settle (Discipline Scientist for Nonrenewable Resources), and B. Schardt (Program Manager on OSTA-1) at NASA Headquarters, Washington, D. C. In addition, the authors wish to thank the many individuals who provided a wide range of helpful information and data, particularly R. Kusmiadi (Geological Research and Development Centre of Indonesia), P. Martin-Kaye (Hunting Geology and Geophysics Ltd.), J. B. Gladden (Savannah River Ecology Laboratory), R. J. P. Lyon (Department of Applied Earth Sciences, Stanford University), D. Deckelbaum and J. Hargith (UCLA Map Library), L. Brooks, L. Deaton, S. Ruff, and L. E. Young (U. S. Department of Agriculture), C. S. Breed, S. J. Gawarecki, M. J. Grolier, J. F. McCauley, G. G. Schaber, and G. W. Weir (U. S. Geological Survey), and D. Serwer (Scientific Attaché, U. S. Embassy, Brasilia).

Abstract

Images acquired by the Shuttle Imaging Radar (SIR-A) in November, 1981, demonstrate the capability of this microwave remote sensor system to perceive and map a wide range of different surface features around the Earth. A selection of 60 scenes displays this capability with respect to Earth resources – geology, hydrology, agriculture, forest cover, ocean surface features, and prominent man-made structures. The combined area covered by the scenes presented here amounts to about 3% of the total acquired. Most of the SIR-A images are accompanied by a Landsat multispectral scanner (MSS) or Seasat synthetic-aperture radar (SAR) image of the same scene for comparison. Differences between the SIR-A image and its companion Landsat or Seasat image at each scene are related to the characteristics of the respective imaging systems, and to seasonal or other changes that occurred in the time interval between acquisition of the images.

Contents

Section I
Introduction

On November 12, 1981, the United States National Aeronautics and Space Administration launched Space Shuttle Columbia on its second orbital mission from the Kennedy Space Center, Cape Canaveral, Florida, U.S.A. The spacecraft carried its first scientific payload, part of which was the Shuttle Imaging Radar system (SIR-A). The objectives of the SIR-A Experiment were to acquire radar images of a wide variety of different geologic regions around the Earth, to demonstrate the capability of the Shuttle as a platform for making spaceborne scientific investigations, and to analyze and interpret the data in the radar images.

The SIR-A Experiment was a complete success (Ref. 1). The radar sensor operated as expected and met all of its design goals. Plans to acquire radar imagery of about 10 million km^2 of the Earth's surface were met despite curtailment of the mission from 4 to 2½ days. The radar coverage corresponds to about 480 min of sensor operation time. High-resolution images were acquired over portions of every continent and some of the oceans between the latitudes of approximately 41°N and 35°S (Fig. 1).

This atlas of SIR-A images is a sequel to two similar publications of orbital radar images of the Earth acquired by Seasat SAR in 1978 (Refs. 2 and 3). Each SIR-A image is presented in conjunction with one or more different spaceborne images for comparative purposes, or with a sketch map or photograph for illustration of features described in the text. On the facing pages of each scene, the SIR-A image appears at the left. The companion image or images to the right are subscenes mostly from Landsat multispectral scanner (MSS) band-7 or band-5 images and/or subscenes from Seasat SAR images. A few subscenes from Landsat MSS band-4 and band-6 images are presented; there is one example each of a Heat Capacity Mapping Mission scene and of SIR-A repetitive coverage. The interval between the acquisition of the SIR-A image and the corresponding image(s) of each scene ranges from 1½ h (Scene No. 54) to 9 yr and 3 mo (Scene No. 42). In many scenes, the SIR-A and companion images record major changes in surface features that resulted from either natural phenomena or human activities.

Preliminary studies have been made of the SIR-A images of a variety of terrains and ocean surface features. SIR-A images of the hyperarid Arabian Desert in southwest Egypt show that the radar penetrated the unconsolidated wind-blown sand sheets in this area to depths of 2 m or more; buried drainage channels not previously seen on any images acquired at optical wavelengths (Ref. 4) are revealed. Steep slopes in the Appalachian Plateau are selectively enhanced on SIR-A images; on corresponding Seasat SAR images, the steep slopes are obscure or obliterated by layover (Ref. 5). However, gently sloping topography is more clearly perceived on Seasat SAR images. These differences result mostly from the difference in incidence angle between the SIR-A and the Seasat SAR imaging systems. In the Eastern Desert of Egypt, the SIR-A coverage shows that major geologic units are readily discriminated by their morphology and characteristic texture on the radar images (Ref. 6). Despite the large SIR-A incidence angle and the low SIR-A returns from ocean surfaces, the oceanic coverage by SIR-A reveals internal waves and other surface features with a clarity comparable to that of Seasat SAR images.

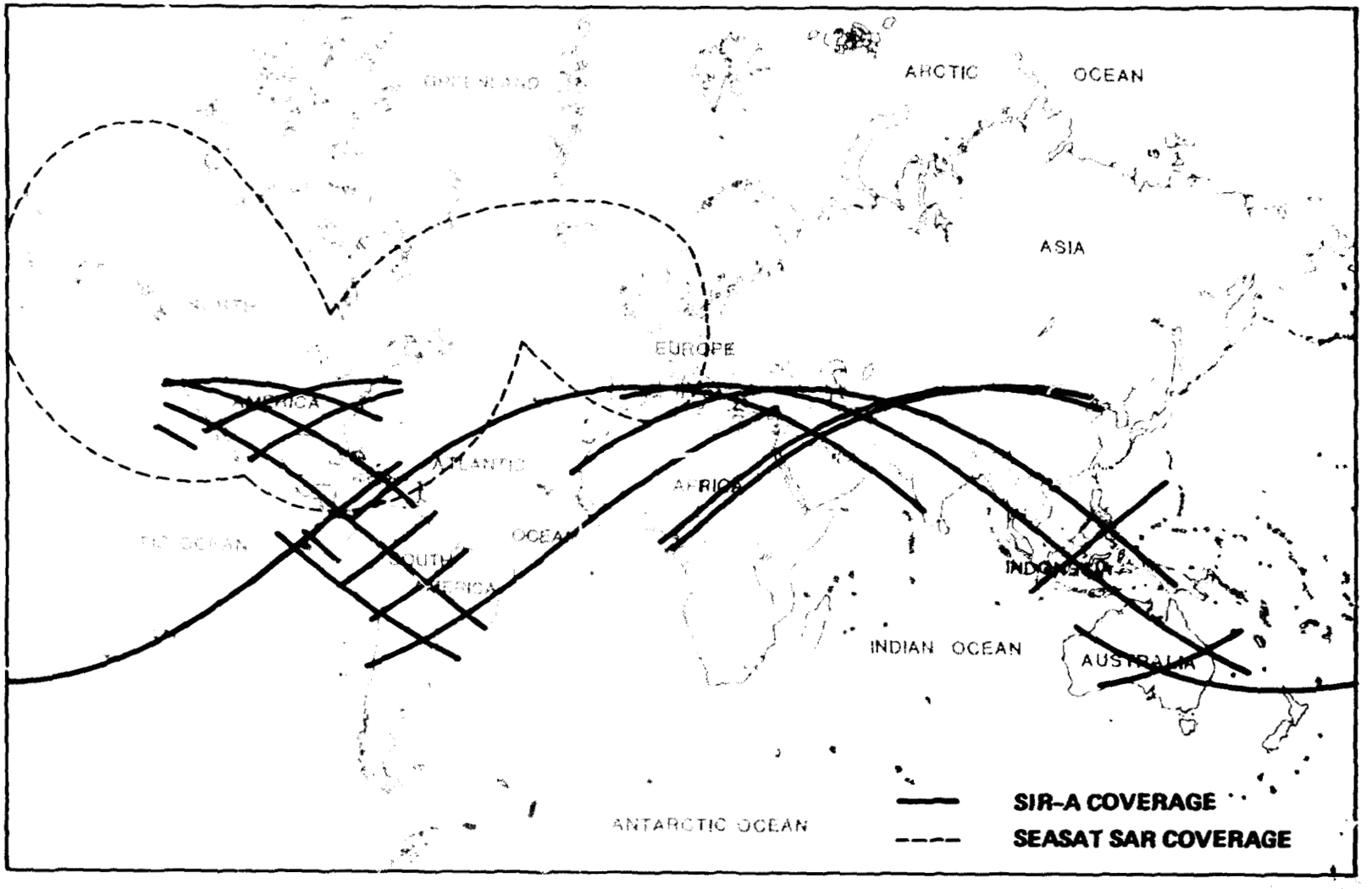

Figure 1. Areas of SIR-A and Seasat SAR coverages

Each SIR-A image in this atlas covers an area approximately 100 km in azimuth by 50 km in range, as seen by the imaging radar. The images are grouped into four main classes to illustrate a wide range of Earth surface features. Geologic folds, faults, and intrusive structures, and landforms characteristic of volcanic, eolian, and other geologic processes, are included under "Nonrenewable Resources." Many of the scenes in this class are of

inaccessible localities about which little is known. Examples of "Renewable Resources" include scenes of selected drainage networks, varied agricultural patterns, forested areas, and urban areas. The class "Oceanographic Features" includes scenes of disturbances and inhomogeneities of the ocean surface caused by the interaction of oceanic and atmospheric forces. Scenes chosen to illustrate "Man-Made Features" display prominent structures that locally dominate the environment.

The text that accompanies each scene is intended to draw attention to the salient points of the SIR-A images, and to comparisons that can be drawn with the corresponding image(s); it is not intended, of course, to be a final or exhaustive study, but rather a stimulant for further study and interpretation. A glossary of acronyms and technical terms used in the atlas is provided (Appendix A).

Summary details of image identification and date of acquisition of the images in this atlas are tabulated under the "Index of Images" (Appendix B). The image products are available from a variety of different sources. SIR-A images may be obtained by requesters within the United States at the following address:

National Space Science Data Center
Code 601.4
NASA-Goddard Space Flight Center
Greenbelt, Maryland 20771

Scientists outside the United States should direct their requests to:

World Data Center A
Rockets and Satellites
Code 601
NASA-Goddard Space Flight Center
Greenbelt, Maryland 20771, U.S.A.

Seasat SAR images are available from:

National Oceanic and Atmospheric Administration
Satellite Data Services Division
Room 100, World Weather Building
Washington, D.C. 20233

Landsat image products may be ordered from:

Landsat Customer Services
EROS Data Center
Sioux Falls, South Dakota 57198

Section II
SIR-A, Seasat SAR, and Landsat MSS System Characteristics

The SIR-A sensor is a synthetic-aperture radar (SAR) imaging system. The radar sensor generates a high peak-power signal that is frequency modulated. This signal is radiated through a planar array antenna toward the Earth's surface (Fig. 2). Returned echoes are collected by the antenna, and amplified and detected by a receiver. The time delay and Doppler history of the returned echoes are coherently recorded on optical film. This holographic record is the signal film. The signal film is processed in an optical correlator where the synthetic aperture is effectively formed. By using the information from thousands of echoes, a high-resolution image is generated and recorded on image film. The image is a two-dimensional representation of the surface scattering, which in turn is a function of physical surface properties such as slope, small-scale roughness, soil moisture, and dielectric constant. In general, radar backscatter is dominated by different surface properties through the 0- to 90-deg range of local incidence angles (Fig. 3).

The SIR-A sensor has numerous system characteristics in common with Seasat SAR, and several significant differences. The important differences that bear on feature perception and image interpretation occur mostly in the radar incidence angle and the image resolution (Table 1). The former is governed primarily by the antenna look angle, and the latter by the system bandwidth and the length of the transmit pulse. Other notable differences between the SIR-A and the Seasat SAR systems are seen in the orbital parameters of the spacecraft, and the method of recording the radar signal data.

Landsat multispectral scanners are passive remote sensing systems that record reflected solar radiation in several optical and near-infrared wavelengths simultaneously. The radiation is processed in spectral intervals or bands as follows:

MSS band	Wavelength, μm	Type of radiation
4	0.5 to 0.6	visible green
5	0.6 to 0.7	visible red
6	0.7 to 0.8	invisible near-infrared
7	0.8 to 1.1	invisible near-infrared

The selection of a suitable Landsat MSS image for comparison with the SIR-A coverage at each scene in this atlas was governed by the availability and the quality of images with a minimum of cloud cover, and by the known spectral response characteristics of vegetated and nonvegetated surfaces in the four spectral bands listed above. Generalized spectral reflectance curves of vegetated and nonvegetated surfaces are given in Figs. 4(a) and (b), respectively.

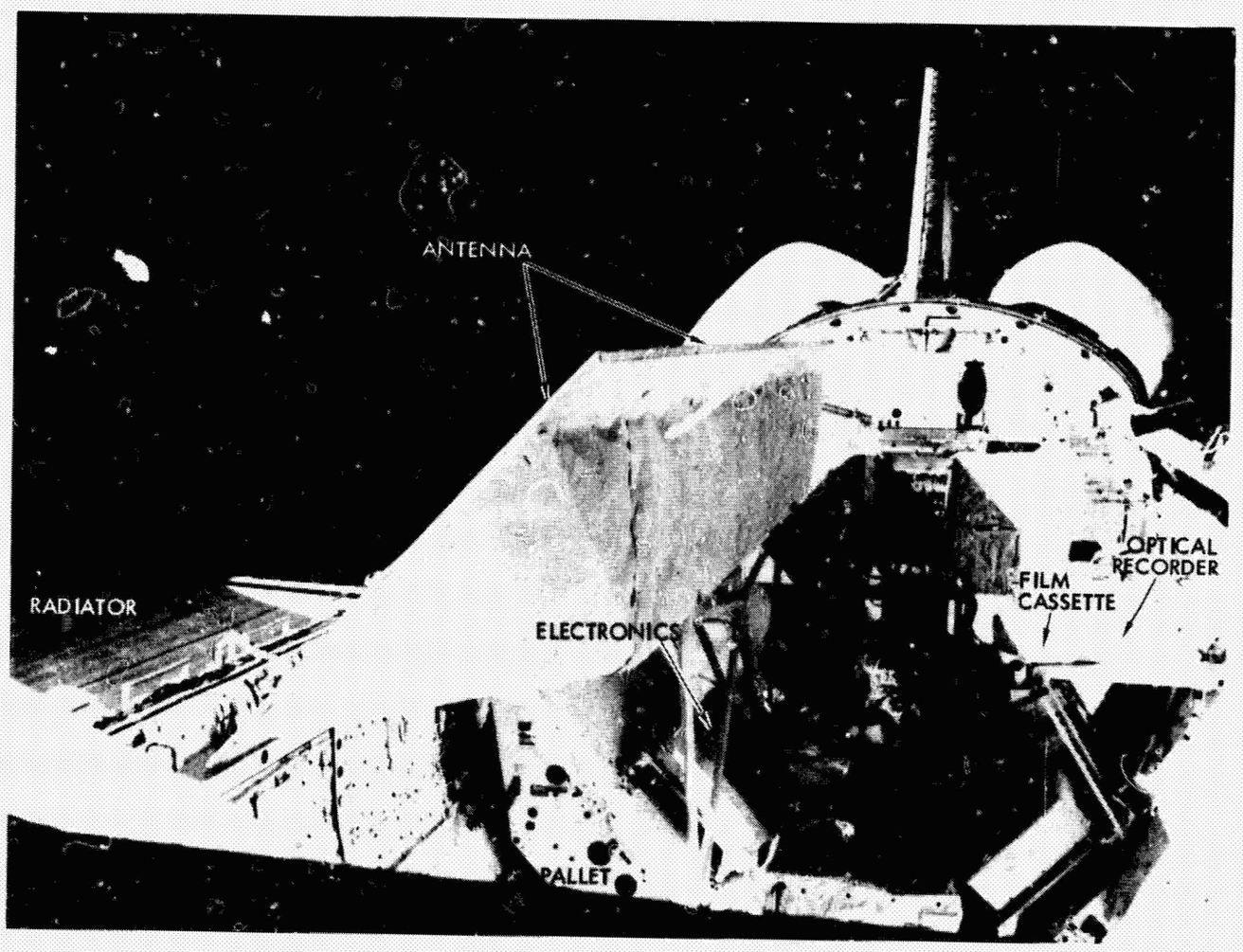

ORIGINAL PAGE
BLACK AND WHITE PHOTOGRAPH

Figure 2. SIR-A system on board Space Shuttle Columbia; the planar array antenna is shown deployed during mission operations, November 13, 1981

Green, actively growing vegetation has a reflectance peak in the visible-green wavelength; consequently it appears bright on Landsat band-4 images. Green vegetation is unique among common ground-cover types because of its strong absorption in the visible-red wavelength (band 5) and strong reflectance at near-infrared wavelengths (bands 6 and 7). Aging or unhealthy yellow or brown vegetation in various stages of senescence lacks both the green reflectance and the red absorption of green vegetation, though it is highly reflective at near-infrared wavelengths (Fig. 4(a)). Nonvegetated sur-

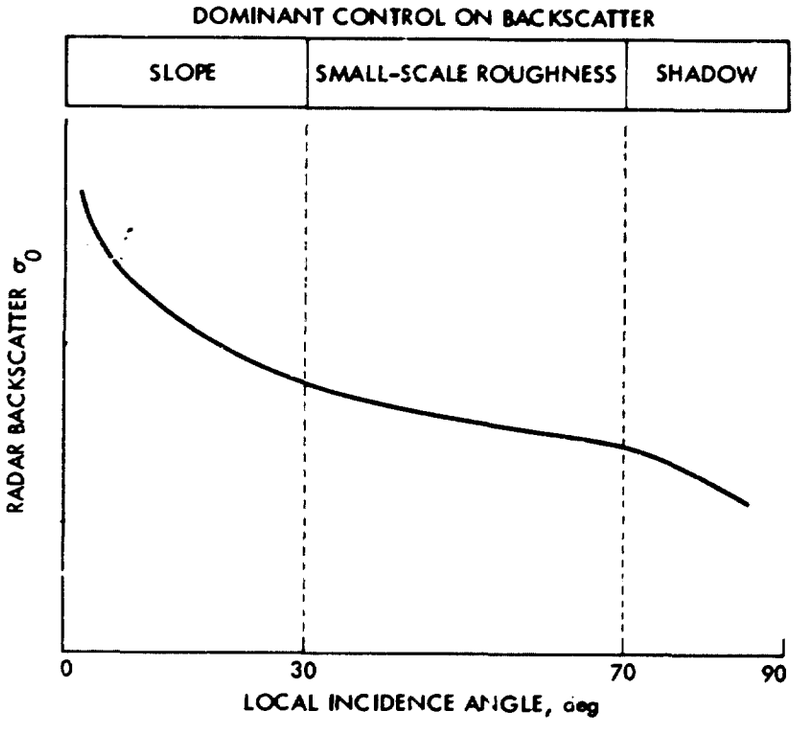

Figure 3 Generalized radar backscatter curve showing the dominant controls on backscatter through the 0- to 90-deg range of local incidence angle

Table 1. SIR-A and Seasat SAR system characteristics

Parameter	SIR-A	Seasat SAR
Orbit		
Altitude, km	259	795
Inclination, deg	38	108
Radar		
Frequency, GHz	1.278	1.275
Wavelength, cm	23.5	23.5
System bandwidth, MHz	6	19
Transmit pulse length, μs	30.4	33.4
Pulse repetition frequency, Hz	1464 to 1824	1463 to 1640
Transmitted peak power, W	1000	1000
Time-bandwidth product	182	634
Polarization	HH	HH
Antenna		
Dimensions, m	9.4 x 2.16	10.74 x 2.16
Look angle, deg	47 ±3	20 ±3
Incidence angle, deg	50 ±3	23 ±3
Swath width, km	50	100
Resolution, m	40 x 40	25 x 25
Data recording	*Onboard: optical*	*Ground station: digital*
Signal correlation	Optical	Optical and digital

faces that expose light-colored rocks or concrete are strongly reflective at near-infrared wavelengths (bands 6 and 7). Dark-colored rocks that are typically basaltic in composition, and asphalt surfaces are significantly less reflective in each of the four MSS bands (Fig. 4(b)). The reflectivity of soil lies between the values for light- and dark-colored rock; however, in any band it is influenced by the moisture content. Muddy water is reflective at green and red wavelengths (bands 4 and 5) and strongly absorptive at near-infrared wavelengths (bands 6 and 7). From the foregoing considerations, it has been found that Landsat images in MSS bands 5 and 7 are optimal for contrast and comparison with the SIR-A images. In many instances, band 5 images provide complementary image tones in heavily vegetated scenes. Band 6 images are presented only in specific instances where the image quality is superior to that of the corresponding band 7 image. With the exception of Scene No. 20, all the Landsat MSS images in this atlas are photographic reproductions that have not been altered by special digital processing.

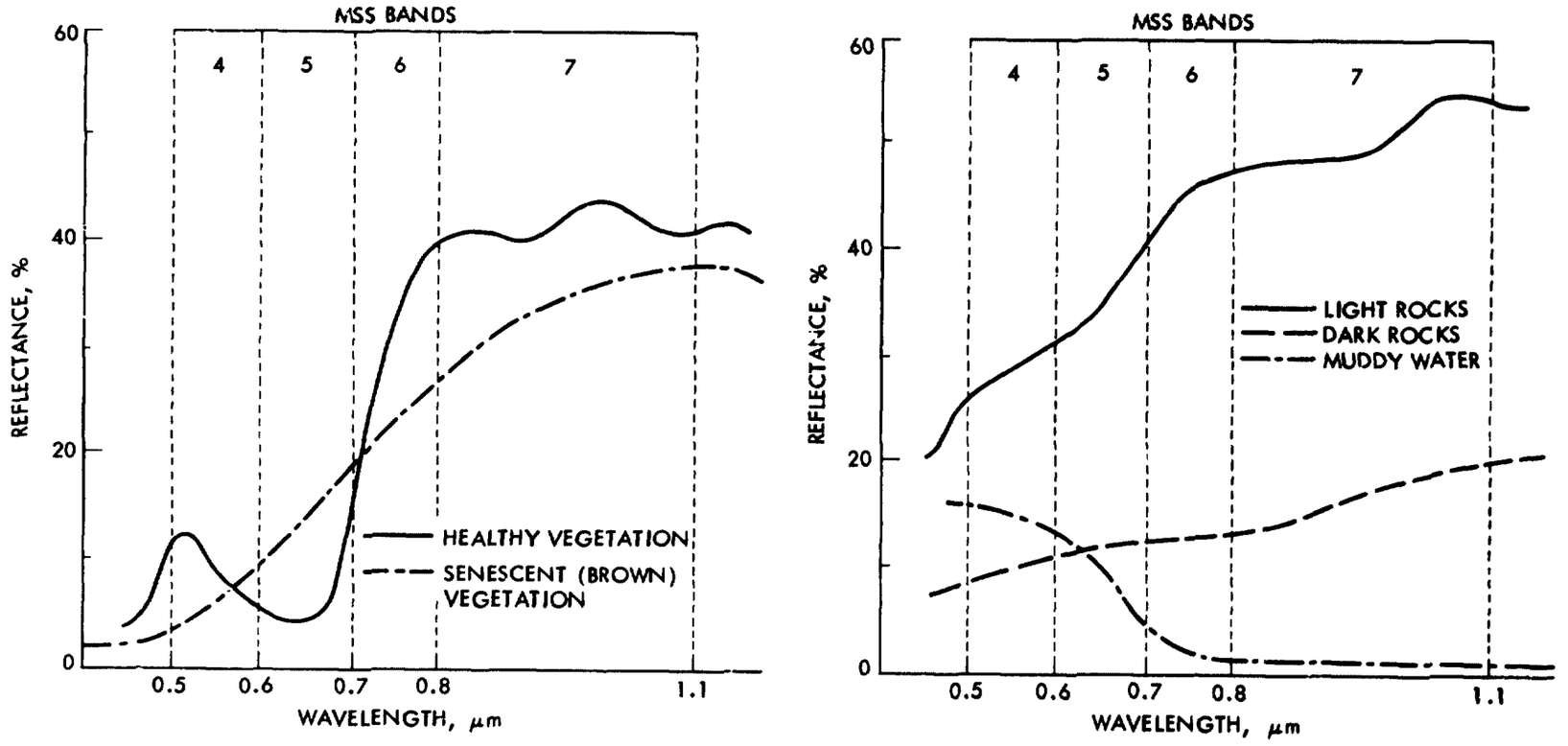

Figure 4. Generalized spectral reflectance curves at optical and near-infrared wavelengths in Landsat MSS bands 4 through 7 for (a) vegetated surfaces (courtesy of B. N. Rock), (b) nonvegetated surfaces

Section III
Description of Selected SIR-A Images

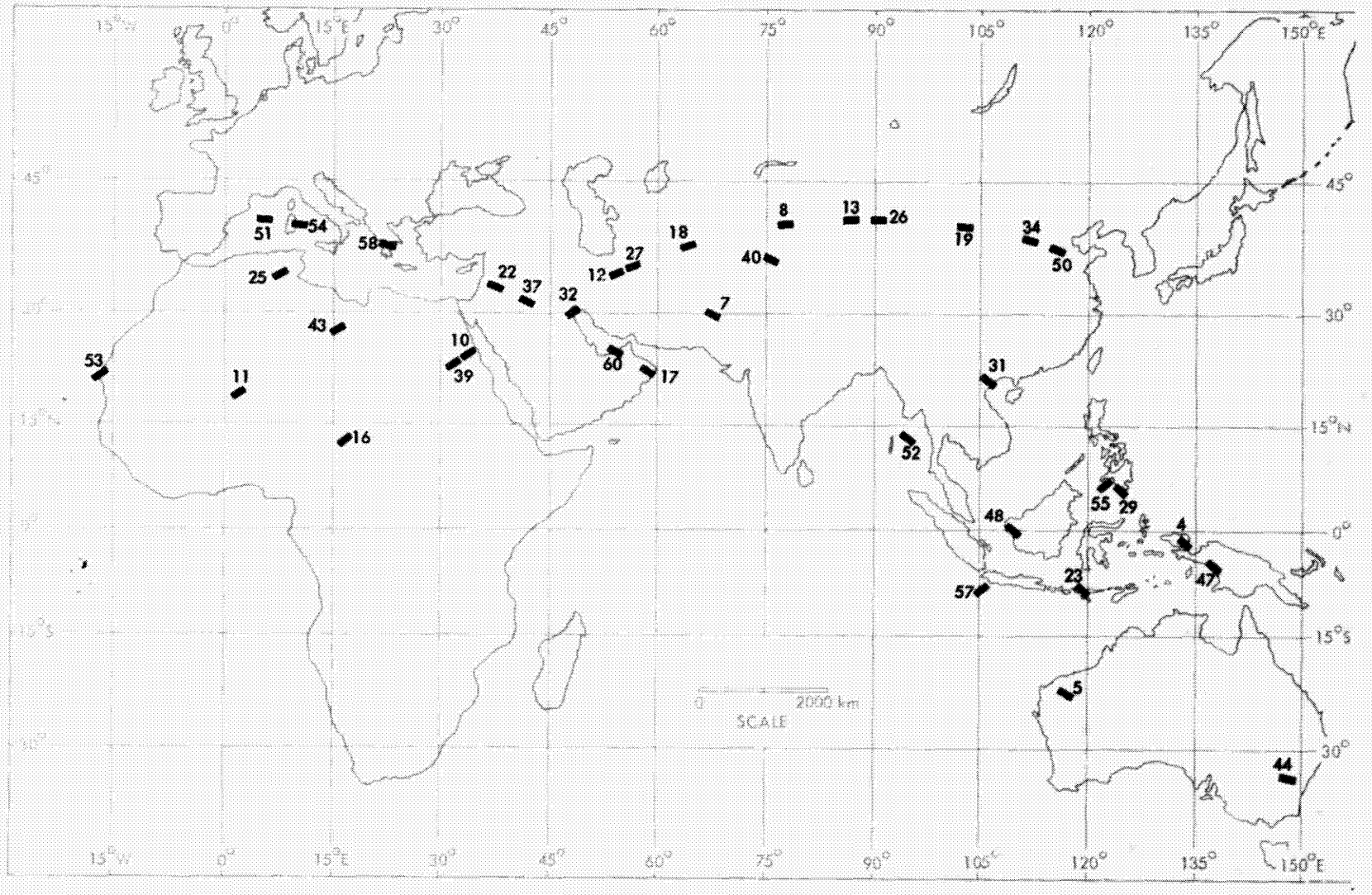

ORIGINAL PAGE IS
OF POOR QUALITY

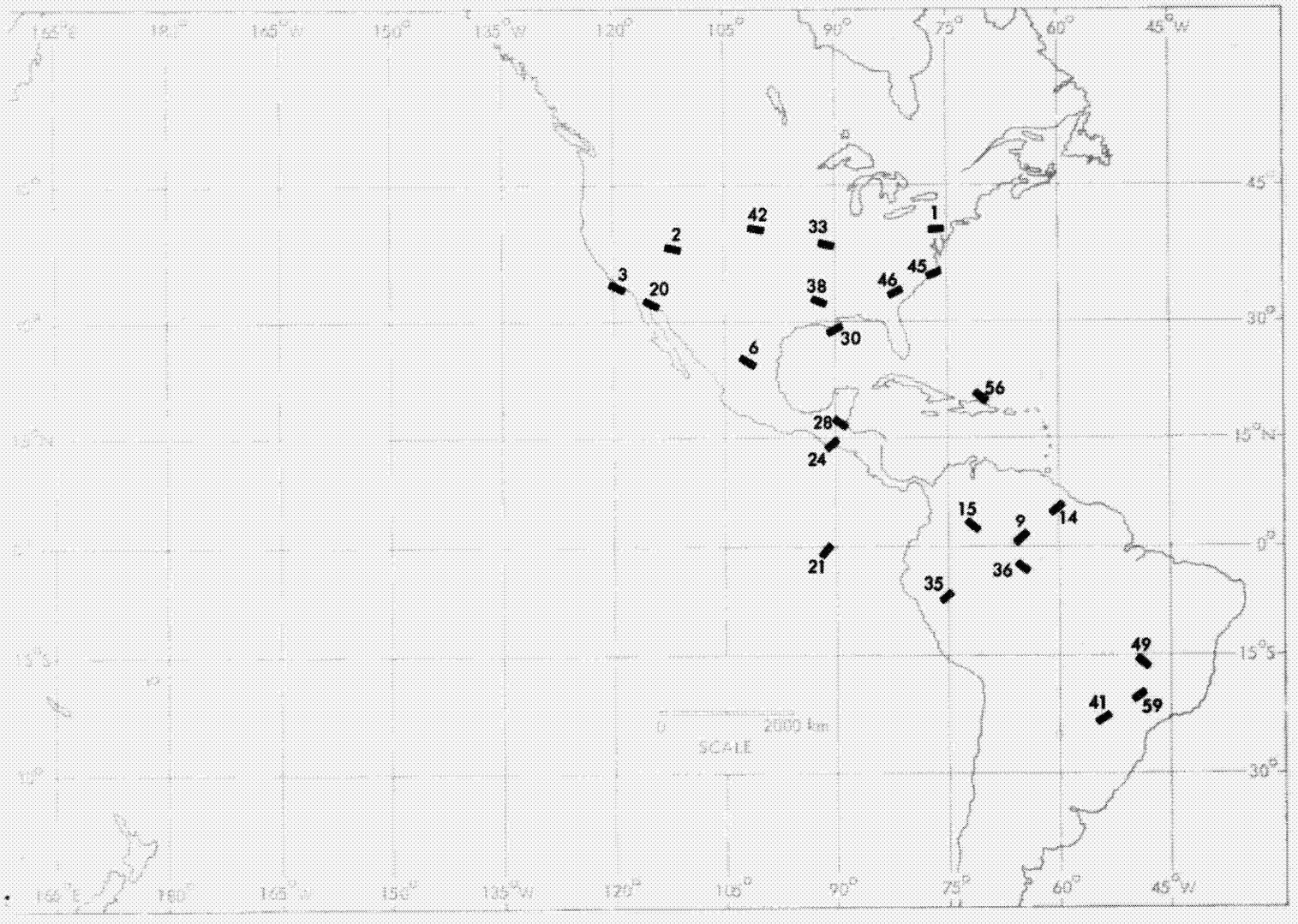

Figure 5. Geographic locations of selected SIR-A images

A. Nonrenewable Resources

The Earth's topography and landforms provide important information concerning this planet's natural nonrenewable resources. Topography is enhanced on SIR-A images, particularly in hilly or mountainous areas where the slopes are 20 deg or more. Structures such as folds, faults, and bedding are readily perceived from the image patterns and the contrasts in image tone and texture. Fold and fracture patterns are clearly displayed on SIR-A images, both in areas of extensive rock outcrop (Scene Nos. 5, 7, 8, and 13) and in areas of heavy vegetated cover (Scene Nos. 1, 4, and 9). Circular features that appear enhanced by the radar response to surface morphology include eroded dome structures (Scene No. 5), curvilinear fracture patterns (Scene No. 9), granite plutons (Scene Nos. 10 and 11), salt domes (Scene No. 12), and volcanic cones of varying dimensions (Scene Nos. 20 through 24). Erosional landforms in dissected terrains are enhanced by the strong contrast in radar backscatter from the upland surfaces and the lowland valleys (Scene Nos. 14 and 15).

The SIR-A coverage provides the first clear spaceborne images of the topography and structures in remote, inaccessible, perennially cloud-covered areas (Scene Nos. 4, 9, and 14). Limitations that exist in the perception of dune morphology are governed by the orientation and form of the dunes and by the local incidence angle (Scene Nos. 16 through 19). In areas where the surfaces are relatively level, such as dry lakes (Scene Nos. 25 through 27) or deltaic plains (Scene Nos. 30 through 32), the SIR-A image tones of surface features are strongly influenced by the small-scale roughness characteristics of the surface materials. Modulation of the SIR-A backscatter by slope and by surface roughness characteristics provides distinctive image textures in areas of extensive karst topography (Scene Nos. 28 and 29).

(i) Folded and Layered Structures

1. Appalachian Mountains, Pennsylvania, U.S.A.

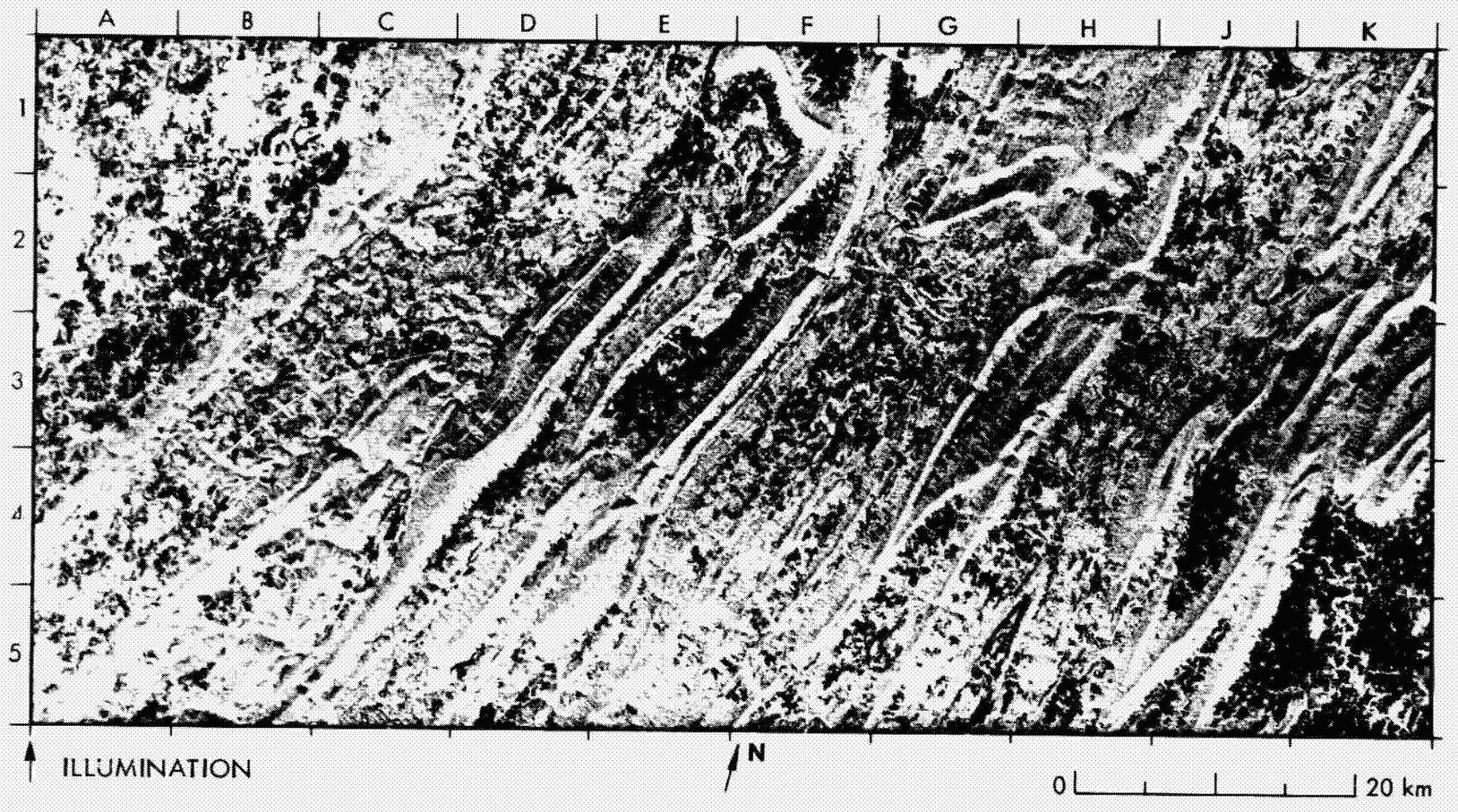

This scene extends across the strike of the folded Appalachian Mountains, from the Allegheny Plateau (A4 to C1) to the Great Valley (K5). The bright returns from the forested mountain slopes are modulated by slope effects, i.e., foreslopes appear brighter than backslopes on the radar image. The mottled distribution of dark returns reflects mostly the agricultural pattern on the level-to-gently-sloping valley surfaces. The regional structure of alternating anticlines and synclines is expressed in the form of the numerous subparallel mountain ridges in the area. The lenticular form of adjacent pairs of mountain ridges represents breached doubly plunging anticlinal structures as, for example, between

Landsat Band 7

Dickeys Mountain and Tuscarora Mountain (H5 to K2). Multiple reflections from clusters of buildings and from appropriately oriented streets produce very bright returns from cities such as Bedford (E2) and Mercersburg (K5).

In the corresponding near-IR image acquired by Landsat nine years previously at approximately the same time of year (November), the mountains and ridges are strongly enhanced by solar shadowing. The increasingly dark appearance of the forested mountain slopes is the result of modulation by shadowing effects, whereas the level-to-gently-sloping cultivated areas are bright.

2. San Rafael Swell, Utah, U.S.A.

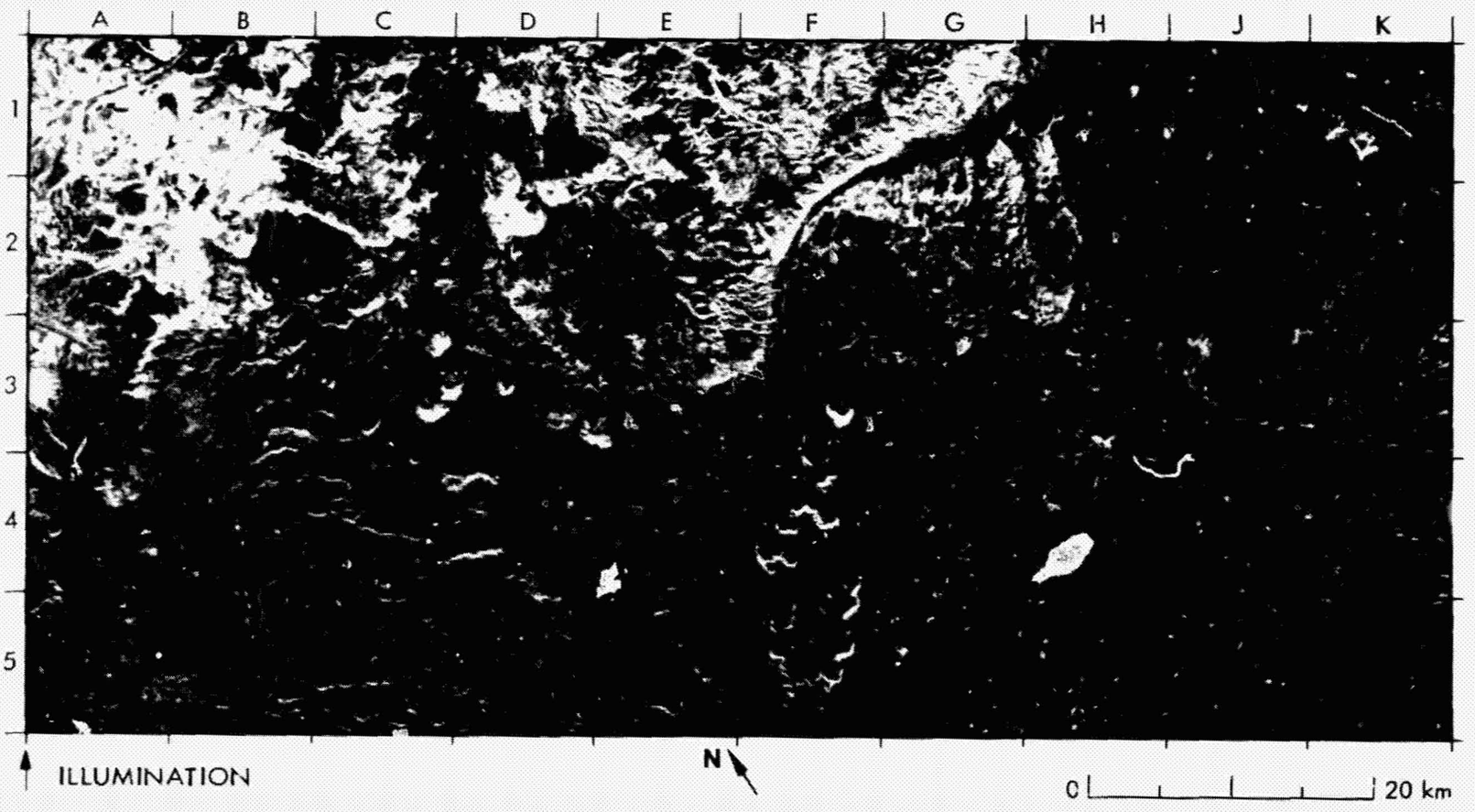

This large dome in eastern Utah is composed of continental and marine sediments that were uplifted and folded in the Late Cretaceous. On this SIR-A image of its southern portion, geologic units can be traced over large areas. The curving structure that extends from G1 to E2, for example, is the San Rafael reef, which is composed of Navajo Sandstone and rocks of the Carmel Formation. Repeated transgression and regression of Mesozoic seas in the area resulted in formations of economic importance, such as coal and the uranium-bearing Salt Wash Sandstone, which was enriched by mineralizing fluids because of its permeability.

The accompanying image was produced from Heat Capacity Mapping Mission (HCMM) data (Ref. 7). The nominal resolution of the HCMM image is 600 m. The area common to the SIR-A swath is bounded by black lines. Bright areas on the HCMM image correspond to high thermal inertia. One formation of high thermal inertia is the massive Navajo Sandstone. The cliffs it forms can be seen on the SIR-A image at D5 and E1 to E2. Low thermal inertia formations include unconsolidated alluvial deposits in the San Rafael Desert at H1, H2, K1, and K2, and the Tununk Shale at D5 and E5.

(The text is by courtesy of D. L. Evans.)

HCMM

ORIGINAL PAGE IS
OF POOR QUALITY

3. Santa Ynez Mountains, California, U.S.A.

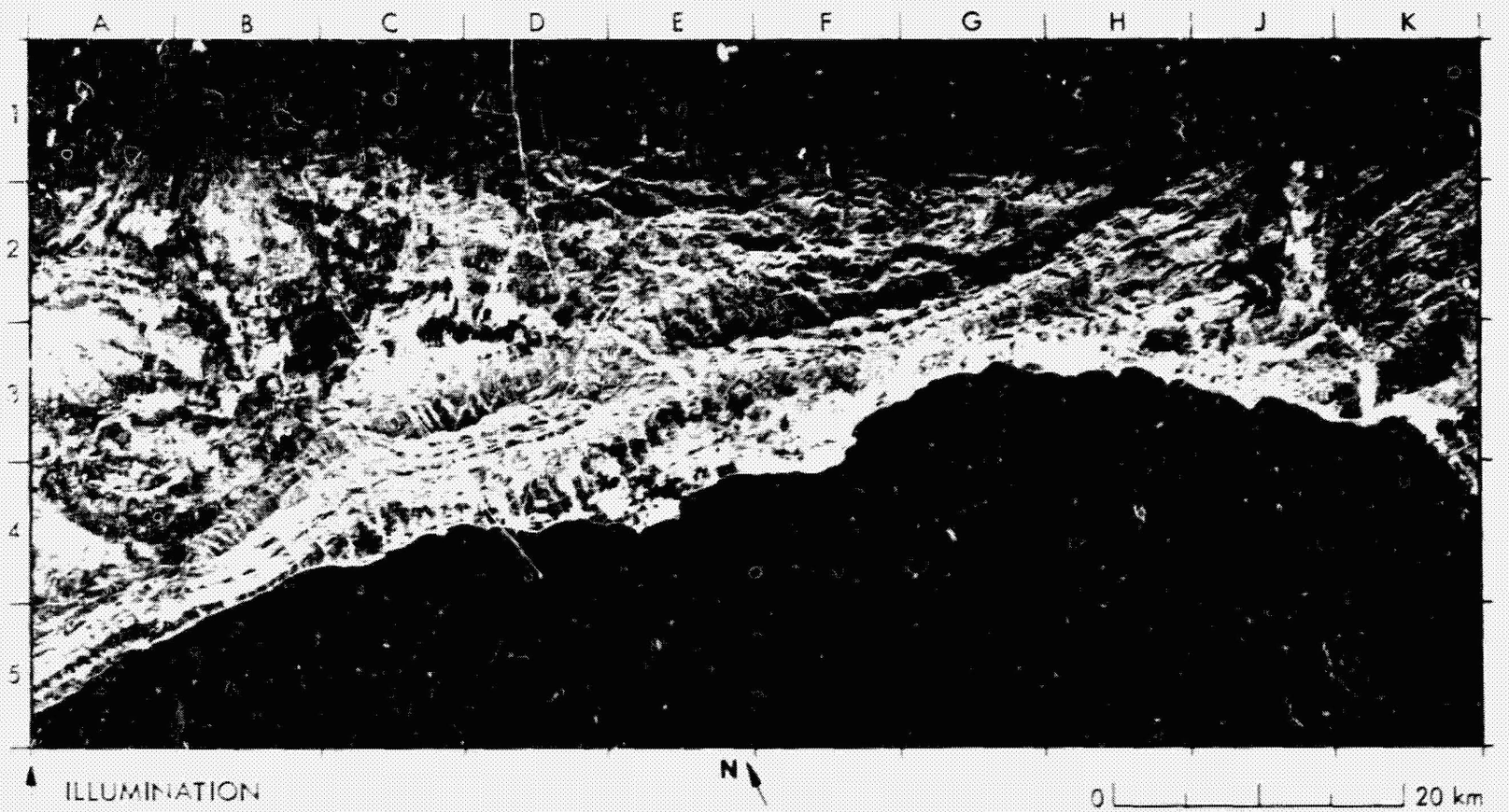

The California coastline from Ventura (K3) westward through Santa Barbara (E4) toward Point Conception is dominated by folded sedimentary layers of the Santa Ynez Mountains (A5 to K1). The large dark features on the image are Lake Cachuma (C2/D2) and Lake Casitas (J2). The Santa Ynez River is visible from Lake Cachuma westward to B3. The strike of the layered rocks in the mountains is clearly displayed by the bright linear tones along the scarp slope from A5 to J1. The bedding is offset by the South Branch of the Santa Ynez fault at B4 and B5. The dip slopes are indicated by the pattern of flatirons to the north. This pattern is abruptly terminated by the Santa Ynez Fault, which extends the full length of the mountains.

Brightness of the terrain on the SIR-A image varies significantly in response to changes in local surface roughness. The Little Pine Fault (D1 to F2), for example, is evidenced by a change from dark on the ocean side of the fault to bright on the mainland side. This is because the smoother Plio-Pleistocene sedimentary rocks south of the fault reflect the radar energy away specularly; however, the more rugged Mesozoic ultrabasic intrusive rocks and the Franciscan Formation to the north scatter the radar energy diffusely and produce bright radar returns.

The mosaic of Seasat images shows significant differences from the

Seasat SAR

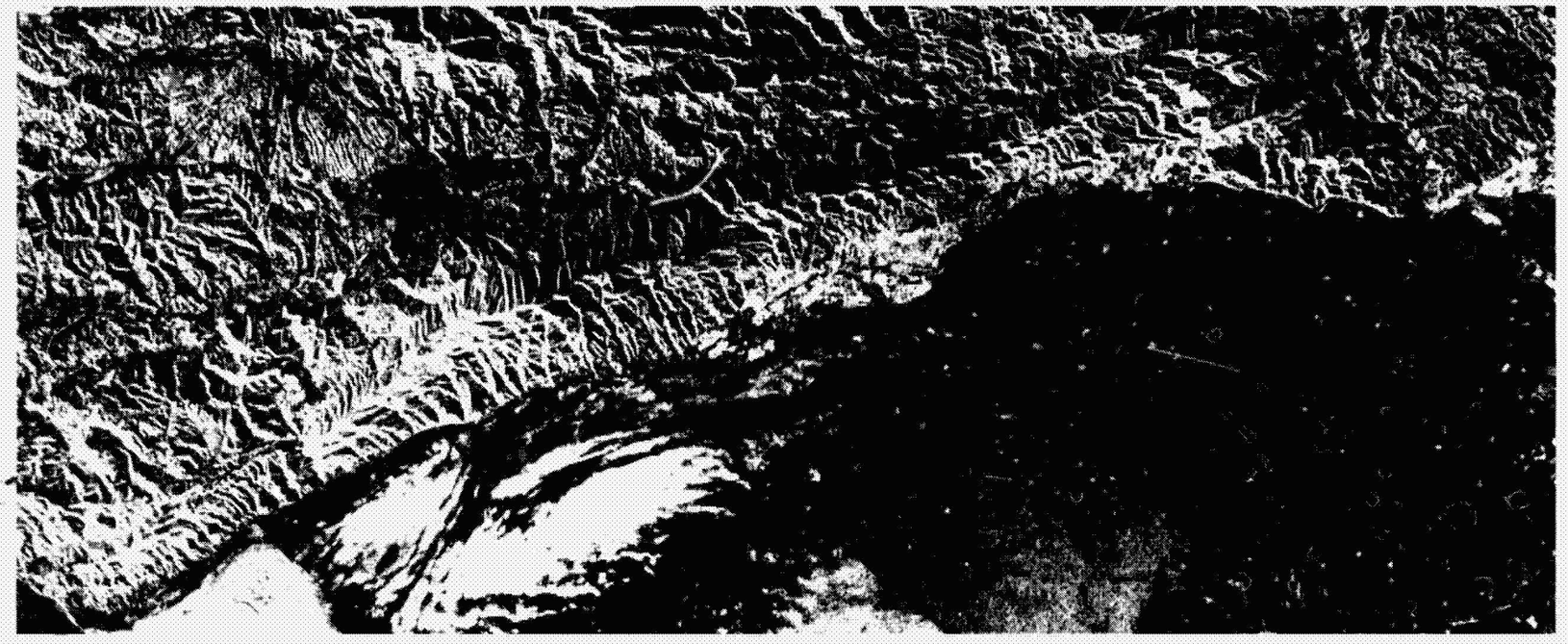

SIR-A image due to such factors as illumination direction, resolution, and incidence angle. Bedding along the Santa Ynez Range on the Seasat image is obscured by the dominant returns from the steep slopes of the drainages; however, on the SIR-A image the bedding is quite pronounced. The drainage channels normal to the coastline are easily traceable on the SIR-A image, but on the Seasat image are obscured because of layover. On the other hand, the obvious drainage patterns on the Seasat image (A1 to C2 on the SIR-A image) are not seen on the SIR-A image. The above differences are due to differences in the local incidence angles of the Seasat and the SIR-A imaging beams.

A further contrast in the Seasat and the SIR-A images that shows the difference local incidence angle can make is seen in the radar returns from the ocean surface. The small incidence angle of the Seasat SAR produces bright tones on the Seasat image due to ocean surface roughness. The large incidence angle of SIR-A produces a black tone on the SIR-A image due to specular reflection. Bright point targets that correspond on both the Seasat and the SIR-A images southeast of Santa Barbara (e.g., G4 and H3) are oil platforms.

A color coregistered image of the Santa Ynez Mountains is given as the frontispiece of this report.

4. Lengguru Fold Belt, Irian Jaya, Indonesia

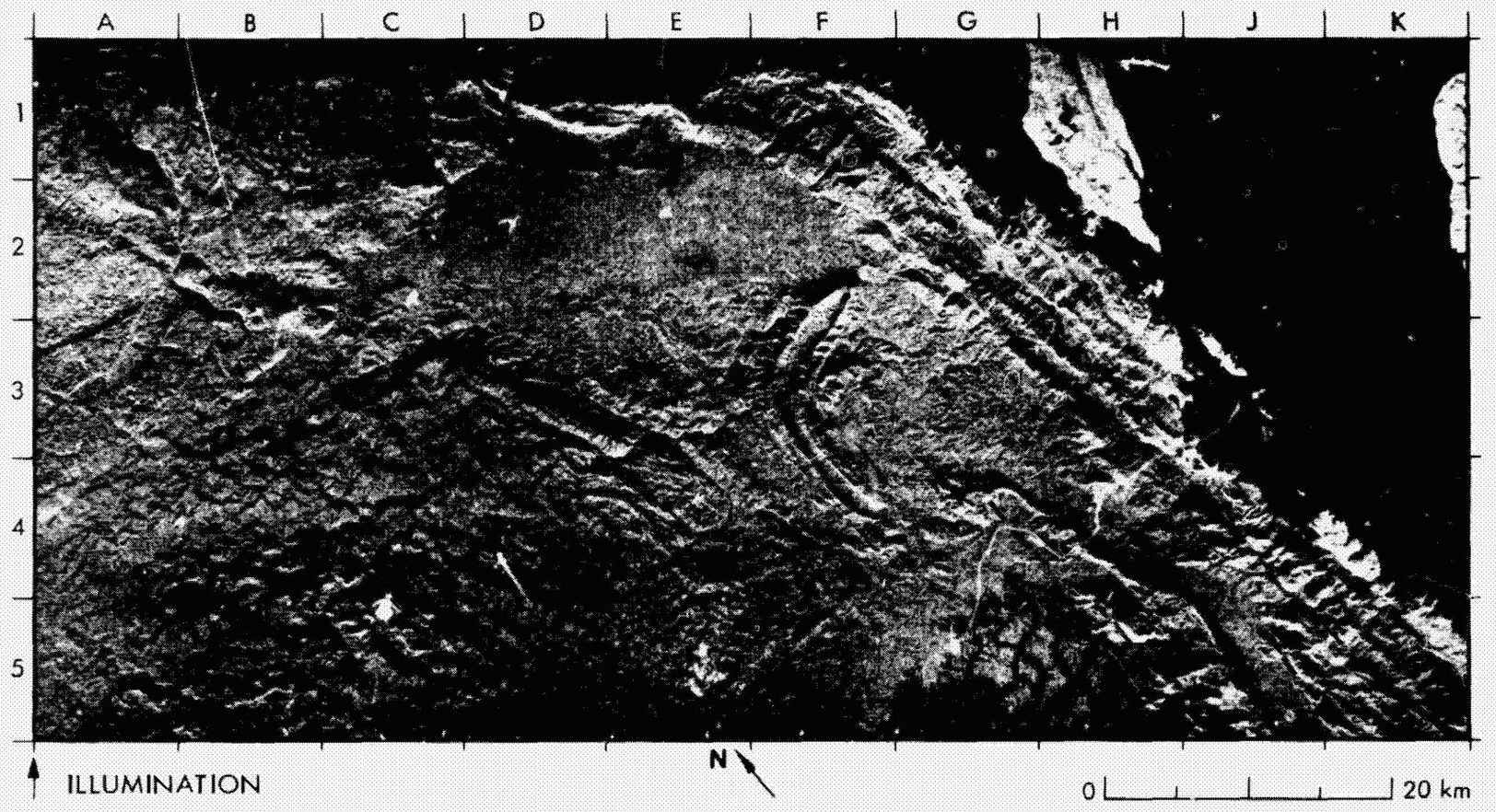

The Vogelkop Peninsula (Jazirah Doberai) of Irian Jaya is located at the north margin of the Australian continental plate. Two widely divergent structural trends dominate the area. The first includes the broad sweep of the mountains from A1 to F1 and the strike of the layered rocks from A4 to D4, which are aligned approximately with the trend of the Sorong Fault zone that lies north of this image. This zone of transcurrent left-lateral faulting marks the boundary between the Australian plate and the Pacific ocean plate; its trends—from west to east to southeast—are mapped on the Mar and the Manokwari geologic quadrangles (Refs. 8 and 9). Axes of plunging anticlinal and synclinal folds that conform with these trends are shown by dashed lines on the SIR-A image at D5, E5, F2/F3, and F5.

The second structural trend is revealed by the fold axes of the Lengguru fold belt (F4 to J3 through J5 to K5), which are oriented toward the north-northeast in the Masikeri Range (K5 to F1). Another major indicator of this trend is a north-northeast fault that passes through Rumberpon Island (H1); it is evidenced by a narrow depression that extends to a linear bay.

The intersection of these two structural trends is spectacularly displayed by the outline of the fold structure at F2 to F4. To the east of this fold, the first trend is superimposed on the second, as shown by numerous east-west linear valley segments (F1 to H3) that transect the north-south-oriented Masikeri Range.

Landsat Band 7

A triangular-shaped area with corners at A1, C1, and A3 has a pitted texture characteristic of a karst terrain with numerous large sinkholes. The karstic nature of this surface is further emphasized by the pattern of jointing (A3 to B3), which is enhanced from the surrounding terrain on the SIR-A image. In contrast, the lowland area from D2/E2 to F5/G5 is a tropical rainforest. The forest canopy of the level D2/E2 area produces a mostly homogenous medium-gray tone on the image, while further south the canopy is modulated by slope effects that reveal the undulating topography. South and to the east, the coastal lowland at the head of Bintuni Bay (G5/H5) shows a distinctive boundary between medium- and light-gray tones. This boundary marks the landward limit of a mangrove swamp.

Few Landsat images of the area are available, and virtually none is cloud-free. The Landsat coverage in the near-IR wavelength shown here is a mosaic of images acquired in November 1973 (right) and in August 1978 (left). While these images are among the best available, they reveal two important shortcomings. First, the topography of the coastal region in the right image is virtually indistinguishable because the solar shadowing is inadequate. Second, most of the landforms on the left image are obliterated by clouds and the shadows of clouds. No Landsat image is available that shows the fold structures seen on the SIR-A image in the area bounded by D3, F2, D5, and F4.

5. West Pilbara Goldfield, Hamersley Range, Western Australia

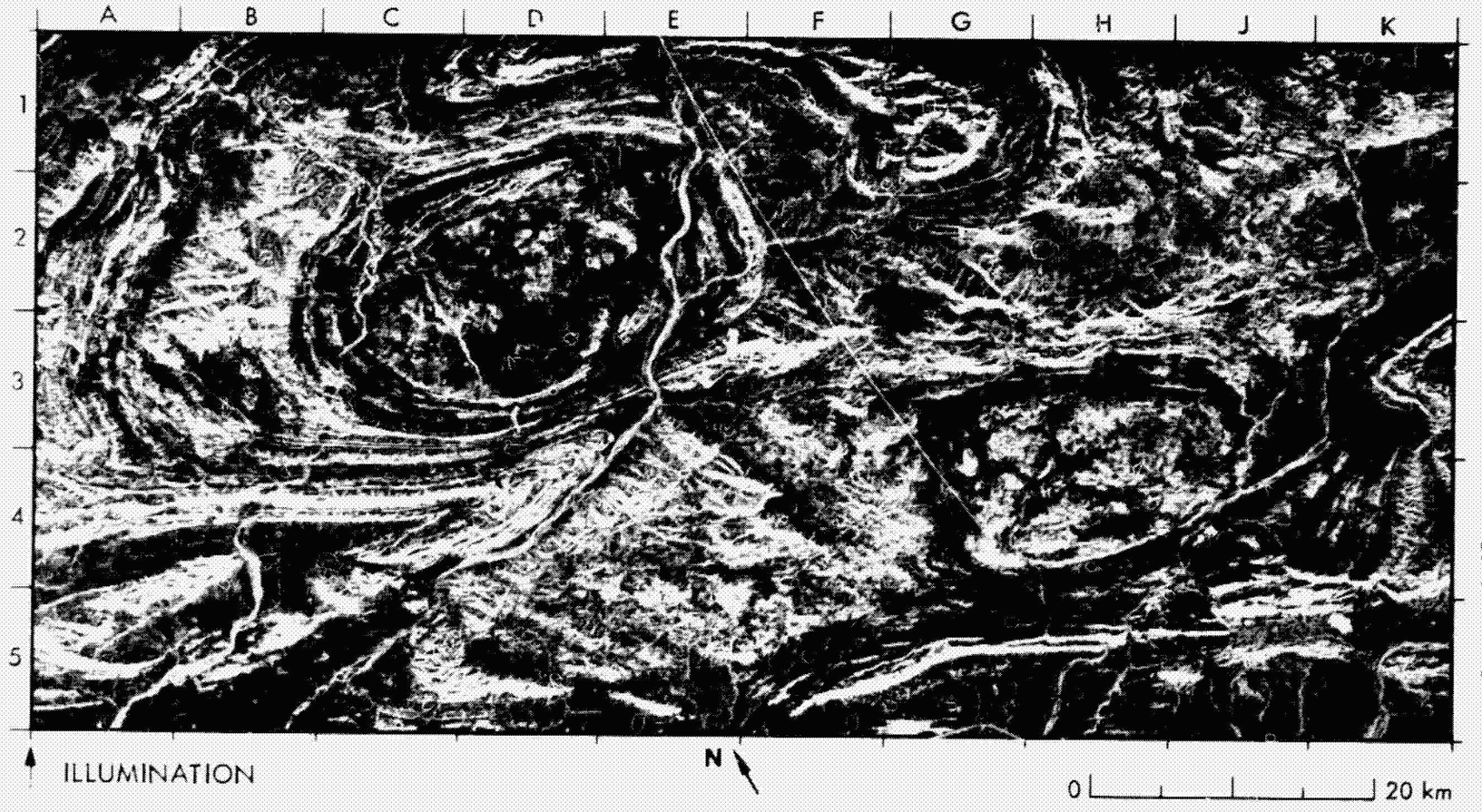

The Hamersley Iron Province exposes the most complete succession of Proterozoic rocks in Western Australia. The outcrop distribution shows that two fold trends have been superimposed, resulting in a dome and basin pattern. The area is noted for massive deposits of hematite that occur in jaspilite on the limbs of major synclines (Ref. 10).

The Rocklea Dome (C2 to E2 and C3 to E3) exposes a core of Archean granite, which appears medium to dark gray. On the Landsat mosaic taken in the visible-red wavelength, the granite is bright. Medium- to dark-gray areas on the Landsat images within the granite core represent pisolitic limonite deposits in old river channels that are not readily perceptible on the radar image. A large north-trending dike that transects the granite from D3 to C2 is bright on the radar image, presumably because of a surface-roughness differential relative to the host rock. The dike is visible but less prominent on the Landsat image to the left of the junction line. Numerous smaller northwest-trending dikes appear as thin bright lines within the granite.

Landsat Band 5

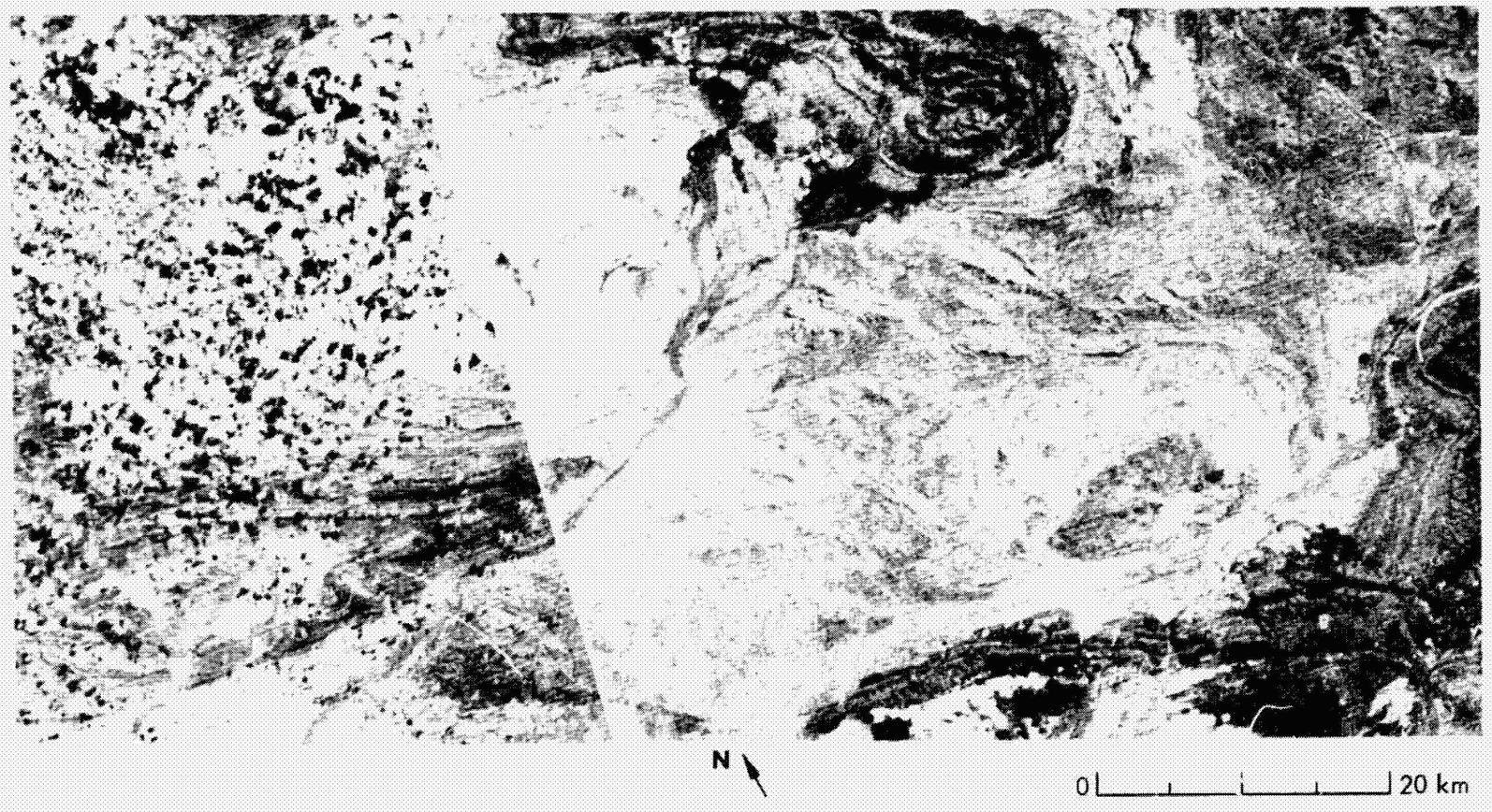

The outcrop width of the surrounding Proterozoic layered rocks varies with the dip. The outcrop width is very narrow at B4 to D4 where the dip is 70 deg or more and quite wide to the west at A2 to B2 and A3 to B3 where the dip is 40 deg or less. Lateral offsets of the outcrop in the area from A3 to B1 result from faults that trend parallel with the small dikes in the granite core. Another prominent dome to the southeast (centered at H3/H4) shows mostly bright radar returns from the core area and medium-gray tones on the Landsat image.

The rocks mapped in this area are Lower Proterozoic volcanics. The outcrop pattern shows plunging synclines centered at G1/G2, from E3 to A5 (Hardey Syncline), and from D1 to F1 (Turner Syncline). A major hematite deposit occurs on the south limb of the Turner Syncline (D1/E1).

6. Sierra Madre Oriental, Coahuila, Mexico

The Sierra Madre Oriental is a fold belt of Jurassic and Cretaceous sedimentary rocks in northeast Mexico. In this scene, which is mostly in the State of Coahuila, there is a strong contrast in the folds on either side of a major corridor (D1 to D5), which contains the city of Saltillo (D2 to D4). To the east of this corridor the mountains are tightly folded and reach elevations in excess of 4000 m. The folds consist of extensive subparallel, doubly plunging anticlines and associated synclines, and the rocks are mostly Jurassic to Lower Cretaceous. West of the corridor the mountains are more gently folded in wide-open patterns and elevations do not exceed 2700 m. The folds are breached, doubly plunging anticlines, and the rocks are mostly Upper Cretaceous. The folds have an east-west trend on each side of the corridor at Saltillo. About 20 km east of Saltillo, this trend changes to the southeast through a broad sweeping curve (H1 to G5).

Landsat Band 6

The mountain slopes support a mixed forest of broadleaf and coniferous trees. On the SIR-A image, the mountain slopes range from light to medium gray, and the radar response is modulated by slope effects. Bedding structure is locally visible (H3 to K3 and J2 to K2). On the Landsat image in the near-IR wavelength, the forested mountain slopes are medium to dark gray, and the albedo is modulated by solar shadowing. Bedding is not seen on the Landsat image. Relatively level, smooth, and partially vegetated surfaces in the intermontane areas are floored with clastic Cenozoic sediments that appear dark gray to black on the radar image (e.g., E3). These surfaces show a high albedo at the IR wavelength and are relatively bright on the Landsat image. Rectangular patterns in varying shades of gray in the lower right part of the radar image (H4/H5 to K4/K5) denote cultivation. This area is in the State of Nuevo Leon.

7. Sibi District, Baluchistan Province, Pakistan

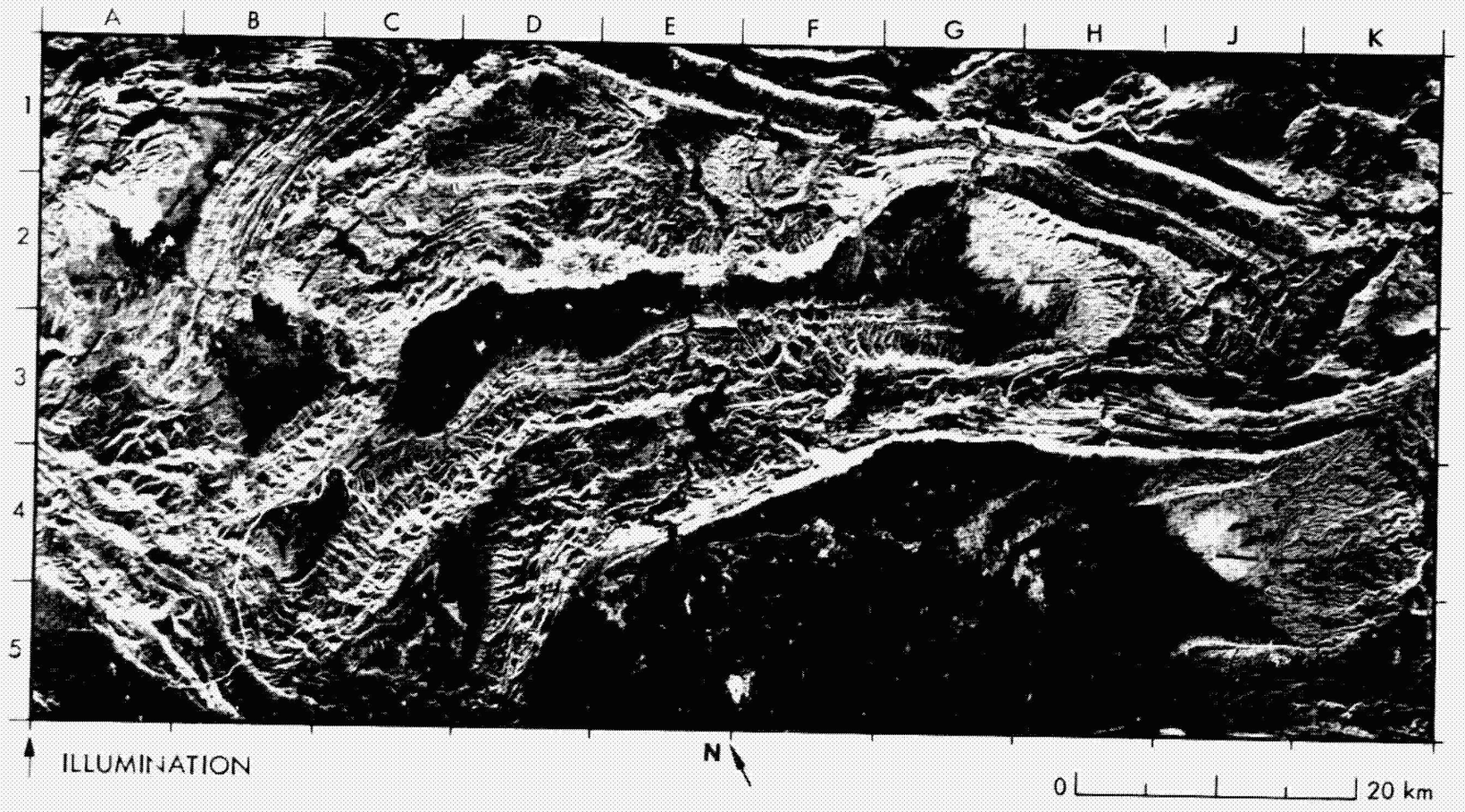

In this arid region of Baluchistan Province, the hills and mountains consist mostly of extensive ridges, and the lowlands are formed by the intermontane basins. The ridges are underlain by sandstone, shale, and limestone strata of Tertiary age. The basins are floored with Quaternary gravel and alluvium. The rocks have been broadly folded and faulted (Ref. 11). Vegetation is sparse and restricted to local areas adjacent to streams as at Sibi (E5/F5). Numerous stream channels that originate in the hills and ridges at about 800 to 900 m elevation dry up on the basin floors at about 300 m. A notable cross-cutting stream channel formed by the Nari River transects the ridges (E3 to E4) and proceeds beyond Sibi to the Kachhi Plain south of the area covered in this scene.

Bedding traces along the ridges are strongly enhanced and appear bright on the radar image (e.g., C1 to B3, and D5 to K3). Steeply dipping to vertical or overturned strata appear as very narrow traces; more gently

Landsat Band 7

dipping strata yield a pattern of flatirons as at F3/G3. The form of the ridges denotes a series of plunging anticlinal structures, as at J5, G3 to J3, G1, and H1. The alluvial cover in the basins yields low radar returns that appear medium to dark gray on the image. The basins are synclinal, and the approximate positions of major synclinal axes are indicated by dashed lines on the radar image. A normal fault from E1 to K2 is evidenced by a remarkable contrast in image texture across this extensive linear feature. Numerous other faults of lesser extent occur in the area of this scene. The Landsat coverage in the near-IR wavelength provides a complementary image. Ridges are dark, and enhanced by solar shadowing. The enhancement is less pronounced than on the SIR-A image. Alluvial deposits in the basinal areas provide a high albedo, and appear very bright.

(ii) Linear and Intrusive Structures

8. Kalpin Chol and Chong Korum Mountains, Xinjiang, China

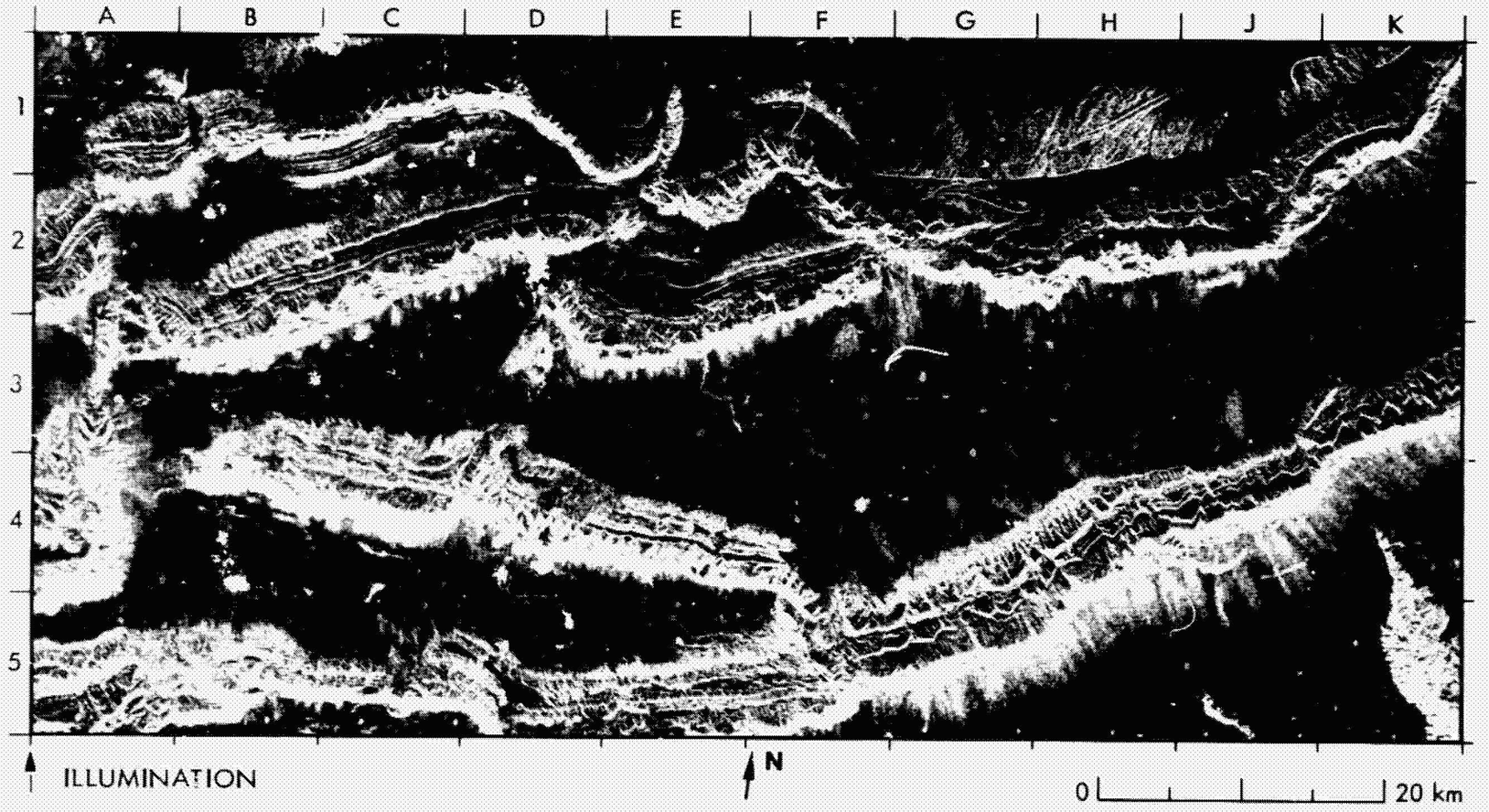

One of the most striking examples of extensive linear structures seen on SIR-A and Landsat images is displayed here by the Kalpin Chol Tagh (mountains) and the Chong Korum Tagh in northwest Xinjiang Province, China. These mountains have been folded and faulted from late Tertiary to Quaternary times. The area exhibits active tectonism and intense earthquakes.

The lineament from A1 to A5 is a fault with up to 10 km of horizontal displacement. The lineaments at B5 and C5 are active faults that offset the Kalpin Mountains. An earthquake of magnitude 6.8 on the Richter scale was recorded along the fault at C5 in 1961.

Dip directions in the area bounded by B2, B3, D2, and D1 indicate the presence of a syncline that plunges to the west-southwest. The pattern of flatirons (e.g., K3 to G5) denotes the dip direction of the layered rocks that underlie the dip slopes. Rock slides on the north side of the mountains (D4 and C5) locally obliterate traces of the bedding. Bedrock consists primarily of limestone, sandstone, and shale sequences of Lower-Paleozoic age.

Comparison of the SIR-A and the Landsat images shows significant

Landsat Band 7

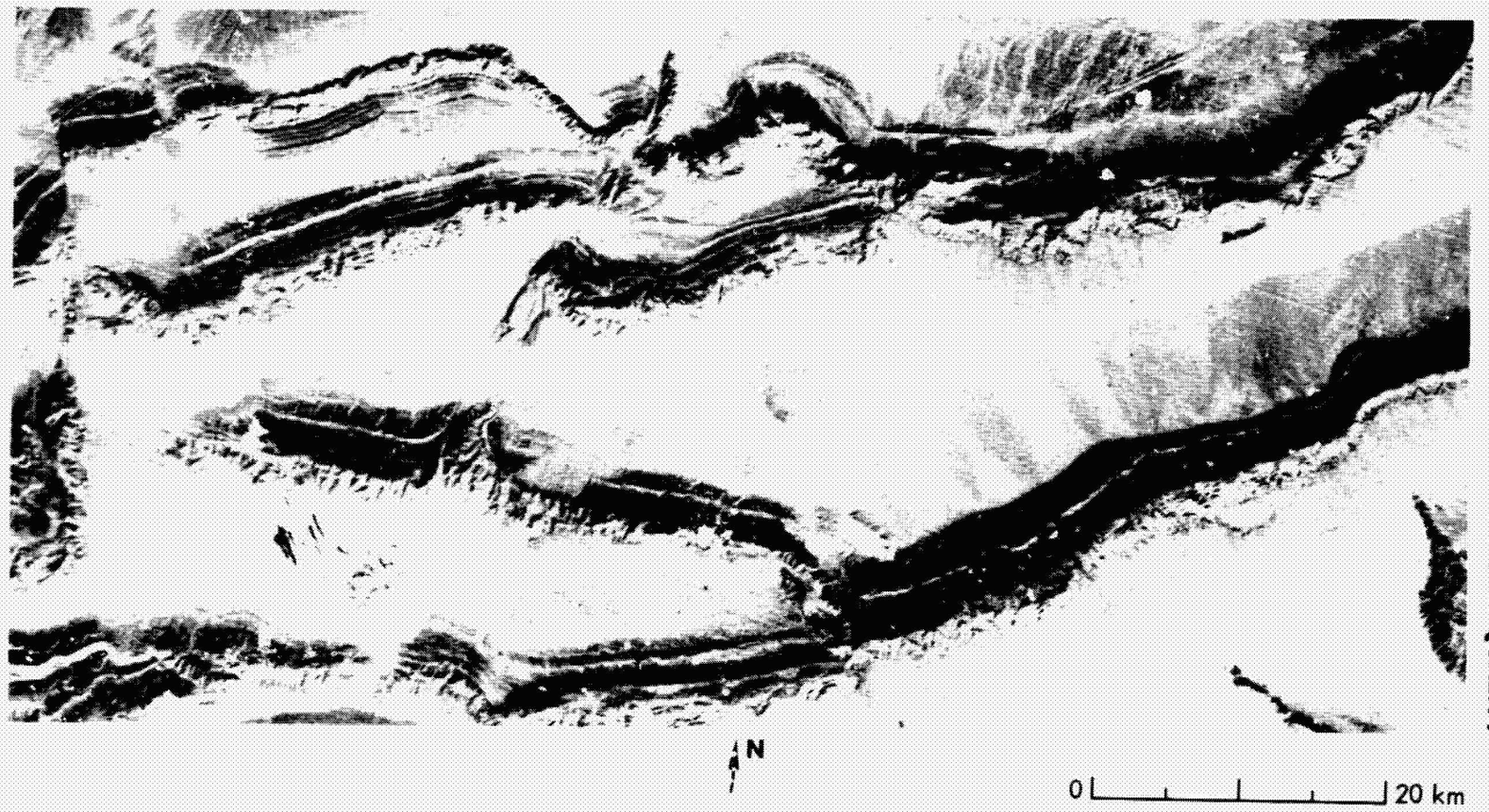

differences. Geometric compression of the scarp slopes along the south side of the mountains results in bright radar returns that obscure the details present on the Landsat image, which lacks this compression. Bedding structure on the dip slopes is enhanced on the SIR-A image because of radar sensitivity to the change in slope, but less clear on the Landsat image because of shadowing. Alluvial fans at the base of the slopes (e.g., from K1 to D3) show more contrast on the SIR-A image because of the sensitivity of the 23-cm wavelength radar to small changes in gravel size. In the intermontane basins, fine-grained alluvium and salt deposits appear dark on the SIR-A image but bright on the Landsat image. The alluvium and the salt deposits show specular reflection on the long-wavelength radar (SIR-A), but are highly reflective in the near-IR wavelength (Landsat).

The small lake at E3/F3 shows a bright halo that is probably the result of local vegetation.

9. Sierra imeri, Amazonas, Venezuela

The portion of the Amazon rainforest shown here is in Venezuela, about 50 to 70 km north of the Brazilian border. Detailed maps of this remote area are not available. The dense vegetation yields a generally uniform medium- to light-gray tone on the SIR-A image. Despite this heavy cover, the topography of the area is well displayed on the radar image, because slope effects locally modulate the backscatter to produce bright tones at foreslopes and dark-gray tones at backslopes.

Such effects are noticeable in the area of the dissected plateau from A5 to D2/E2 to E5. This plateau is underlain by ancient layered rocks that are the equivalents of the Roraima Group in Brazil. Linear escarpments and canyons in the plateau are probably fault-controlled. Subtle changes of gray level on the east-facing pediment slope below the plateau from

Landsat Band 7

A4 to D2 may reflect vegetation changes.

The dissected mountains east of the Rio Siapa (F1 to F5) are underlain by Archean granitic rocks that have been tectonically deformed. The tectonism has produced a strong northwest jointing pattern that is clearly displayed on the SIR-A image in the area bounded by G2, F5, J5, and K1. This corresponds with a regional tectonic trend that has been mapped in adjacent areas of Brazil. The circular feature at D3, D4, E3, and E4 is probably a pluton or a carbonatite.

The Landsat coverage shown here in the near-IR wavelength is a mosaic of the best available images (i.e., those with the least cloud cover). These Landsat images show very little of the topographic features seen on the SIR-A image.

10. Eastern Desert, Egypt

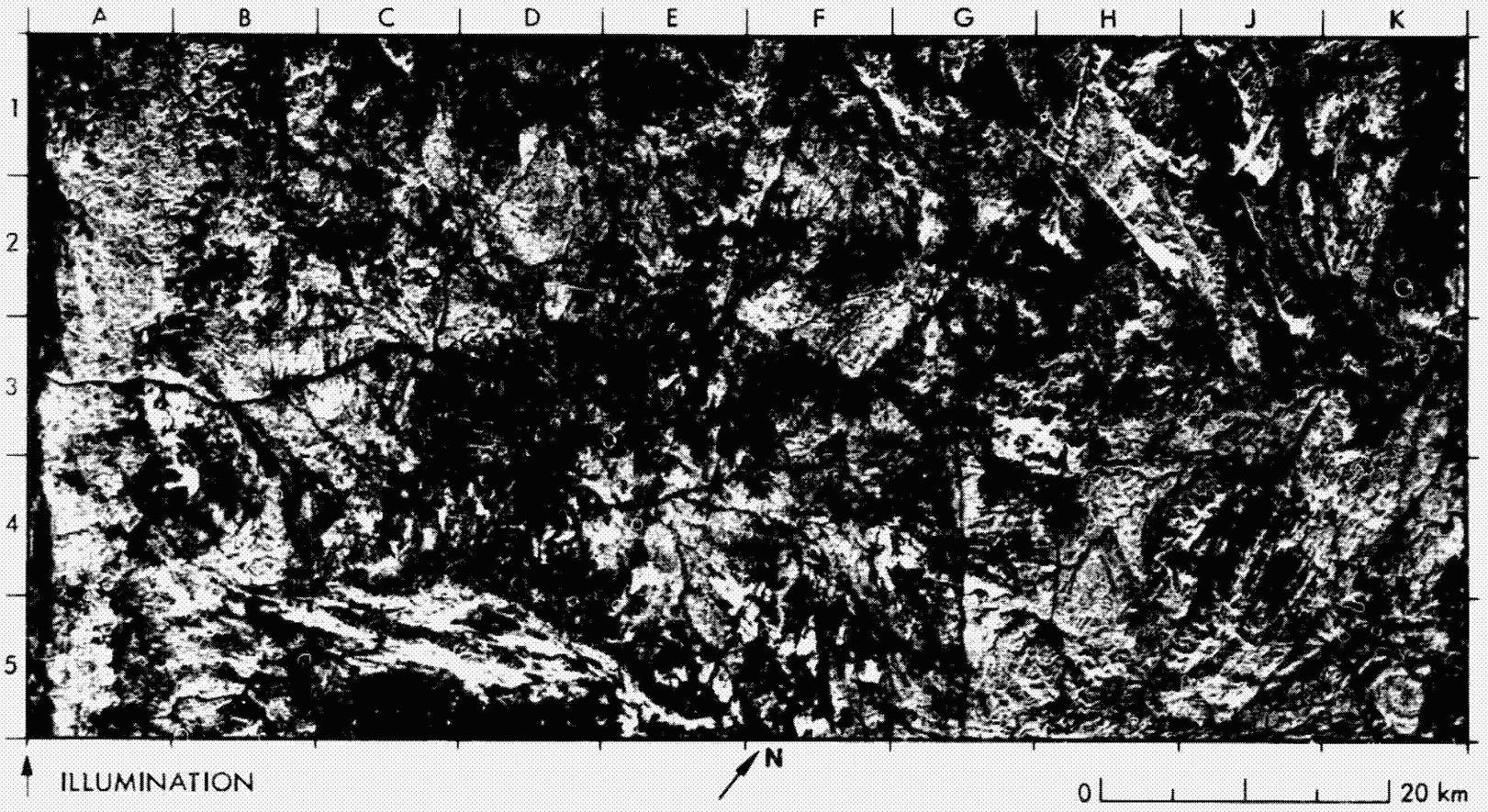

This desert is a late-Precambrian shield between the Nile River and the Red Sea. It is approaching a peneplained condition, and major rock types can often be distinguished on the basis of their outcrop morphology.

Ultramafic bodies occur in areas of high relief (B4/B5, C4/C5, D5, and E5), which appear bright on the radar image. Granite plutons are characterized by their circular outline and by the presence of dike swarms (D3). Resistant outer zones of the plutons form high-standing hills (bright) that surround strongly weathered cores (dark) as at H1/J1. The plutons intrude a metavolcanic-metasedimentary complex, which makes up the remainder of the Precambrian outcrop area.

On the Landsat image (near-IR wavelength), the high-standing hills appear dark, but the weathered cores have a high albedo and appear bright. Nubian Sandstone appears bright on the radar image and shows a distinctive dendritic drainage pattern (A1 to A5). Recent sand and gravel are smooth at the radar wavelength and they appear dark, especially along the dry river beds (wadis) as from A3 to D2 and E4 to G2. On the Landsat image, the dry river beds are bright.

Major faults are also apparent on the radar image, some of which have not been previously mapped. The age constraints on some of the units affected by faults or lineaments allow construction of a relative chronology among three lineament sets observed on the radar image.

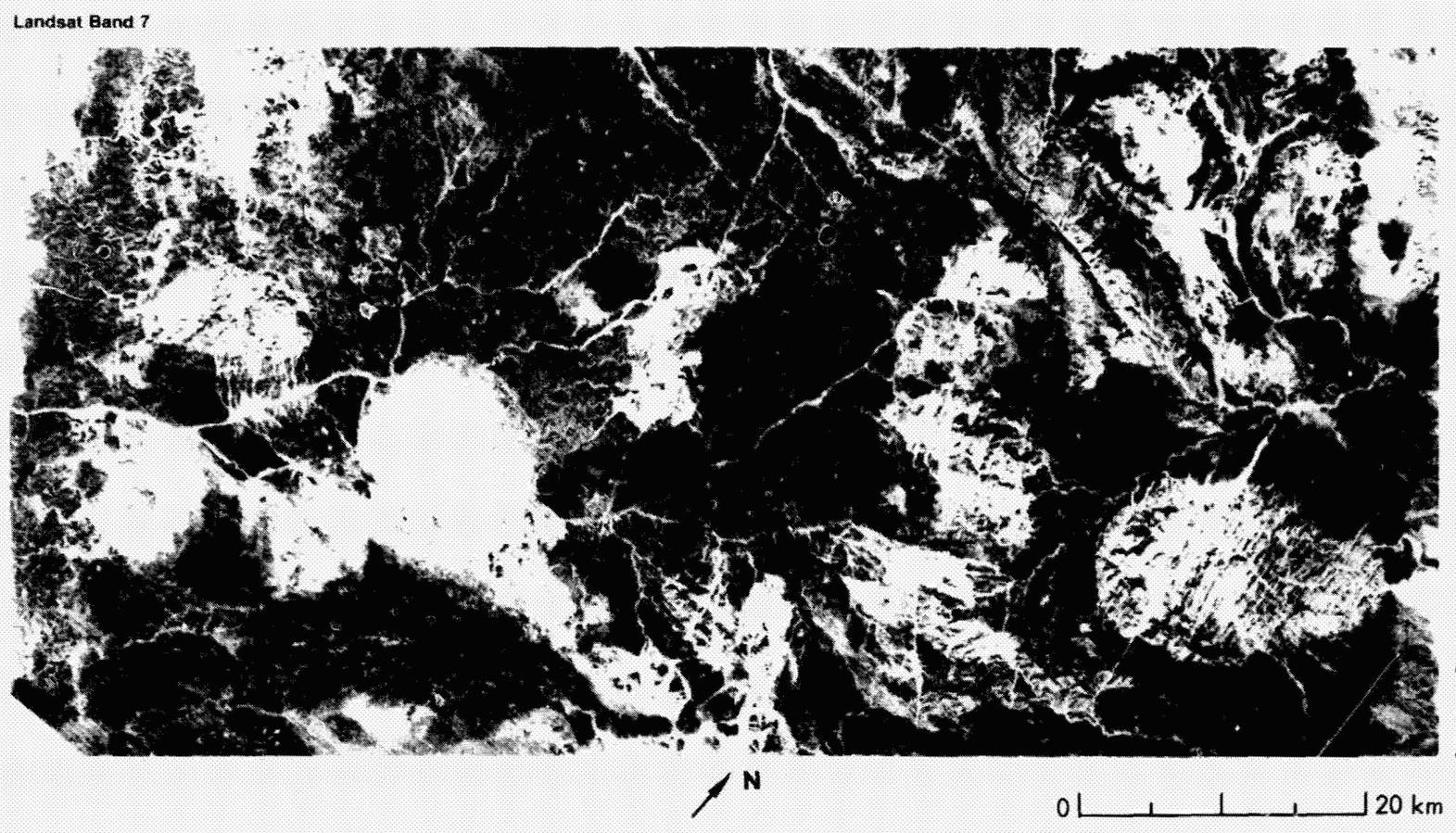

The oldest lineaments trend west-northwest (E1/F1 through F2). They do not visibly cut any of the granite plutons, and they are displaced by faults in the second lineament set, which have a northerly trend, such as that from F1 to E5. A left-lateral displacement of 2 km on this fault is observed in the pluton at E2/F2. The strike of this fault is approximately parallel to that of the Dead Sea-Gulf of Aqaba Fault, which is an active left-lateral transform fault. Another fault in this second set transects the Gebel Kadabora pluton at J4. This major north-trending fault set was therefore active after intrusion of the posttectonic plutons; it may be related to post-Cretaceous transform faults associated with Red Sea rifting. The offset on the Gebel Kadabora fault is more clearly displayed on the Landsat image.

The third lineament set trends northwest, parallel to the Red Sea coast in this area. A major fault in this set (A1 to A5) provides a strong contrast on the radar image between bright tones from the Nubian Sandstone on the upthrown side and dark tones from the Recent alluvium that covers the downthrown side. This feature is an extension of previously mapped faults to the north and south. It forms part of one of the longest well-defined lineaments in the Eastern Desert.

(The text is by courtesy of T. H. Dixon.)

11. Sahara Plateau, Mali (West Africa)

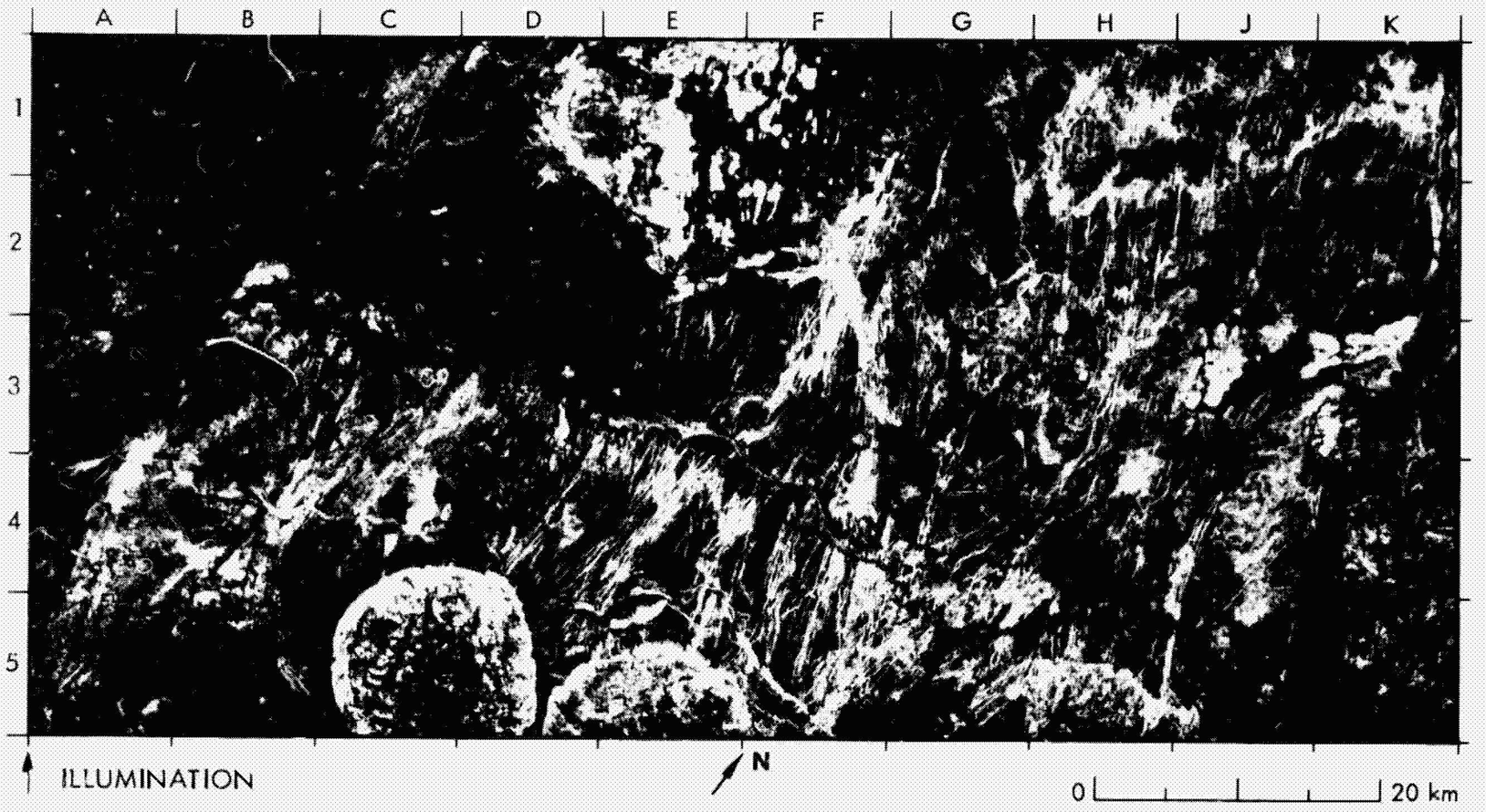

Approximately 300 km west of the boundary point common to Mali, Niger, and Algeria lies this exceptionally arid area in eastern Mali, which is inhabited by only nomadic tribes. It is underlain by a Precambrian gneissic basement assigned to the Kibaran orogeny (900 to 1100 Myr). The basement has been widely intruded by younger granite plutons and associated dikes. The plutons form circular mountains with sheer cliffs that rise about 200 m above the surrounding plateau. They appear very bright on the SIR-A image, particularly around their margins; notable examples are Adrar Idjounyan (C5/D5) and Adrar Ilebjan (D5 to F5). Other less topographically distinct plutons occur from G5 to J5, K1 to K3, and in the area bounded by D1, F1, E2, and F2. Smooth level areas within the plutons are eroded cores that appear dark on the radar image.

Thin, bright wavy lines through the plutons conform to the trend of adjacent dikes, which parallel the north-south regional tectonic structure in the area. Local deviations from this trend occur as an arc (F4/G4) where the dikes trend northwest toward the pluton at F2. They may be

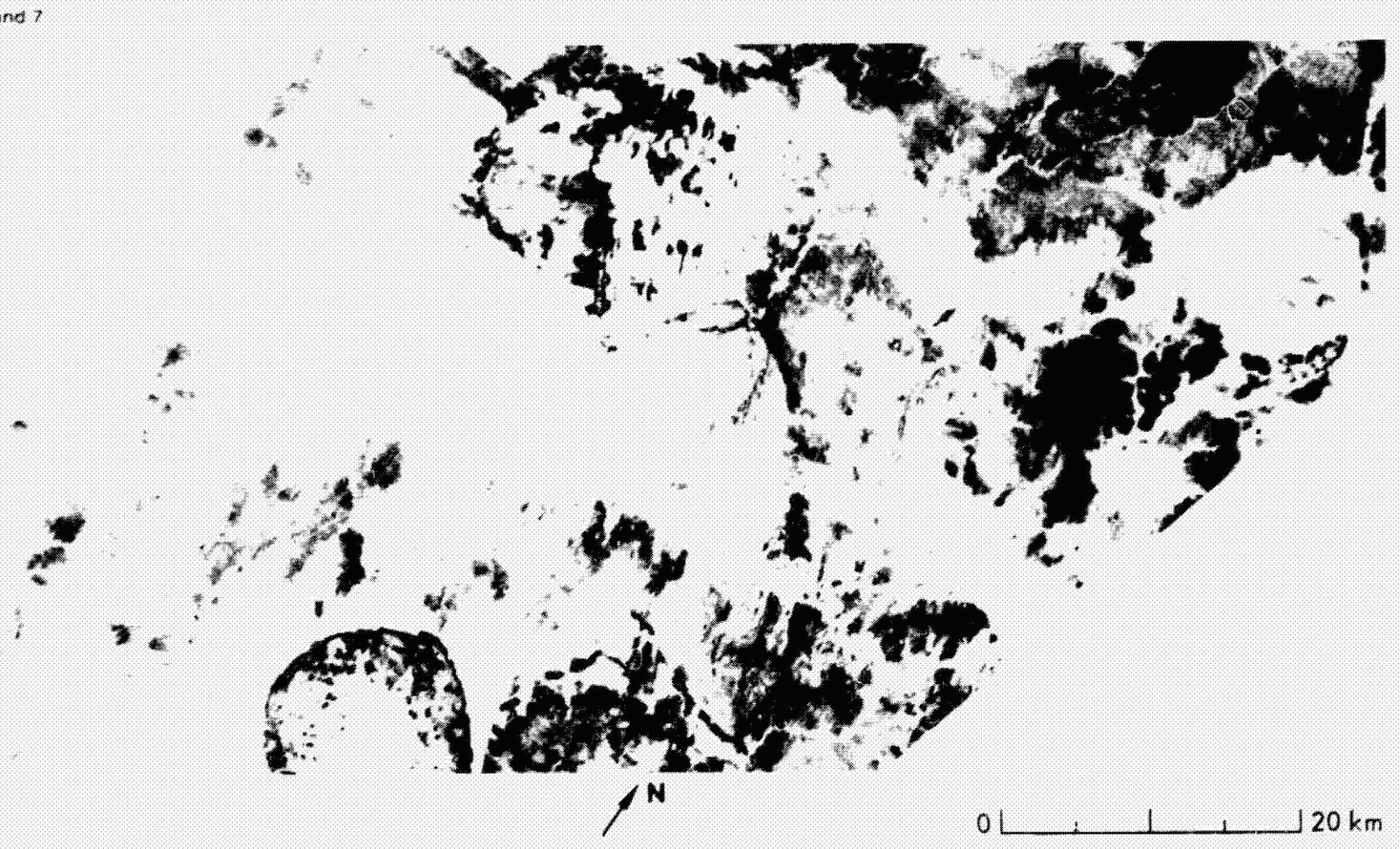

feeder dikes associated with the intrusion of the pluton. Linear offsets a' E2/F2 and H2 denote postintrusion faulting. Offsets on the northwest margin of Adrar Idjounyan (C4/D4) are oriented to the northwest. The total area occupied by the dikes in this scene suggests that a substantial degree of east-west dilation must have occurred to allow their emplacement.

Level areas of stabilized sand on the Sahara Plateau are very dark on the image, as are drainage courses filled with sand (A1 to D3). The area is drained by the Tilemis Valley southward some 200 km to the Niger River. The Landsat image in the near-IR wavelength was acquired about 9 years before the SIR-A image, at the same season in November. On the Landsat image, the rock outcrops are dark, while smooth sand-covered surfaces are bright. The outlines of the plutons are moderately clear though the dikes are obscure.

12. Salt Domes, Great Kavir, Iran

These domes lie southeast of the Caspian Sea among deposits that range in age from Eocene to Miocene and form part of the Central Iranian Depression. The elliptical domes are 5 to 8 km across the major axis. Surface roughness probably accounts for the very bright radar returns of the central part of most domes on the image, but local slope conditions are likely responsible for the strong signals at those margins that lie normal to the radar illumination. Several dome-like features that appear on the SIR-A image (e.g., G2 and H2) are not shown on the geologic map of the area (Ref. 12).

The relation of the intrusive domes to the surrounding sedimentary rocks is seen clearly at F1/F2 through G1/G2. The predominant formation is the Upper Red, the middle part of which is dark in tone; the upper part is brighter and folding is more apparent. Swamp and mudflat deposits overlay this formation unconformably (see sketch map). The southwest portion of this image from A3 to A5 through C3 to C5 is a large salt flat. The boundary of this flat (see sketch map) is very bright and irregular.

Thrust faults in this area (H1 to K2 and D3 to H5) have a bright linear appearance on this image. Synclines and anticlines (D2/E2 and H4 through K3 to J5) show distinct outcrop patterns.

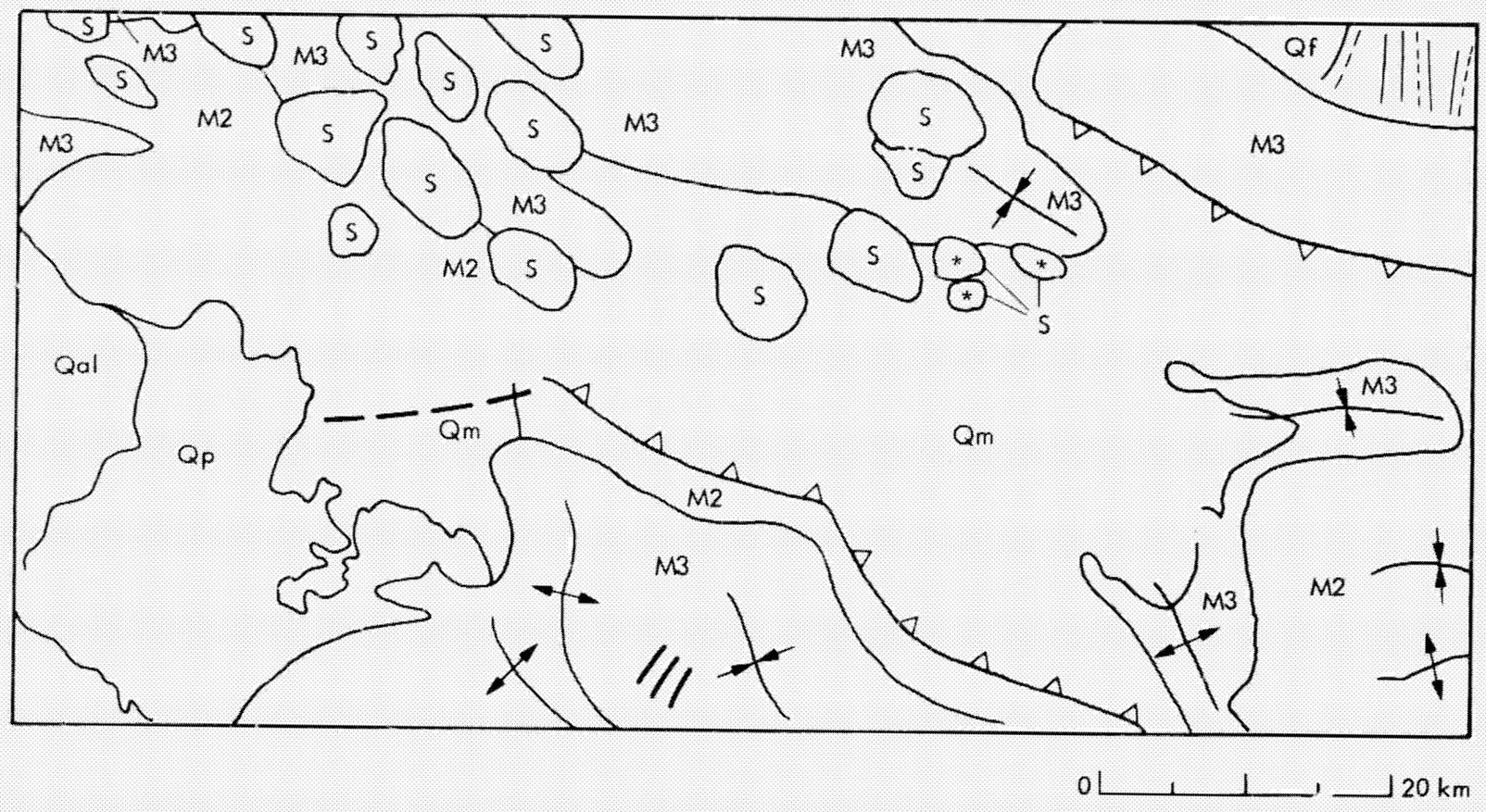

QUATERNARY	Qal	ALLUVIUM
	Qf	ALLUVIAL FANS
	Qm	SWAMPS, MUDFLATS
	Qp	PLAYAS, SALT FLATS
MIOCENE	M3	UPPER PART OF THE UPPER RED FORMATION
	M2	MIDDLE PART OF THE UPPER RED FORMATION

ANTICLINE

SYNCLINE

THRUST FAULT

FAULT

S SALT DOME

* INDICATES UNMAPPED AS OF 1977

13. Altyn Tagh Fault System, Gansu, China

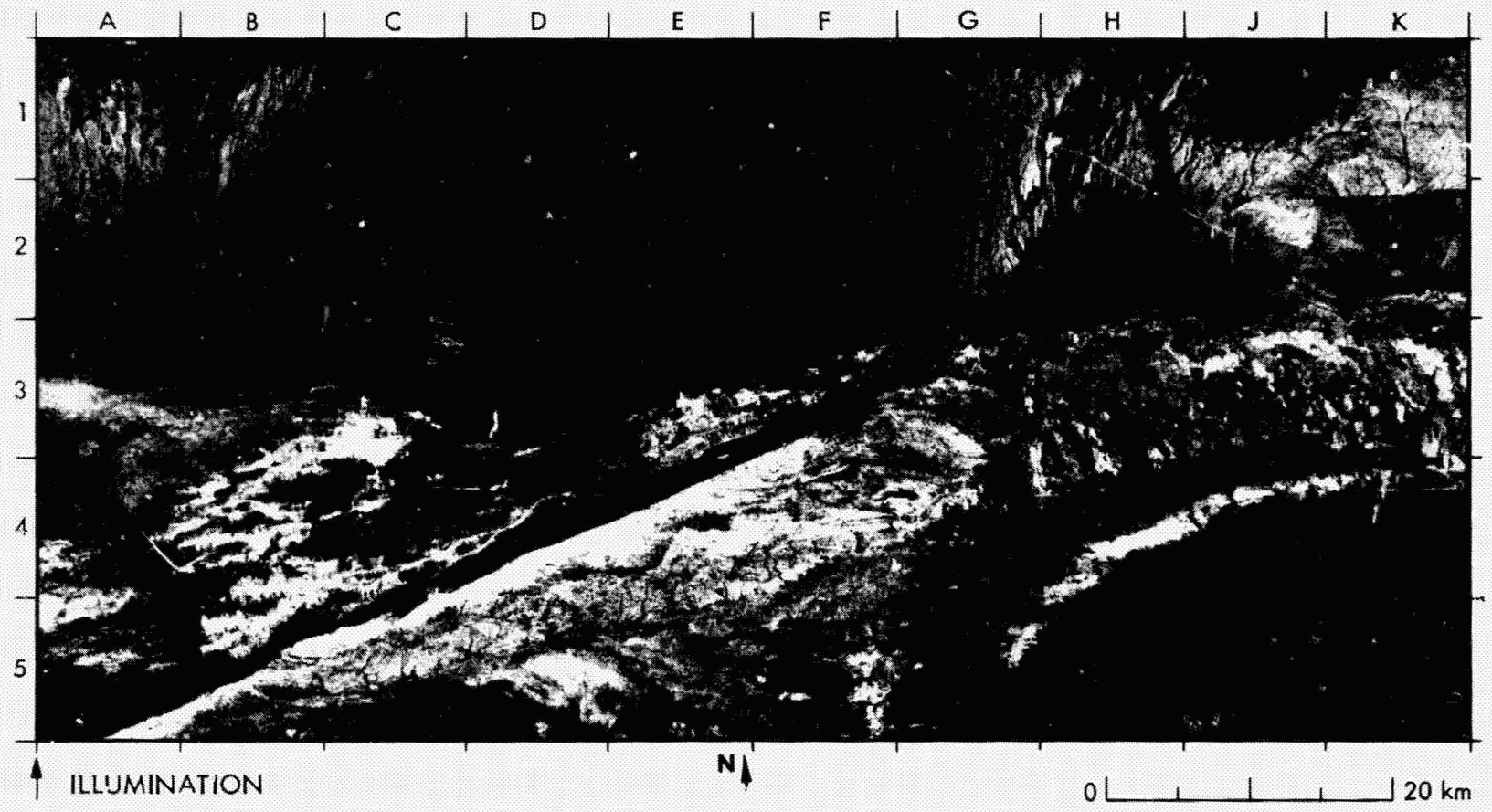

The linear topography from A5 through G3 to K2 represents the surficial expression of a complicated thrust and strike-slip fault system in north-central China. The system shown in this SIR-A image is a linear extension of the Altyn Tagh Fault to the west, and, to the east, it bends southeastward to join the Gansu Fault. The Altyn Tagh and the Gansu are major left-lateral strike-slip faults. The faulting and deformation extend over 3000 km, from west of the Tarim Basin to the Shanxi Graben (Ref. 13).

The trace of the fault from A5 to G3 is marked by a strong contrast in image tone. Truncation of ridges and left lateral drag are most evident from G3 to D4. The fault and truncated ridges are clearly evident on the Landsat image in the near-IR wavelength. The abrupt change of gray tone in the upper parts of J2 and K2 on the SIR-A image probably represents a fault that separates bedrock outcrop (bright) from alluvial cover (medium to dark gray). A corresponding change of image tone is not evident on the Landsat image.

A large alluvial fan in the area from K5 through K4 to G5 on the radar image is mostly dark gray, probably due to low backscatter from smooth surfaces. Bright radar returns along the outer margin from G5 to K4 indicate coarse-grained sand deposits at the base of the fan. To the east,

Landsat Band 7

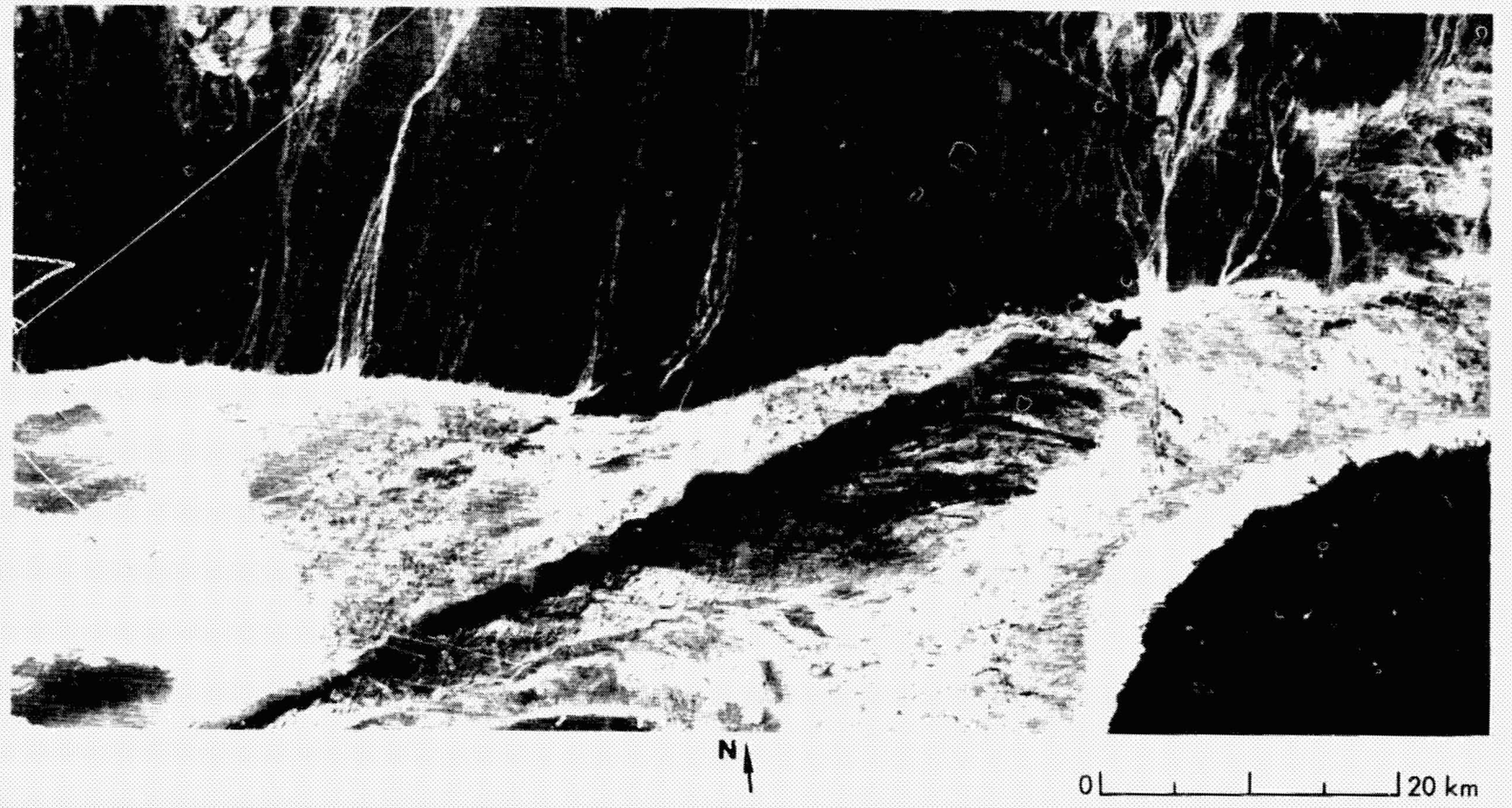

beyond the limits of the image, much of the water that reaches the fan from the Shule Nan Shan (mountains) to the south is diverted by canals for irrigation. The Shule River flows north through the fan (off the image to the east) and bends sharply to the west at K3. From there it drains west to an interior basin beyond A3, closely following the foot of the alluvial cover in the upper half of the image. This cover is at the foothills of the Bei Shan, off the image to the north. It is easier to follow the drainages in the alluvial cover on the Landsat image. However, differences in image tone across the alluvial cover on the SIR-A image suggest differences in gravel size that are not evident on the Landsat image.

The area receives less than 100-mm annual rainfall and it is sparsely populated. Irrigation permits limited agriculture in the Shule valley, as seen by the pattern of fields adjacent to the town of Anxi (C3), and at E4/E3 to F3. The dominant crops consist of millet, corn, and winter wheat. A reservoir and dam on the Shule at G3 on the SIR-A image are more strongly contrasted on the Landsat image. Thin bright lines from A1 through C3 to H3 and from F1/G1 to K2 represent road and rail routes, respectively.

(iii) Dissected Plateau and Plains

14. Pakaraima Mountains, Guyana (South America)

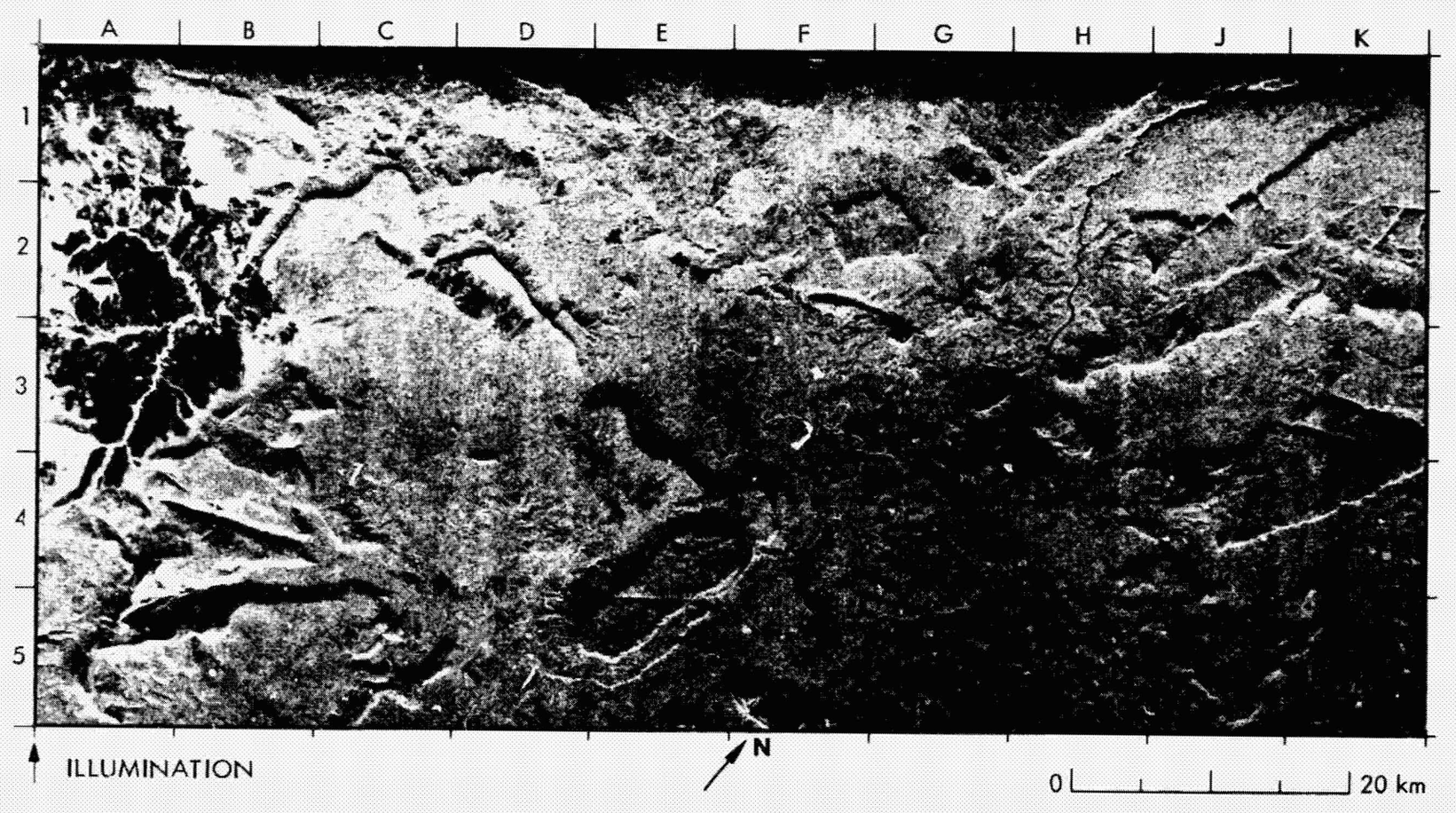

The Pakaraima Mountains in western Guyana are a series of dissected plateaus and mesas with elevations from 1000 to 1500 m. The area is covered by a dense tropical forest that yields a generally uniform medium-gray tone on the SIR-A image, except at A1 to A3/B3, where the forest gives way to savanna grassland. Deep precipitous canyons cut the plateau; the canyons are enhanced on the image by bright returns at the foreslopes and shadowing at the backslopes.

The upland is directly underlain by flat-lying sedimentary rocks of the Roraima Formation. The plateau escarpment (B1 through E4) follows an easterly linear trend for about 40 km.

The wide lowland valleys are underlain by mostly basic igneous intrusive rocks of Mesozoic age. Extensive linear segments of stream

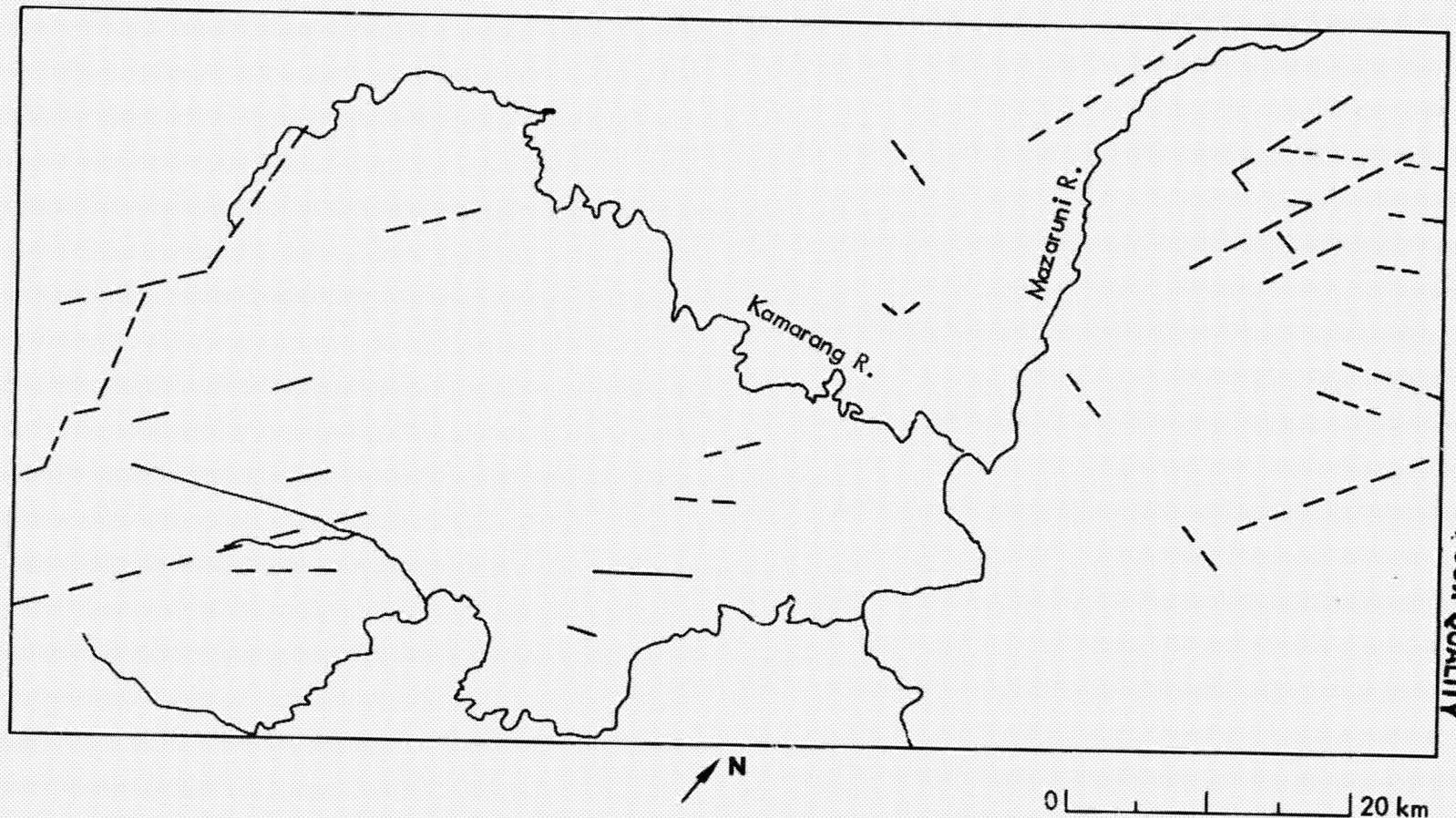

valleys and drainages are shown by dashed lines on the accompanying sketch map; these features are structurally controlled. The Kamarang River channel (A4 through B1) shows linear offsets that follow joints and/or faults. The Masaruni Valley is situated in a north-trending linear trough (H1 through K1) about 10 km wide.

There is a subtle textural difference on the radar image between the plateau and the lowland valleys. This difference is most pronounced in the area bounded by H2, F3, G5, J5, and G3. The relatively small dark-gray lowland areas adjacent to major streams (e.g., F4/F5, A4/A5, and D2/E2) are forest areas cleared by slash-and-burn methods to make room for transient subsistence agriculture. Very few Landsat images of the area are available—none are cloud-free.

15. Plains and Forest Lowland, Meta, Colombia

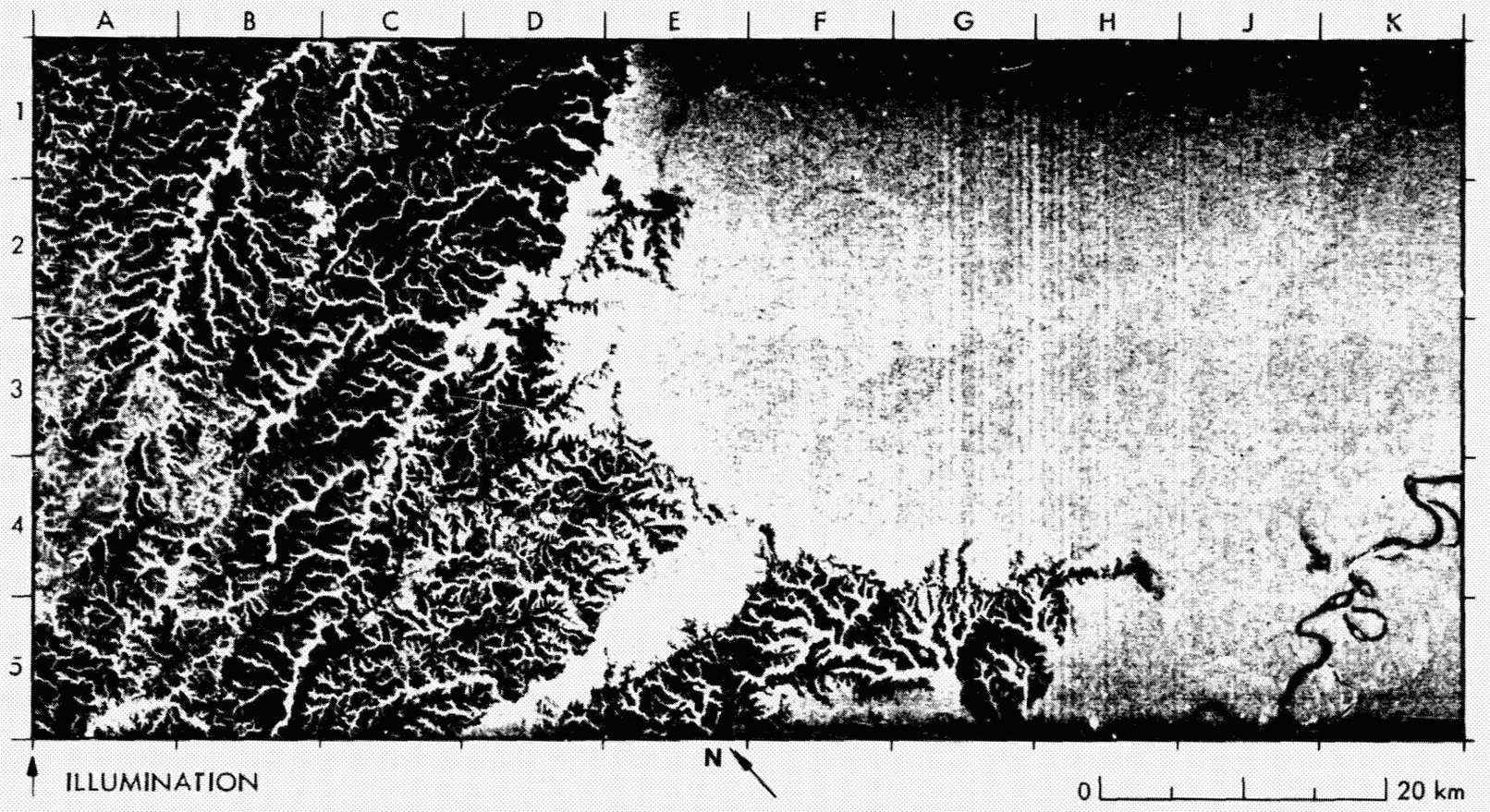

This scene in east-central Colombia covers part of the upper southwest drainage of the Orinoco Basin. The region is drained northeastward by the Guaviare River (J5 to K4), which is a major tributary of the Orinoco, and by numerous smaller tributary streams. The terrain shows a strong contrast in elevation and surface cover.

The dense tropical rain forest to the south and east lies at elevations mostly below 100 m. This forest canopy provides uniformly bright radar returns over a large area, and obscures the channels of small streams that can be seen only with difficulty (e.g., from D5 to K1). Abandoned meanders of the Guaviare, however, are outlined by their horseshoe shape, and by the strong contrast in image tones from black (open water) to medium and light gray (forest). Bright tones that locally outline sectors of the abandoned meanders probably come from vegetation standing in water. Bright tones also mark a former position of the stream channel (J5/K5), where it has been filled in by vegetation and accreted sediment.

To the north and west, the surface consists mostly of dissected plains with a predominant grassland cover. The boundary with the rain forest is strongly marked on the radar image by a contrast from bright to

Landsat Band 7

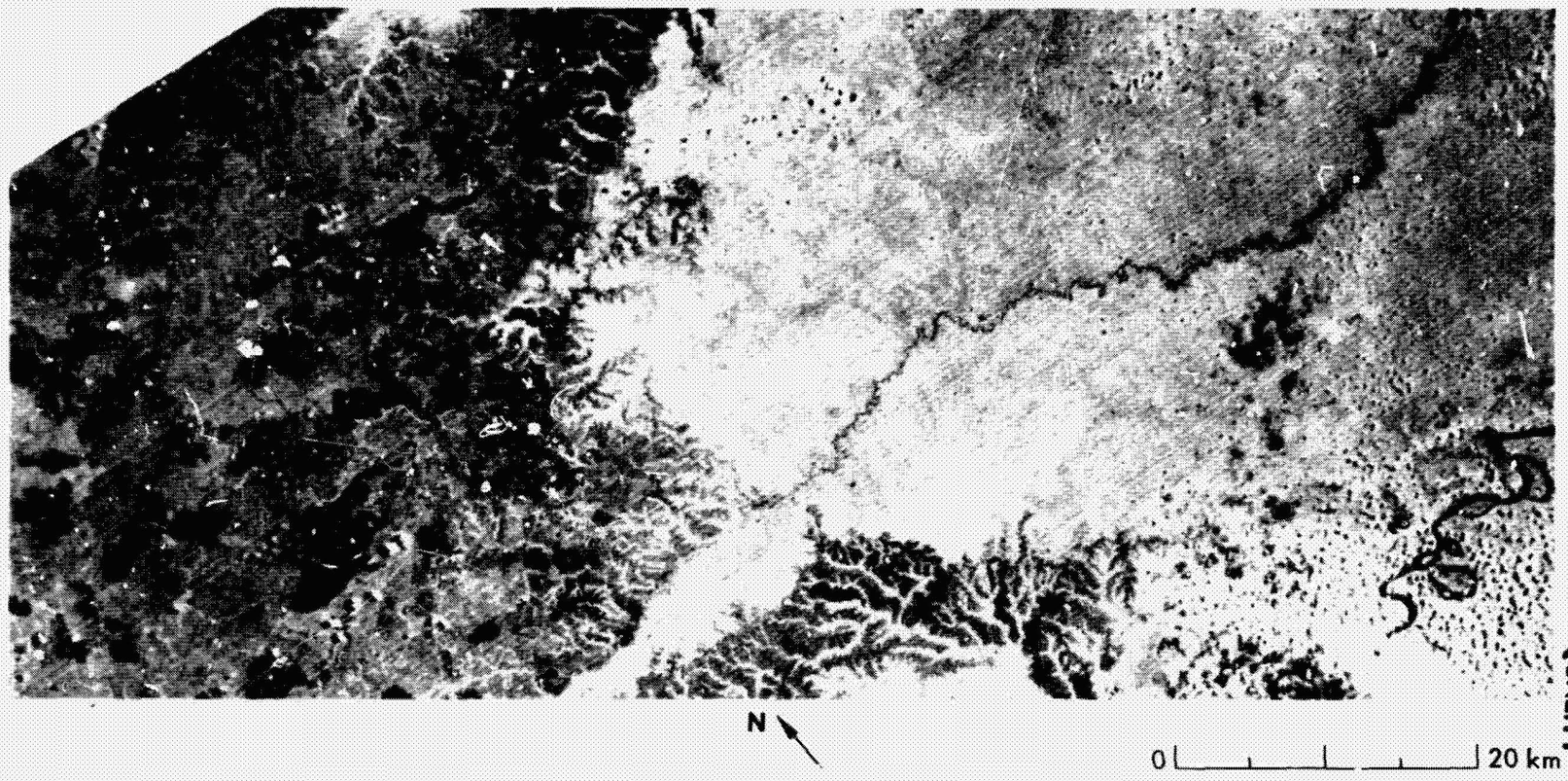

dark tones; it coincides closely with the 200-m contour shown on the geologic map of Colombia (Ref. 14). The grasslands, which rise to elevations above 300 m, yield low radar returns and appear in medium-to-dark shades of gray. The plains are underlain by terrace deposits of glaciofluvial origin. These deposits have been deeply dissected by a well-developed dendritic drainage network. The drainage pattern is strongly enhanced on the SIR-A image by the bright returns from the forested stream channels. There is no area of major habitation in this scene; it is quite remote with a population density of less than one person per km^2. The grassland is used for grazing livestock.

The Landsat image in the near-IR wavelength shows a relatively high albedo from the lowland tropical forest and from the stream channels that dissect the plains. The grasslands on the plains reflect a range of darker gray tones. Large expanses of dark gray result mostly from controlled burns used to clear dead vegetation and renew the fertility of the soil.

(iv) Dunes

16. Dunes Northeast of Ndjamena, Chad (Central Africa)

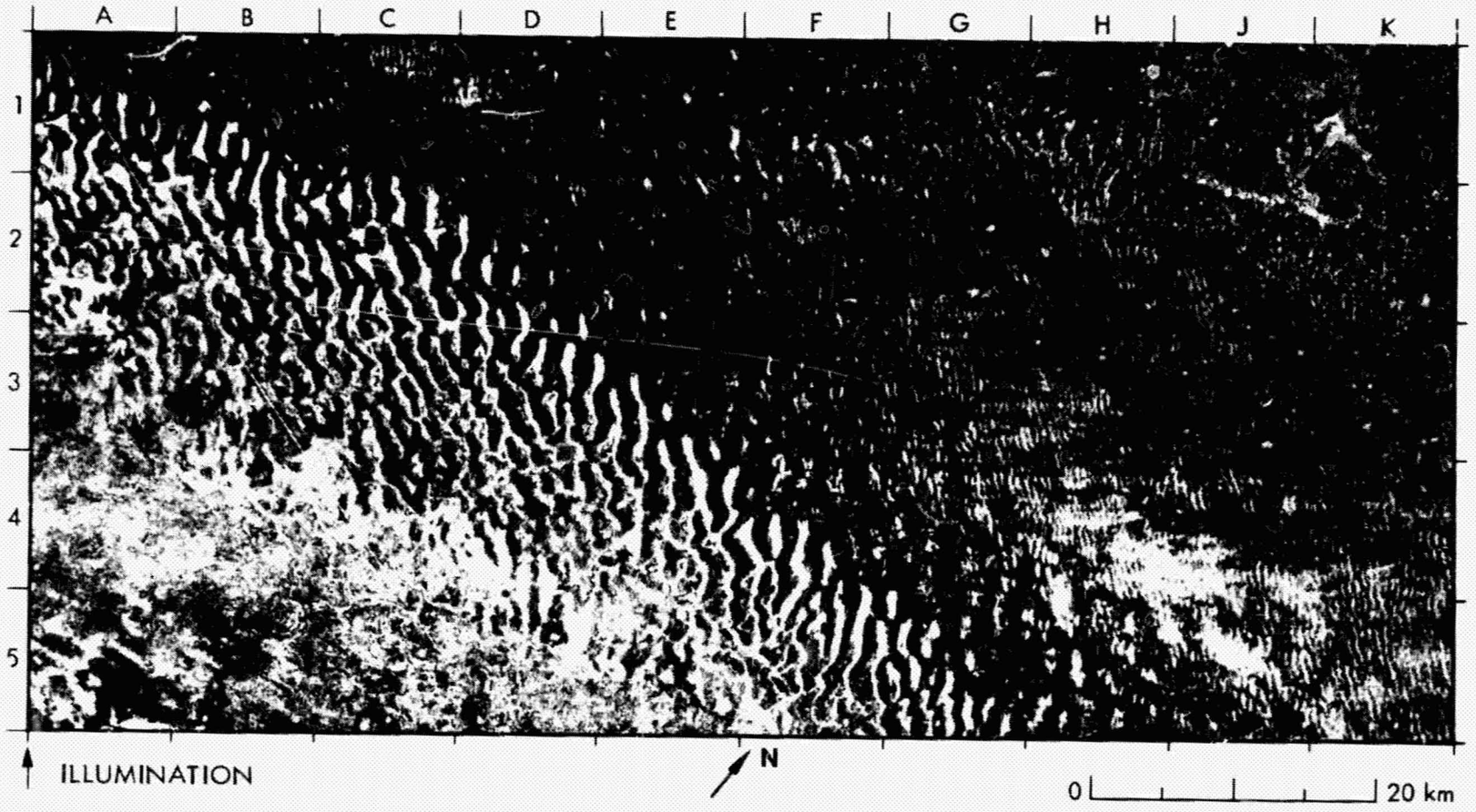

The Lake Chad Basin is in the intertropical convergence zone that is subjected to southwest and northeast Saharan winds, depending on the season. The dunes are oriented with their long axes transverse to the prevailing winds. They are part of a sand sea built by the prevailing winds from reworked alluvium during one or more episodes of aridity when ancestral Lake Mega-Chad receded.

Recession of the lake left widespread arrays of large dune ridges standing above the interdune flats. These arrays are characterized by abandoned or ephemeral drainage channels, wind-eroded lake beds, rough salt playas, and vegetation. The dune ridges from A1 to G5, whose long axes are aligned parallel to the direction of the incident radar beam, are mostly dark. The identification of dune patterns on the SIR-A image results from the bright response of the vegetated interdune flats, which are grassy savannas. The existence of this vegetation is verified on the Landsat image, where the interdune flats appear dark because of chlorophyll absorption in the visible-red wavelength. A near-IR wavelength

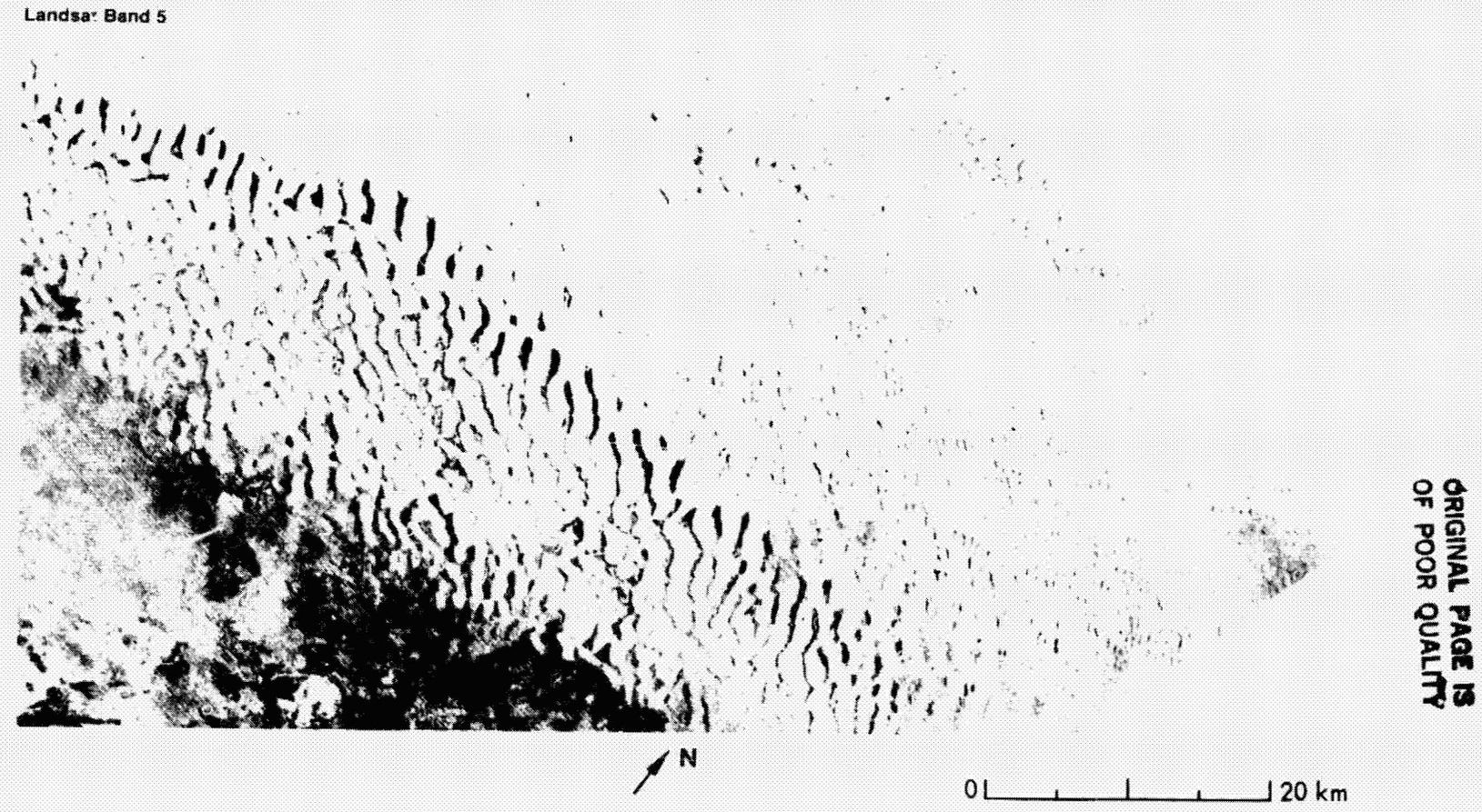

Landsat image of the same area, however, is also dark in the interdune area, indicating that the area is wet. A recent map of the region shows these flats are intermittent lakes.

The overall irregularity of the large sand ridges is typical of old, vegetated, inactive dunes that have been weathered and eroded under conditions of climatic oscillation. The occurrence of the intermittent lakes indicates additional erosion due to water. The drainage pattern at A5 through B5 indicates the slope of the terrain and suggests that rainfall is prevalent. Close comparison of the SIR-A image acquired in November 1981 and the Landsat image acquired in February 1975 shows little change in the general shapes of the larger dunes during the interval.

The dunes in the darker region bounded by A1, K1, and K5 are smaller and more sparse. The vegetation in this region is denser savanna shrubland.

17. Dunes, Oman, Arabia

The Ramlat Al Wahibah sand sea along the eastern coast of Oman meets the Arabian Sea at the bright linear feature (K3 to K5), which is the sand and gravel coastline just south of Ra's Jibsh. Small crescentic dunes cover the eastern part of the image (H1 to J4), while large linear compound dunes cover most of the upper half. In some locations, these dunes reach heights of 90 m above the surrounding ground. Their average wavelength is about 2 km. At G4 to C4, the dunes are linear simple, with a much smaller wavelength. The area at A5 is covered by sand and gravel deposited by the Wadi Matam. The Ramlat Al Wahibah sand sea ends abruptly at Jebel el Madar, off the image to the north. These dunes were formed by northerly winds. Because their surfaces are smooth, the dunes return a weak radar signal; it is the desert

Landsat Band 7

vegetation or gravel in the interdune flats that returns a signal strong enough to make the dune morphology visible. A change in vegetation density is most likely the reason for the change in radar backscatter along the curvilinear boundary between A2 and F2.

This area is in one of the more remote parts of the Arabian Peninsula. The only habitation is the small coastal fishing town of Sharkh (K5).

Although the SIR-A shows a relatively bright ocean because a near-surface wind generated small-scale roughness on the surface, local variations in small-scale roughness on the Landsat near-IR wavelength image are not apparent. The morphology of the dunes on the Landsat image is visible because of solar shadowing.

18. Kara Kum Desert, Turkmen S.S.R.

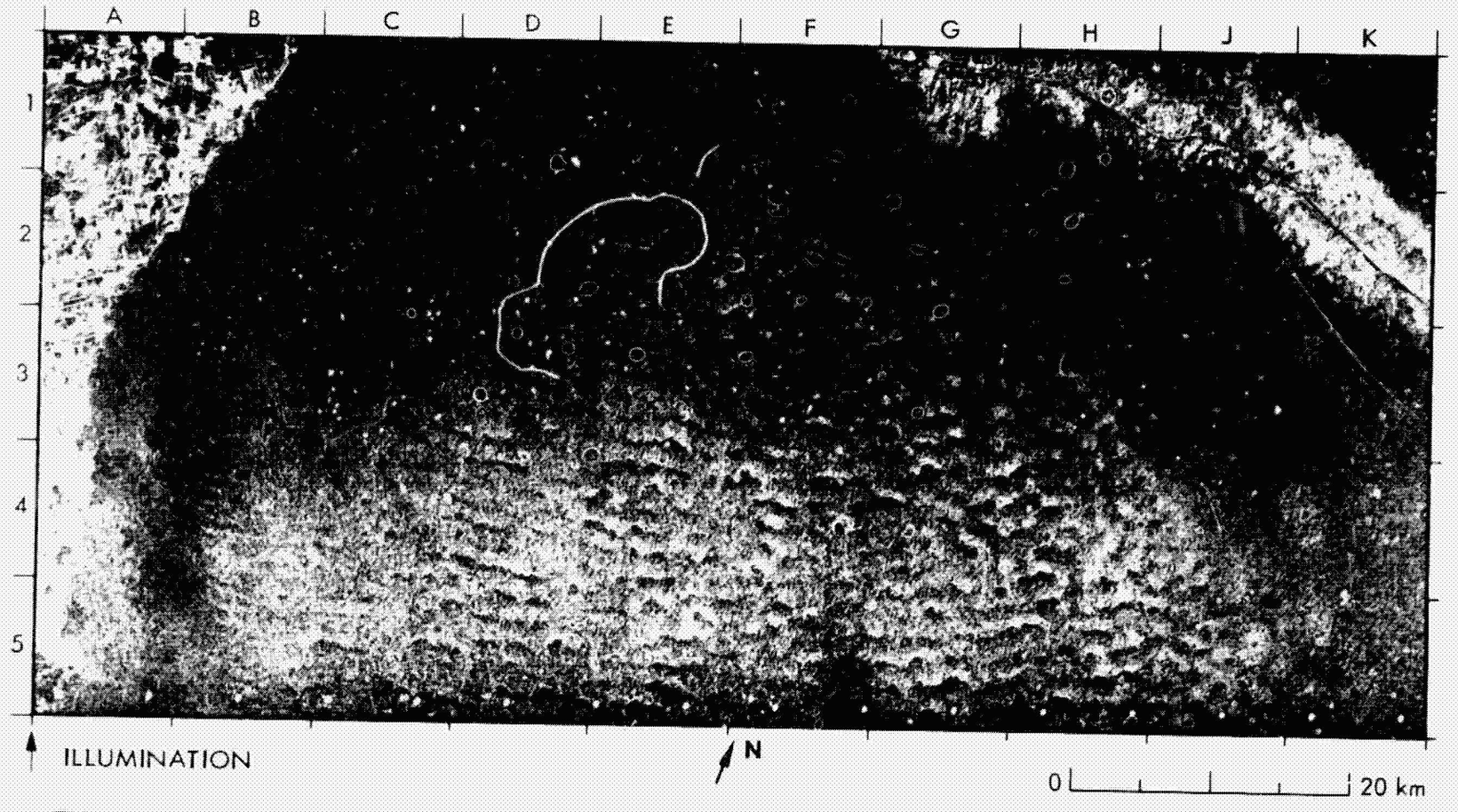

This southern part of the Kara Kum desert lies east of Mary in the Turkmen S.S.R.; it is situated on an alluvial plain north of the mountains that border Iran and Afghanistan. Precipitation in this region is less than 100 mm/yr, and the cotton farming towns of Mary and Bayram-Ali (just above the left corner of the image) depend for irrigation on the Karakumskiy Canal (G1 to K2), which is fed from the Amu Darya River to the east. This canal, started in the fifties, is now 1000 km long. The cultivated fields from A1 to B1 through A3 surround the Murgab river.

The dunes of the Kara Kum consist of reworked alluvial sands deposited thousands of years ago by the ancient Amu Darya, whose

Landsat Band 7

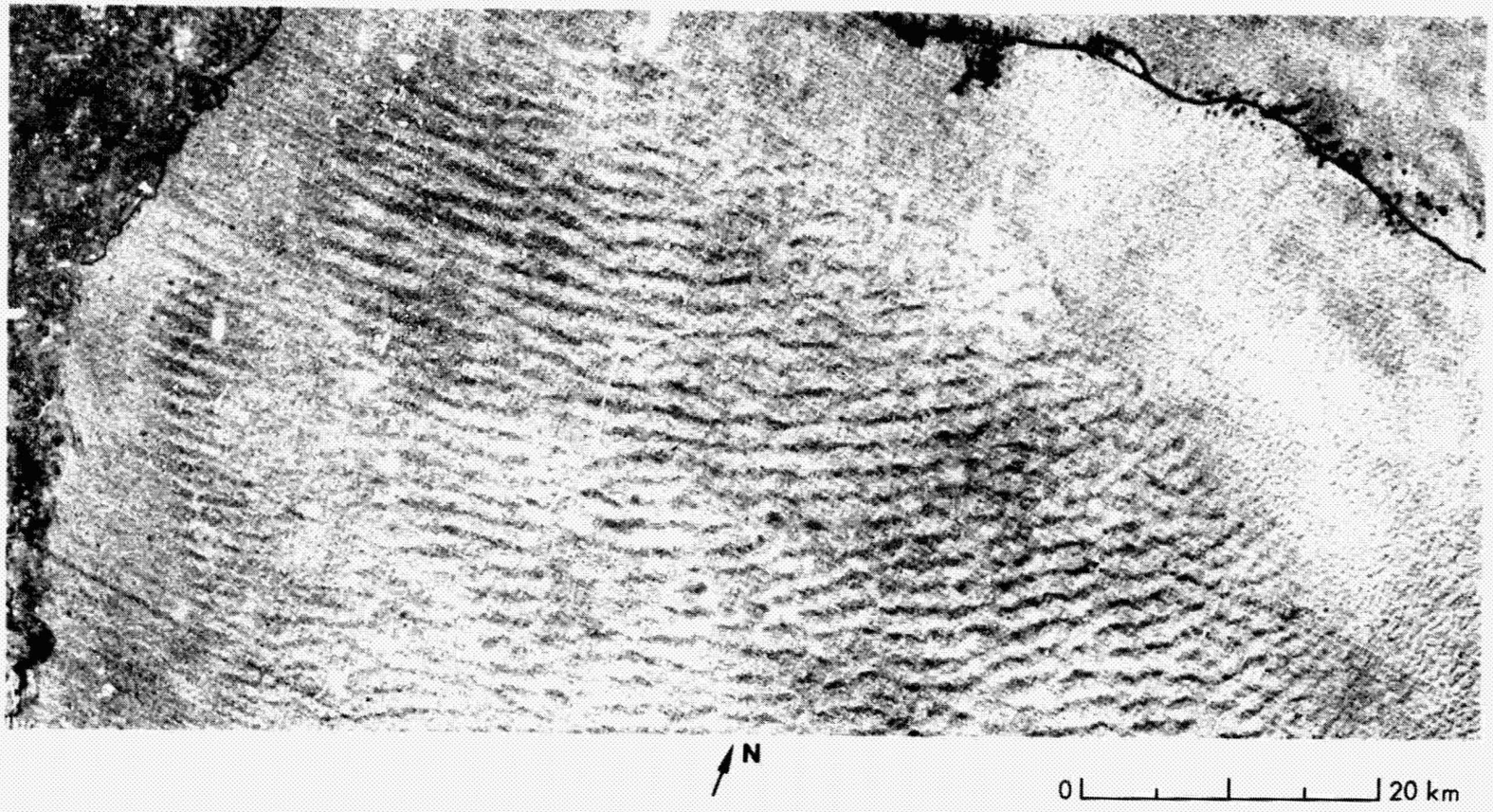

course has gradually shifted to the east. These dunes have a barchanoid form consisting of adjacent crescentic segments. The SIR-A image shows mainly the large dunes, which are about 25 meters high. Their slipfaces are oriented toward the south with their ridge axes perpendicular to the direction of illumination. This orientation leads to a large difference in the incidence angle from one side of the dune crest to the other, which results in a significant difference in radar backscatter. In the Landsat image in the near-IR wavelength, the dunes are perceptible because of solar shadowing, but the cultivated fields along the Murgab River cannot be distinguished as they can on the SIR-A image.

19. Badain Jaran Desert, Nei Monggol, China

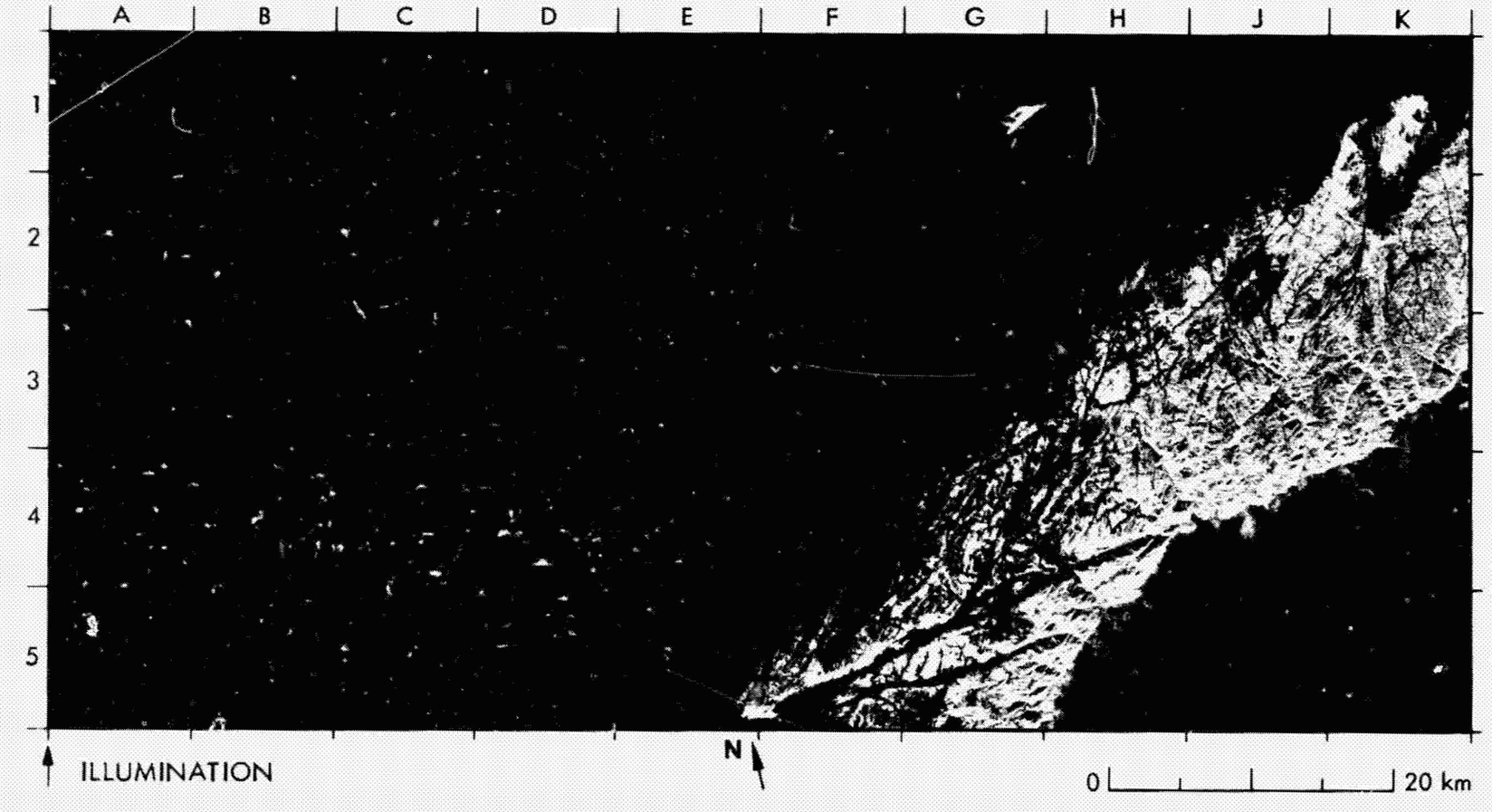

The Badain Jaran Shamo (Desert) of Inner Mongolia, China, contains some of the tallest dunes on Earth, reaching heights of more than 300 m. They are compound crescentic dunes (megabarchanoid) with numerous spring-fed interdune lakes.

The SIR-A image shows that specular returns from the crescentic dunes come solely from the south-facing portions of the major east-southeast-facing slip faces. This suggests that sand-dune migration is southward, driven by northerly winds.

The Landsat image, however, taken in the visible-red wavelength, shows that each wavy dune ridge consists of numerous adjacent crescentic segments, about 2 km across the crescent, and that the steeper slope faces the east-southeast.

It is clear, then, that the SIR-A image gives a false impression: because only the south-facing part of each curved slip face was normal

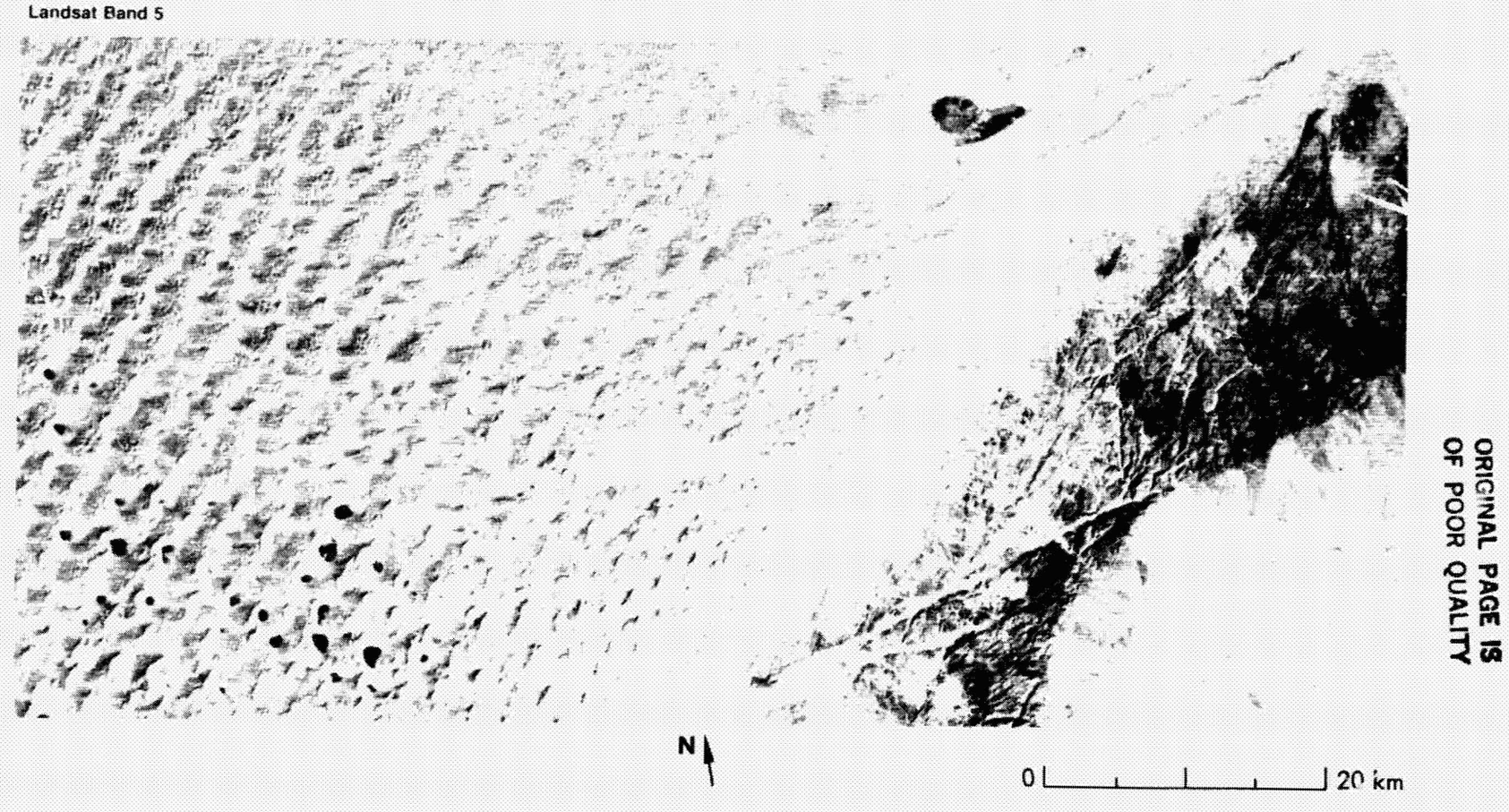

to the radar beam, the resulting image suggests that dune orientation is 67 deg south of the true direction.

Near the Yabrai Shan Mountains (F5 to H5 through K1 to K3), the megabarchanoid ridges grade into isolated sharp-crested dune ridges and star dunes, the result, probably, of the mountain ridges' effect on the transporting capacity of the winds. The change in dune shapes was not detected by SIR-A because the long axes of the narrow ridges near the mountain lie almost parallel to, rather than normal to, the direction of the radar beam.

Numerous spring-fed interdune lakes are clearly seen in the lower left of the Landsat image. They give a response as dark as that of the dunes on the radar image, where the lakes are outlined by thin bright lines that probably represent thickets of reeds and other marsh vegetation.

(v) Volcanic Terrain

20. Pinacate Volcanic Field, Sonora, Mexico

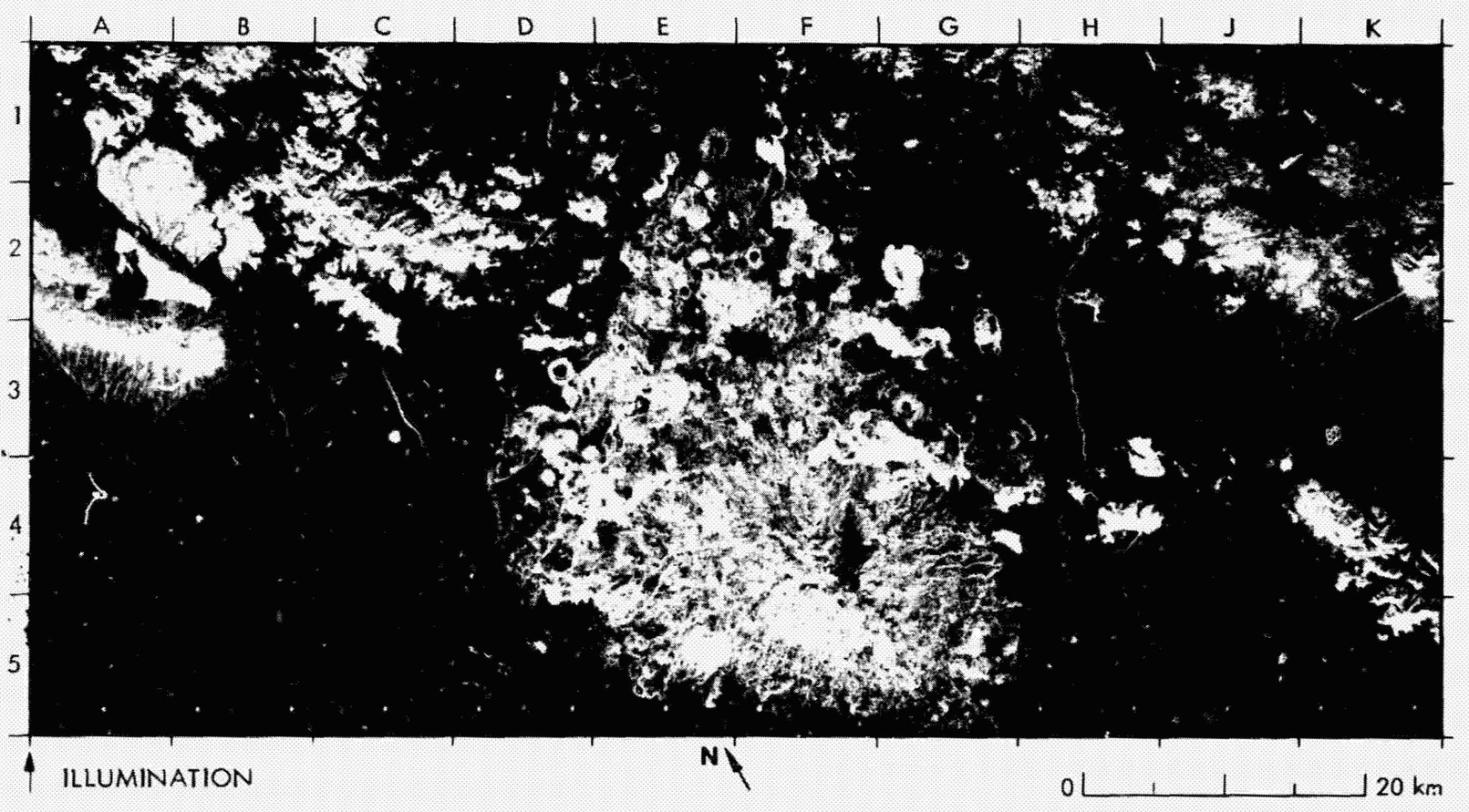

This basaltic volcanic field (D1 to D5 through G1 to G5) covers over 2000 km² and reaches an elevation of 1200 m at Sierra Pinacate (F4). Over 650 exposed basaltic flows, nearly all of them aa-type, range in age from Late Pleistocene to Holocene. The accompanying Landsat image has been high-pass filtered to display the dark volcanic field and the bright sand dunes simultaneously. The image tone is the high-passed average of bands 4, 5, and 7.

The youngest lava flows in the Pinacate Volcanic Field are brightest on the radar image. This results from their roughness, which decreases with age because of erosion and infilling with eolian material. On the Landsat image, the youngest lava flows are the darkest.

The volcanic field is characterized by eleven large, tuff-rimmed explosion-collapse craters and numerous small cinder cones. The small size and smoothness of the cinder cones renders them dark and difficult to discern on the radar image, though several can be seen along a northwestward trend that intersects Sierra Pinacate at F4.

The influence of ground water on the creation of these spectacular craters is emphasized by the fact that several of them are located along the former course of the Sonoyta River, now located at H1 through H5. Some reveal a multistage history of explosion and collapse. The larger

Landsat Bands 4, 5, and 7

craters are readily perceived on both the SIR-A and Landsat images. They range in diameter from 900 to 1600 m and include MacDougal (D3), Elegant (G3), Sykes (E3), Cerro Colorado (G2), and Celaya (F2). The craters have gullied, moderately rough rim slopes that produce a bright ring on the radar image. On the Landsat image, the relatively dark ejecta produce a dark image tone. The crater floors appear dark on the radar image and bright on the Landsat image because of infilling with smooth fine-grained material from the crater walls and playa deposits.

The volcanic field is encroached on the west and south by the Sonora dunes. Because the dunes are smooth and lack vegetation, they appear on the radar image as barely discernible northwest-trending black bands, as at B4. They are outlined by the lighter interdune areas, which are slightly rougher and have a limited vegetation cover. On the Landsat image, the dunes appear brighter than the interdune areas. The surrounding block-faulted mountains show a northwest trend that is typical of the basin-and-range tectonics in the region. The mountains are formed primarily of pre-Tertiary granitic and metamorphic rocks.

(The text is by courtesy of R. G. Blom.)

21. Western Galápagos Islands, Ecuador

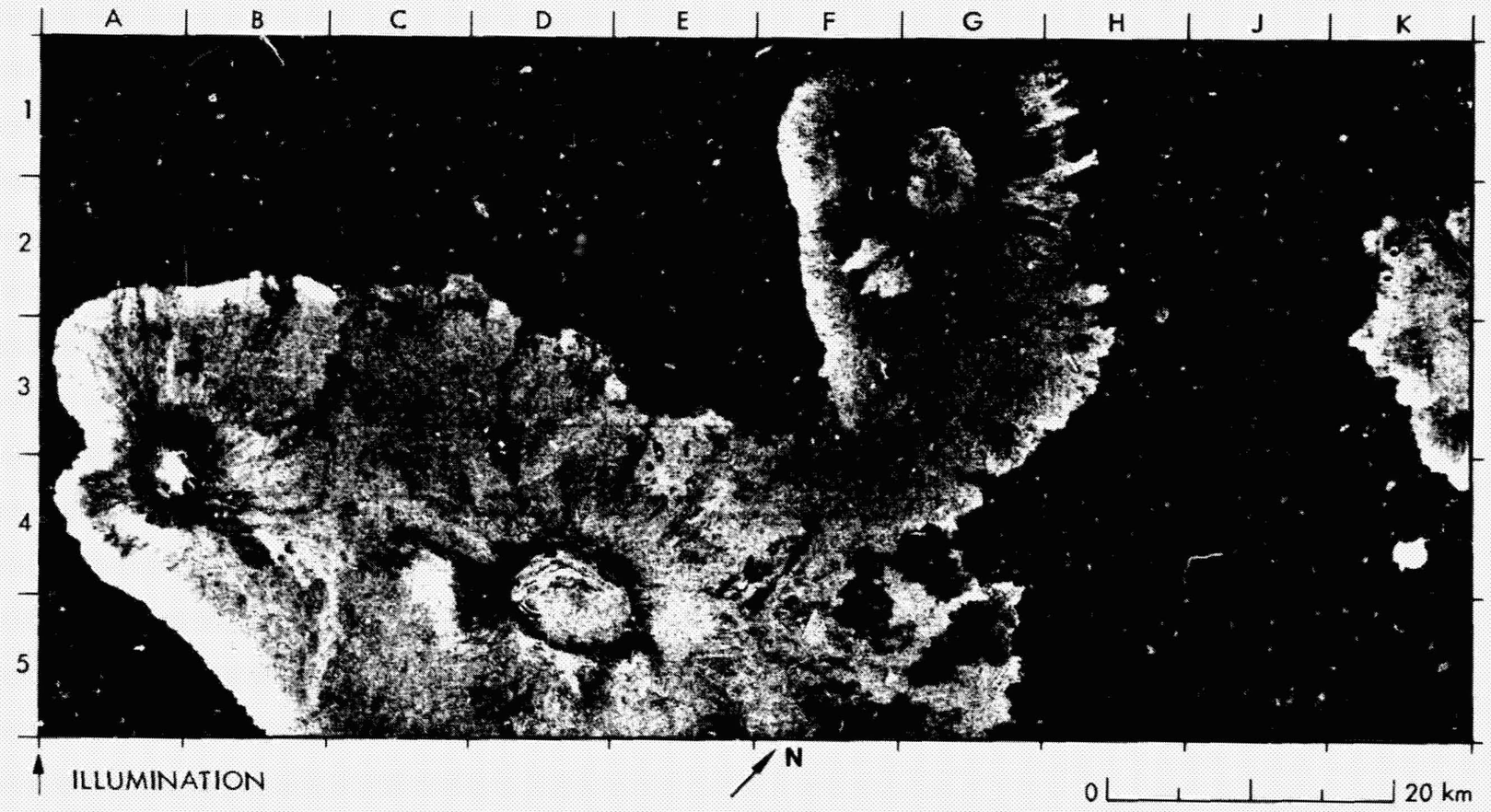

A portion of Isabela Island dominates this SIR-A image of an area approximately 1000 km west of Ecuador.

The Galápagos Islands are of particular interest because of their proximity to the Galápagos Rift, which is an active spreading center. Santiago (or James) Island (K2/K3) and Rábida (or Jervis), the small island at K4, are both single-shield volcanoes, although several parasitic cones can be seen on Santiago Island at K2.

Isabela Island, which dominates this image, is composed of six coalescing-shield volcanoes, five of which have been active in historic times, and three of which can be seen on the SIR-A image.

Alcedo Volcano (G1) rises 1130 m above sea level. This is the smallest volcano on the island and has had the fewest historic eruptions. Much of the volcano is covered with vegetation. However, fresh flows, which are bright on the SIR-A image at G1/H1 and F2, are dark on the Landsat image, which was taken in the visible-red wavelength. Sierra Negra Volcano (D4, D5, E4, and E5) reaches 1080 m above sea level.

Landsat Band 5

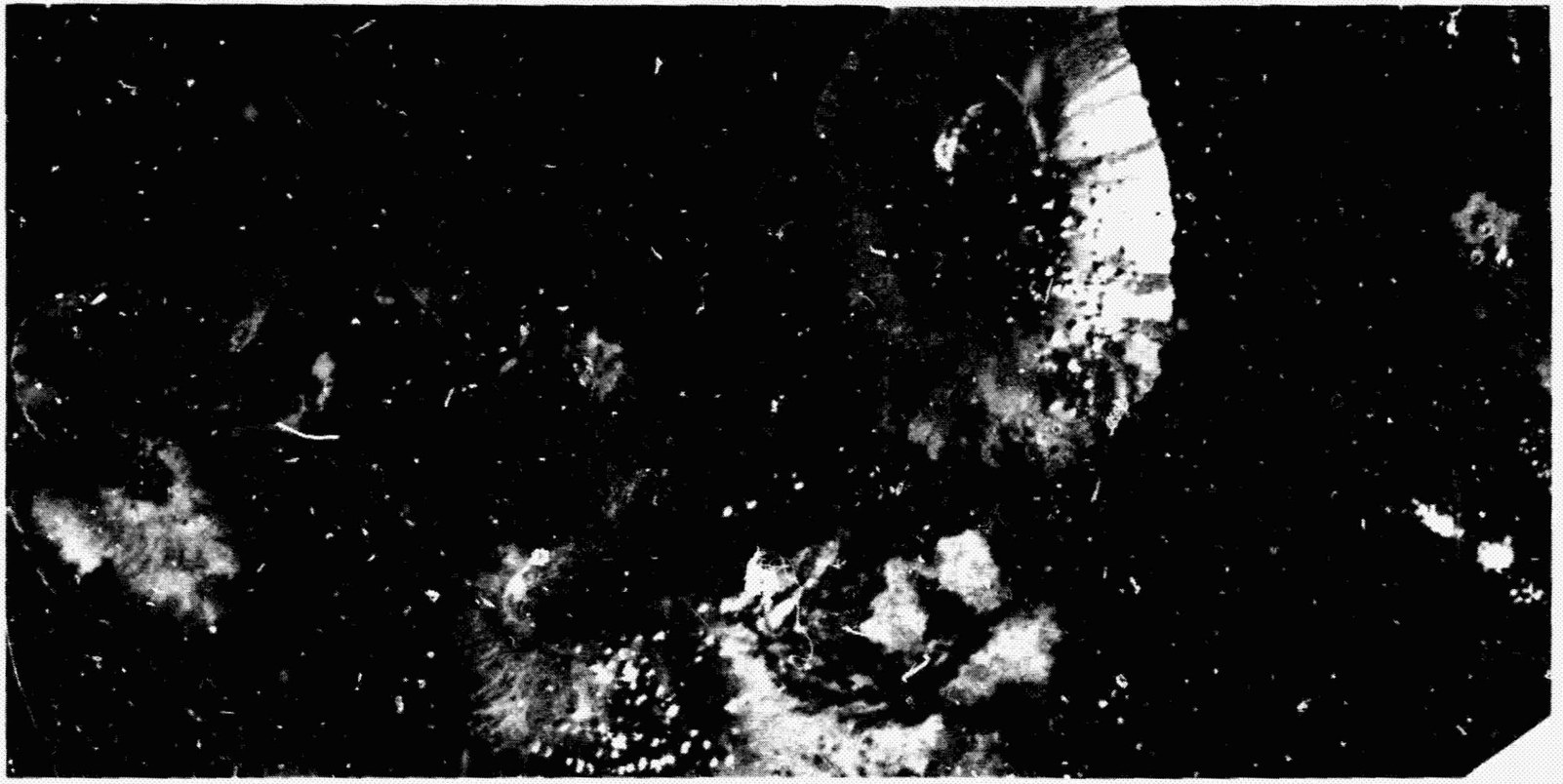

N

0 20 km

ORIGINAL PAGE IS
OF POOR QUALITY

This volcano is the oldest on the island and has the shallowest caldera.

Cerro Azul Volcano (A3/A4), the youngest volcano on the island, rises 1690 m above sea level. Fissures that radiate from the main caldera control the associated cones and flows. There is also a fissure zone at A4 through C4 that links Cerro Azul and Sierra Negra. Two eruptions on the lower slopes of Cerro Azul between 1963 and 1973 filled this area with aa and pahoehoe flows. There have also been pyroclastic eruptions of Cerro Azul that covered the higher slopes of the volcano with ejecta. A tuff cone can be seen at the northeast edge of the caldera floor (B4).

The combination of Landsat and SIR-A images of this area make it possible to estimate surface roughness and vegetation cover of the various flows.

(The text is by courtesy of D. L. Evans.)

22. Volcanic Field Northeast of Damascus, Syria

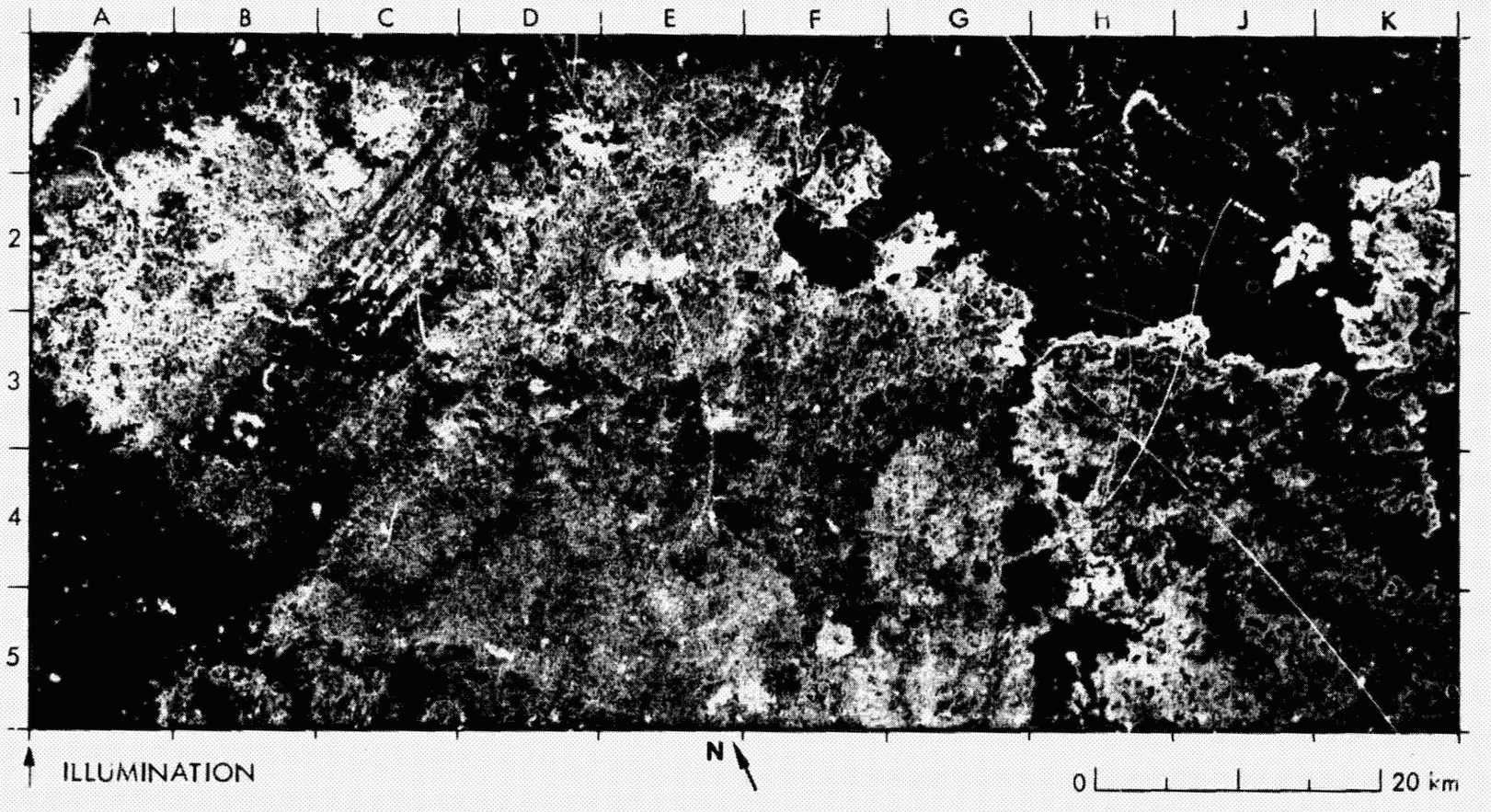

The lava flows and volcanic cones that occupy most of this scene are located in western Syria, northeast of Damascus, toward the northwest margin of a widespread volcanic field. This field extends southeast for about 450 km, through Jordan, to the Al Harrah region of northern Saudi Arabia. It is composed of basaltic and andesitic rocks that are mostly Neogene in age.

The lava flows on the SIR-A image range from medium- to light-gray tones. They show a pronounced margin that can be traced from F1 to K2 and from K3 to K4. The abruptness of this margin reflects the contrast between the rough surfaces of the lava front, which appear bright, and the smooth, level surfaces of the material at the base of this front, which appear dark. The lava surface is extensively pitted in the area bounded by C1, F1, K4, and A2, with dark returns (e.g., H4/H5) coming from depressions that are probably floored with layers of wind-blown sand.

A large cluster of cones is situated in the B2/C2 and B3/C3 area. The SIR-A image shows an east-southeast alignment of the cones from C2 to E2 and from C3 to E3, which is evident though less clear on the Landsat image in the near-IR wavelength. A south-southeast fracture

Landsat Band 7

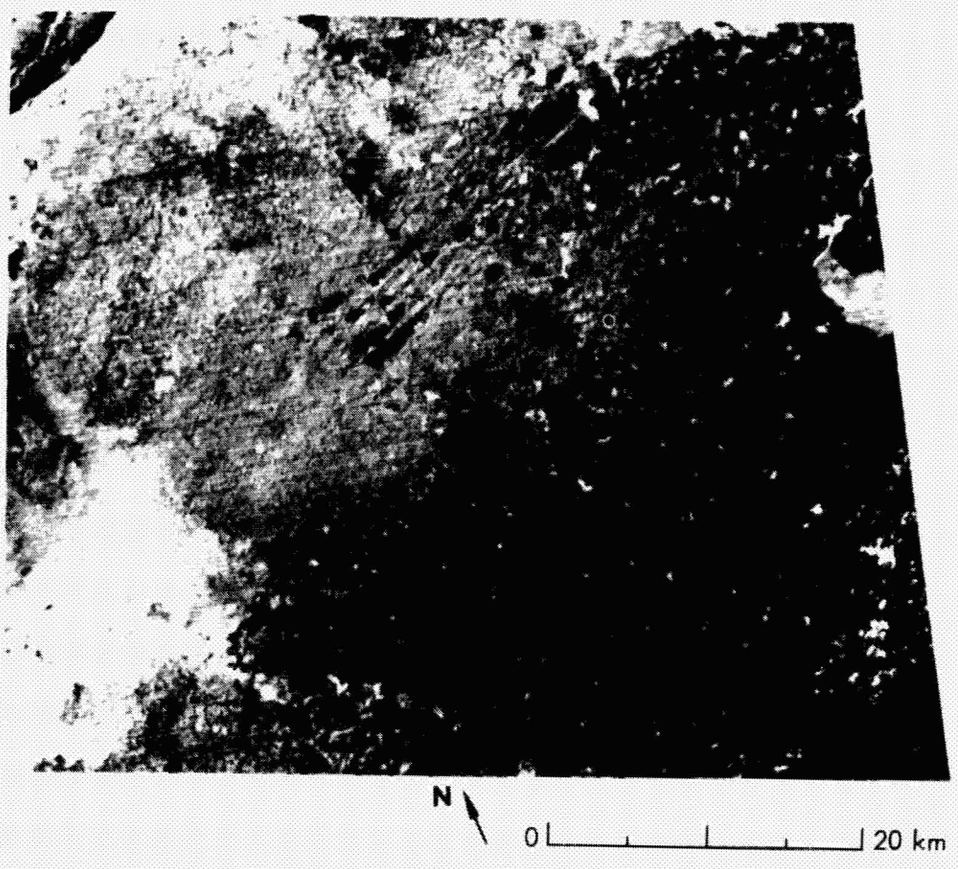

pattern from C2 to E3 and from C3 to E5 is clearly displayed on both the radar and the Landsat images.

Two phenomena point to the possibility of eolian deposition over the volcanic field. First, the trace of the lava margin from A3 to B4/B5 to A5 and from A2 to B1 is diffuse and irregular. Second, the clustered cones are situated to the southwest of parallel linear sand streaks that extend to the northeast. A dominant southwest wind could account for both phenomena: selective deposition of sand partially obscured this margin of the flows and created the linear sand streaks that formed in the lee of the volcanic cones.

The brightness of the radar returns from the lava surfaces shows significant local variation. Very bright returns represent rougher and probably younger flows than the darker returns from smoother, probably older flows. Notable examples are at D1/E1, F2/G2, E3, and F5. These contrasts are less clear on the Landsat image.

23. The Lesser Sunda Islands, Indonesia

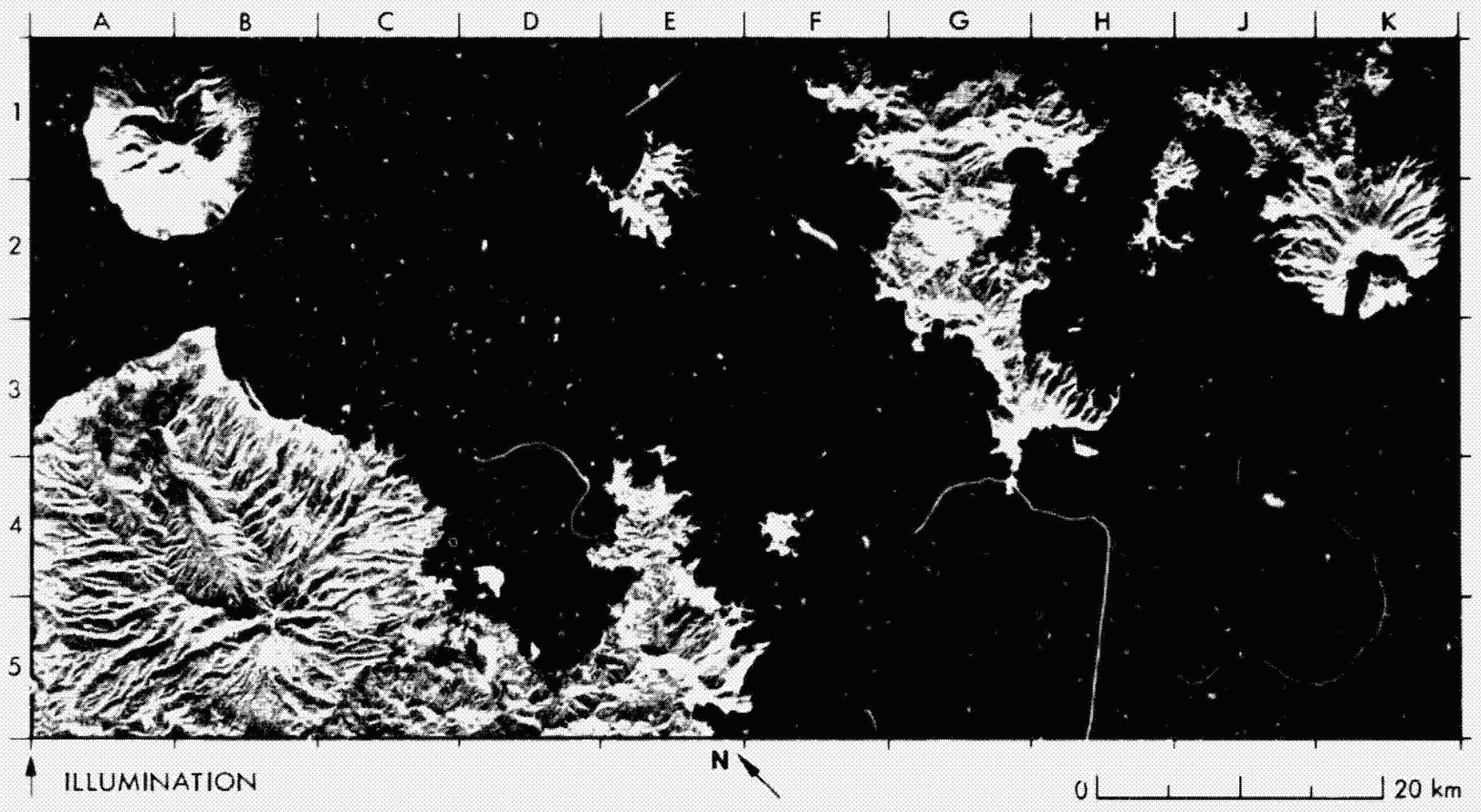

The Lesser Sunda Islands in this portion of the Banda Arc consist of stratovolcanoes composed of andesitic and basaltic lavas, with interbedded breccia and tuff (Ref. 15). The volcanic rocks range in age from Lower Miocene to Recent. Extinct Neogene eruptive centers at Mt. Maria, Mt. Saboke, the island of Banta, Mt. Otcta, and Mt. Orora show a deeply dissected radial drainage pattern. The caldera at Mt. Maria on Sumbawa (B5) is breached to the north. Differential earth movements are inferred from the partial submergence of calderas, notably on the island of Banta (D1, D2, E1, and E2) and by the reticulated form of the coastlines along the southern portions of the islands of Banta, Komodo,

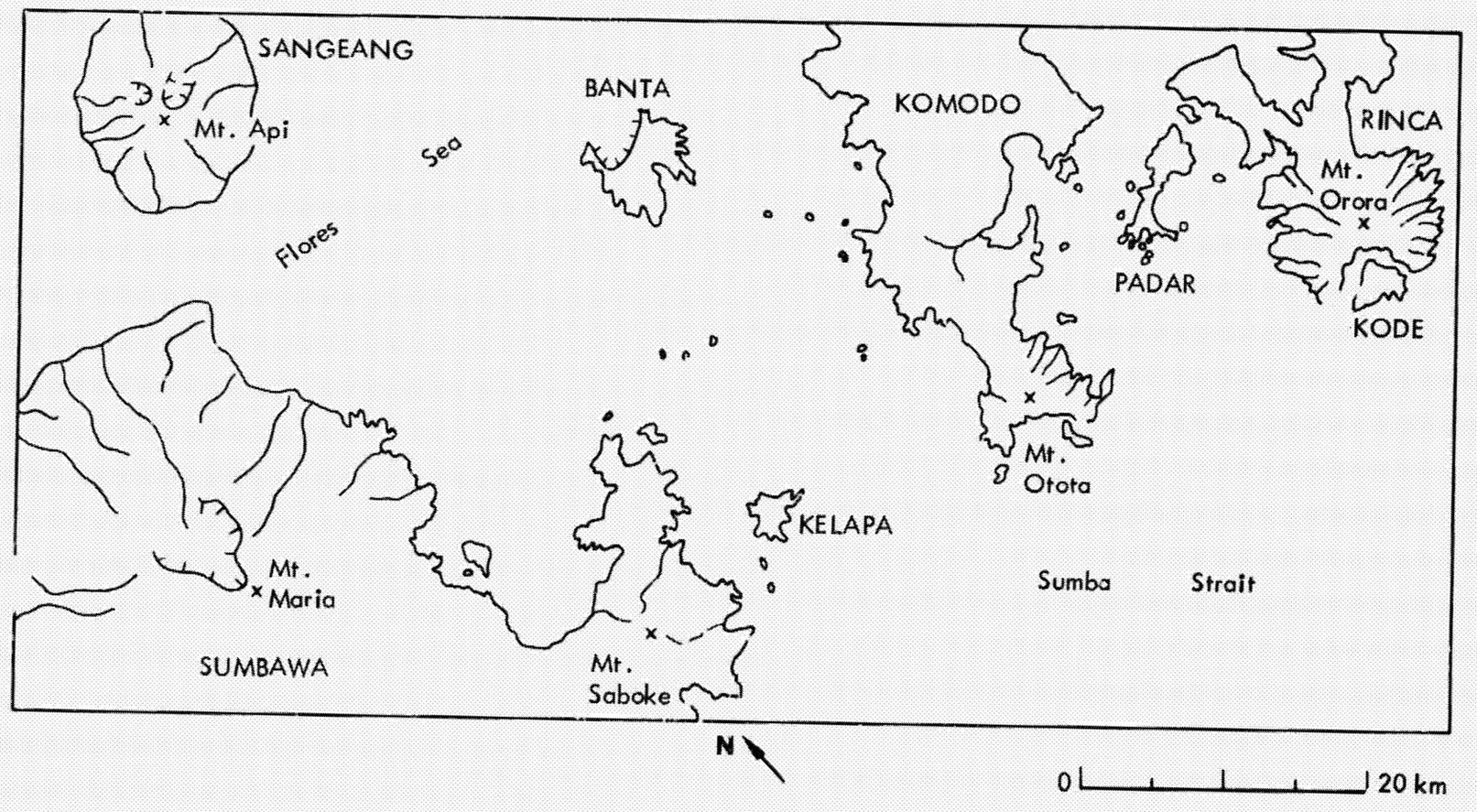

and Rinca. The stratovolcano at Mt. Api on the island of Sangeang (A1, A. B1, and B2) is active. It has several flanking calderas near the summit and steeper and less deeply dissected slopes than the older volcanic cones. Also, the coastline is comparatively smooth in outline. Bright linear patterns on the water surface between the islands of Sumbawa and Komodo represent areas of roughness at the scale of the radar wavelength (23 cm). The roughness may be caused here by the convergence of marine currents.

24. Central American Volcanic Belt, Guatemala

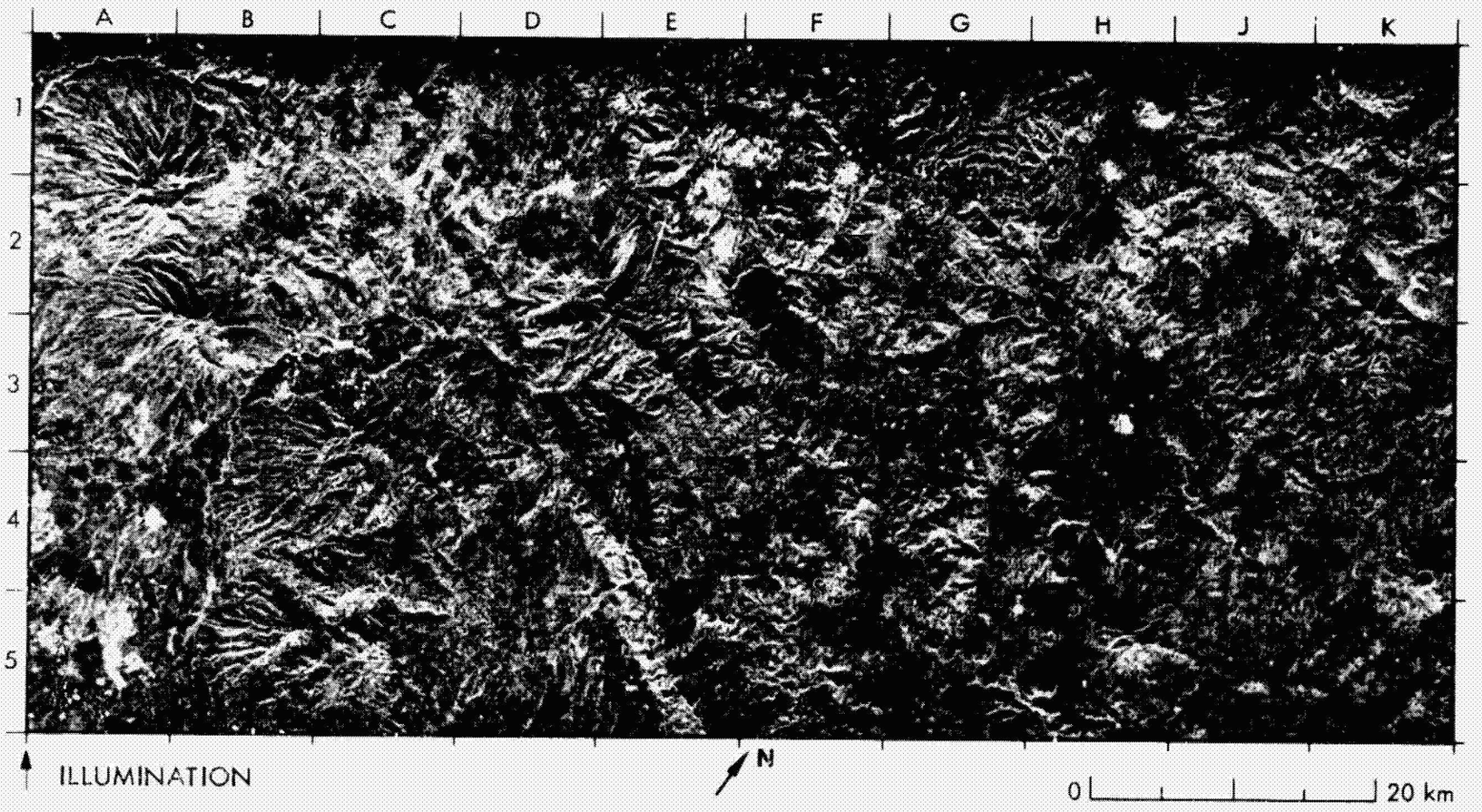

Landforms in this area of southern Guatemala include numerous extinct stratovolcanoes with elevations from 1600 to 2000 m, small lava domes, cinder cones, and calderas and their associated lakes; the Pacific coastal plain lies from A3 to A5. The volcanic rocks are Tertiary to Quaternary in age, mostly of intermediate to acidic composition.

Some of the larger stratovolcanoes are Tecuamburro (A2/B2 to A3/B3), Cruz Quemada (B3/C3 to B4/C4), and Suchitan (H5/J5). The Rio de los Esclavos (C3 to A5) drains the area toward the Pacific Ocean.

The SIR-A image shows bright radar returns from the steep slopes of the volcanic cones. The large caldera at E2/F2 to E3/F3 contains Lake Ayarza. This caldera is clearly defined by the bright returns from its steep northwest wall, and by the land/water boundary that marks the margin of the lake. Another large caldera at H4 also provides bright radar returns from its steep northwest wall. However, because it contains a very small lake (Retana), the caldera is less clearly outlined. On the Landsat image in the near-IR wavelength, the outline of this caldera is more pro-

Landsat Band 7

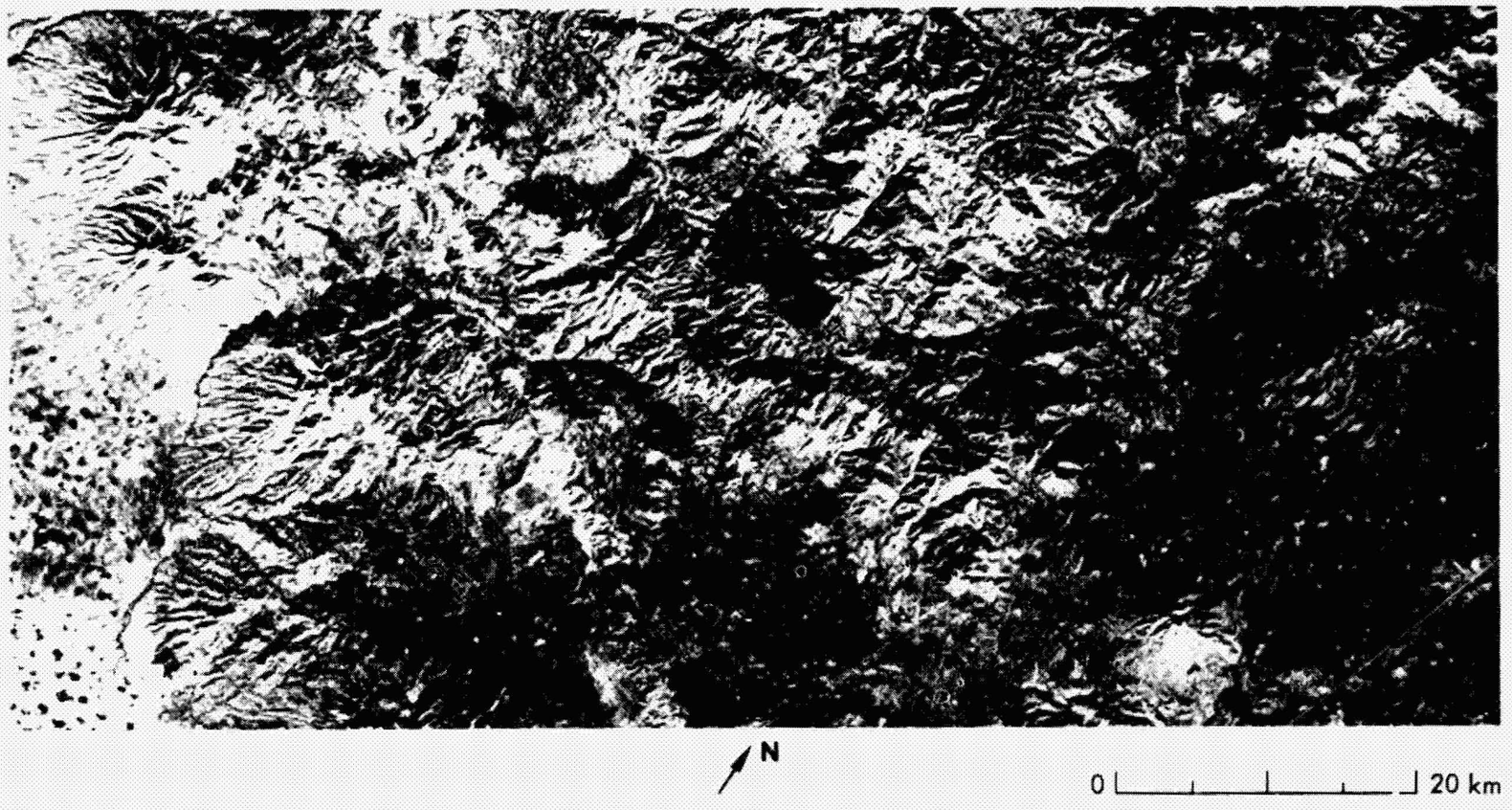

nounced. Other small lakes in central craters include Lake Hoyo (H3, lower left) and Lake Ipala (K4, lower right). Small cinder cones to the east of Suchitan volcano (H5 to K5) are equally perceptible on the SIR-A and the Landsat images.

The alignment of linear features from C1 to E5, and the offset in this alignment at E4 (lower left) are mapped as a fault zone on the geologic map of Guatemala (Ref. 16). This alignment is less clearly defined on the Landsat image.

Perception of towns or villages on the SIR-A image is strongly dependent on the orientation of the streets and buldings relative to the direction of radar illumination. The town of Monjas (H3), about 16 km northwest of Suchitan volcano, appears bright on the radar image, though it is a small municipal town. The much larger Department capital of Jutiapa (F5/G5), however, which is situated an approximately equivalent distance southwest of the volcano, is scarcely perceptible on the radar image.

(vi) Dry Lakes

25. Chott Merouane and Chott Melrhir, Algeria

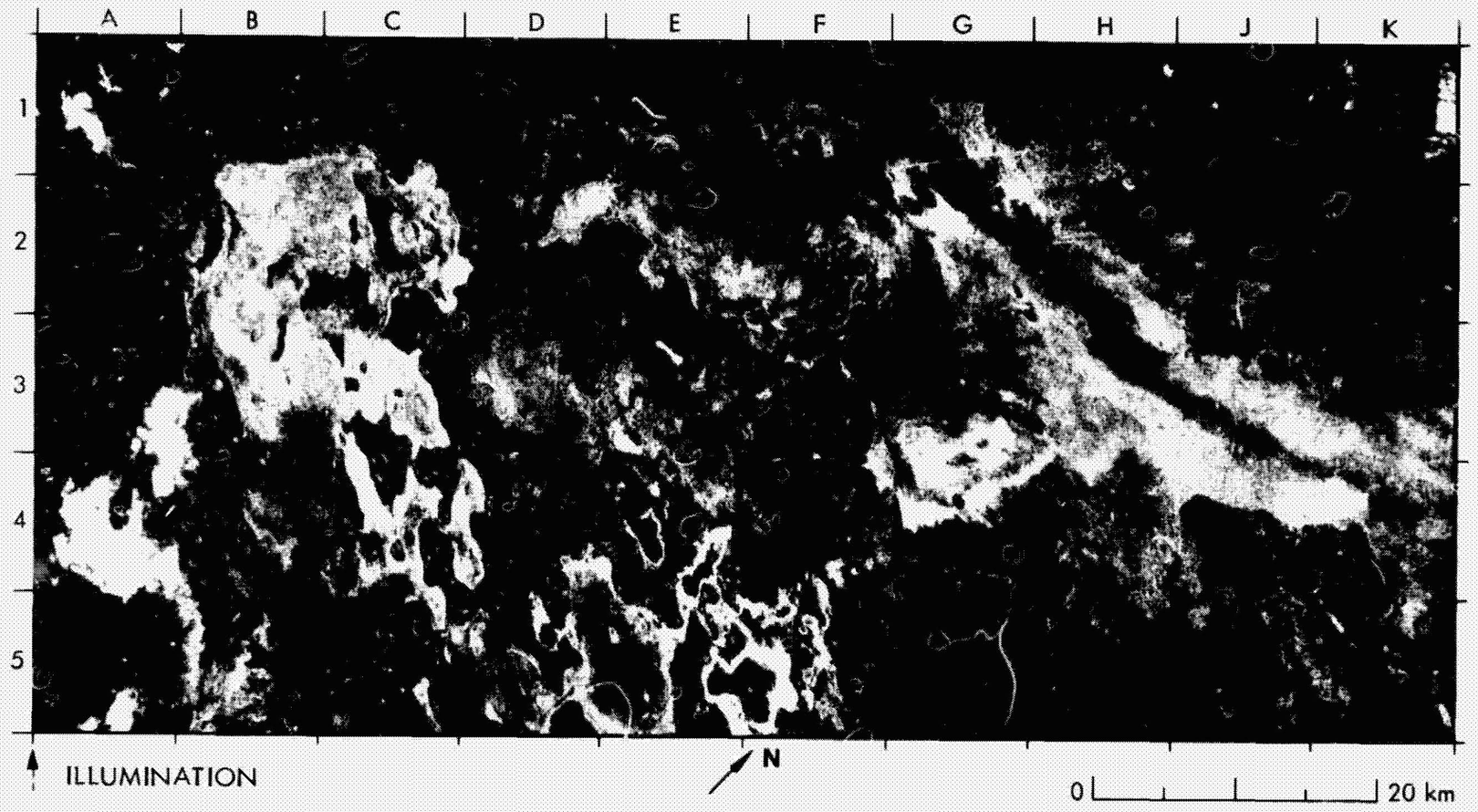

Chott Merouane (B2 to C2 through B5 to C5) and Chott Melrhir (E2 to H2 through E3 to H3) are located in the Sahara of northeast Algeria, some 80 km south of the Aures Mountains. The chotts are playas situated 40 m below sea level. Their surfaces are level, and they contain layers of salt deposits. Occasionally in winter the chotts are partially filled with a thin layer of water. Chott Merouane is flanked to the northwest by calcareous rock outcrops of Pliocene age (A1 to C1), while Chott Melrhir is bounded to the south and west by sand dunes (D2, E3, and G5 through K5). The small towns of El Hour (A1), Ourir-Mrhaier(A3/A4) and Krelil (A5) produce very bright returns on the SIR-A image. The bright returns from the surface of Chott Merouane suggest a wide range of roughness at the scale of the radar wavelength (23 cm). The moderate-to-dark returns from the surface of Chott Melrhir imply a smoother surface.

The surface of Chott Merouane on the corresponding Seasat SAR image appears quite similar to that on the SIR-A image. However, the floor of Chott Melrhir appears substantially different on the Seasat image

Landsat Band 4

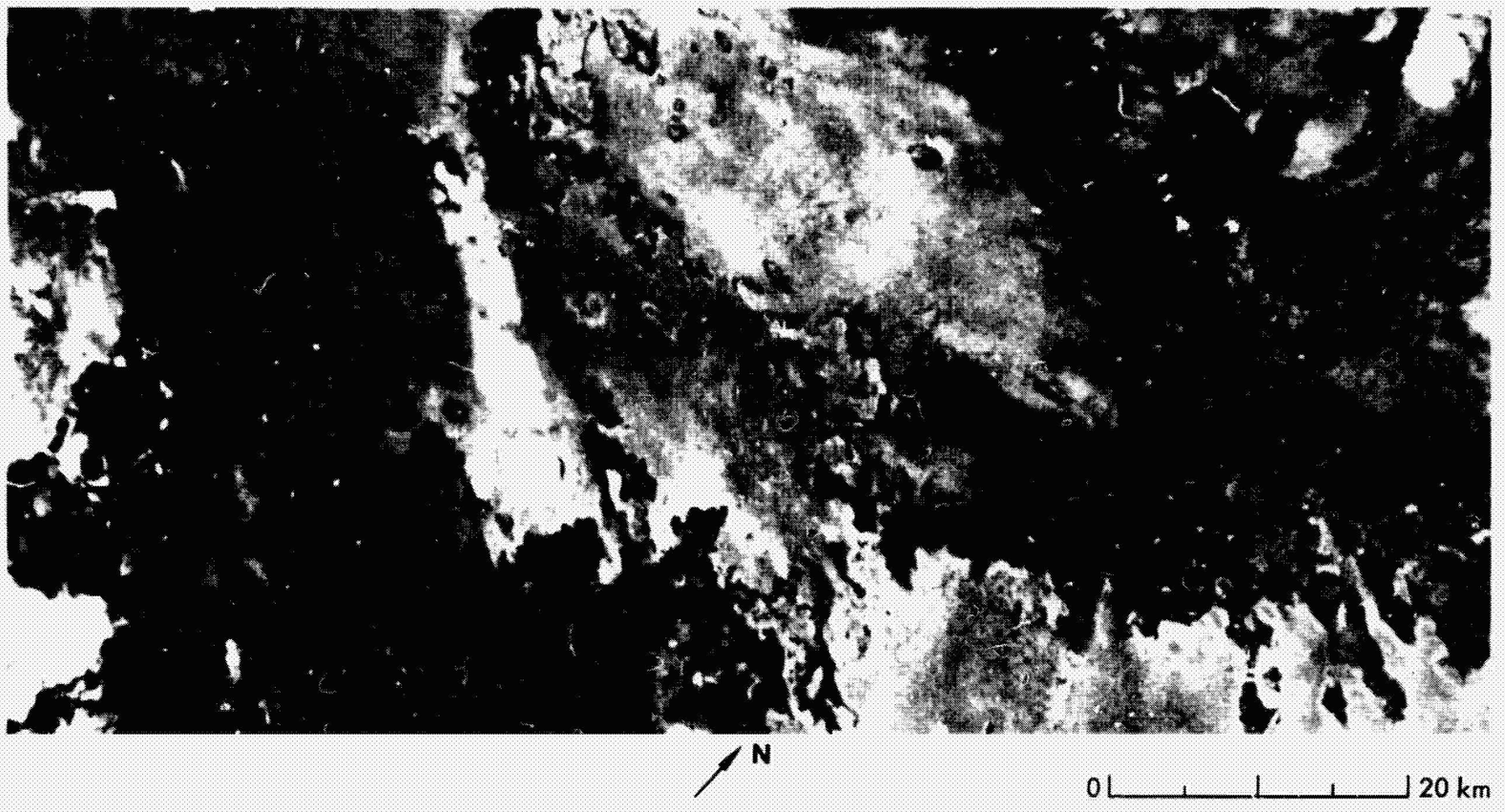

The Landsat image in the visible green wavelength was acquired slightly less than five years prior to the Seasat SAR image, and almost nine years before the SIR-A image. Comparison of the three images shows very little change in the outline of the chotts during this time interval. At the left side of the Landsat image, the towns and oases appear dark because they are strongly absorptive at this wavelength. The surfaces of the chotts show a wide range of albedo. Chott Merouane appears moderate to dark, in contrast with the radar images where it is moderate to bright. Chott Melrhir appears moderate to bright on the Landsat image. This suggests a strong reflectance from salt deposits. The contrast between the surfaces of Chott Merouane and Chott Melrhir on any one of the three images may be the result of differences in the amount of alluvium supplied in each case.

(The text is by courtesy of Ph. Rebillard.)

Seasat SAR

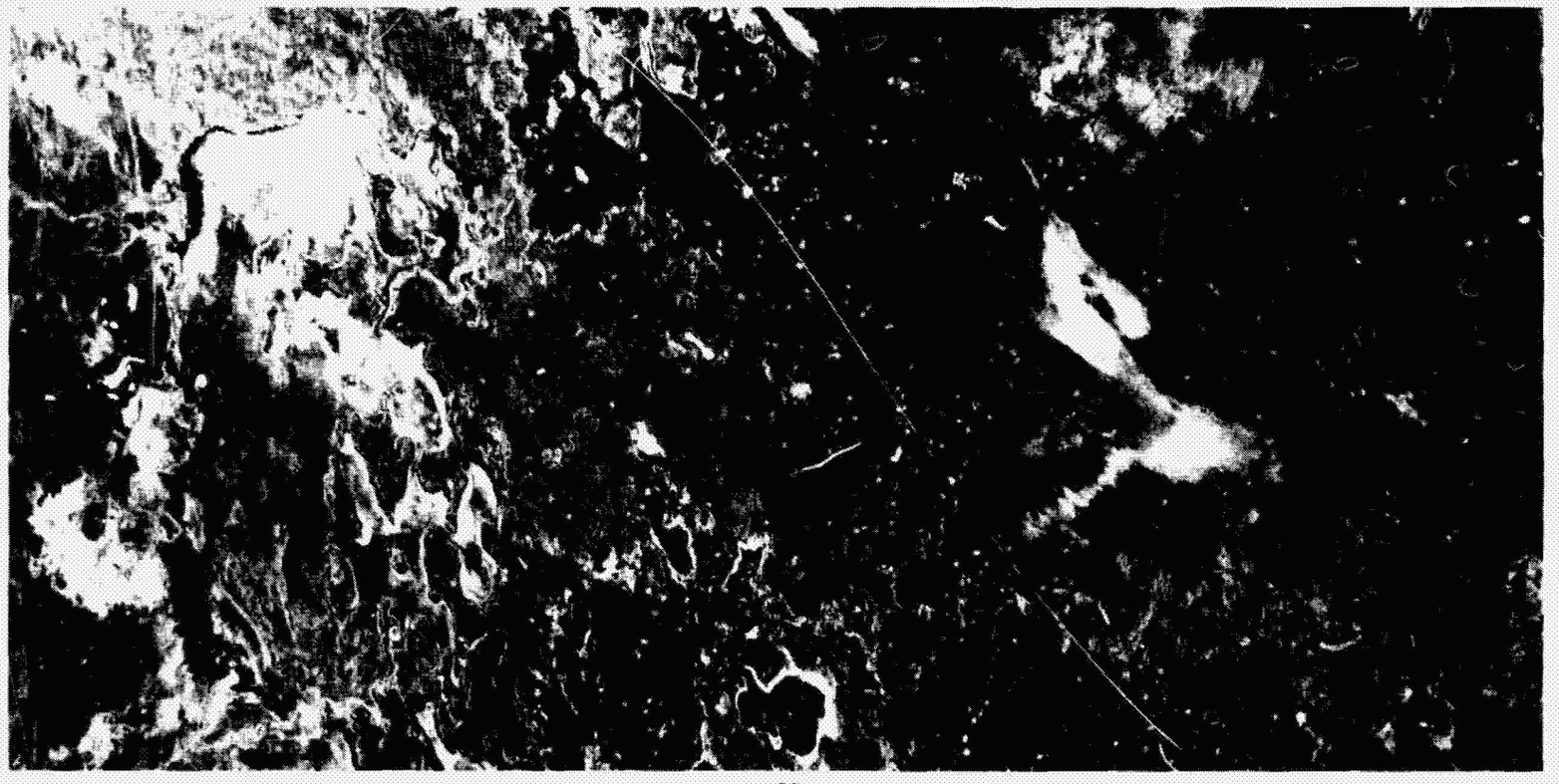

because it presents a mostly low level of radar backscatter. The difference between the SIR-A and Seasat SAR images in the backscatter from the surfaces of the chotts may be due to the difference in the incidence angle of the two radar imaging systems. It may also be related to such seasonal effects as the presence or absence of surface moisture.

Differences in the perception of extended linear features on the SIR-A and on the Seasat SAR images relate to differences in the direction of scene illumination. For example, bright linear features on the left side of the Seasat SAR image represent railroads and highways that are oriented near-normal to the direction of scene illumination. The same features on the SIR-A image (A1 to A5) are nearly parallel to the scene illumination, and consequently they are almost invisible on the image. Linear features on the Chott Melrhir that are nearly normal to the illumination direction of the SIR-A image appear bright (G1 and G2 to H2). These features, which are man-made, are not visible on the Seasat SAR image where they are nearly parallel to the illumination direction.

26. Northern Lop Nur, Xinjiang, China

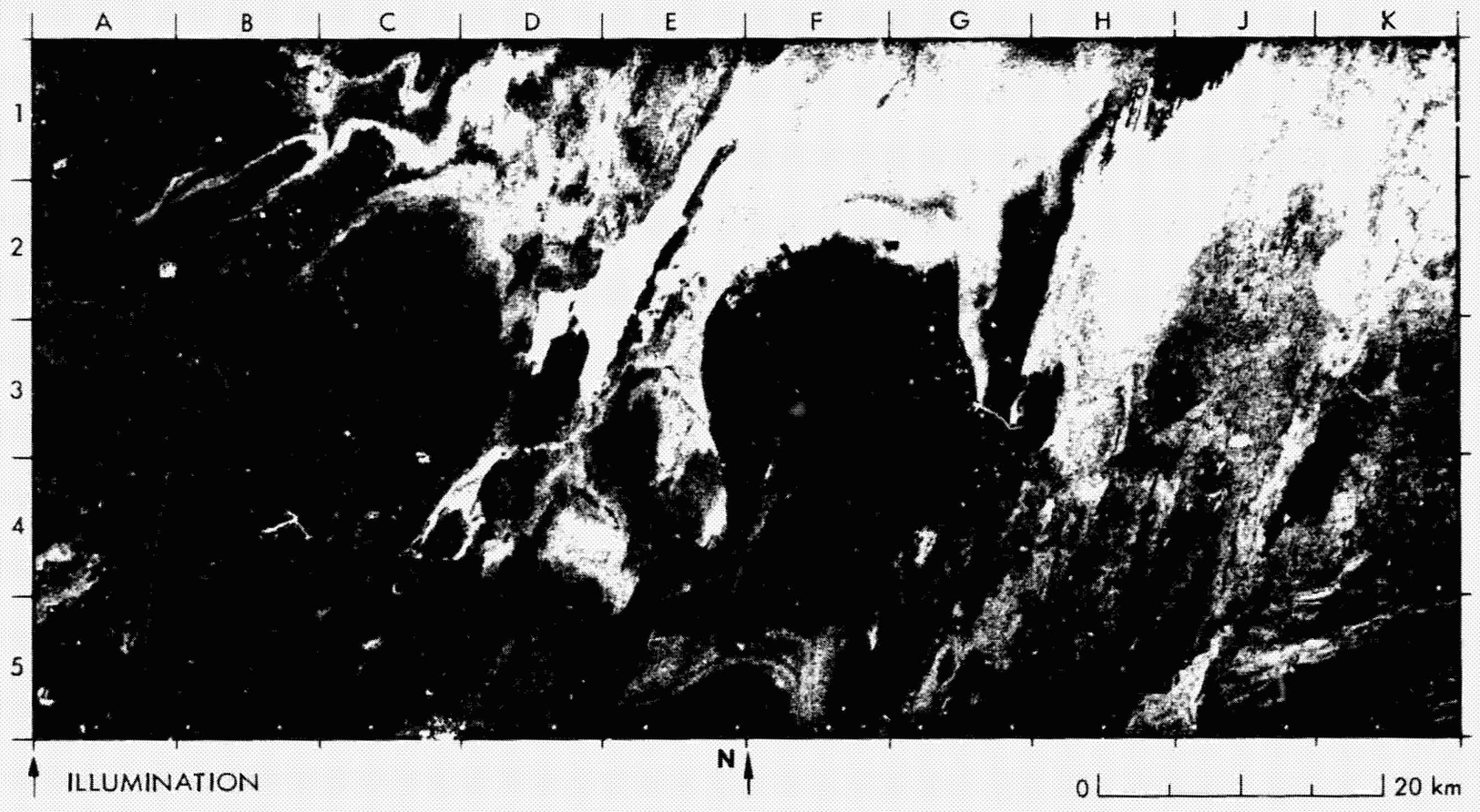

The area shown on these SIR-A and Landsat images is just north of Lop Nur at the east margin of the Tarim Basin in northwest China. Although the region is classified as wasteland and has less than one person per km^2, it is well known both because of its interesting geometric pattern and its important role in the history of desert research. In areas to the east and west of the present Lop Nur, the Swedish explorer Sven Hedin first described yardangs in 1905. Yardangs are closely spaced, aerodynamically shaped ridges and troughs commonly several hundred meters long. They were originally ascribed to wind erosion and thought to be limited to weakly consolidated lacustrine beds. It has been shown recently, however, that yardangs are also common in the hyperarid parts of the world and occur in materials ranging from crystalline igneous and metamorphic rocks, through Mesozoic sandstones and shales, to tough recrystallized Eocene limestones and well-indurated Quaternary sediments.

Yardangs in the Lop Nur region are easily visible on the SIR-A image

Landsat Band 7

at H1/J1 through H2/J2, and at A3. They appear bright on the image due to their extreme roughness relative to the 23-cm radar wavelength. Individual yardangs several kilometers in length can be easily identified on the SIR-A image, but appear as only faint streaks on the corresponding Landsat image. The yardangs in this region trend north-northeast.

Note the overall difference between the SIR-A and Landsat images. The Landsat image is almost a negative of the SIR-A image. The central circular feature in the images (F2 through F4 and G2 through G4)—a dry salt bed—is very reflective in the near-IR wavelength. The high sun angle at the time of this Landsat image (59 deg) adds to the brightness of the feature relative to not only the SIR-A image, but other band-7 Landsat images acquired at lower sun angles. At the SIR-A wavelength, this dry salt bed appears extremely smooth. It is dark on the radar image because of specular reflection. Twenty to thirty years ago, this circular feature was the center of the present-day Lop Nur.

27. The Great Kavir, Iran

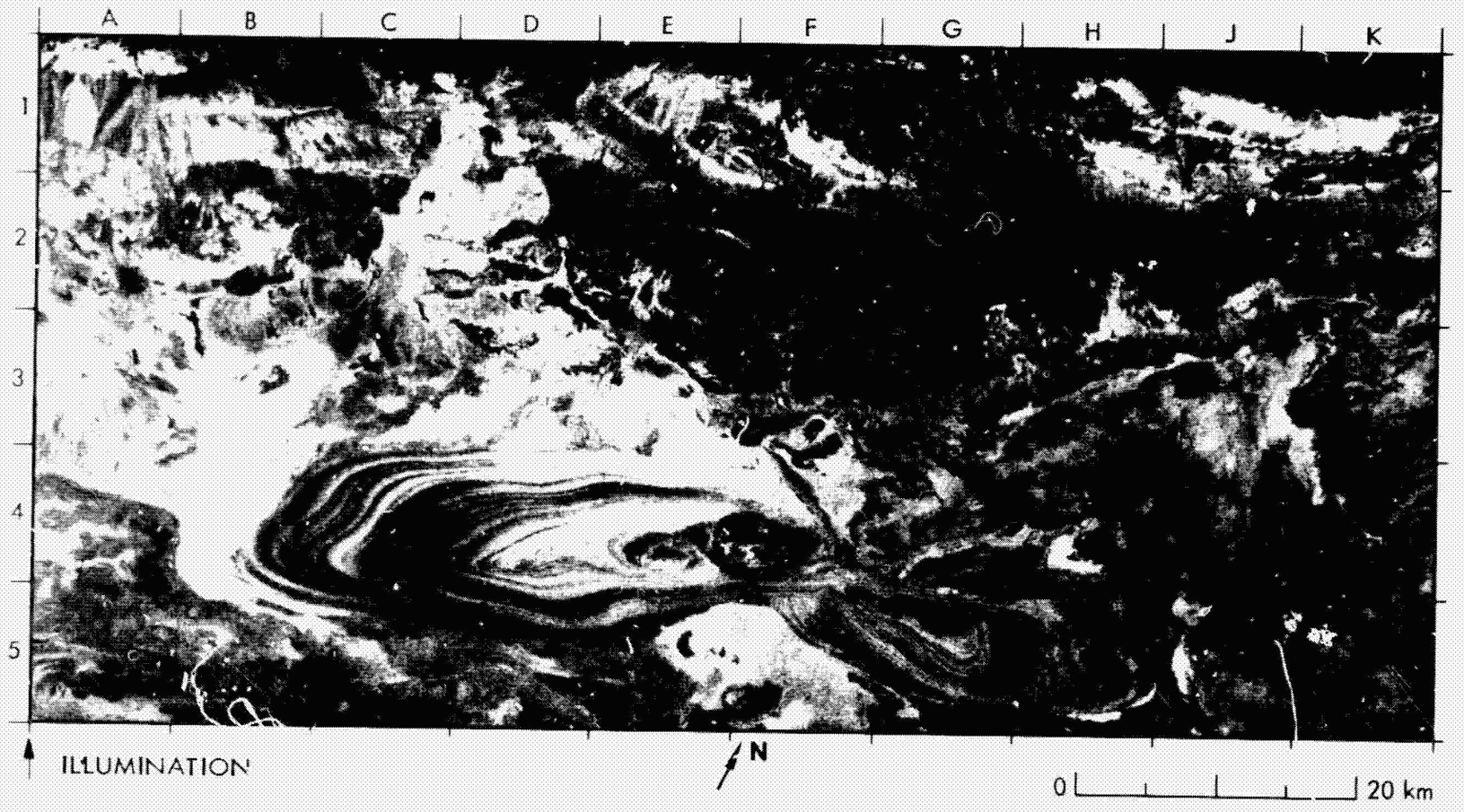

This part of the Great Kavir Desert is about 300 km southeast of Tehran, Iran, in the innermost part of the central Iranian depression. This depression was affected by strong Neogene-Quaternary subsidence (Ref. 12). Because the area is remote, it was not surveyed until 1973.

Most of the area is covered by Quaternary materials that include alluvium, and playa and eolian deposits. The area to the lower right of the image (H3 to H5 through K3 to K5) consists of playa deposits and salt flats. At K3 and from D3 to A3, the cover is primarily swamp. Alluvial fans are apparent from E2 to K2 and from A1 to B1.

The most prominent structural feature in the image is a large, doubly plunging anticline from B4 to H5. The outcrop pattern reflects the differences in backscatter of the sedimentary layers. The structure is composed of pre-Oligocene deposits that were folded in Pliocene times. A large fault cuts through the center of the anticline at F4/F5 through J4. The outcrops are part of the Upper Red Formation. The upper part of the Upper Red Formation outcrops in a narrow band from A4 to C5, where it appears bright.

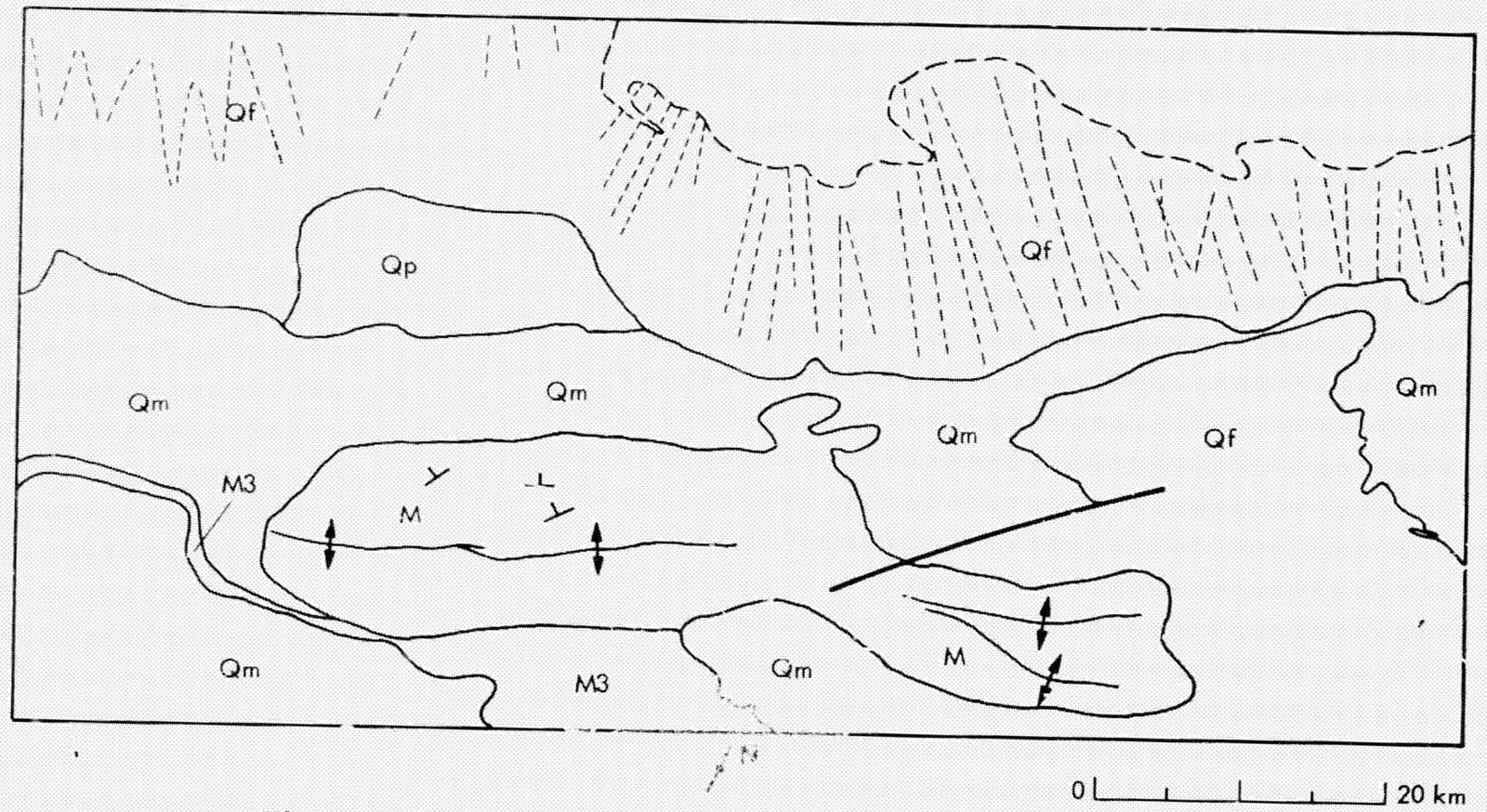

QUATERNARY	Qf	ALLUVIAL FANS
	Qm	SWAMPS, MUDFLATS
	Qp	PLAYAS, SALT FLATS
MIOCENE	M	UPPER RED FORMATION
	M3	UPPER PART OF THE UPPER RED FORMATION

ANTICLINE

FAULT

DIP AND STRIKE

(vii) Karst Terrain

28. Maya Mountains, Belize (Central America)

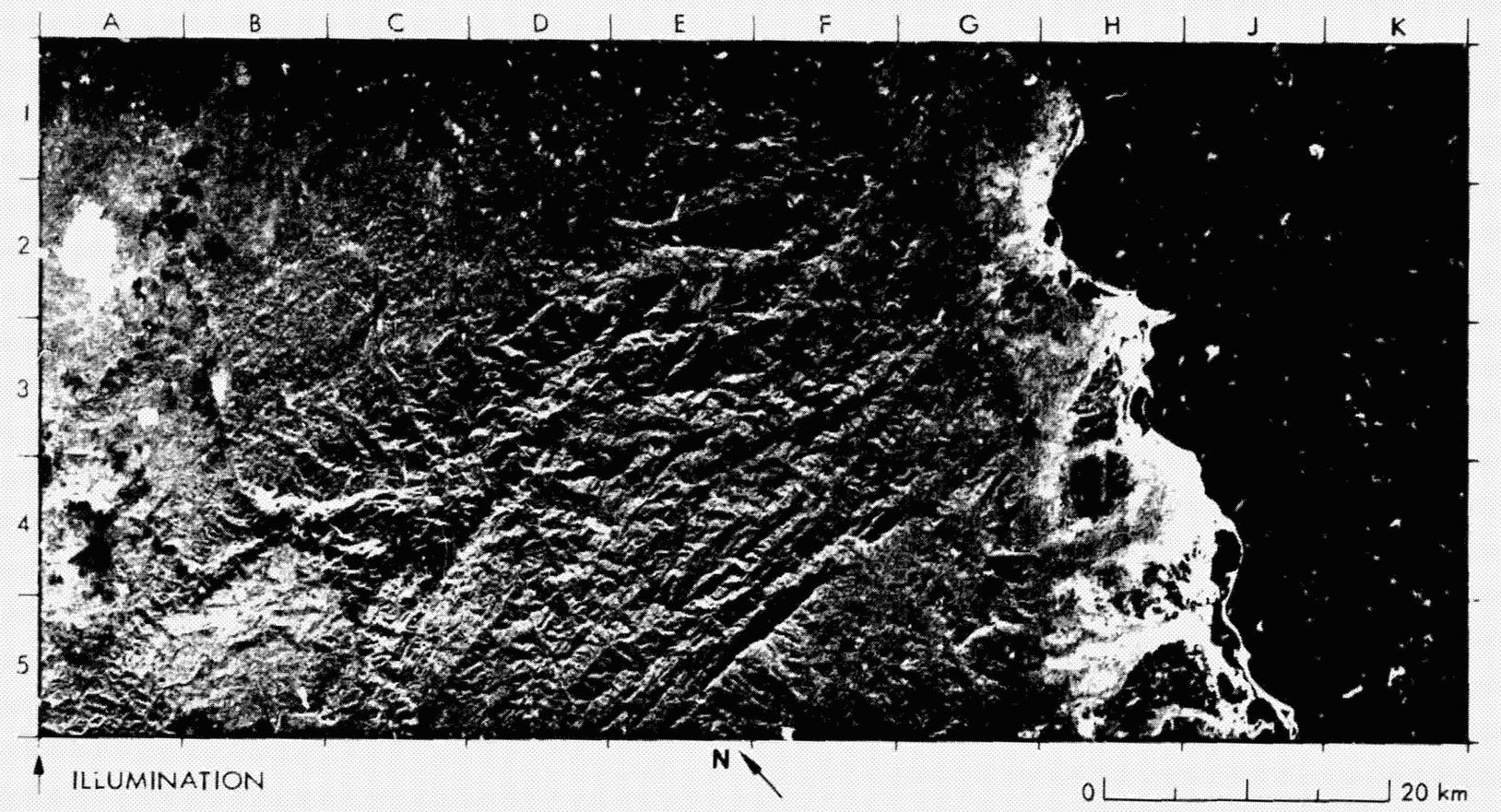

This area of central Belize has a heavy cover of tropical vegetation. On the SIR-A image, it yields an even, diffuse radar return that is modulated by slope changes. The vegetation has been cleared adjacent to the Belize River in the areas that appear as dark patches (B1 to B2). Major geologic units are shown on the generalized geologic map. The mountainous terrain in the center of the image is composed of continental-sedimentary and metamorphic rocks. The rocks form rugged topography due to resistance to erosion, or possibly due to recent uplift along faults shown on the map.

Three bodies of intrusive plutonic rocks at B5, F2 to G2, and F5 to G5 are characterized by low rounded topography that results from rapid weathering and erosion in the tropical climate. Smoother topography characterizes the marine sediments at A1 to A3, and the Quaternary alluvium along the coast. This topography is probably the result of their unconsolidated nature. The knobby texture from A5 to D1 is characteristic of karst topography in humid tropical climates. Sinkholes are numerous, and there are several blind valleys and disappearing streams in the area. A notable example of a stream that terminates in a sinkhole is seen in the upper left corner of B5 and the upper right corner of A5. The mainland coast is characterized by marsh, lagoons, barrier bars, and offshore barrier reefs.

(The text is by courtesy of T. Farr.)

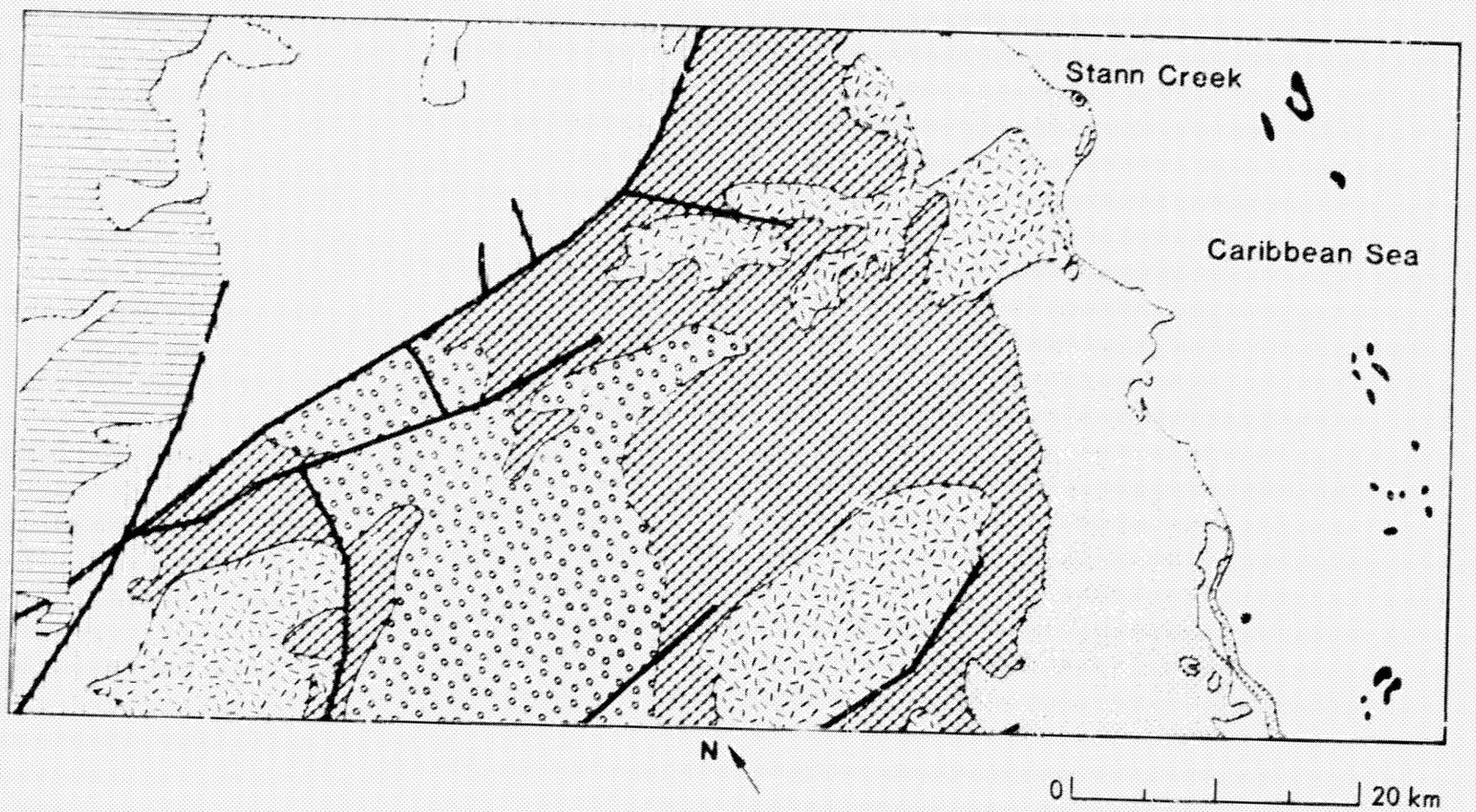

QUATERNARY ALLUVIUM
PALEOCENE-EOCENE MARINE SEDIMENTS
CRETACEOUS CARBONATES
CARBONIFEROUS-PERMIAN CONTINENTAL SEDIMENTS
UNDIVIDED PLUTONIC ROCKS
PALEOZOIC UNDIVIDED METAMORPHIC ROCKS

CONTACT
FAULT

Modified From: Geologic Map of Guatemala, First Edition, 1970

29. Cotabato Province, Mindanao, Philippines

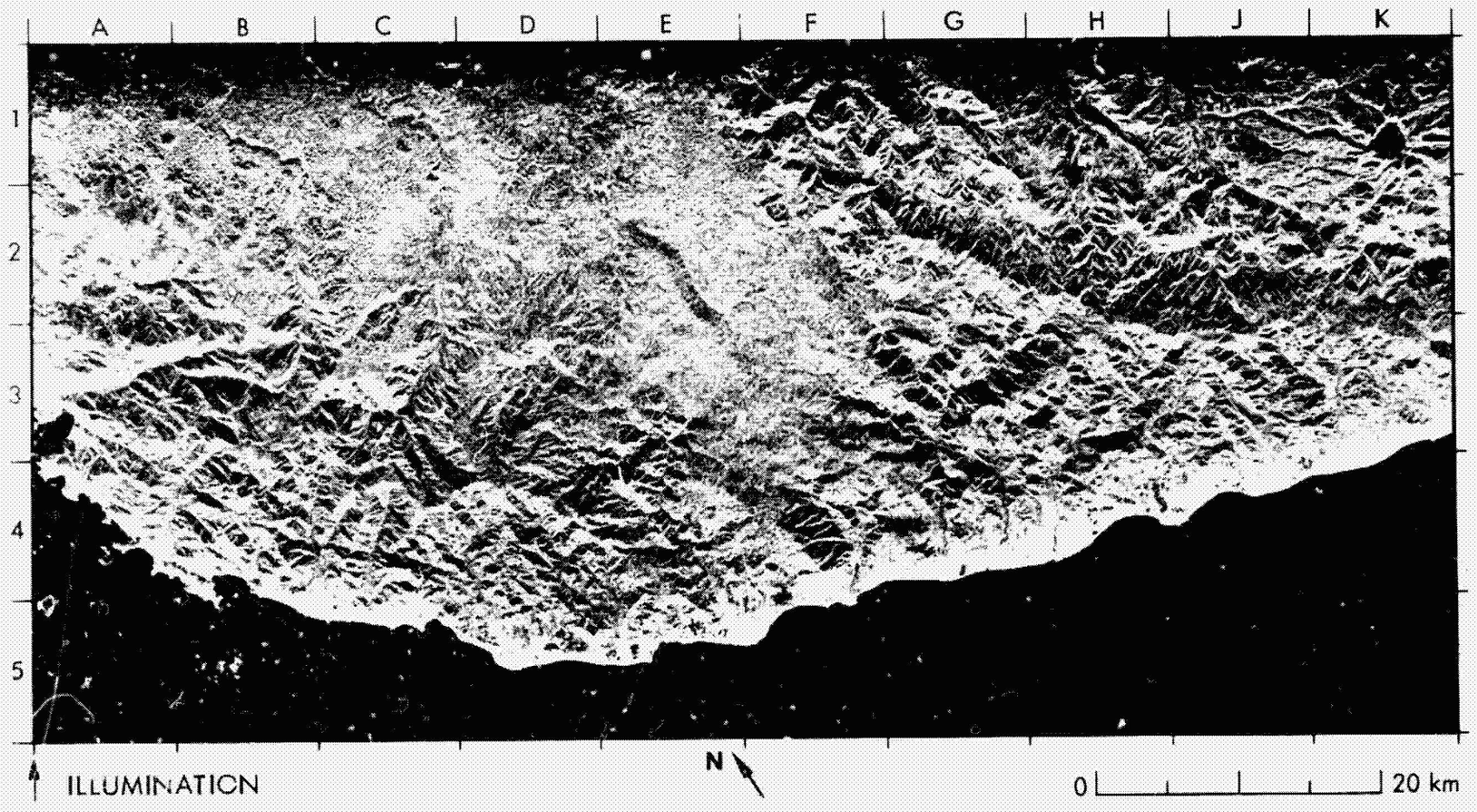

A range of contrasted image textures that represent the varied lithology and structure in southern Mindanao, Philippines, is displayed in this SIR-A image. A narrow coastal strip extends southeastward from Port Lebak (A3 to K3). Notable linear to curvilinear alignments of topography that occur about 5 km inland and parallel to the coastal trend from A3 to D5, and in an east-northeast direction from C2 to A4, probably denote fault structures. A dominantly karstic plateau of Lower Cretaceous age covers the area bounded by A1, E1, and F3; this plateau is deeply incised by northward draining streams. Deep canyons at B1, C1, and E2 are evidenced by the bright image tones from the foreslopes, and by shadows or dark-gray tones from the backslopes.

The alternation of light and dark image tones along and across the image has a high spatial frequency in this area. The very high spatial frequency that produces the fine image texture at E1 contrasts with the lower spatial frequency and coarser texture at A1. Both textures are characteristic of carbonate terrain that has undergone deep chemical

Landsat Band 7

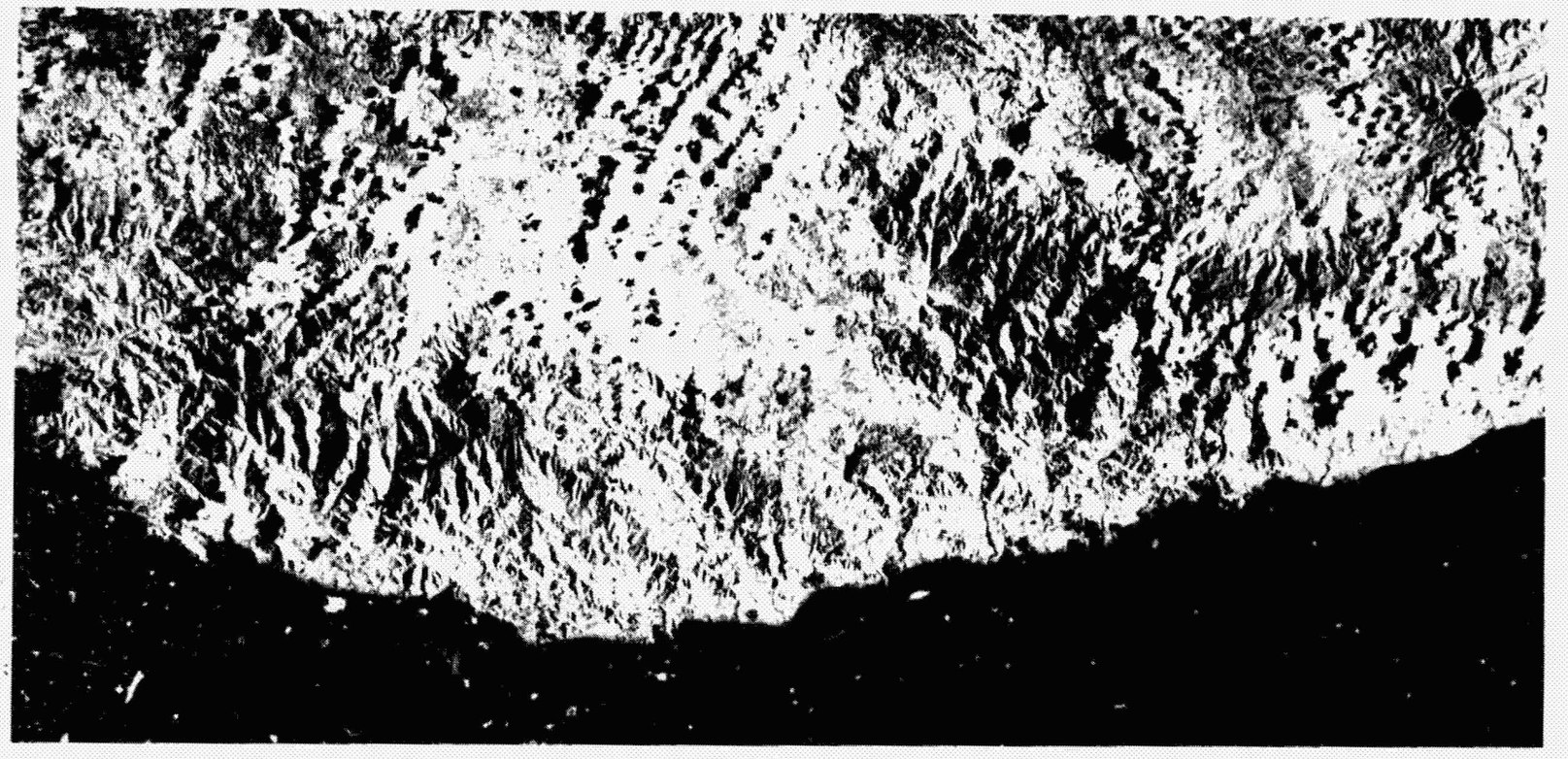

weathering and erosion (karst) in a hot, humid climate. Differences in the coarseness of the texture may reflect subtle differences in the lithology and relative solubilities of the carbonate bedrock.

A major structural feature is the mountain range from F2 to J2, which runs parallel to the northwest-trending Mindanao lineament just beyond the upper margin of the image. The abrupt contact between this range and the adjacent karstic plateau (E1 to F3) is suggestive of a fault boundary, or unconformable rock relations. The highest peak in the mountain range is Mt. Busa (H2/J2) at about 2270 m elevation. Parker volcano at 2040 m and Maughan Lake in the crater of the volcano are situated some 12 km to the east. The image texture in the area from J1 to K1 is typical of volcanic flows.

The Landsat mosaic in the near-IR wavelength shows the karst plateau in the area from A1 to C1 on the SIR-A image. The fine texture in the area equivalent to E1 is obscured by cloud on the Landsat image.

30. Mississippi River Deltaic Plain, Louisiana, U.S.A.

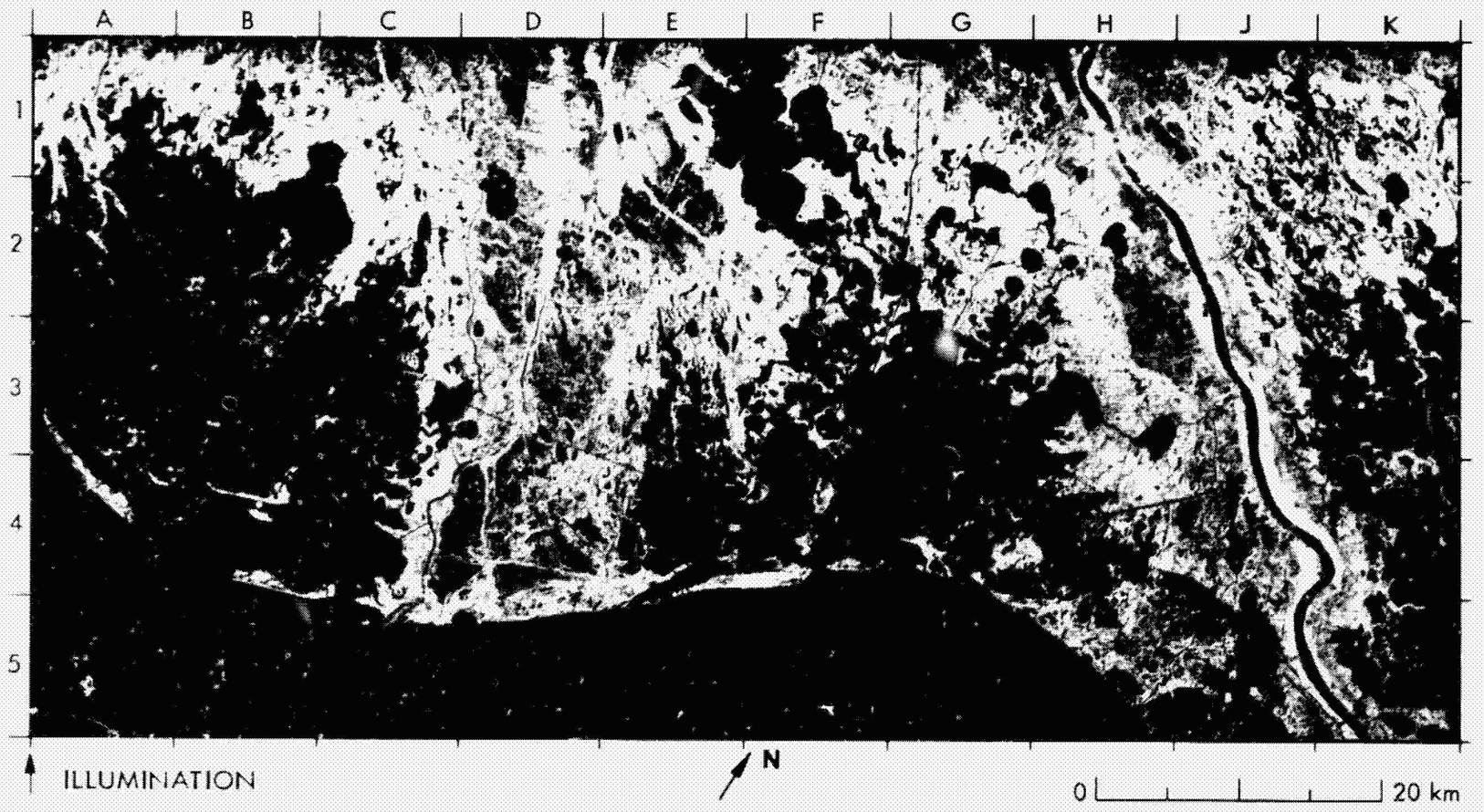

The Mississippi River deltaic plain consists of a succession of major overlapping deltaic complexes spread over a wide area of southeastern Louisiana. These complexes provide a 5000-year record of significant changes at and near the mouth of the river. The SIR-A image covers portions of two of these complexes: the former Plaquemines Delta (G1 to K1 through H4 to K4), and the former Lafourche Delta (B1 to E1 through C4 to E4). The present delta with its familiar birdfoot outline extends southeast beyond the lower right margin of the image. Moderate-to-bright radar returns come from the grasses and sedges that are characteristic of the saline- to brackish-water marsh, which occupies much of the land area in this scene. Dense stands of swamp trees and man-made structures both yield very bright returns. They occur mostly in areas parallel to the levees of the Mississippi River (H1 to K5), and along Lafourche and adjacent bayous (D1 to E1 and D2 to E2).

The water/land interface is strongly contrasted on the radar image. Offshore oil rigs and platforms form point targets that provide very bright

Landsat Band 5

returns, notably at A3 and B5 to D5. A cluster of subparallel, thin bright lines shoreward from the coast and east of Bayou Lafourche (D4/D5) represents a succession of ancient beach ridges that are locally termed "cheniers."

Vegetation in the visible-red wavelength on the Landsat image is strongly absorptive and appears dark. Extensive sand beaches, cheniers, sediment-laden water, mudflats, and man-made structures have a high albedo at this wavelength; they appear relatively bright on the image. Swamp trees that appear bright on the radar image and dark on the Landsat image can thus be distinguished on the Landsat image from man-made structures and other features that appear bright on both images. The albedo of the water on the Landsat image varies with the degree of suspended sediment. Thus the water/land interface is locally obscure. The offshore oil rigs and platforms cannot be seen on the Landsat image.

31. Red River Deltaic Plain, Viet Nam

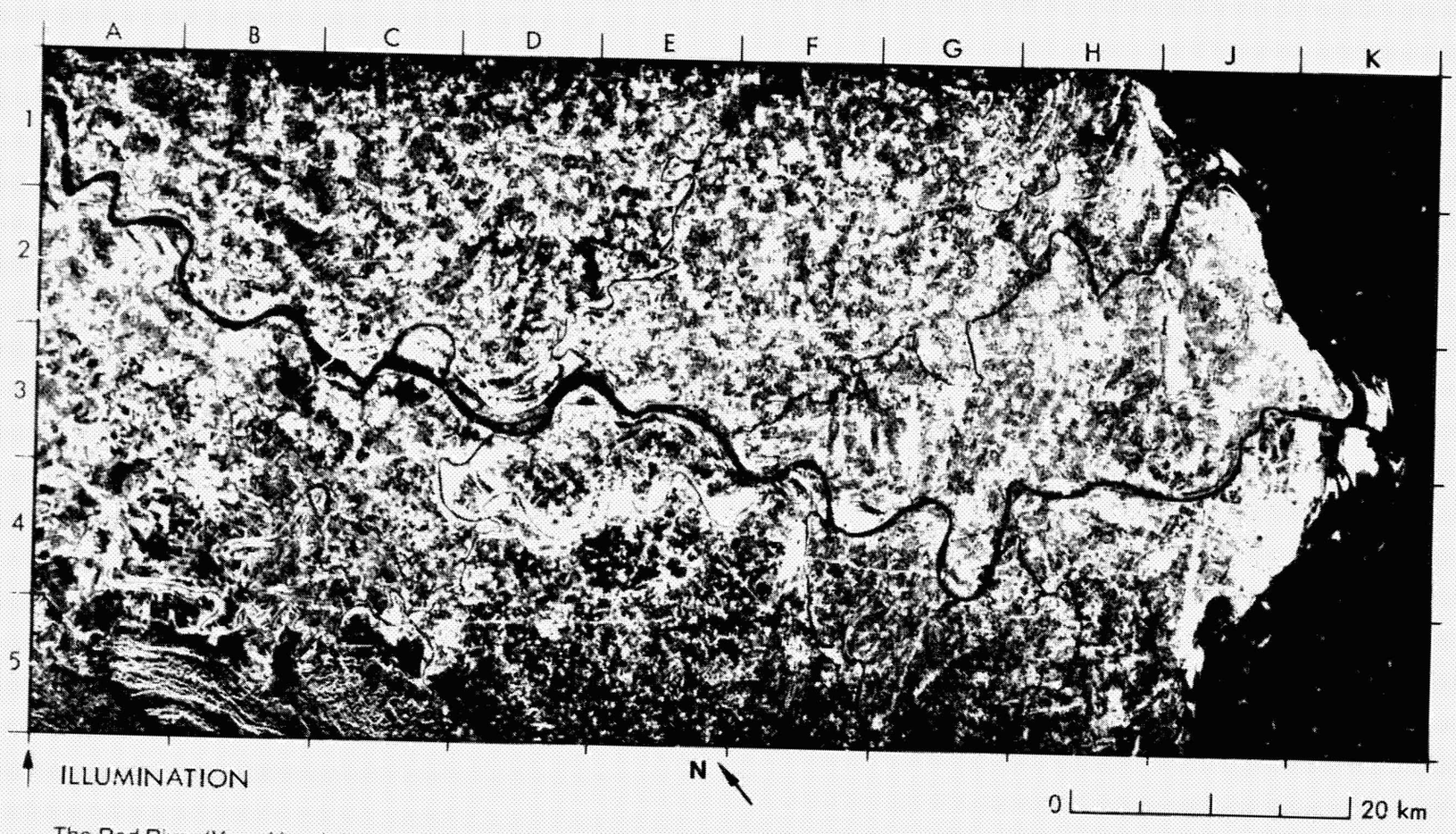

The Red River (Yuan Hong) rises in Yunnan Province, south China and flows in a long, remarkably linear valley through the mountains to the lowlands of north Viet Nam. The city of Hanoi (just beyond the left margin of A1) is situated at the apex of the deltaic plain that widens southeastward toward the Gulf of Tonkin. The margins of the plain are clearly defined by linear mountain ranges; part of one (A5 through C5) is shown here. The plain is approximately 140 km wide at the shoreline. At Hanoi, the river channel divides into two major distributaries. The Red River forms the main distributary, which drains the western part of the plain from A1 to K3. The Duong River drains the northern and eastern part of the plain to the port city of Hai Phong (not covered on the image).

Interconnecting channels and smaller distributaries drain the intervening area of the deltaic plain. Deposits from the mouth of the Red River distributary have prograded some 14 km seaward beyond the plain. A

Landsat Band 7

lesser progradation is evident at the mouth of the Thai Binh distributary (J1). The seaward margin of these deposits is characterized by extensive mudflats, which are black on the radar image. On the Landsat mosaic, taken in the near-IR wavelength, the mudflats are medium to dark gray. Sand ridges along the coast (H1 to K3 to J5) appear bright on both the radar and the Landsat images. On both images as well, bright arcuate lines that bend toward the sea represent relict beach ridges. These ridges are much more pronounced than the cheniers in the deltaic plain of the Mississippi River, U.S.A. (see Scene No. 30). The ridges extend about 35 km inland, as far as the cities of Nam Dinh and Thuan Nghiep, to the west and to the east of the Red River respectively, at F4.

32. Shatt al 'Arab, Persian Gulf

The Shatt al 'Arab (E1 to E4/F4) at the head of the Persian Gulf forms the outlet for the combined drainages of the Tigris and Euphrates Rivers. This channel includes the Qosbeh Reach (E2), and Al Faw Reach (E3 to E4). The seaward margin of the delta is characterized by mudflats that are locally dry at low water, but covered at high water during southeast gales.

The mudflats appear black on the radar image because of specular reflection of the radar energy from the smooth surfaces. Open water is dark gray, as from B1 to C5 through K5 to K2. A swamp area on Abadan Island at F3/F4 yields similar dark-gray image tones. Date-palm plantations yield strikingly bright radar image tones along the banks of the Shatt al 'Arab, and along the adjacent Khowr-e Bahmanshir (F1 to F4/G4).

On the Landsat image in the near-IR wavelength, open water is black, mudflats are medium gray, and the swamp on Abadan Island is

Landsat Band 7

distinguished by dark-gray tones. Dikes and sea walls are bright on the radar image, as from C1 to E4, but they are not perceptible on the Landsat image. Shoreward of the mudflats, the unimproved desert surfaces show a range of dark- to medium-gray tones on the radar image (e.g., C1 to D1), and medium-gray to bright tones on the Landsat image. Terminal facilities are visible on the radar image from C2/D2 to D3, on the Landsat image in the area that corresponds with C2 to D2 on the radar image, they are not visible. Presumably the facilities had not been constructed at the time of Landsat's acquisition in August 1977. Bright point-target returns on the radar image reveal pipelines from E1 to E3/D3, and lighthouse buoys that mark the navigation channel gulfward from the mouth of the Shatt al 'Arab at F4 to F5.

B. Renewable Resources

The Earth's renewable resources imaged by SIR-A are grouped here under hydrology-drainage networks, agriculture, forest cover, and urban areas. The perception of drainage channels on the SIR-A images (Scene Nos. 33 through 40) is largely dependent on the local image contrast along and adjacent to the channel. The wide channels of major trunk streams (Scene Nos. 33, 35, and 36) are readily discerned from the dark tone of the water. Narrow channels of low-order tributaries may be outlined by the radar returns from riparian vegetation (Scene Nos. 33 and 34) or, in the case of dry channels, from deposits in the channel (Scene No. 37). Significant alterations in stream channels that have undergone extensive flooding are apparent by comparing the SIR-A image with corresponding Landsat MSS coverage acquired years earlier (Scene Nos. 35 and 36); this technique can also be applied to detect man-made changes on a floodplain (Scene No. 38). A single example of mountain valley glaciers (Scene No. 40) shows a pronounced structural control of the drainage pattern. SIR-A images of agricultural scenes (Nos. 41 through 44) commonly show image tones the inverse of those on Landsat band 5 images. This occurs where an active vegetated canopy yields multiple backscatter at the radar wavelength, but is strongly absorptive at the visible-red wavelength (Scene Nos. 41 and 42). SIR-A backscatter from circular fields is related to multiple reflections from standing crops (Scene No. 42) and to specular reflection and/or Bragg scattering from plowed furrows (Scene No. 43). Changing patterns of agriculture are evident from the images of Scene No. 44. Forest canopy produces a generally uniform tone on SIR-A images (Scene Nos. 45 through 48). Radar images of urban areas show systematic changes in radar reflectivity from buildings; these changes depend on the orientations of the reflecting surfaces (Scene Nos. 49 and 50).

(ix) Hydrology—Drainage Networks

33. Mississippi, Missouri, and Illinois Rivers, U.S.A.

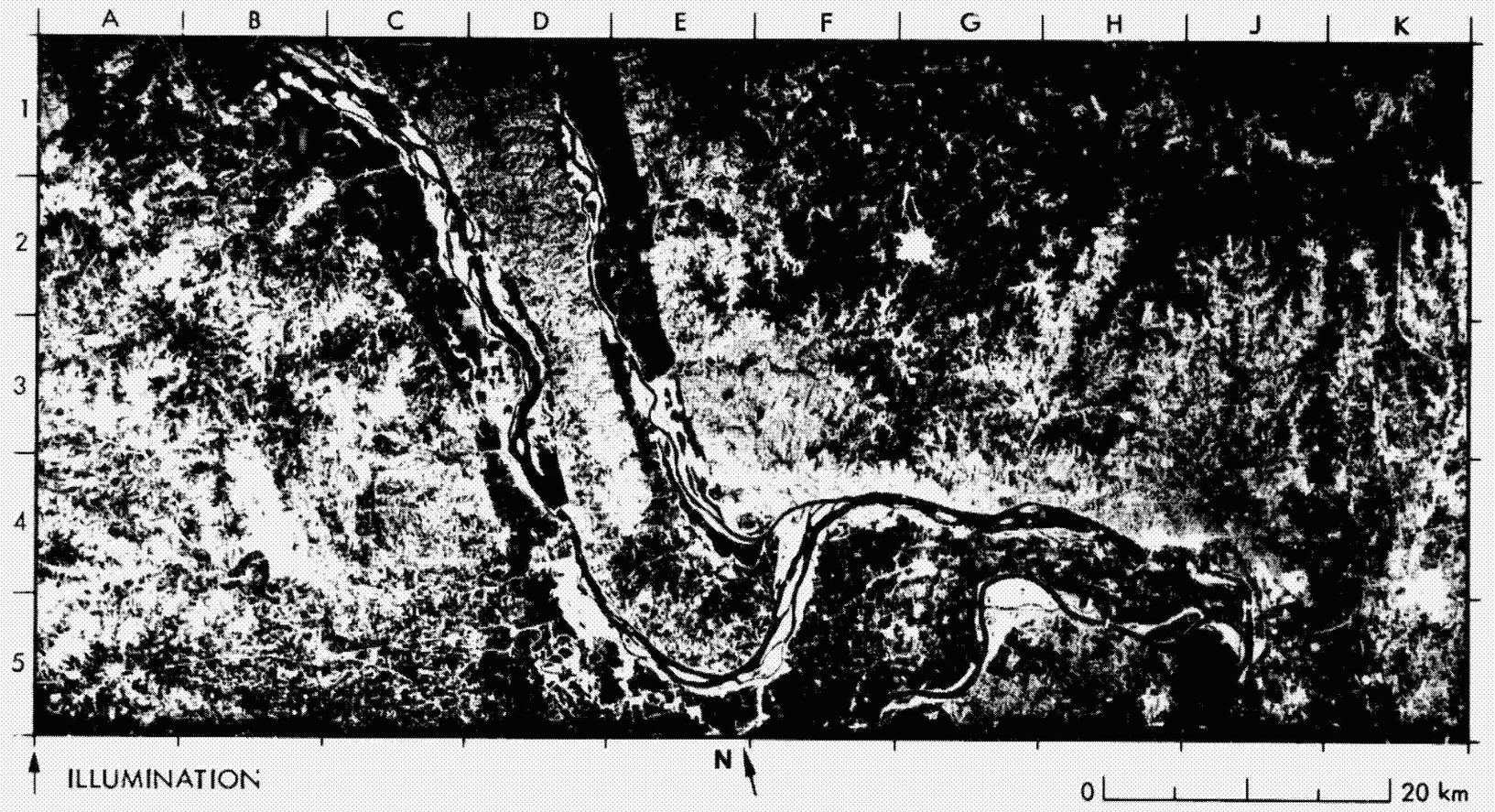

A plexus of drainage channels occurs where the Illinois River (D1 to F4) and the Missouri River (F5 to J5) join the Mississippi River (B1 to J5) to carry their combined discharge south to the Gulf of Mexico. These rivers were major routes for explorers, traders, and settlers. They have been harnessed with a system of locks, as at Cap au Gris (D4) and Alton (H4), so that today they provide an arterial system of inland waterways that carries a significant volume of commercial traffic. The floodplains of the Illinois and the Mississippi Rivers were formed by glacial meltwaters in Pleistocene time. Each floodplain is approximately ten times wider than the stream channel that now flows through it. The smooth curvilinear outlines of the floodplains are clearly displayed on the SIR-A image. Very bright radar returns come from the forest cover in the floodplains, while the cultivated fields provide weak radar backscatter as reflected by medium-to-dark shades of gray on the image. A dendritic drainage pattern on the upland areas adjacent to the floodplains is revealed by the bright radar returns from the wooded slopes of low-order

Landsat Band 7

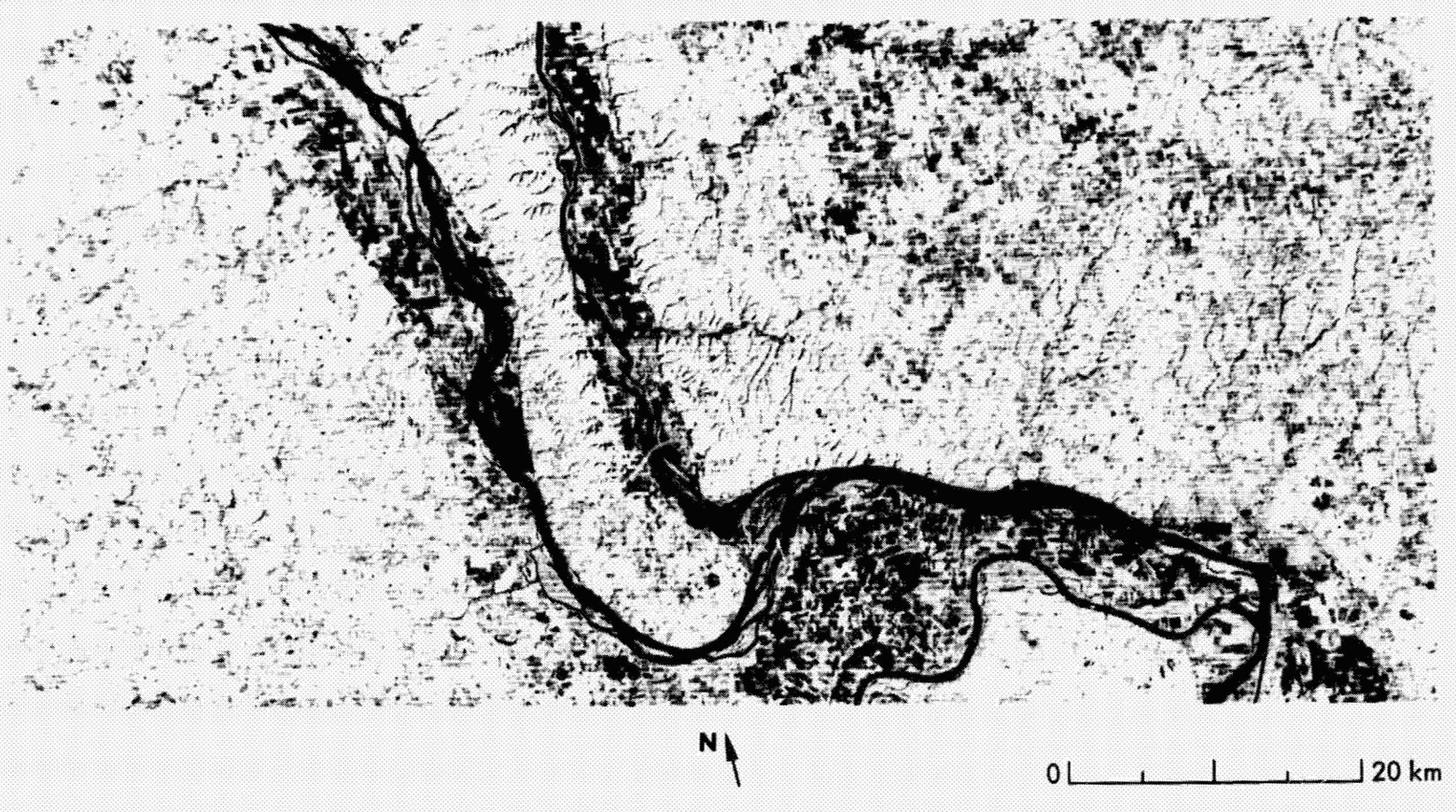

tributary streams. The area west of the Illinois River is more extensively dissected than the glaciated plains to the east of the river. Urban areas provide moderate-to-very-bright radar returns, depending on the orientation of major structures relative to the radar illumination. The city of Jerseyville, Illinois, (F2/G2) appears very bright on the radar image. The much larger cities of Alton, Illinois, (H4/J4) and Florissant, Missouri, (G5/H5) show bright returns only from appropriately oriented streets, buildings, and railroad yards.

The Landsat image in the near-IR wavelength more clearly outlines the water/land interface. This is notably true for the numerous ponds on the upland surface in Missouri, west of the Mississippi River. The Landsat image also provides [illegible]nction between cultivation in the floodplains and that in [illegible]plands.

34. Lüliang Shan, Shanxi, China

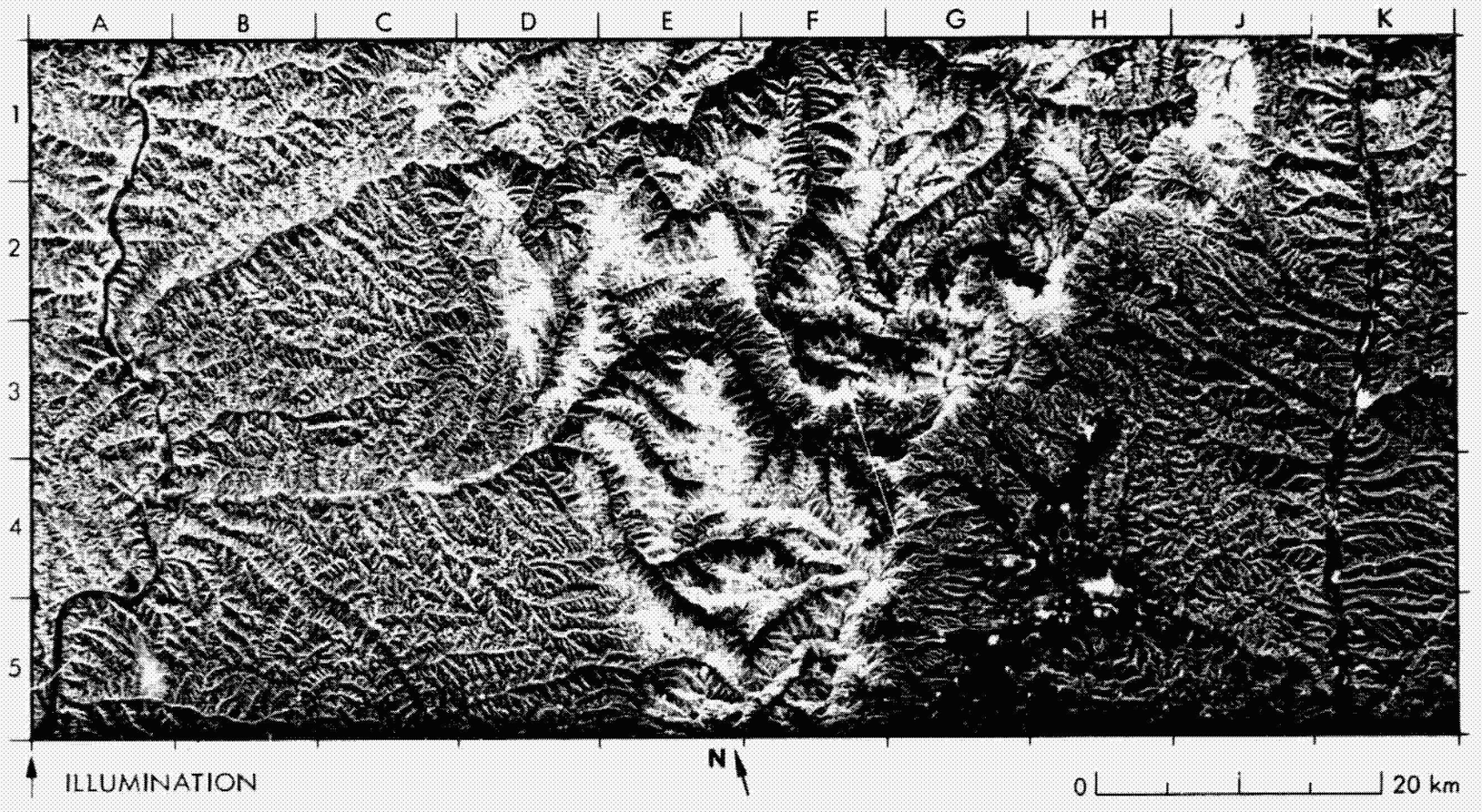

The extensive dendritic patterns shown in these images of a portion of Shanxi Province, China, are drainages from the Hei-ch'a Shan (mountains) (F4/G4 to F5/G5) and the Lüliang Shan (G1/G2 through J1/J2) that run into the Huang He (Yellow River) (A1 to A5) and the Fen He (K1 to K5). Smaller rivers, including the Lan-i He (D1/D2 to A2), the K'u-yeb He (B5 to A5), and the Yu-fen He (F3 to A4/B4), contribute to this network. The Huang He carries a heavy volume of sediment. It has a high albedo and appears very bright on the Landsat image in the visible-red wavelength. The Fen He is less heavily laden with sediment and it appears in darker image tones. No distinction in image tones is displayed by the rivers on the SIR-A image.

The more mountainous region in the center of the image is about 1000 m higher than the Huang He valley and 500 m higher than the Fen He valley. Bedrock consists mostly of Triassic sedimentary rocks, which

Landsat Band 5

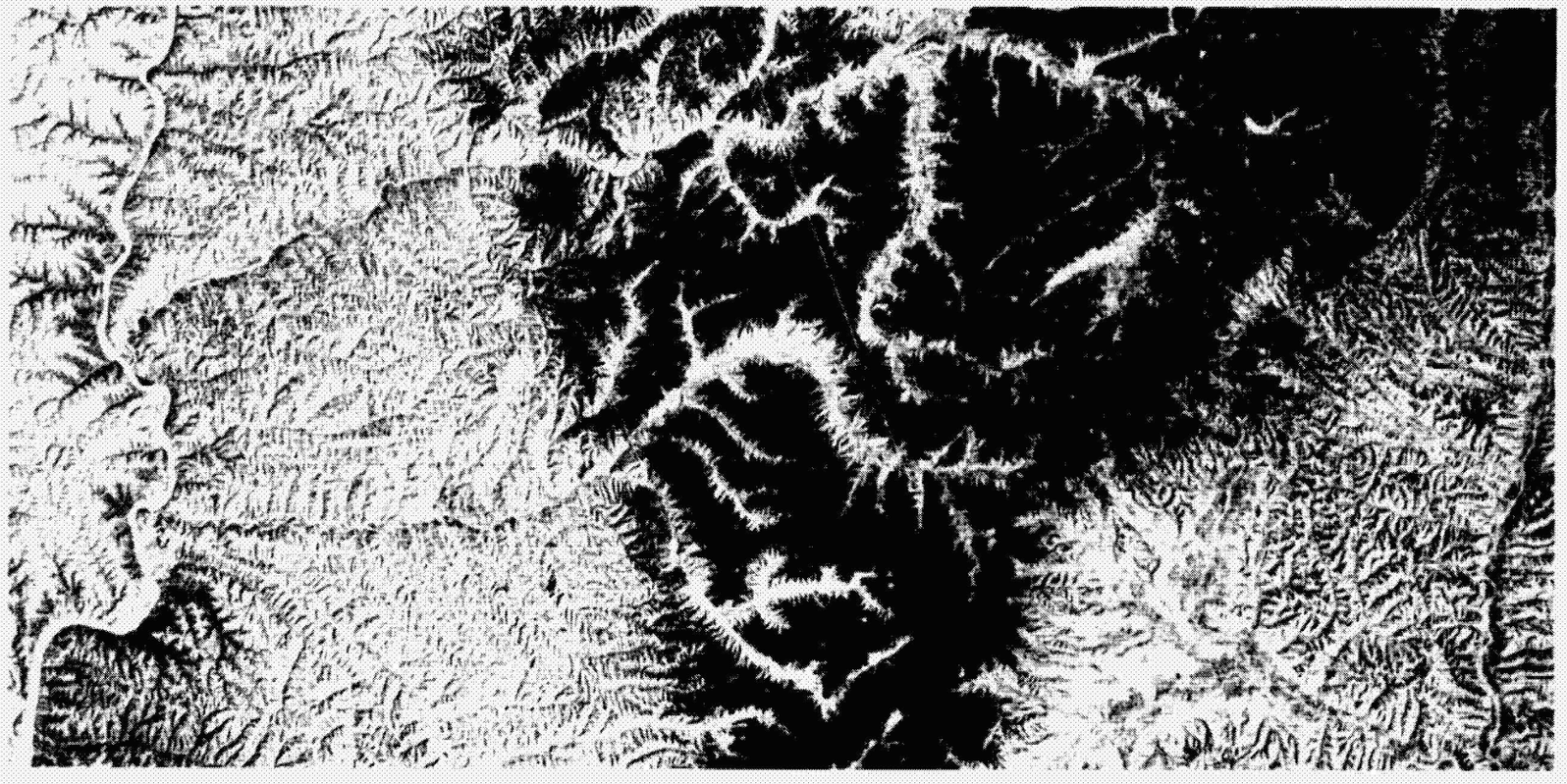

overlie an ancient platform.

This mountainous region is extremely dark on the Landsat image because of absorption by broad-leaved forest canopy. The increase in vegetation from lowland to upland follows the 1500-m contour lines very closely. The vegetated upland cannot be distinguished from the surrounding lowlands on the Landsat image in the near-IR wavelength. The SIR-A image is very bright in the vegetated uplands due to the roughness of the canopy relative to the radar wavelength. Vegetation is also prevalent in the valleys that join the Huang He.

Agriculture in this hot, dry region is supported by some irrigation. Winter wheat, millet, and kaoliang are the primary crops. Near-surface and deep coal deposits have been mined to some extent in this region. The river banks have a population density of about 50 people per km^2. The city of Lan-hsien is at H4 and Lao-ch'eng is at H3/H4.

35. Rio Ucayali, Loreto, Peru

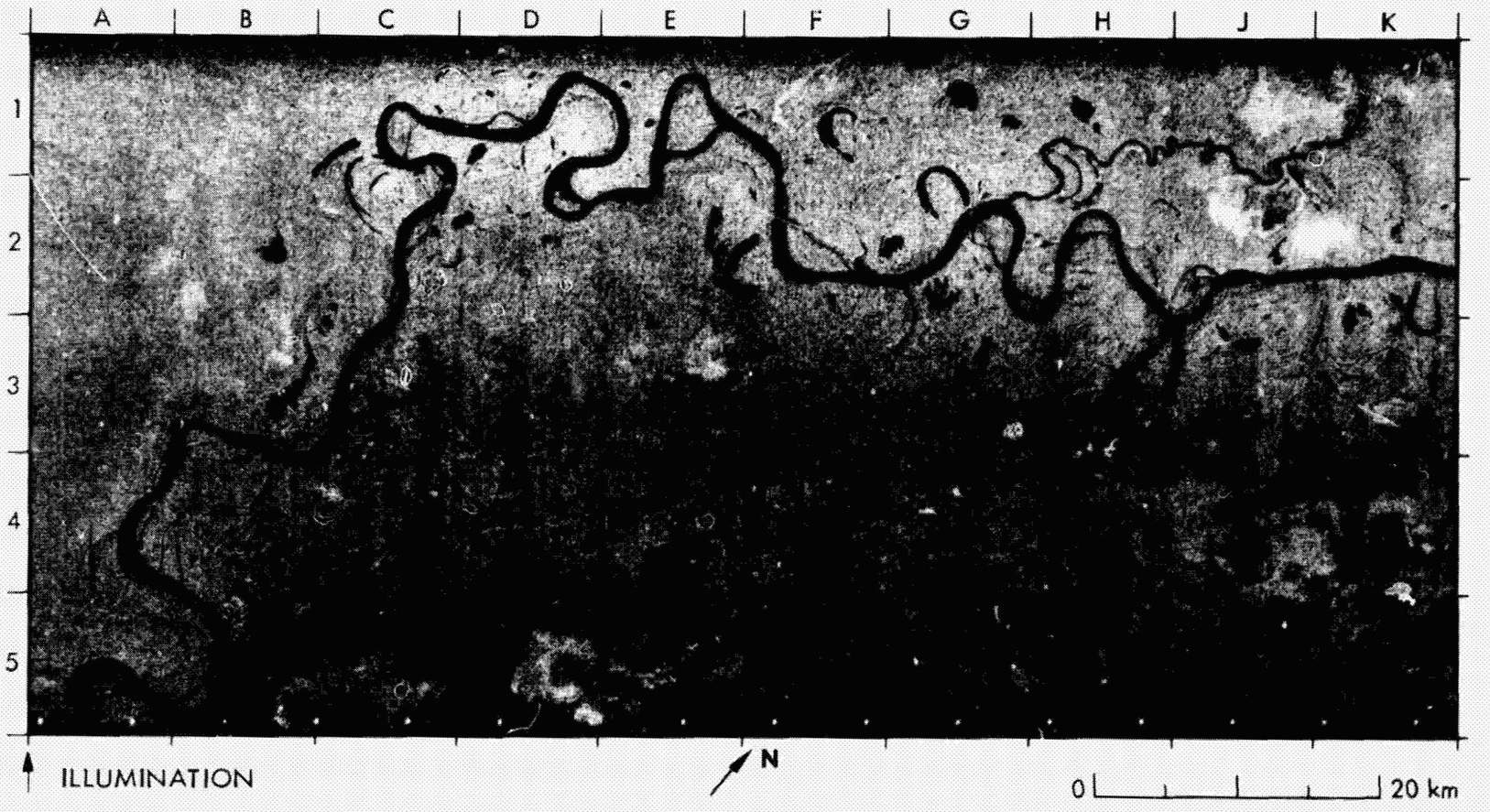

At first glance, an obvious difference between these images of the Rio Ucayali in eastern Peru is in the tone of the river. It is exclusively black on the SIR-A image because of specular reflection of the radar beam from the smooth river surface. On the Landsat image in the near-IR wavelength (band 6), the Rio Ucayali is light gray. Only the oxbow lakes and other bodies of stationary water appear black. This is because the near-IR wavelength in band 6 is sensitive to the large volume of suspended sediment in the water. In the visible-red wavelength, the high albedo of the sediment-laden river saturates the Landsat band-5 image to white.

Closer examination of the images shows important differences in the course of the river between the time the Landsat image was acquired in October 1972 and the time the SIR-A image was acquired in November 1981. A pronounced change occurs in the bend in the river at H3/J3. The meander loop on the Landsat image is cut off on the SIR-A image, and the resultant oxbow lake is partially filled in. In addition, the multiple

Landsat Band 6

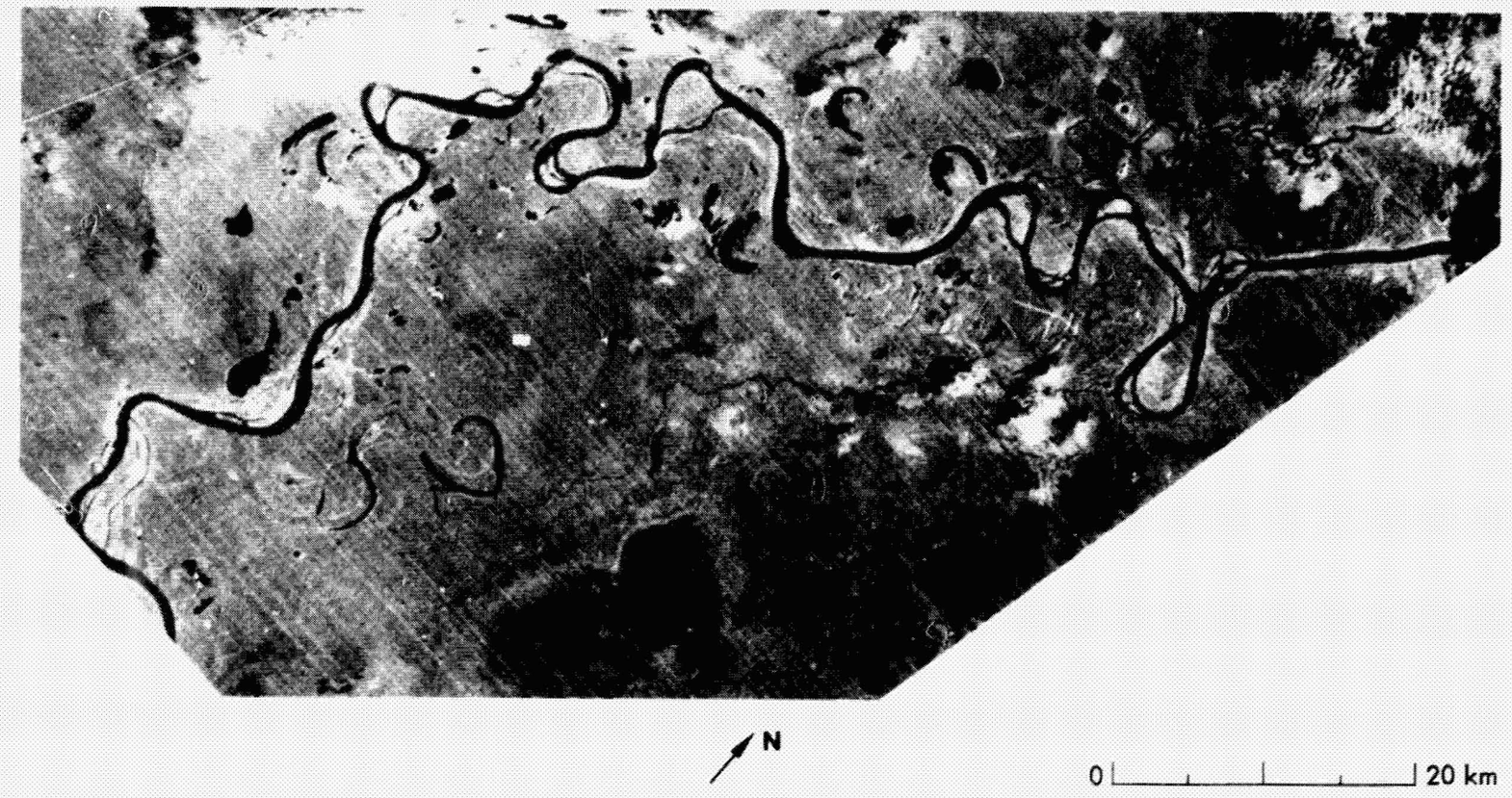

river channels immediately north of this oxbow have been replaced by a wide single channel.

Other changes in the river channel are evident on the SIR-A image at C1, D1/E1, and G2. The island in the river on the Landsat image has merged with the east bank of the Ucayali at C1 on the SIR-A image. The narrow inner loop on the Landsat image has almost disappeared at D1/E1 on the SIR-A image, and the triple loop on the Landsat image has become a double loop at D2 on the SIR-A image. The inner loop at G2 on the SIR-A image has thinned considerably and has changed course from that shown on the Landsat image.

The floodplain along the Ucayali extends up to 20 km on either side of the river. The flooding in this region, one of the most extensively flooded in South America, accounts for the changes noted above.

36. Ilhas Macuapanim, Amazonas, Brazil

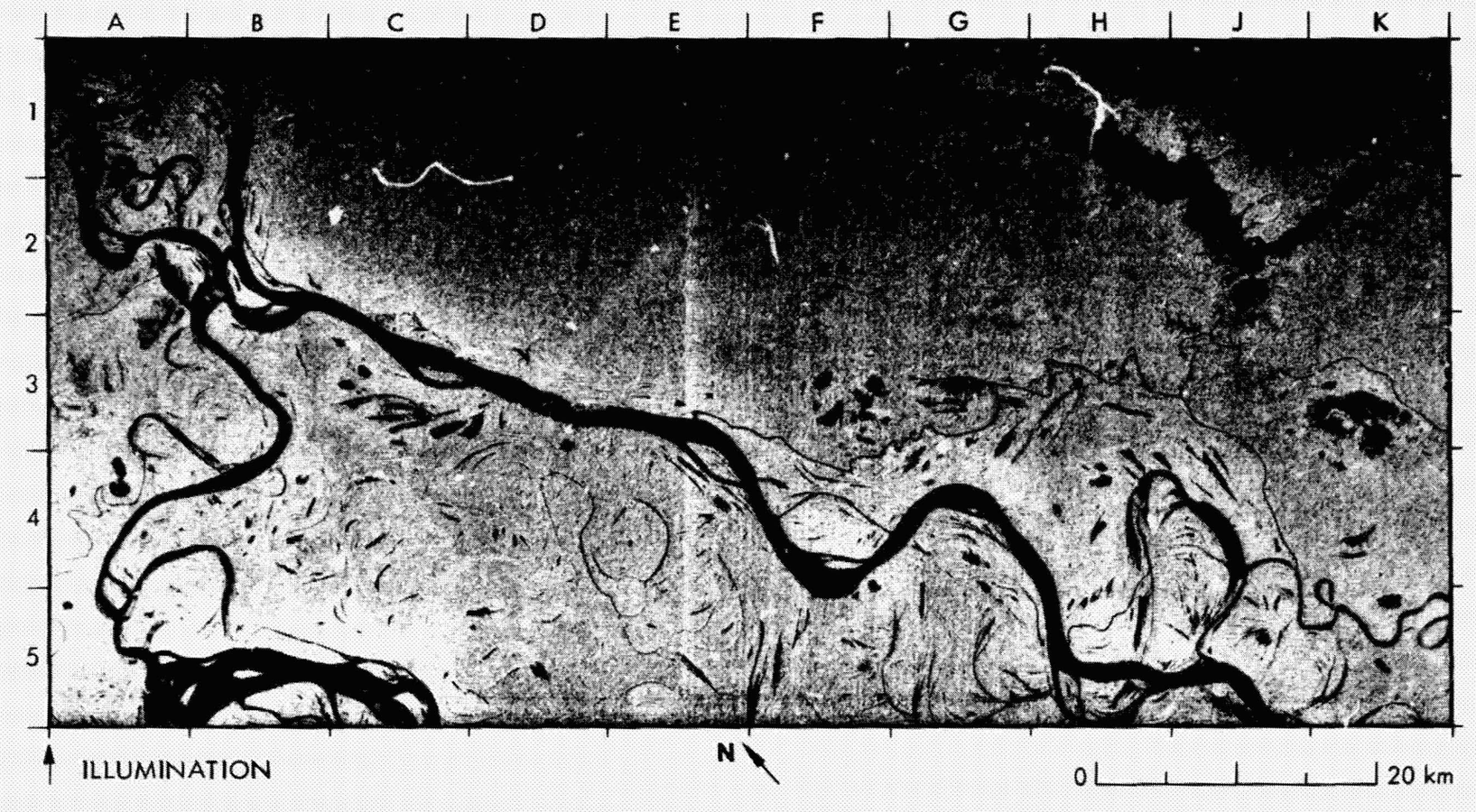

Upstream from the confluence of the Amazon and Japurá rivers in central Brazil, a complex network of active and abandoned river channels surrounds the Ilhas (Islands) Macuapanim. The area covered by this SIR-A image shows part of the large island (A5 to J5 to B2) that is situated between the Amazon (A5 to C5) and the Japurá (A1 to J5), and the smaller Ilha Mapixari (A1, B1 to A2, and B2) that is within the Japurá. The Landsat image (near-IR wavelength) was acquired in 1973, eight years before the SIR-A image. Very little change occurred in the major stream channels during this interval; however, some changes are evident in the minor connecting channels.

In 1973, the primary connection between the Japurá and the Amazon at the Amazon bend was, as shown on the Landsat image, the east-to-southwest flowing loop (A4 to B4/B5 on the SIR-A image). A secondary connection—a narrow, incipient channel with a nearly north-south orientation (A5 on the SIR-A image) and two branches, one flowing southeast (A5/B5 on the SIR-A image) and the other flowing southwest (A5 on the SIR-A image)—created two islands at the north-northwest bend of the Amazon.

Landsat Band 7

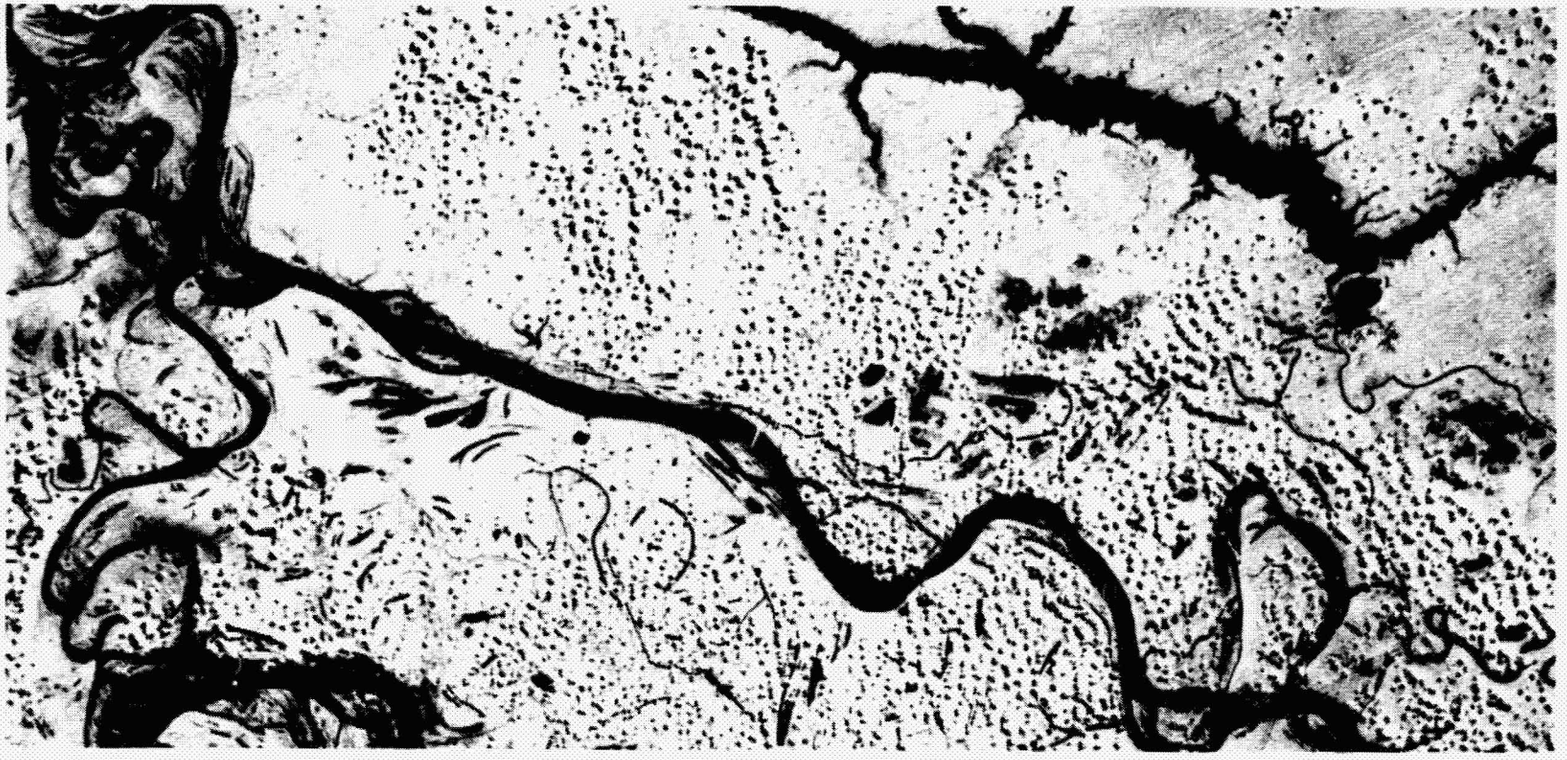

By 1981, this primary connection, as shown on the SIR-A image, had filled with vegetation at its juncture with the Amazon, and the secondary connection had become the dominate drainage link between the two rivers. One of the two islands disappeared altogether leaving only a vestige of the southwest branch. The other island was reduced considerably in size.

Changes in river channels are commonly caused by flooding, but monitoring of the rivers in this area is difficult because of dense vegetation and thick cloud cover; it is not known, therefore, whether the changes noted here were caused by a single massive flood or a series of smaller floods.

Few Landsat images with less than 20% cloud cover have been obtained of this area. The radar, however, is not influenced by cloud cover because of the sensor's longer wavelength. In fact, it is likely the area was covered at least partially by clouds when this SIR-A image was acquired. Therefore, in monitoring the courses of rivers in such cloudy regions of the world as this, the benefits of imaging radar are obvicus.

37. Al Widyan, Saudi Arabia and Iraq

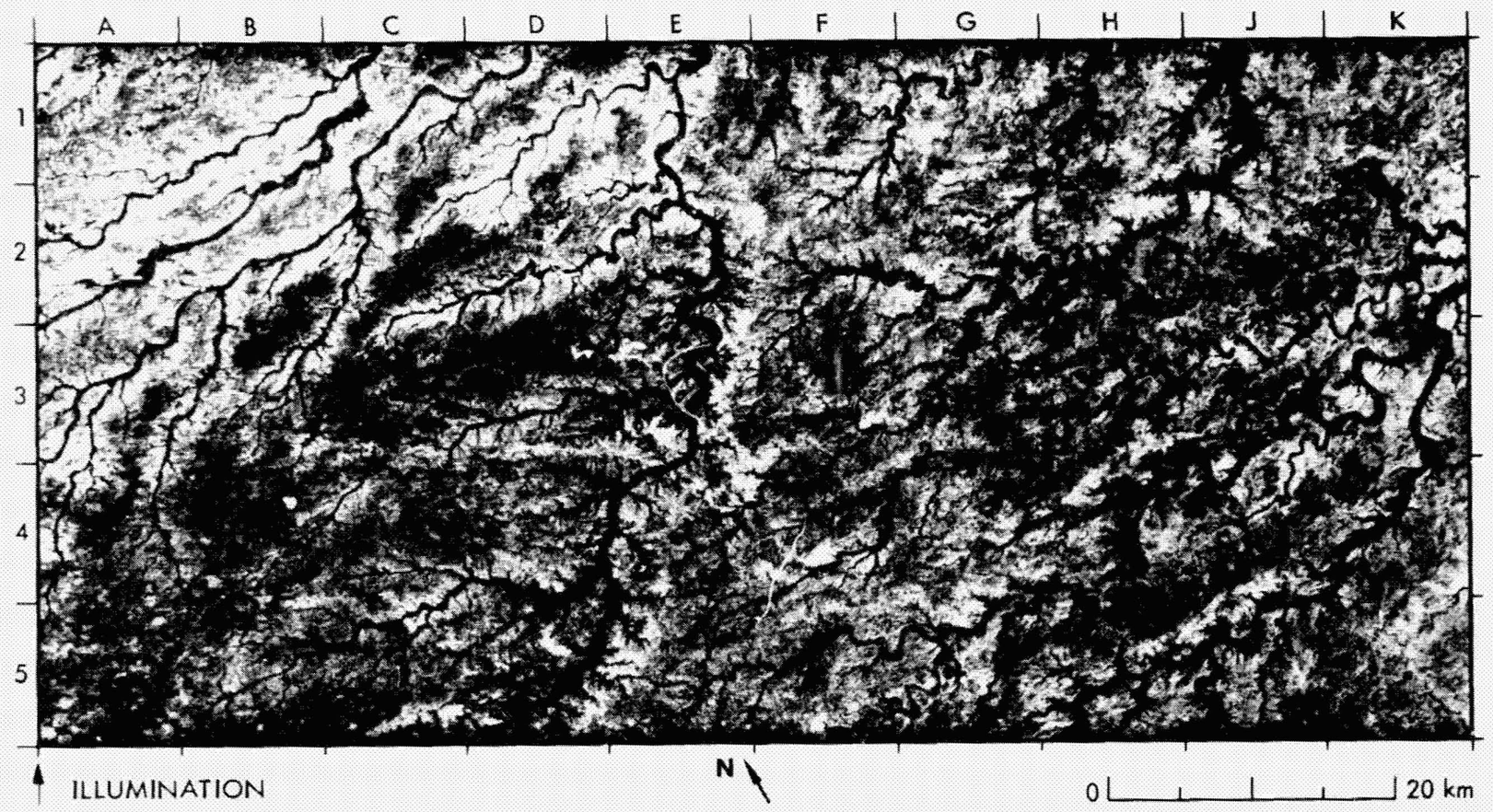

The Widyan region of Saudi Arabia and Iraq is a rugged terrain composed of maturely dissected Cretaceous carbonate rocks. Numerous dry river channels in the area form a northeast regional drainage network. The carbonate rocks include several types of limestone and dolomite that collectively are mapped as the Aruma Formation (Ref. 17). The dry river beds are floored with layers of wind-blown silt and sand. The smooth surfaces exposed by the silt and sand deposits produce very low radar returns, and the dry river beds appear dark gray on the SIR-A image. However, in the arid environment of this area, the outcropping carbonate rocks adjacent to the river beds have rough angular surfaces that produce very strong radar returns. The contrast between the river beds and the adjacent carbonate rock surfaces strongly enhances the

Landsat Band 7

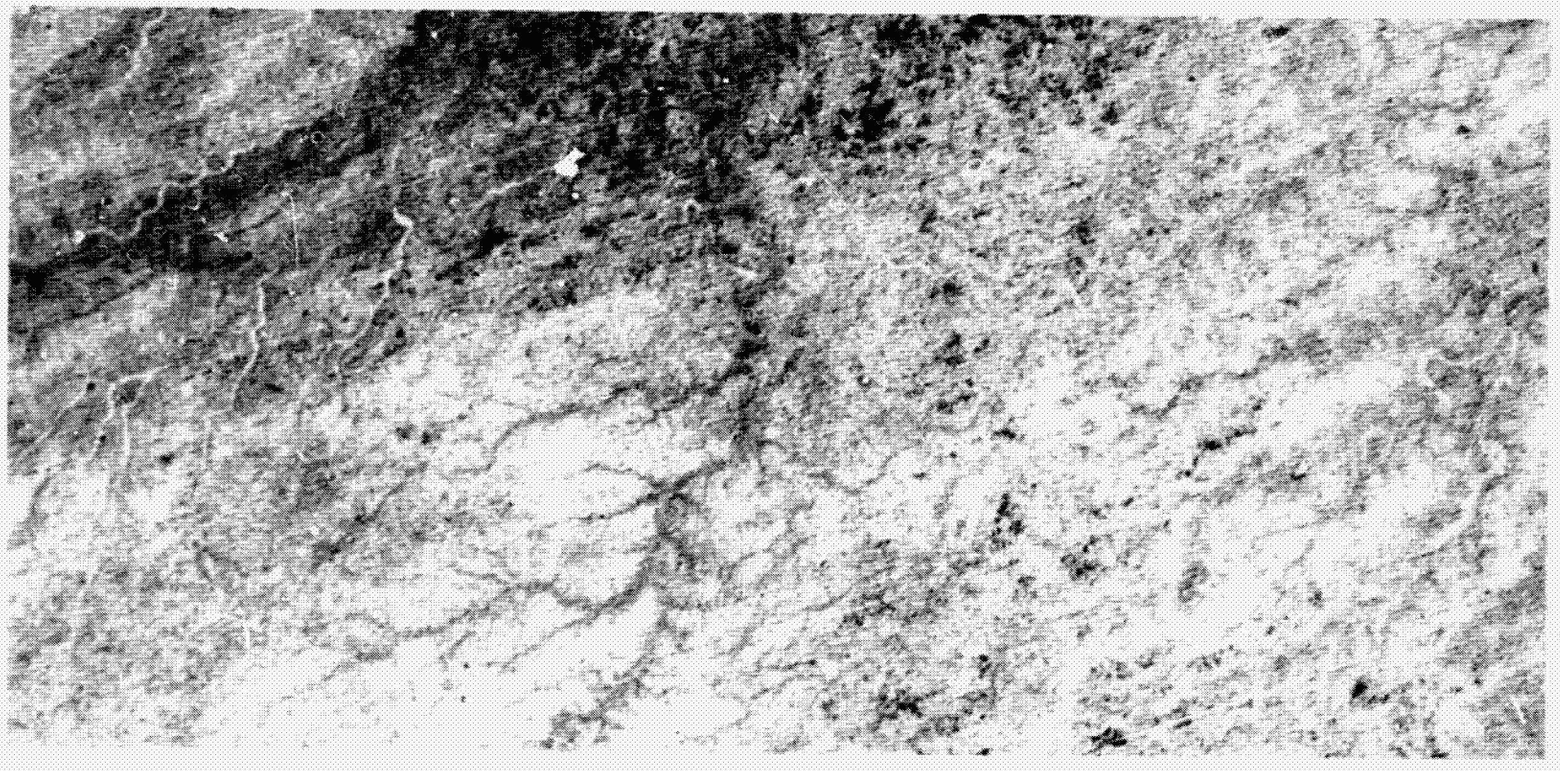

dendritic drainage pattern on the radar image. The patchy distribution of medium-gray tones in the upland areas between the major drainage channels (e.g., D3 to A5) reflects the presence of thin discontinuous sheets of wind-blown silt and sand that locally cover the bedrock.

Major dry river channels on the image are Wadi Tibal (A2/A3 to C1), Wadi Mira (A3/A4 to D1), Wadi Ubayyid (D5 to E1), Sha'ib al Ubaydat (F4 to J1), and Wadi Hamir (H5 to K2).

The best available Landsat image is in the near-IR wavelength. It shows little contrast between the river beds and the adjacent carbonate bedrock.

38. Mississippi River Floodplain, Louisiana, U.S.A.

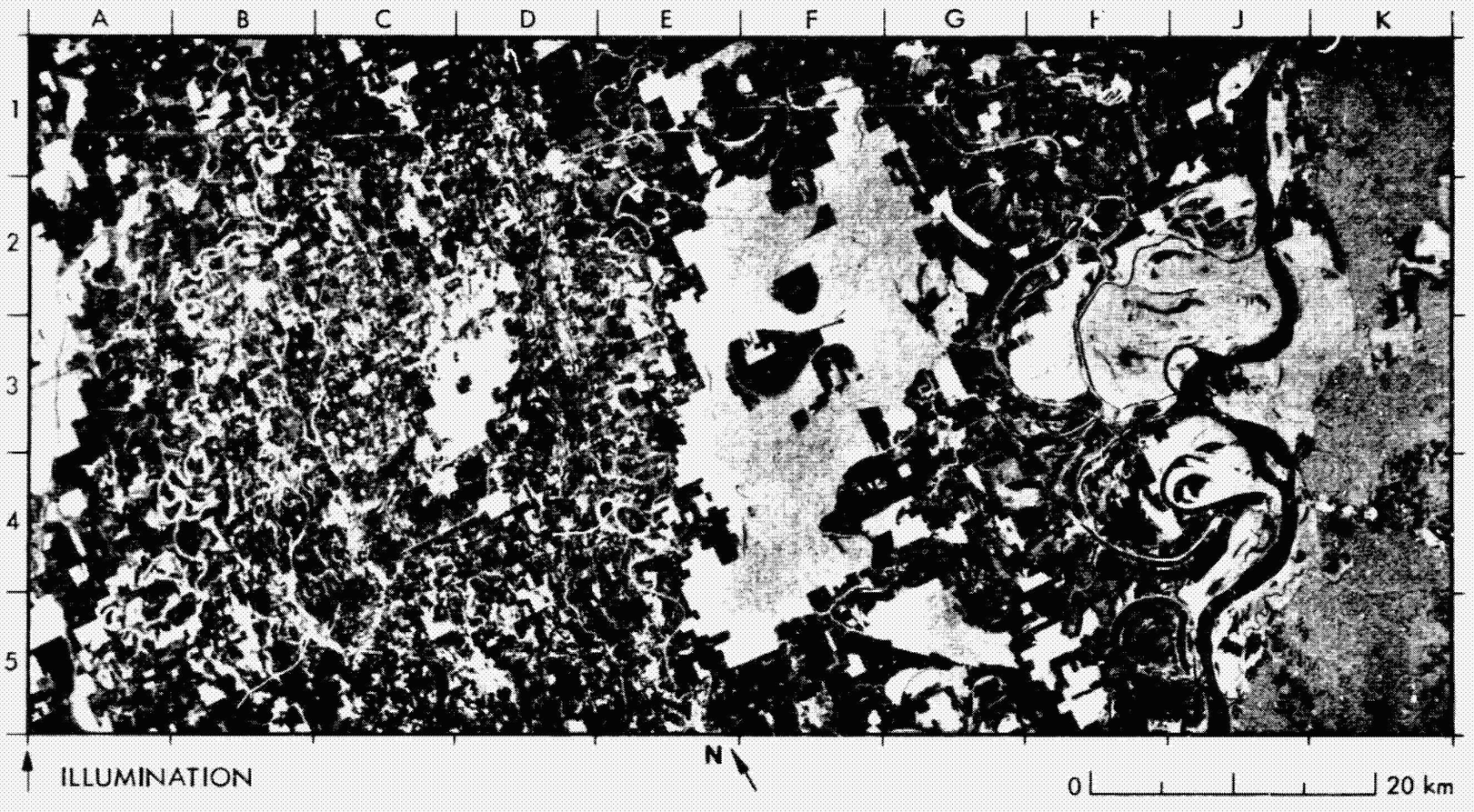

The floodplain of the Mississippi in northeast Louisiana is more than one hundred times wider than the river (J1 to J5). Smaller Yazoo-type streams that drain this floodplain include the Boeuf River (B1 to A5), Bayou Macon (D1 to E5), and Tensas River (F1 to F5). Cultivated areas are characterized by rectangular outlines of dark gray to black. The neighboring forests are medium gray (E1 to F1 through E5 to F5). Forests on the floodplain consist of hardwoods composed largely of oak, hickory, and sweet pecan. Bright radar returns from meander scars and adjacent to cutoffs (E1, G2, and H4) reflect swamp environments that may locally support a cypress-tupelo association. However, the SIR-A image was acquired in November at a season of very low standing water on the floodplain. The corresponding Seasat SAR image, acquired three

Seasat SAR

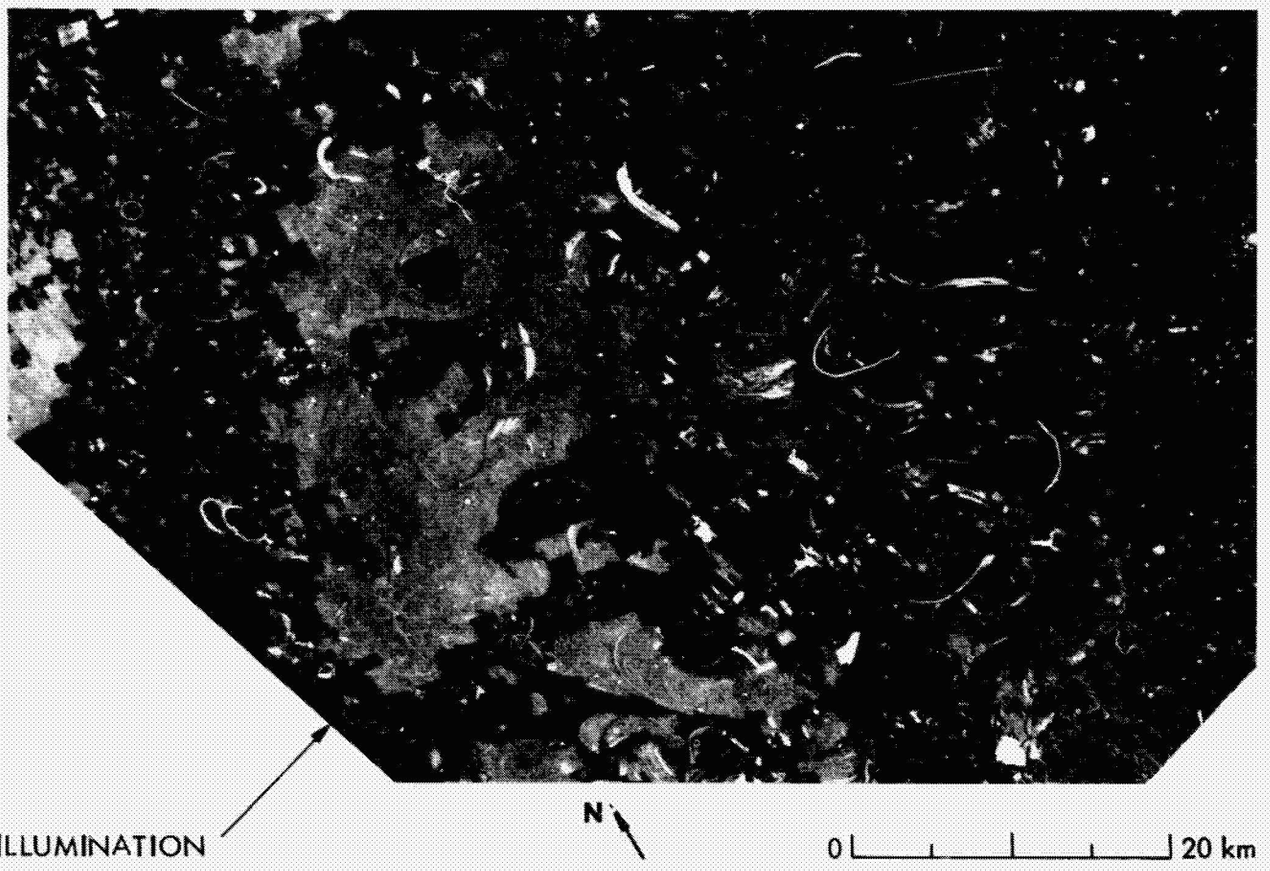

years previously in August, shows much brighter radar returns from the meander scars and cutoffs. This is notably tne case between the Tensas River and Palmyra Lake (F3 to H3). It probably reflects a seasonally higher level of standing water on the floodplain.

Comparison of the SIR-A and the Seasat SAR images reveals a significant increase in clear-cuts on the floodplain during the three-year interval between the acquisition of the respective images. Notable examples adjacent to the Tensas River are seen at F1, F3, and F5. The cleared land is used mostly for cultivation, and occasionally for catfish ponds.

The Landsat image in the near-IR wavelength shows a high albedo from both the cultivated areas and the forest on the floodplain. Total

Landsat Band 7

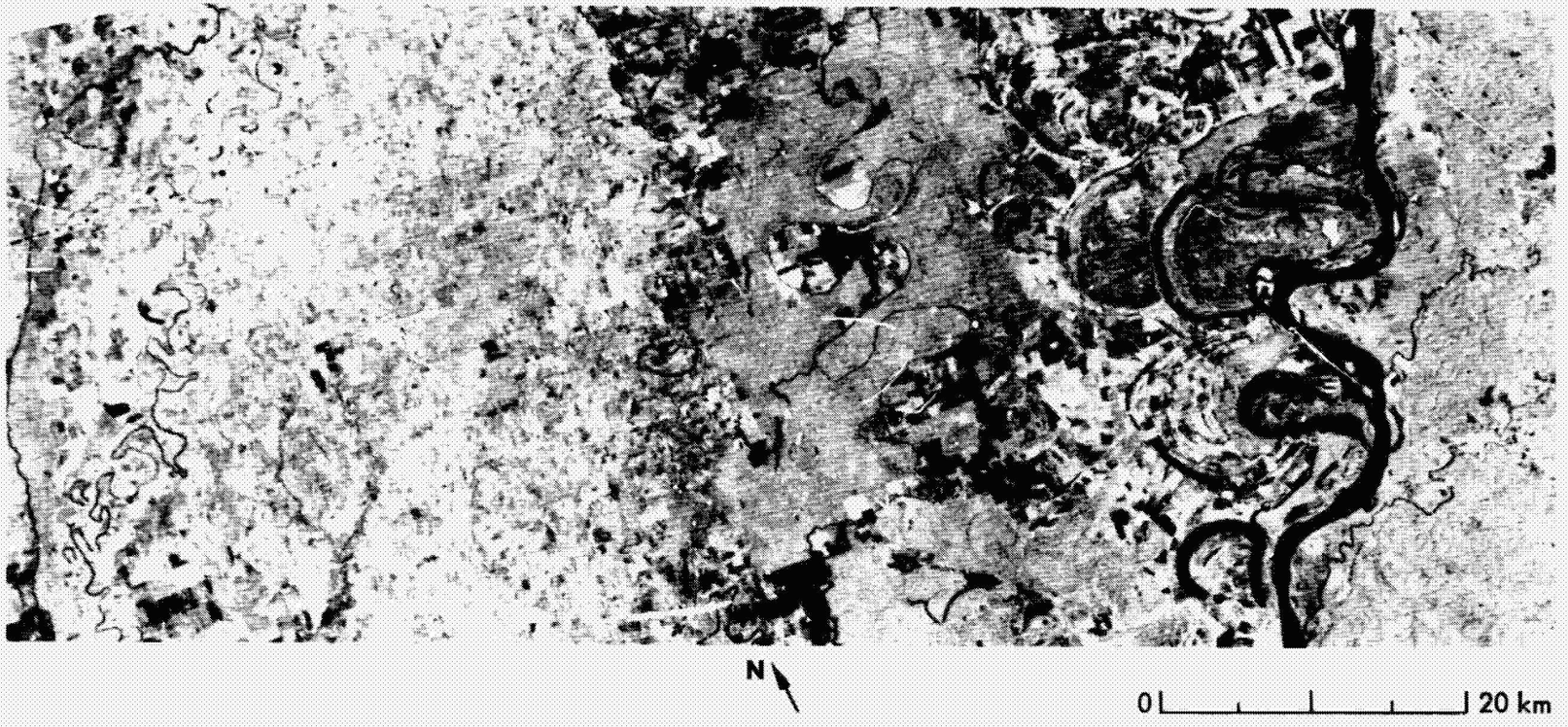

absorption by water surfaces at this wavelength provides a strong water/land contrast on the image. The cultivated areas and the forest cover are distinguished on the Landsat image by characteristic contrasts in outline and image texture. Comparison with the radar images reveals a larger extent of the forest cover at the time of the Landsat image acquisition in October 1972.

39. Nile River, Egypt

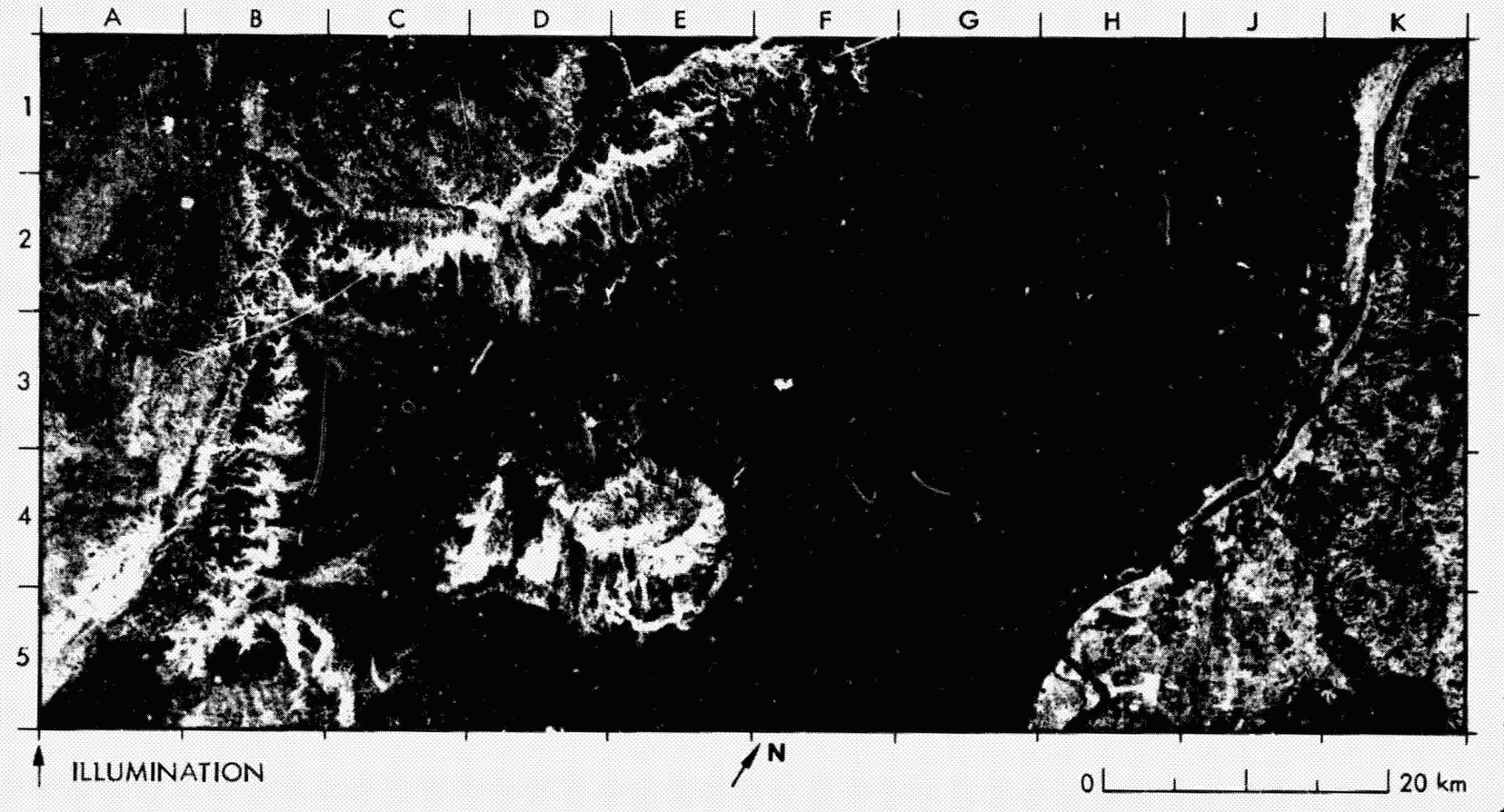

The hard and massive Nubian Sandstone beds of Gebel Silsilah (J3 to J4 and K3 to K4 appear medium to light gray on the image. These beds provided a local source for materials used in the construction of Egyptian temples. A brighter return is provided by the Nile Alluvium, which occurs intermittently on either side of the river, especially at K2 to K1. This high reflectance is probably due to the rough surfaces of gravel deposits. The alluvium has an even brightness, and the sandstone has a more broken texture.

The moderate-to-high backscatter from the Nubian Sandstone outcrops provides a strong contrast with the very low backscatter from the Pleistocene Floodplain deposits (J1 to J3) A similar strong contrast occurs between these deposits and the Gebel Barga (D4/E4), which is a low hill of chalk and Esna Shale. It is more difficult, however, to distinguish Nubian Sandstone from the Esna Shale deposits. This is probably because of the similar textures of the two units.

The Thebes Formation to the left of the image is distinguished from the Esna Shale by its finer texture and smoother appearance. The outcrop of the Thebes Formation in the center of Gebel Barga (E4) is very bright in comparison to the outcrops at D1 through A5. This may be caused by a greater surface roughness and/or steeper local slope conditions.

The Aswan Dam lies just south of Kom Ombo. Pointing toward the dam are the converging traces of power lines at F5 to H1 and G5 to K1. The Kom Ombo Plain to the east of the city (J5) is covered by thick alluvial deposits, which contain stone-age flint implements.

The sketch map was made from the SIR-A image with data supplied by published geologic maps (Refs. 18 and 19).

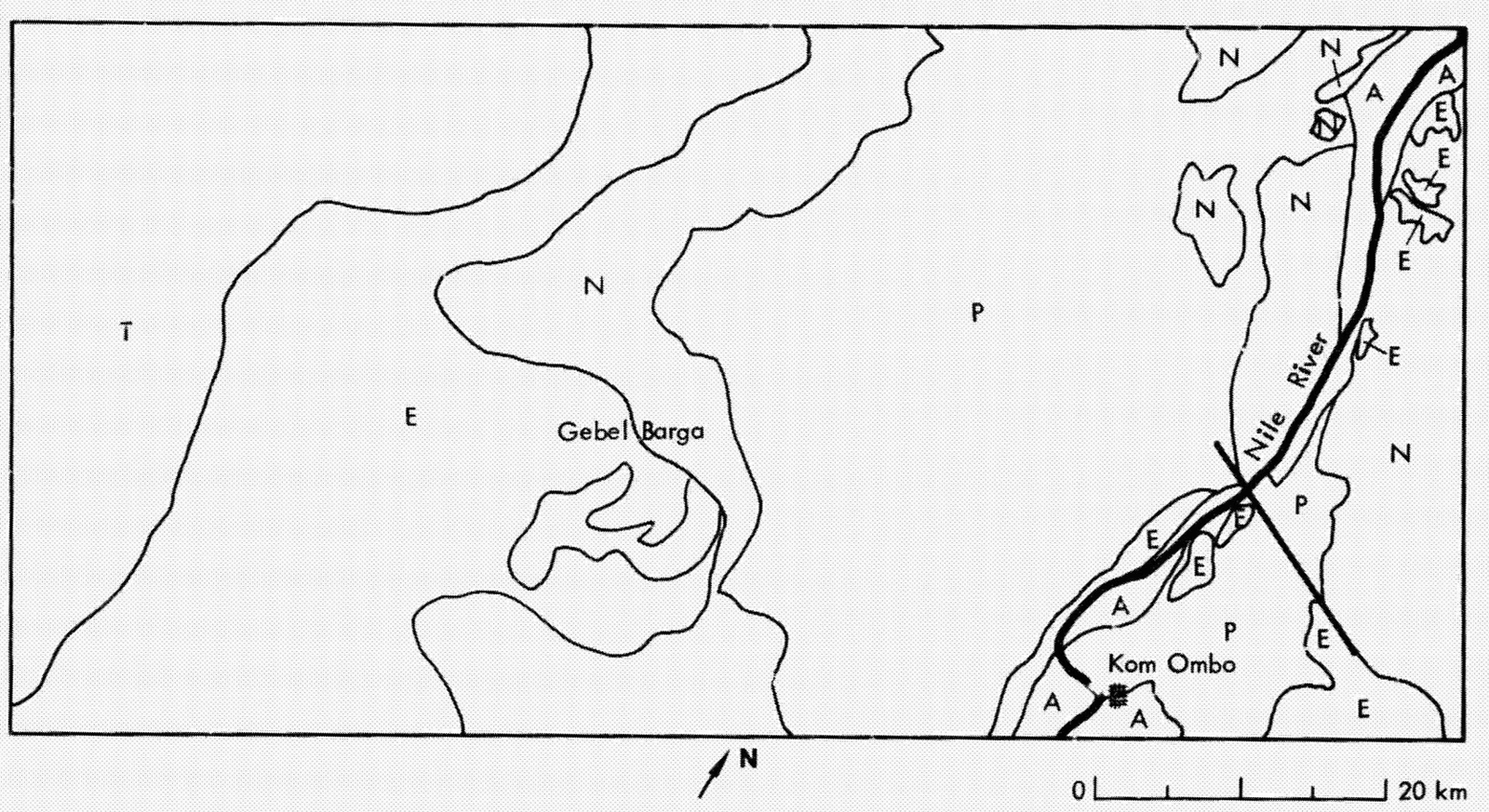

A NILE ALLUVIUM

P PLEISTOCENE FLOOD PLAIN DEPOSITS OVERLYING NUBIAN SANDSTONE

T THEBES FORMATION

E ESNA SHALE

N NUBIAN SANDSTONE

FAULT

4C. Karakoram Mountain Glaciers, Pakistan

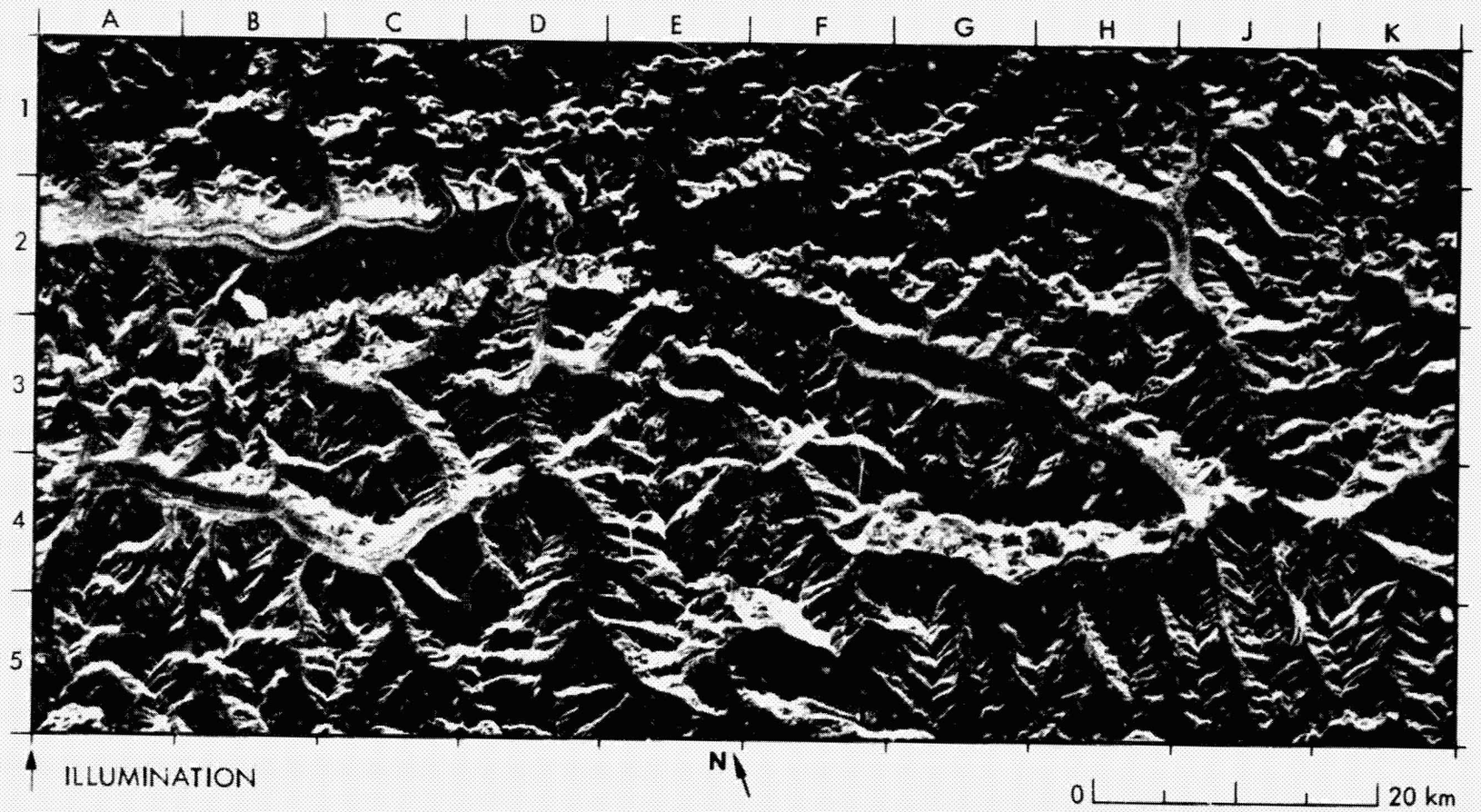

The slopes of the glaciated mountain ranges in northeast Pakistan are steep and rugged, with some peaks at elevations of 7000 to 8000 m. The Karakoram Mountains are located from A1 to K1. Foreslopes on the radar image are compressed and appear bright; backslopes return little radar energy and appear correspondingly dark.

Valley glaciers radiate outward from a major ice divide at E2 to F2. The ice and compacted snow reflect very little radar energy in the vicinity of this divide. A remarkable feature of the major glaciers, which suggests structural control, is their extensive linearity. The Hispar Glacier (D2 to A2) flows westward in a linear channel for about 40 km. The Biafo Gyang Glacier (E2 to H4) flows southeastward in a linear channel for about 35 km. Segments of several other glaciers follow a similar southeast trend.

Landsat Band 7

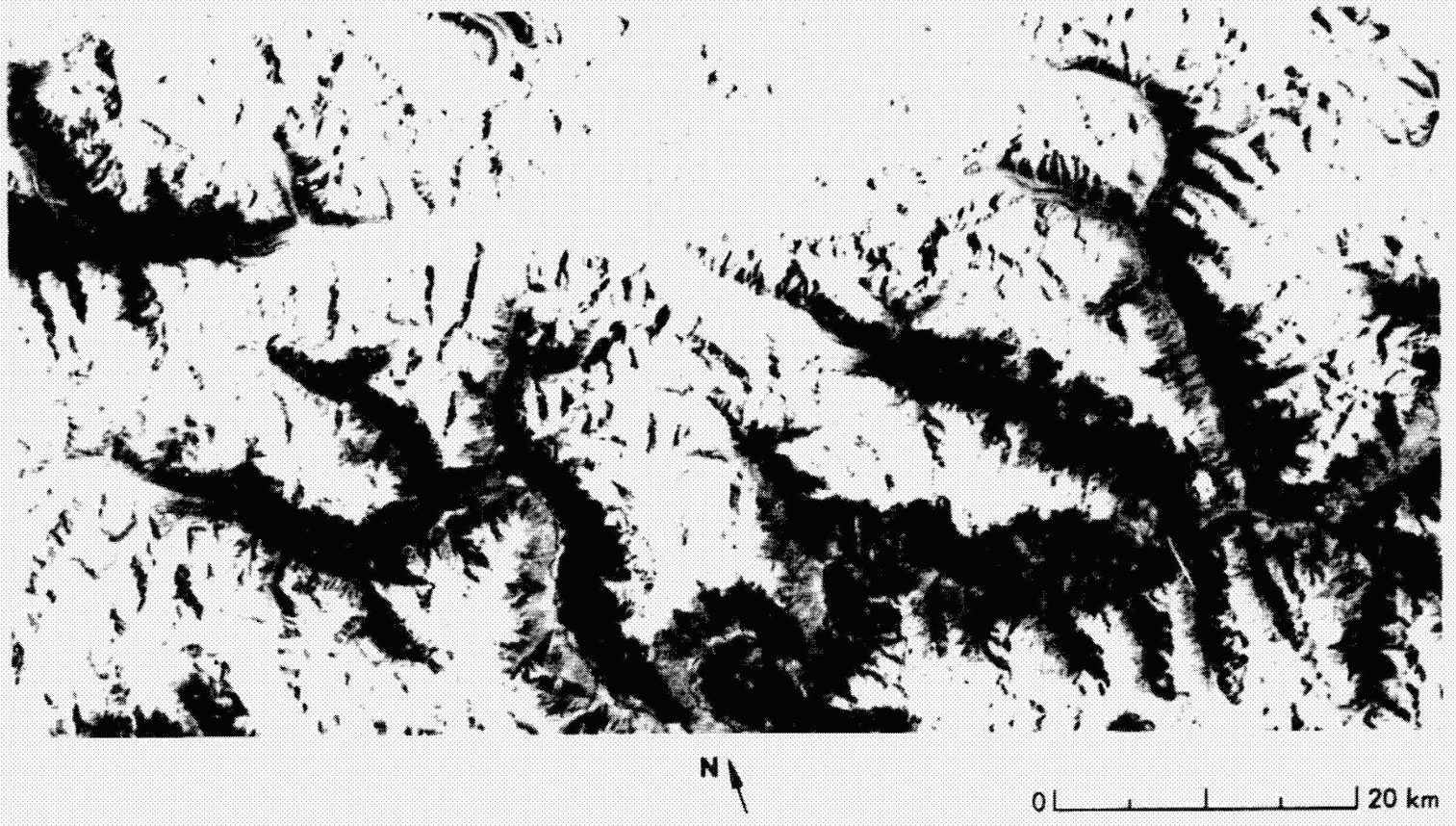

Meltwater from all the glaciers in this scene that are south or east of the Rakaposhi Range (A3 to D2) is carried by the Shigar River (F5) southeastward to the Indus River. Dark linear to curvilinear stripes on the glacier surfaces represent longitudinal moraines. The wavy form of the moraines on the Hispar Glacier suggests a history of glacial surges.

The Landsat image in the near-IR wavelength shows a very high albedo from the snow and glacial ice. The shape and form of the glacial moraines are clearly displayed. Mountain slopes are contrasted by solar shadowing, but do not show the compression that is seen on the SIR-A image.

PRECEDING PAGE BLANK NOT FILMED

(x) Agriculture

41. Highlands, Mato Grosso do Sul—Paraná, Brazil

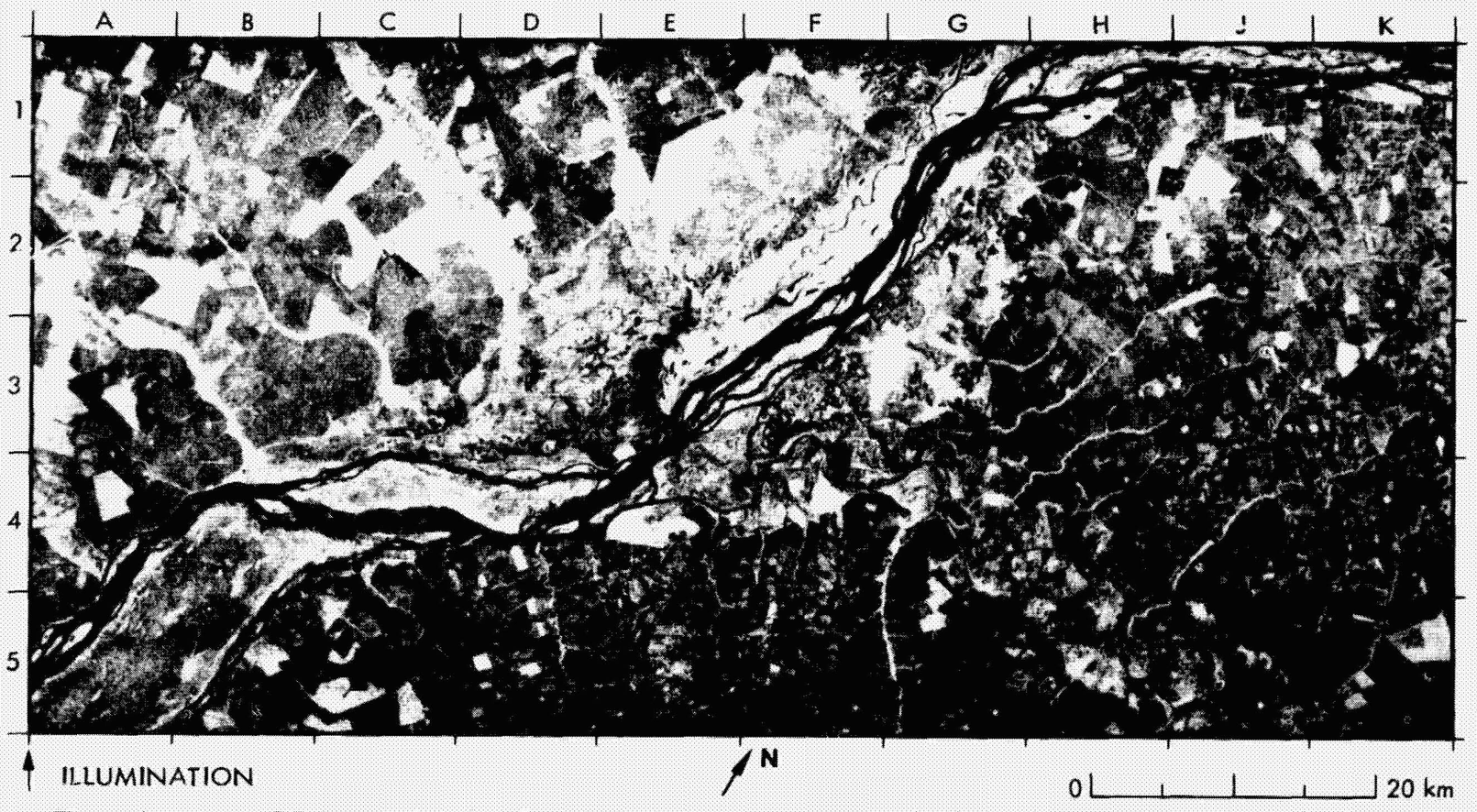

The rural area in this SIR-A scene of southern Brazil is bisected by the Paraná River (K1 to A5), which marks the state boundary between Mato Grosso do Sul (west) and Paraná (east). The terrain consists of rolling upland ranging in elevation from 300 to 470 m. Regional drainage is to the southwest. The Ivaí River (K5 to E4) is a major tributary of the Paraná. Small tributaries of the Ivaí follow linear, nearly parallel courses that probably reflect structural control in the area bounded by K3, E4, E5, and K5.

This area of Brazil is primarily agricultural; the only town in this scene is Icaraíma (E5). The natural vegetation of Paraná State is a tropical forest growing in a humid climate; it consists mainly of broadleaf evergreen species that grade westward into a shrubby deciduous woodland with open patches of savanna grasses in Mato Grosso do Sul. The agricultural pattern east of the Paraná River is dominated by small farms that show medium- to dark-gray image tones on the SIR-A image (e.g., G3 through H4 to K4). Soy beans, coffee, and upland rice are the principal crops grown in the deep red soil of the area. West of the Paraná, the fazendas or ranches are divided into large tracts, whose rectangular or polygonal outlines are strongly contrasted on the radar image. The bright returns are from woodland areas (cerradão), while dark returns are mainly from deforested grazing pastures. The SIR-A image was acquired during the early phases of the growing season, in mid-Novem-

Landsat Band 5

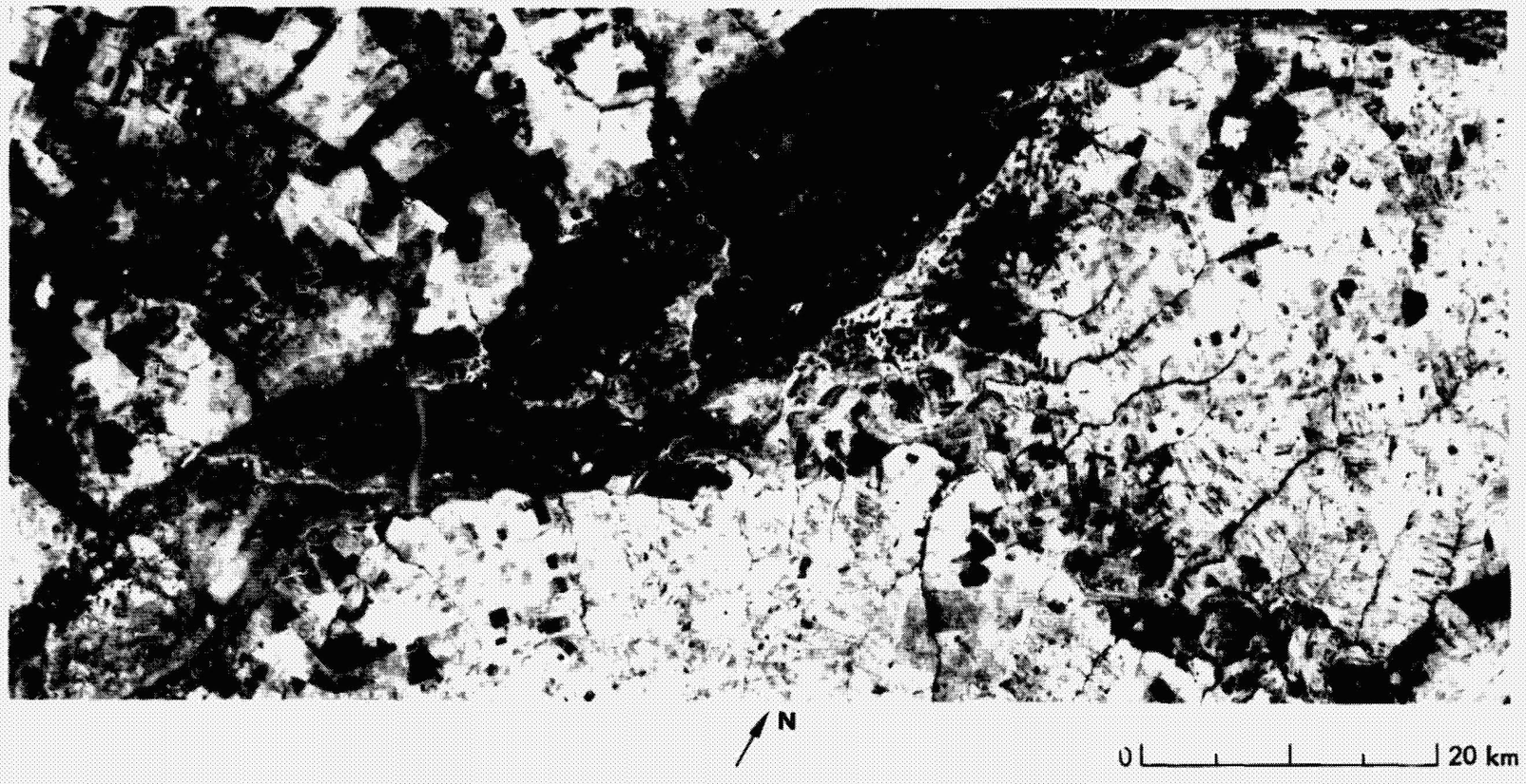

ber, 1981. The Landsat images in the visible-red and the near-IR wavelengths were acquired about six months earlier, on April 21, 1981, at the end of the previous year's harvesting season.

The cultivated areas on the Landsat band-5 image show image tones that are almost exactly the inverse of those on the SIR-A image. The pattern of angular dark-gray tones on the Landsat band-5 image generally represents areas of strong absorption by chlorophyll in the leaf canopy of vigorously growing plants. Bright tones in corresponding areas on the SIR-A image (e.g., at C2 and E1/E2) denote rough surfaces at the scale of the radar wavelength (23 cm). Together, the data from the two images suggest a broadleaf evergreen canopy. Cultivated areas and grasslands that appear medium to light gray on the Landsat band-5 image have exposed bare soil or a cover of senescent vegetation. The comparative smoothness of these surfaces provides little radar backscatter; thus the corresponding areas on the SIR-A image are medium to dark gray.

A notable exception to the complementary relationship of the gray tones in corresponding areas of the Landsat band-5 and the SIR-A images occurs in the lower right corner of C2. This area is medium gray and indistinct from surrounding areas on the radar image, and dark gray and angular on the Landsat band-5 image. However, most of the contiguous dark gray area on the Landsat image corresponds with a light-gray

Landsat Band 7

area on the radar image in C2. This suggests a temporal variation in which the forest cover had been cleared during the interval between the acquisition of the Landsat and the SIR-A images. On the Landsat band-7 image, the land/water interface is strongly contrasted, and the image shows bright returns from almost all of the vegetative cover due to the high albedo of vegetation (either healthy or senescent, agricultural or forest) and bare soil in the near-IR wavelength. A notable exception is the sector west of the Paraná River that appears dark gray, and is therefore absorbent at this wavelength. The corresponding area is light gray on the band-5 image (senescent vegetation or bare soil in April) and dark on the SIR-A image (smooth surface in November). This might be explained as either a recent controlled burn-off or a wet rice field.

The channel of the Paraná River is choked with debris that has accumulated to form numerous islands, including the large Ilha das Sete Quedas (Isle of the Seven Falls) (C4 to A5). The floodplain is approximately 20 km wide. Vegetation and floodplain deposits yield bright tones on the SIR-A image, particularly in the area drained by the Ivinheima River (a Yazoo-type stream) (G1 to E3). The Paraná River channel can scarcely be distinguished from the vegetated floodplain in the Landsat band-5 image because of absorption by the muddy water at this wavelength.

42. Center-Pivot Irrigation, Southwest Nebraska, U.S.A.

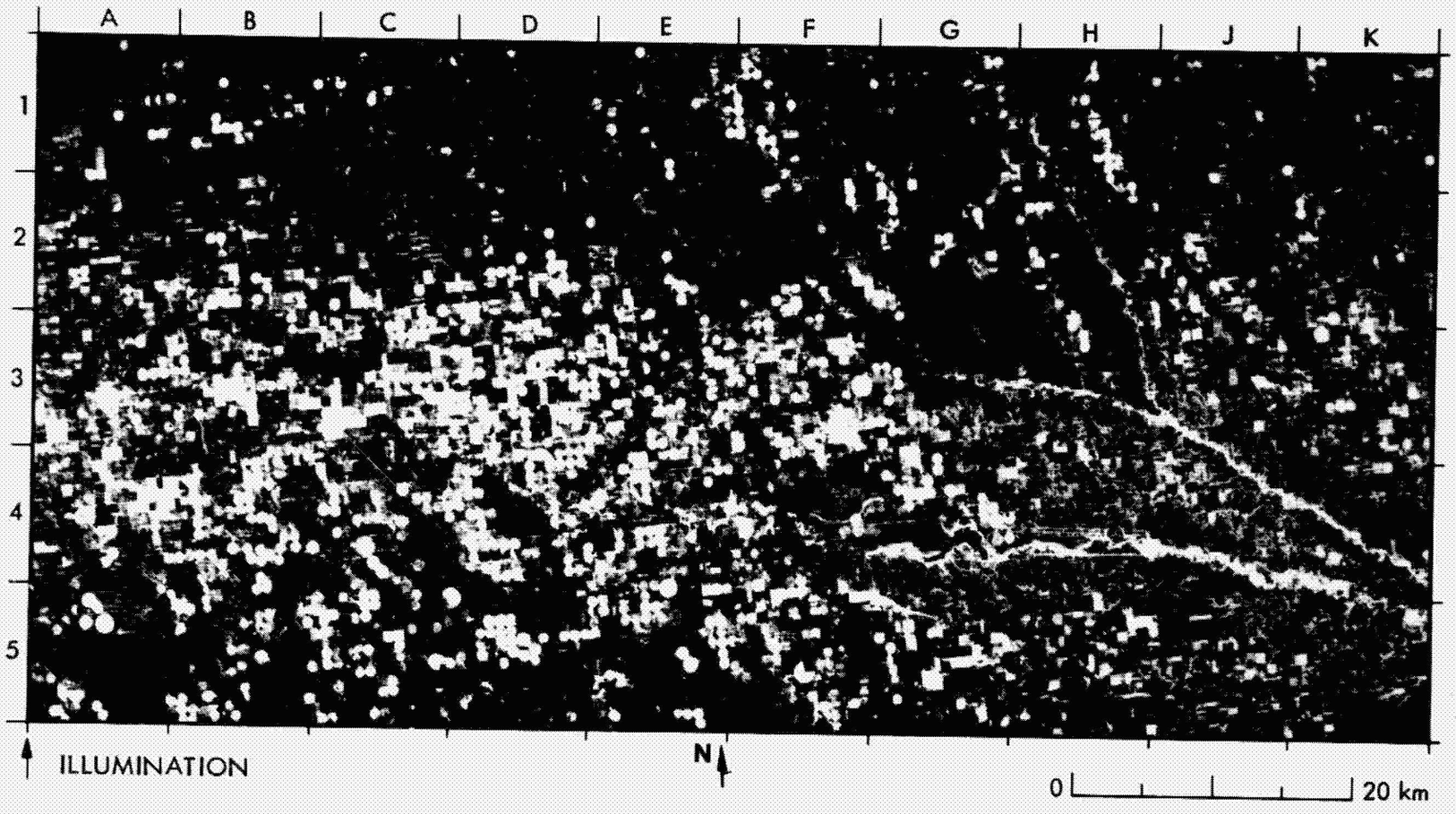

Although center-pivot irrigation waters only 70 to 80% of a square field, it is preferred in this region of Nebraska over conventional, gravity-feed irrigation, which employs a system of linear trenches to distribute water. Center-pivot irrigation makes more efficient use of labor and more efficiently distributes water in areas of sandy soil or steep local slope. Most of the pivots in the SIR-A image are at the center of quarter sections (small circles); a few are at section centers (large circles). The square fields may or may not be irrigated; the unirrigated land is used for grazing.

The principal crops here are corn and wheat. The SIR-A image was acquired in mid-November when the corn had been harvested, but the stalks remained standing in the fields. Winter wheat had emerged. The bright image tone of most of the circular fields and some of the square fields represents strong radar backscatter from the corn stalks. The moderate- to dark-gray tones of the remaining fields, circular or square,

Landsat Band 5

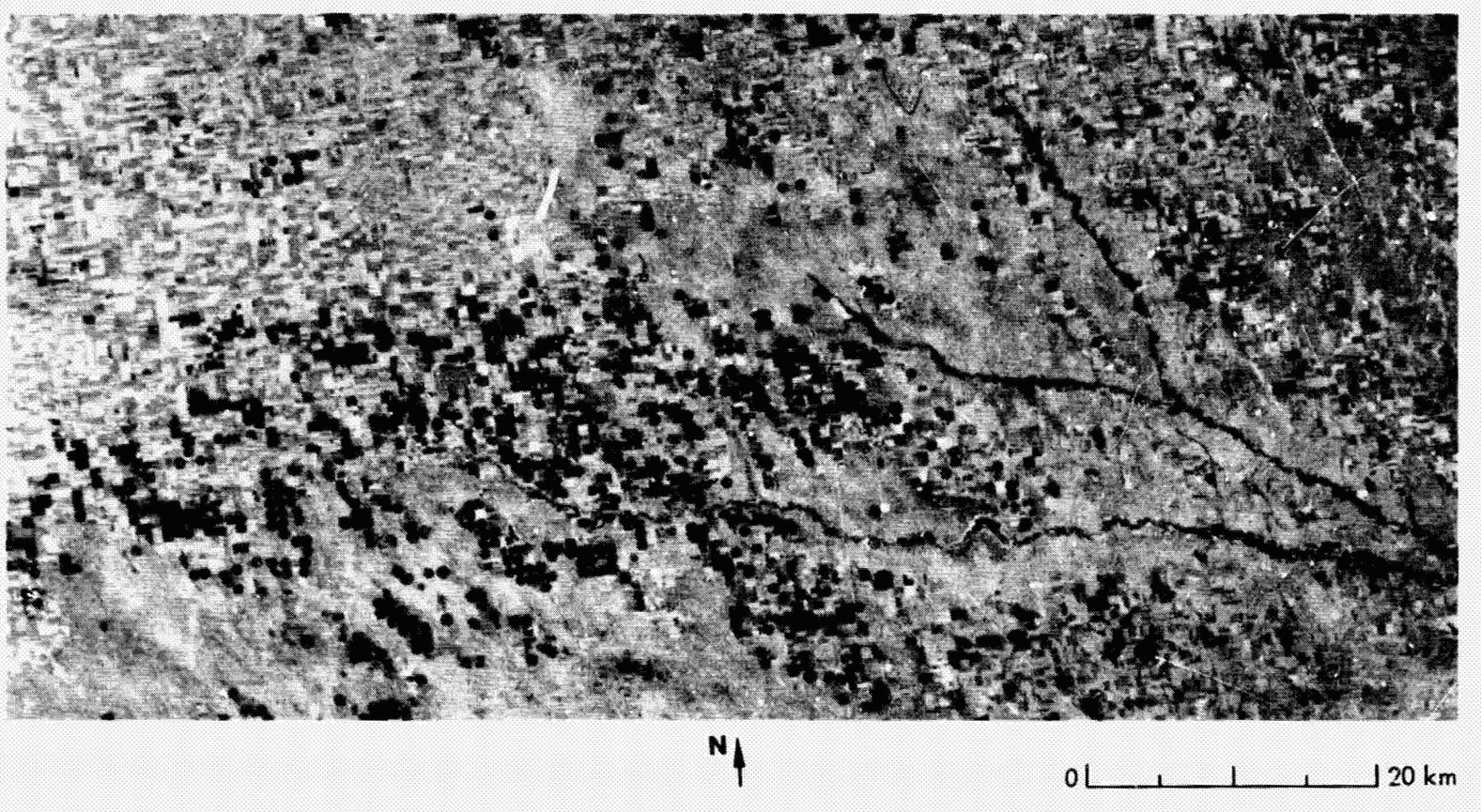

reflect correspondingly weaker backscatter from pastureland and fields with youthful winter wheat.

The Landsat image in the visible-red wavelength, acquired in August about nine years before the SIR-A image, shows only a slightly lesser density of circular agricultural fields in the area. The medium-gray tones of the circular fields contrast strongly with the light grays of the pasturelands, which are concentrated in the northwest (A1 to D1 to D2 to A3 on the SIR-A image). This contrast is probably due to a greater soil moisture and/or the presence of crops in the circular fields. Small areas of sand hills appear as medium-gray tones on the SIR-A image to the north of Spring Creek (G2 to E2), northwest of Enders Reservoir (F4/G4), and westward from D4/D5 to A4/A5. On the Landsat image, the corresponding areas are uniformly light gray, and they show no agricultural patterns.

43. Circular Agricultural Fields, Libya

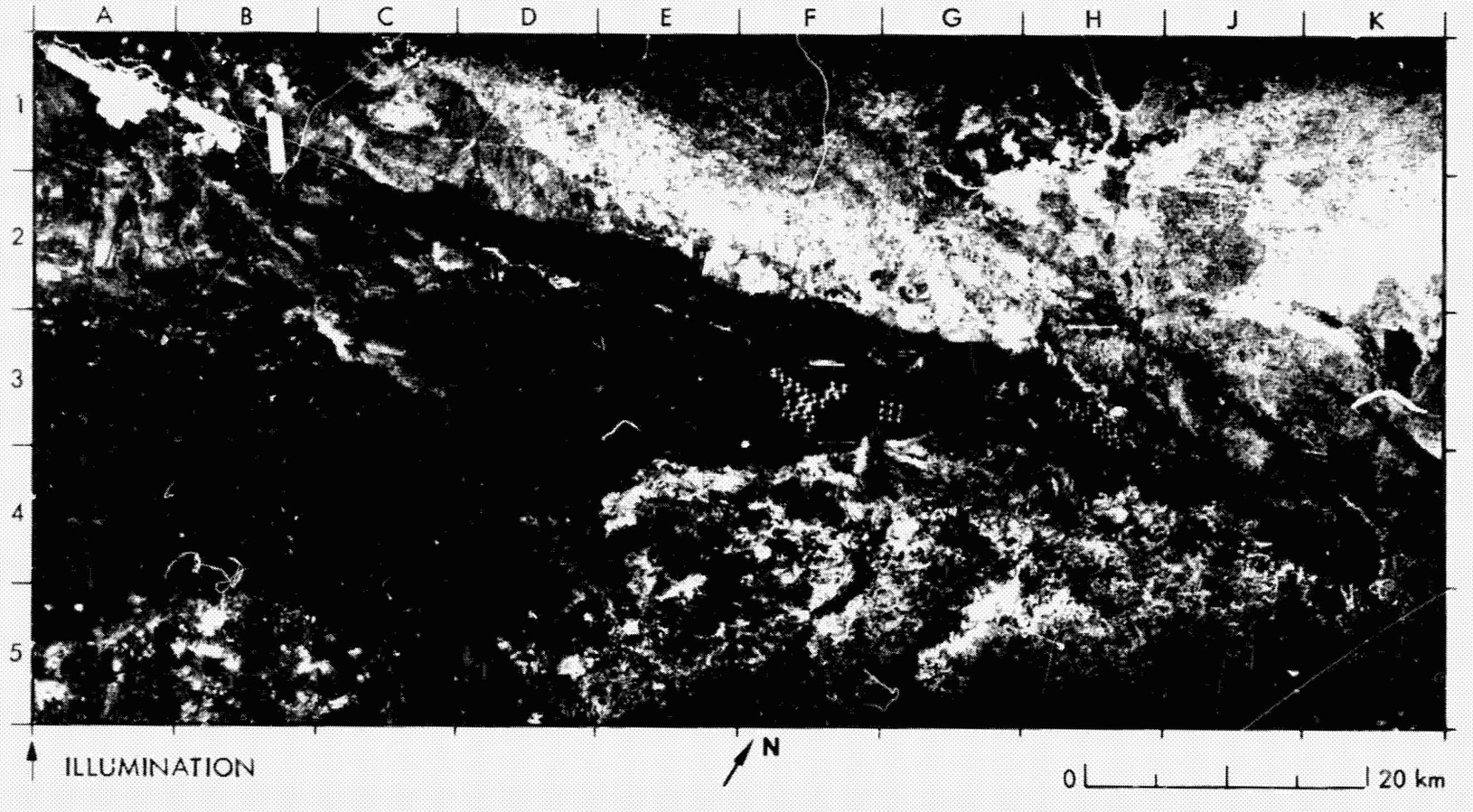

These circular irrigation fields in Libya (F3, G3, and H3/J3), just north of Ramlet Az Zallaf near the cities of Qi'rah Dabdad, Brak, and Ashkidah (F3/G3), are watered by center-pivot irrigation (see Scene 42). Note also the rectangular fields at K4. The circular fields, nearly a kilometer in diameter, are located on sandy Lower-Carboniferous beds that appear dark on the radar image. The surrounding brighter areas are rougher Middle- and Upper-Devonian sandstone.

The consistency of the circular-field patterns may be caused by one or both of two possible mechanisms. Consider the north and south sectors of each field; in these sectors, plowing direction is perpendicular to the radar look direction. As shown in sketch (a), specular reflection from these plowed rows occurs when the local slopes of the plowed rows are not only perpendicular to the radar look direction, but at an angle of about 50 deg to the horizontal. A bright return, then, is produced from the northernmost and southernmost sections of each field, but there is no return from the easternmost and westernmost sections. This effect is

(a) SPECULAR REFLECTION

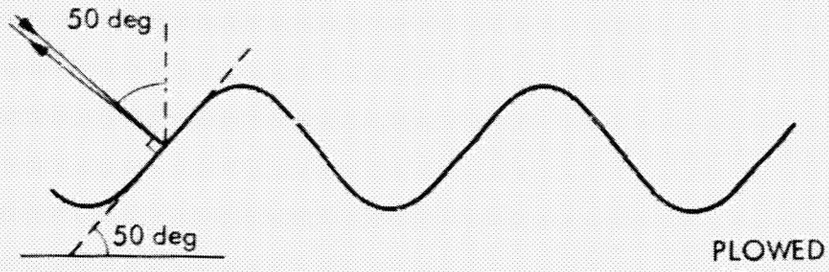

(b) BRAGG SCATTERING

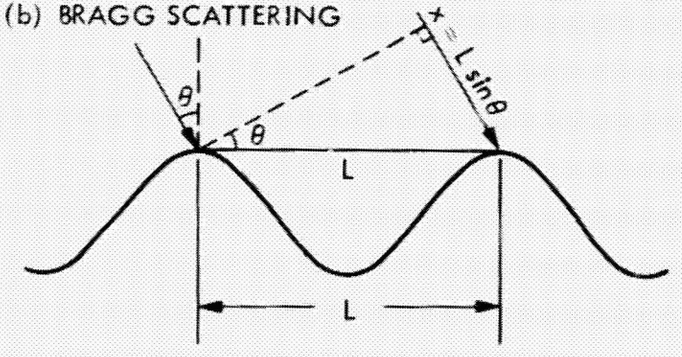

BRAGG SCATTERING WHEN:

$$2x = 2L \sin\theta = n\lambda,\ n = 1, 2, 3 \cdots$$

$$L = \frac{n\lambda}{2 \sin\theta} \sim 0.15n \text{ (meters)}$$

more easily seen in the enlargement of section F3 through H3.

The second effect associated with Bragg scattering may occur as a function of separation between plowed rows (L in sketch (b)). A maximum return from two adjacent rows will occur if the path length difference ($2x$) between the two returns is an integral number of wavelengths. As shown in sketch (b), this will occur when $L = n\lambda/(2 \sin\theta)$ where λ is the wavelength of the radar, θ is the incidence angle, and n is an integer ($n = 1, 2, 3 \ldots$). For $n = 1$, the row separation must be 15 cm for Bragg scattering to occur at the SIR-A wavelength of 23 cm. Again, this effect is strongest in the northernmost and southernmost sections of the field and is ineffective in the easternmost and westernmost sections because of the orientation of the plowed rows with respect to the radar look direction.

Roads in this area are most visible across the darker sandy beds (A1/B1 through B5/C5, F2/F3, and E3). However, one of the main roads is easily distinguishable on the brighter sandstone (H3) because of its perpendicular angle with respect to the radar.

44. Wheat-Sheep Farms, New South Wales, Australia

In this portion of the wheat-sheep farm belt, south central New South Wales, the land slopes regionally toward the west. A short segment of the Lachlan River (B1 to A1) is the only major drainage channel in the scene. There are several small communities in the area, but they are not prominent on the radar image.

Most of the natural vegetation has been cleared and an active agriculture is practiced. Wheat is a major crop, together with some barley and oil seeds. Much of the land is used for grazing sheep and fewer numbers of cattle. Statistics published by the Australian Bureau of Agricultural Economics for 1979–1980 (Ref. 20) indicate that individual farms produce both wheat and sheep. For example, the average wheat farm harvested 290 hectares of wheat and had 1538 head of sheep, while the average sheep farm had 2236 head of sheep and harvested 146 hectares of wheat.

The rectilinear outlines of the fields and cultivated land appear as thin bright lines on the SIR-A image. These lines represent the rough surfaces of boundary roads and fences. Fields that display dark- to medium-gray tones have smooth to slightly rough surfaces. They probably represent the majority of the cropland and grazing land in the area. Bright areas on the radar image are the rough canopies of woodlands. The Landsat image in the near-IR wavelength—acquired almost nine years before the SIR-A image—shows correspondingly dark-gray tones

in some areas that are bright on the SIR-A image. Notable examples are at E4/F4, E5/F5, and C5/D5. However, a complementary tonal response between the near-IR and the radar wavelengths is not uniformly evident on the images. This, in part, is the result of the changing patterns of agriculture, and changes in the environment.

Lake Brewster, the oval at A2 and B2 on the SIR-A image, contains a pattern of medium- to light-gray tones that indicate grazing land. At the time of the Landsat image, however, this area was not a dry lake, but covered by a thin sheet of water that vanished during the prolonged drought that began in 1975.

A much smaller oval of medium gray at the upper center of the Landsat image was a stand of natural canegrass; it was cleared and not a trace of natural vegetation can be seen in the corresponding location on the SIR-A image (E1, right center).

Ridges and mountains provide medium- to light-gray tones on the SIR-A image; on the Landsat image, the corresponding areas are medium to dark gray. Folded mountains of the Lachlan Range (A1 to B5), Sandstone Hill (C2/C3), and the Nabong and Naradhan Ranges (D3 to F3), appear as long narrow ridges. These ridges rise from 150 to 300 m above the level of the adjacent agricultural land. Plunging fold patterns on the SIR-A image in the area from C3 to E4 are discernible also on the Landsat image.

(xi) Forest Cover

45. Lower Coastal Plain, North Carolina, U.S.A.

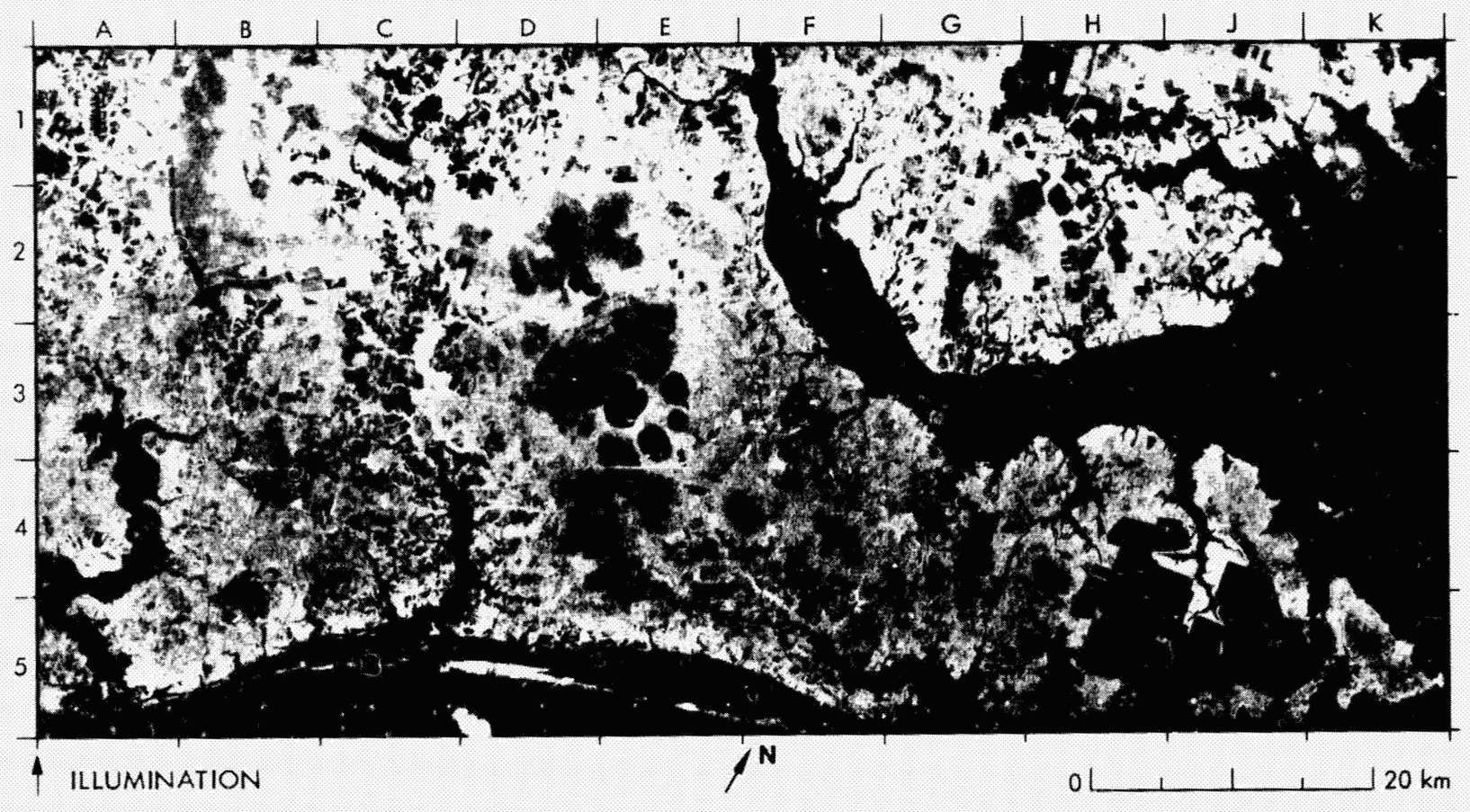

The lower coastal plain, in the southeastern U.S.A., consists of low terraces formed on Tertiary sediments, an abundance of swampland, and some areas of waterlogged peat bog known locally as "pocosin." Barrier islands and tidewater outlets are characteristic of the coastline (A5 through F5). In this scene, the tidewater channel of the Neuse River extends eastward from New Bern (F1) to Pamlico Sound (K2 through K5). The land surface rises from sea level to about 30 m, west of the Hofman State Forest (B1). The Croatan National Forest is situated in the area bounded by D1, E1, D4, and E4. Here the forests consist of species of southern yellow pine, such as loblolly and longleaf, that yield bright returns on the SIR-A image. Shallow lakes clustered in this area are examples of Carolina bays. The smooth open-water surfaces of the lakes return no radar energy and are black on the image. Bright tones on the southeast portion of Ellis Lake (E3, lower right) come from brush growing in the lake, which is only 1 to 2 m deep.

Hardwood swamps characterized by large gums, cypress, maple,

and bay trees provide bright radar returns from areas between and marginal to Great Lake and Ellis Lake (E3). Large pocosin areas that have an open aspect, with stunted shrub and vine species and a thick mat of roots over waterlogged black organic mud, occur north and west of Catfish Lake (E2), north of Great Lake (E3), and south of Ellis Lake (E4). These areas yield low returns and are dark gray on the image. Linear patterns in Wolf Swamp (B1 to B2) and north and west of Great Lake (E3) mark the presence of drainage channels. Numerous linear drainage channels to the east (H4 through K5, H1, J1, and H2) have provided cultivable farmland that is distinguished by linear and rectangular outlines, and mostly dark gray tones on the radar image. The Landsat image in the near-IR wavelength shows a very high albedo from the pocosins and a strong contrast between land and water.

46. Upper Coastal Plain, South Carolina--Georgia, U.S.A.

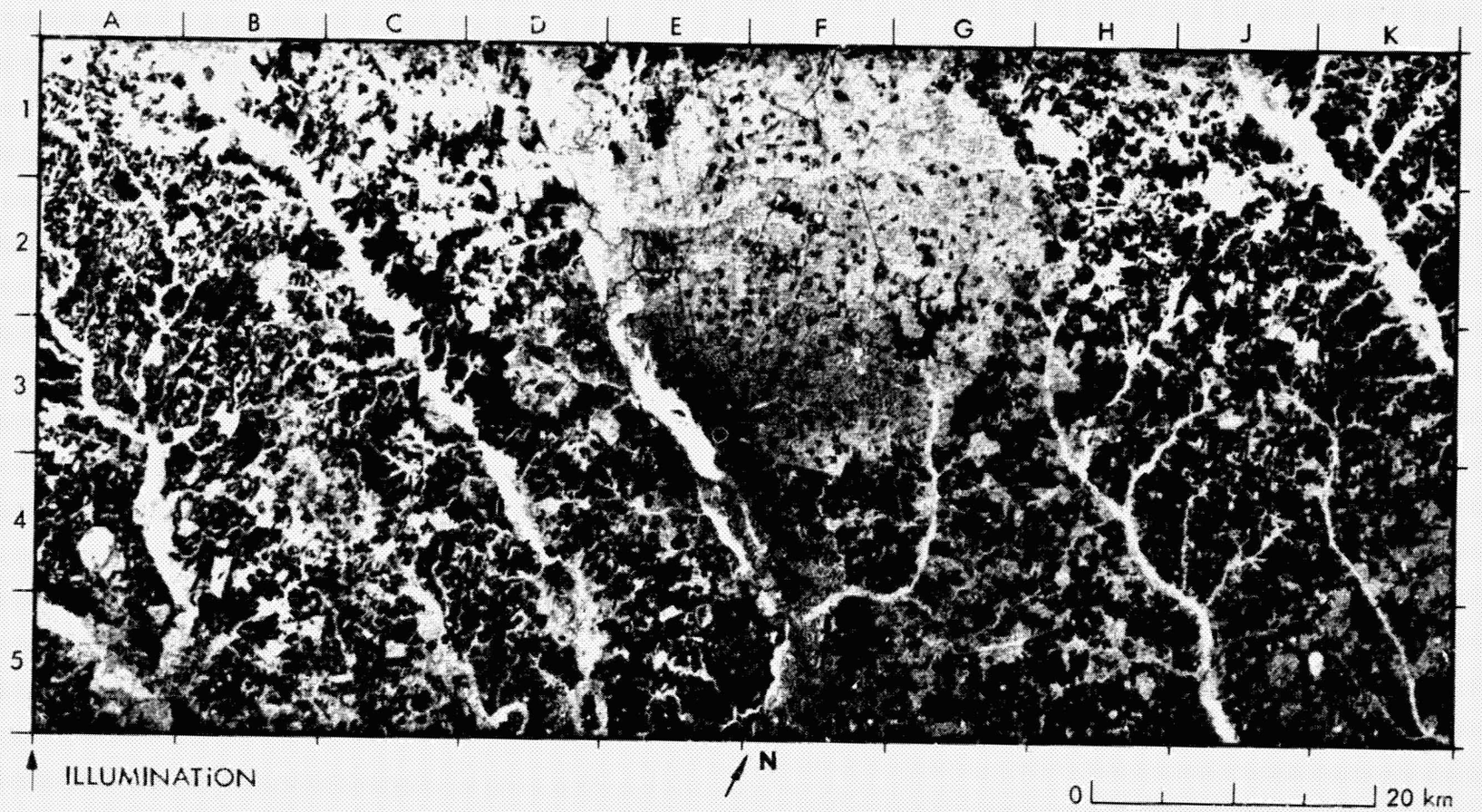

The natural forest of this upper coastal plain ranges from deep swamps through wet bottomlands to dry upland hardwood forests. The plain is deeply dissected by stream channels. Elevations in this scene range from about 30 m in the Savannah River floodplain (F5) to about 120 m in the Aiken Plateau (G1). Much of the original forest on the rolling upland between the streams has been cleared for cultivation. In general, the forest areas are rough and the cultivated areas smooth at the scale of the radar wavelength, making the forest areas appear generally bright and the cultivated areas dark on the SIR-A image. The mottled pattern of the image on either side of the streams indicates land usage, while forest cover is mostly restricted to stream valleys and swamps. A notable exception is the Savannah River Plant (D1 to G1 through E4 to G4). Much of this area has been reforested with pine. It is now managed by the U.S. Forest Service for pulpwood and saw timber production. The numerous small, medium-gray rectangles in this area are clear-cuts made for logging operations. Very bright radar returns come from the

Landsat Band 7

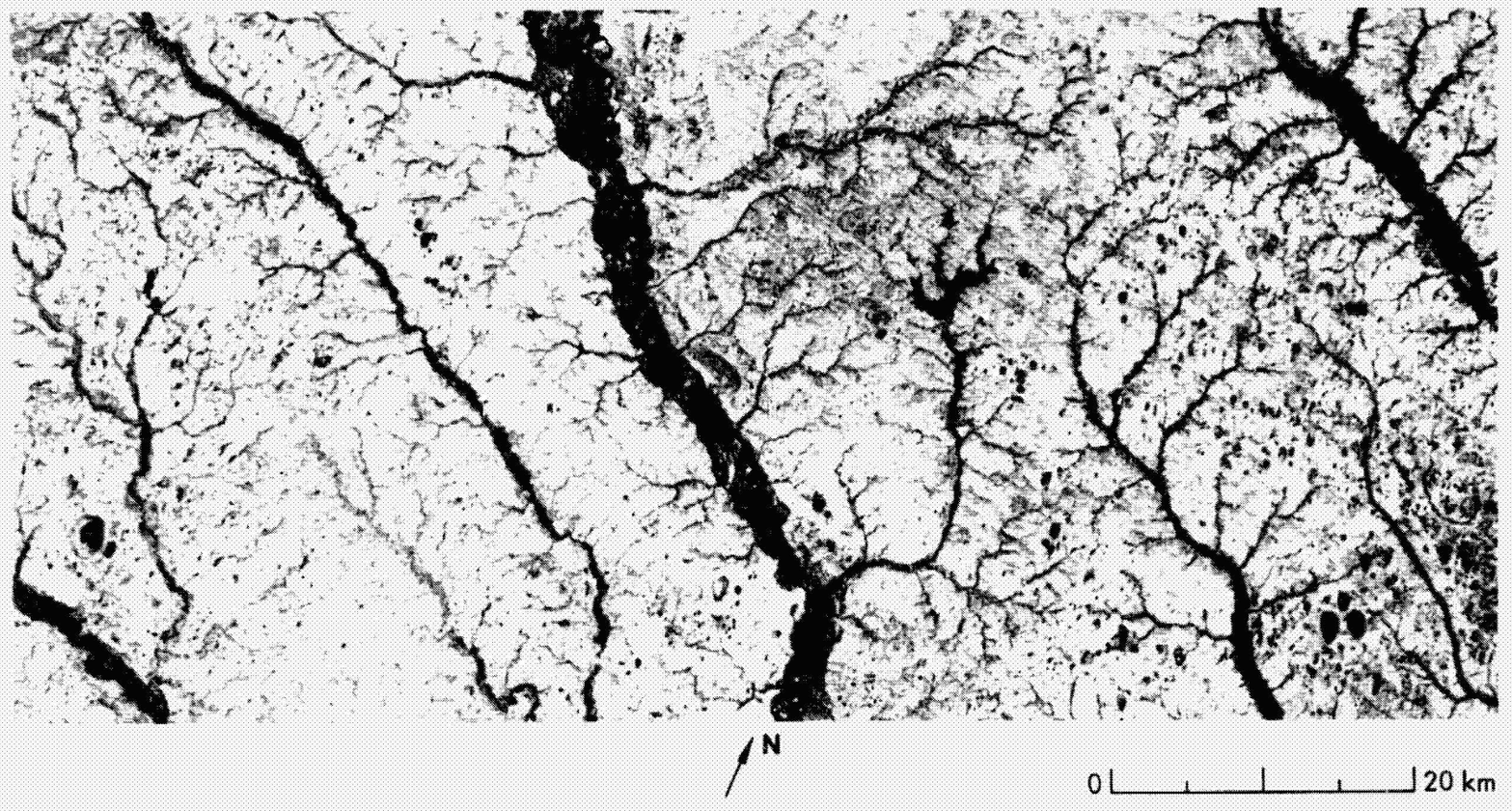

inundated cypress-tupelo swamp forest in the Savannah River floodplain (E3 to E4). Dryer regions of oak, ash, and hickory within the swamp forest yield darker returns on the image.

The swamp and floodplain areas appear moderate to dark gray on the Landsat image in the near-IR wavelength because of strong absorption by the moisture in these areas. High reflectance from the upland forests and from the cultivated areas provides a high image contrast that clearly outlines the drainage pattern on the Landsat image. Open water appears black on both the Landsat and the SIR-A images. However, only large expanses of water that have characteristic outlines, such as the Savannah River (D1 to F5) and Par Pond (G2/G3) are clearly discerned on the radar image. Numerous smaller ponds that are clear on the Landsat image are not readily distinguishable on the radar image from the fields that also produce dark returns.

47. Southwest Coastal Swamp, Irian Jaya, Indonesia

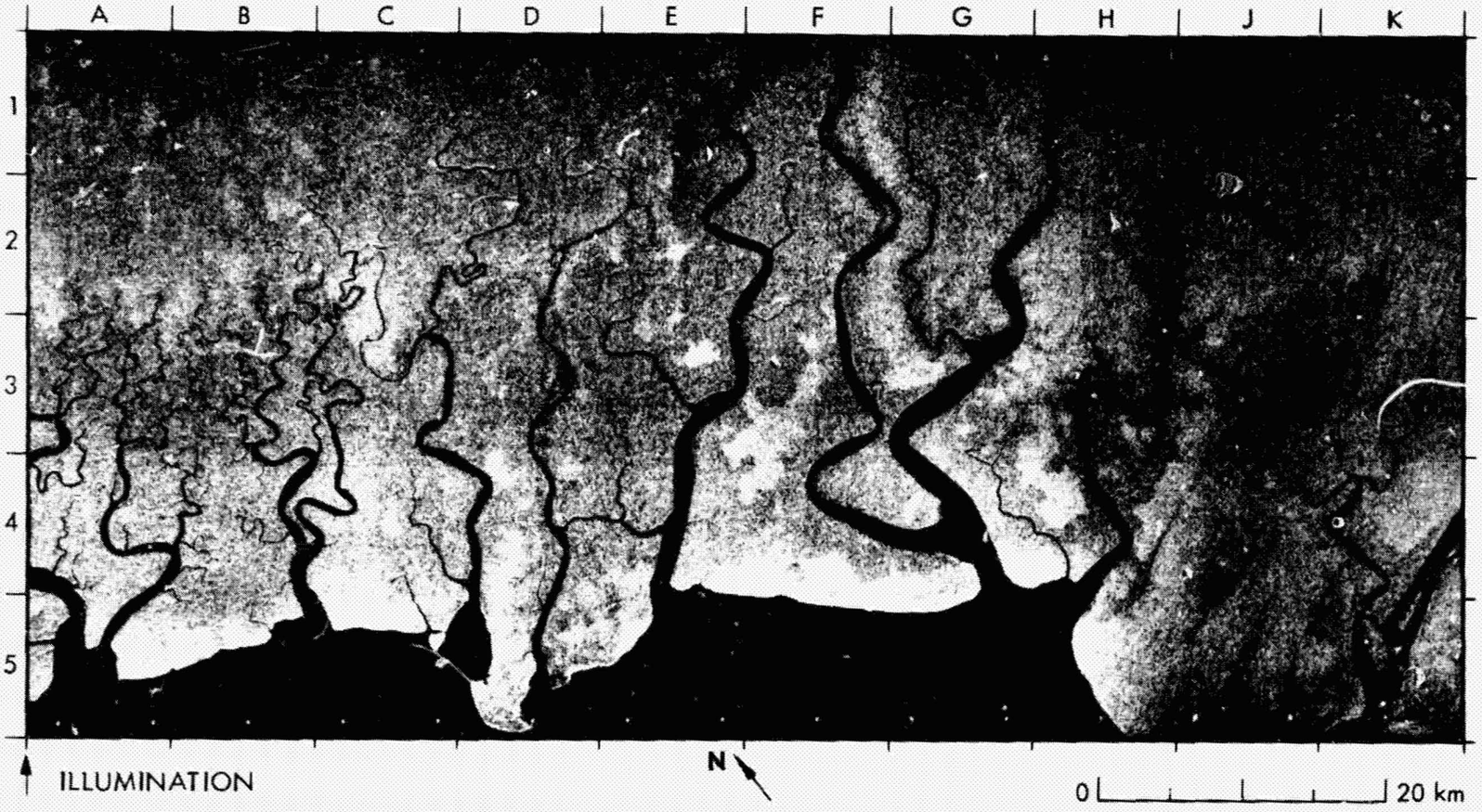

The coastal area of southwest Irian Jaya (West New Guinea) consists of a lowland tropical forest and an associated mangrove swamp that yield a generally uniform medium gray tone on the SIR-A image. Local patches of lighter gray (e.g., F4, G4, and H5) represent areas of the forest where mangroves are absent. At present, we have no satisfactory explanation for the very bright radar returns along some narrow coastal strips of the marshy deltas, as seen northwest from Flamingo Bay (H5 to E5) and along the margins of Laag Island (D5). They may represent artifacts of the radar system.

The area is impenetrable overland; the only thoroughfares to the interior are the rivers that drain the region. These rivers lead 70 to 100 km northward through the coastal lowland forest to the foothills of the massive mountain ranges that form the central core of the island. A sluggish but powerful tidal current in the Arafura Sea periodically inundates the coast to create a bore that reaches 15 km upstream and causes floods of 3 to 6 m.

The Asmat people live here in primitive, isolated villages widely separated along the Casuarina Coast (H4 southward) and at strategic

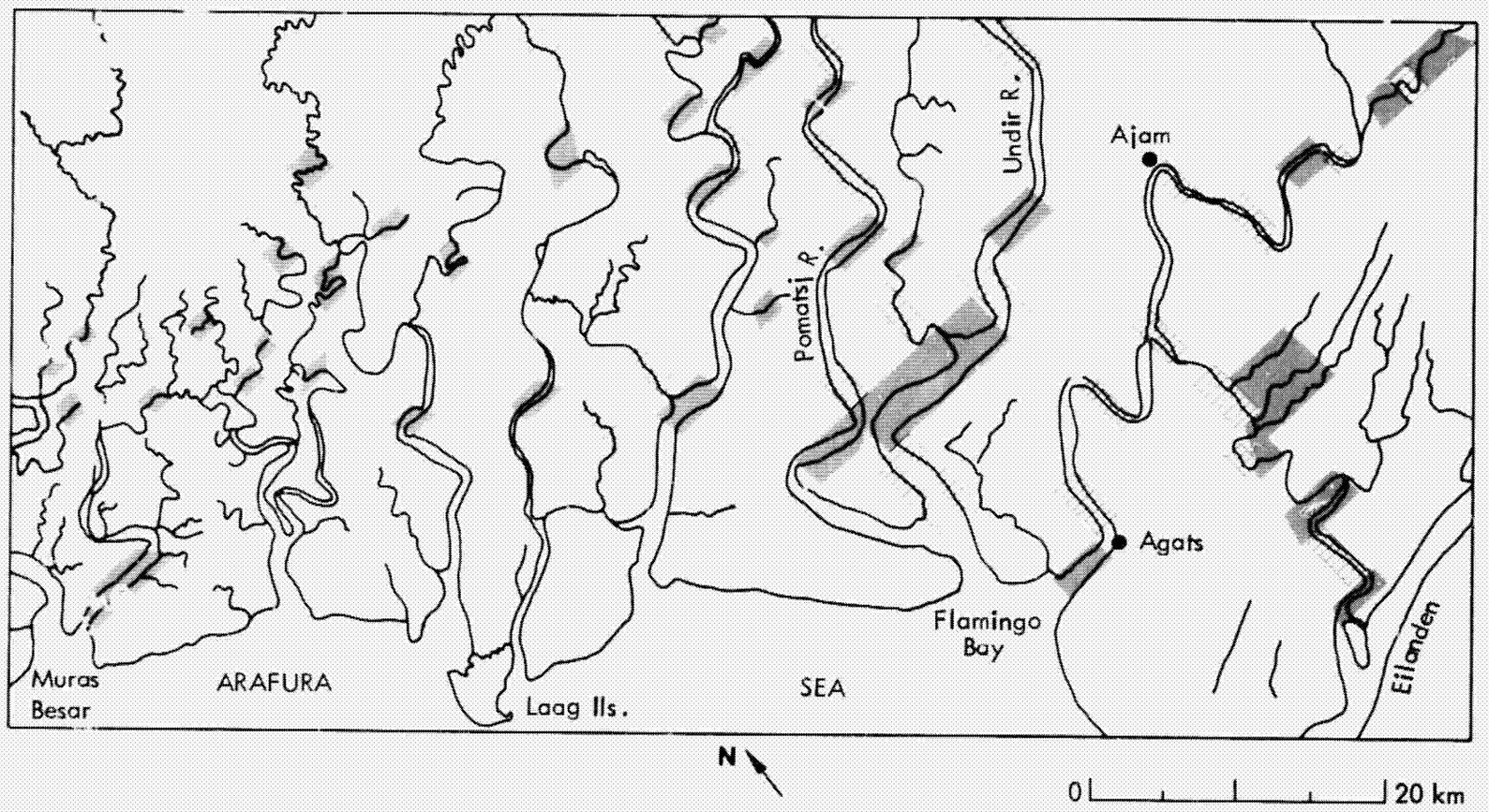

places along the river banks. Their dwellings are built on poles to keep them above the high level of the tidal waters. The villages cannot be distinguished from the forest on the radar image.

The drainage channels on the radar image show many linear segments 5 to 10 km long aligned predominately in two directions. This pattern of dominant alignments is shown on the accompanying sketch map. The most prominent direction is east-west, parallel to the structural trend of the mountains to the north. The conjugate north-south alignment of channel segments is apparent in the area from the Pomatsj River eastward. Although bedrock is totally absent at or near the surface, this alignment of stream segments strongly suggests that drainage in this area is structurally controlled.

Few Landsat images of the area have been acquired, and none reveals more than 30% of the land surface because of perennial cloud cover.

48. Kapuas River and Deltaic Plain, West Kalimantan, Indonesia

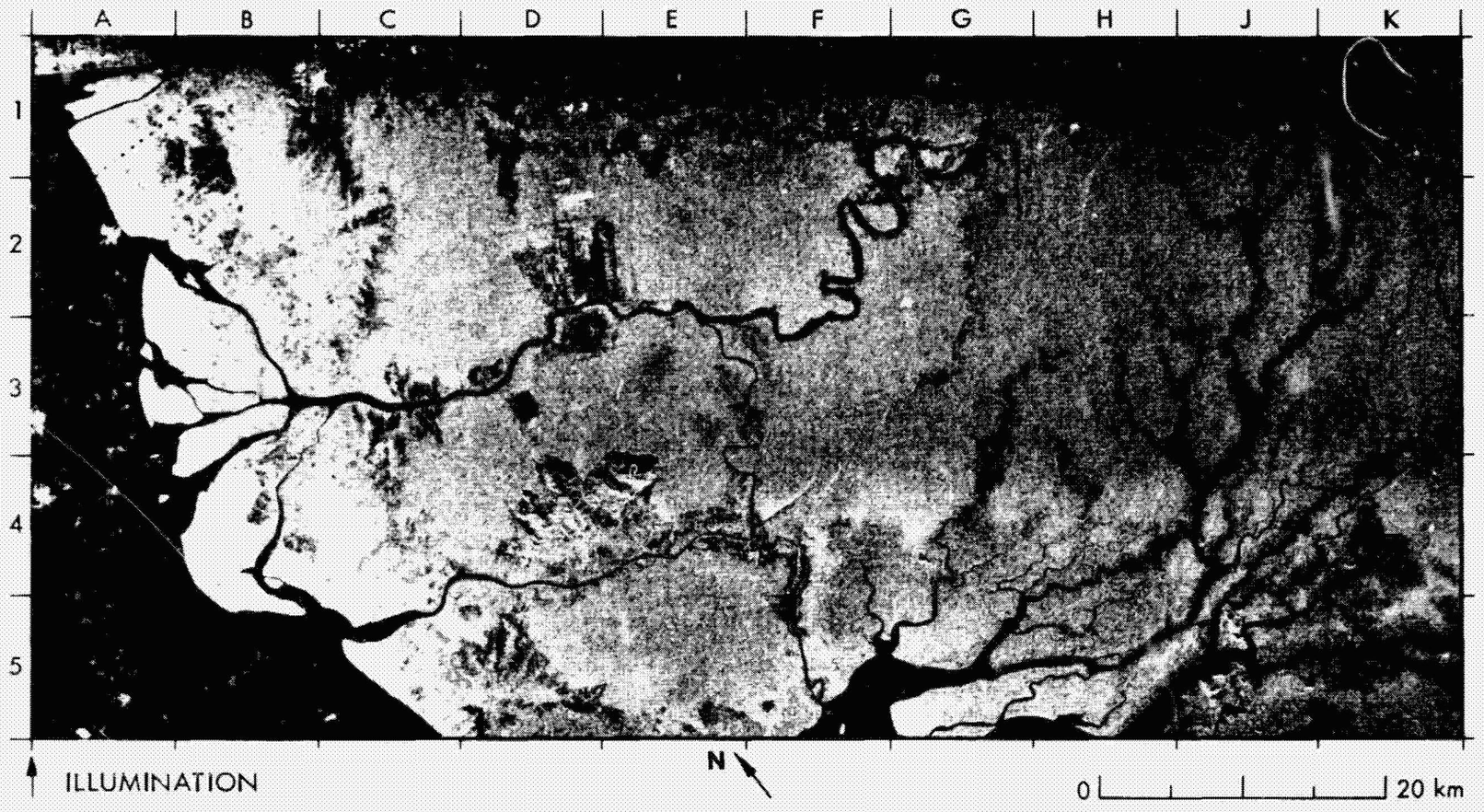

This scene shows the delta and the distributaries of the Kapuas River (A1 to C5) in west Kalimantan (Indonesian Borneo), and smaller streams that drain the coastal plain (K1 to G5). The Kapuas here is distinct from its namesake in central Kalimantan. Much of the area is occupied by swamp forest with a thick leaf canopy that yields medium- to light-gray tones on the radar image. Clear-cuts in the forest have symmetrical outlines and distinctly darker gray tones (D2 to D3). Much of the coastal region from A1 to C5 has been cleared and includes cultivated paddies.

Most of the area is underlain by deltaic and alluvial deposits of Quaternary age. Plutonic igneous rocks underlie the scattered hills and mountains that trend northwest from K5 to D4. The mountains at D4 rise steeply to about 400 m above the surrounding deltaic plain.

The coastal area is one of the more heavily populated regions of Kalimantan, with over 200,000 people in the town of Pontianak on the Little Kapuas River (B1 to D1). Bright radar returns come from waterfront

Landsat Band 7

buildings while the airport runway appears as a long dark strip (D1, lower left). Other evidences of human activity include a linear channel that has been cut from the Kapuas River south into the tropical forest (G1/C2), and numerous fish-trap platforms offshore and across the mouths of the distributaries (A2 to C5, and F5 to G5). The platforms appear as clusters of bright pinpoints on the image. The position of the equator is shown by the dotted line from A2 to B1.

The Landsat image in the near-IR wavelength shows medium- to light-gray tones in the areas of swamp forest, and bright tones in cleared areas of the delta and along the stream channels. The dark tone that corresponds to the adjacent portions of C5/D5 on the radar image suggests that this area was flooded at the time the Landsat image was acquired. Small cumulus clouds scattered across the Landsat scene cast shadows toward the southwest. Larger more extensive cloud cover at a higher elevation casts shadows that obscure portions of the scene from Pontianak southwestward.

49. Brasilia, D.F., Brazil

The capital city Brasilia in the Brazilian Federal District (D.F.) is some 970 km due west of the Atlantic coast, at an elevation of about 1000 m. This district, which covers some 5700 km^2, is surrounded by the State of Goiás. The district boundary is shown by a white outline on the SIR-A image. In 1980, the population of Brasilia, located at F1 and G1 through F3 and G3, was upward of 1.2 million people.

At first glance, the striking features on the radar image are the outlines of the man-made Lake Paranoá (F1/G1 through F2/G2) and the arcuate form of the main motor axis (eixo rodoviário) (F2/F3), which is bisected by the Monumental Axis and terminated to the west at both ends by a major highway. Localities mentioned here are shown on the accompanying sketch map drawn from the radar image.

The main motor axis is symmetrically situated between rows of massive superblocks that provide one of the several types of housing available. Each superblock is a self-contained residential unit consisting of six stories elevated on pylons above ground level. The superblocks include landscaped areas, play spaces for children, supermarket facilities, and primary schools. The broad stone and glass facings of these structures act as corner reflectors where they are oriented normal to the incident radar illumination. The bright returns saturate the radar image to

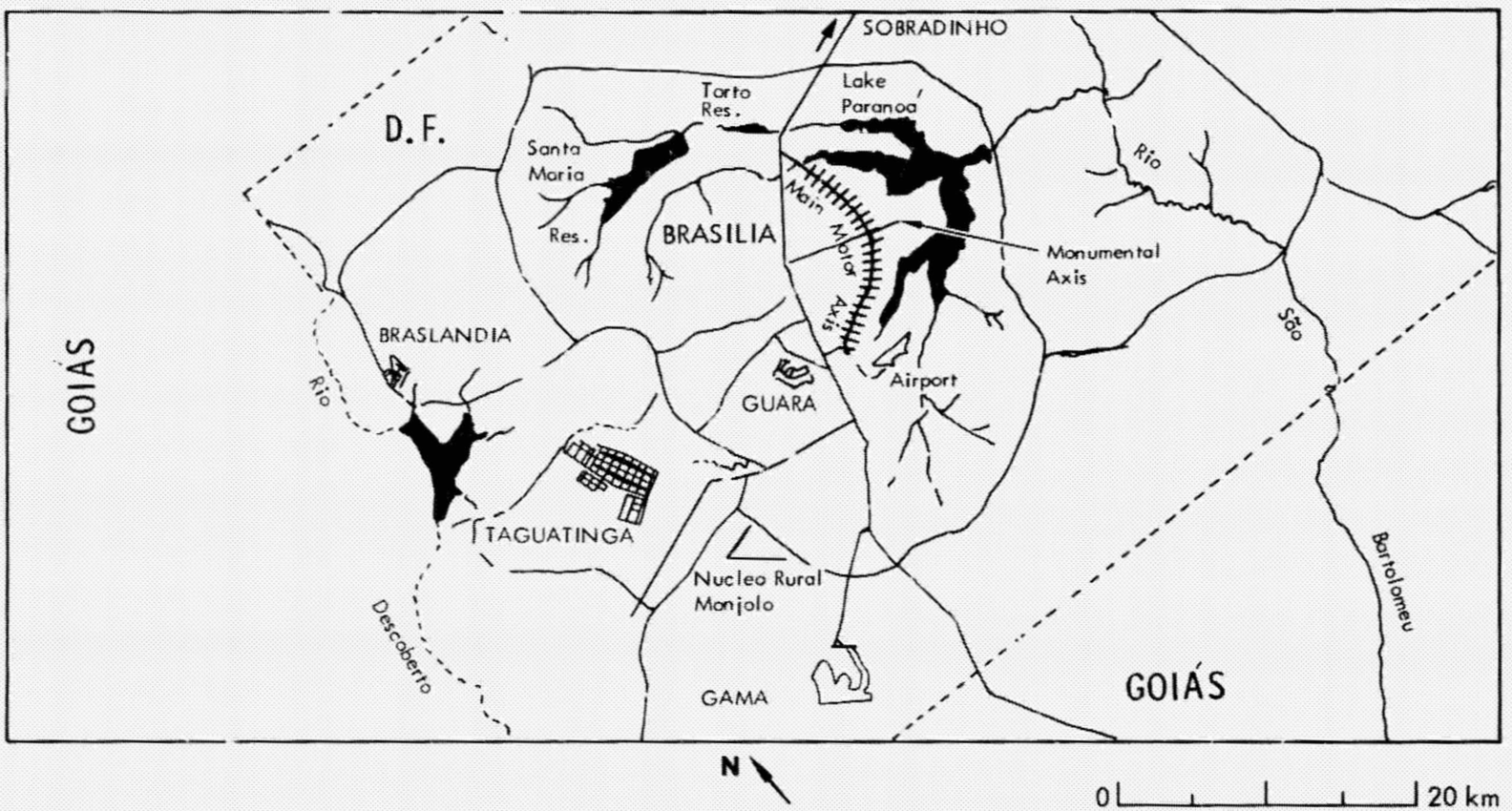

white, as at the right side of F2. Where orientation of the building's reflective surface departs from normal to the radar beam, backscatter from the superblocks is significantly reduced. This results in image tones that vary from light gray to dark gray. It is an excellent example for study of the relationship of radar backscatter to orientation of the scattering surface.

Brasilia is surrounded by a number of smaller satellite towns within the Federal District. In general, these towns are laid out in precise geometric patterns, as at Gama (F5) and Taguatinga (D4 to E4). Gama consists of rectangular and hexagonal sectors. The orientation of the building surfaces relative to the radar illumination produces multiple reflections that saturate the image to white. Only the outline of the town is recognizable. Taguatinga is located on a hill with radial drainage, at about 1285 m elevation. The street layout consists of narrow blocks with small building plots. The blocks appear in light-gray tones on the radar image. Some of the blocks show a dark-gray center portion. The orientation of the reflecting surfaces is probably responsible for the saturation seen on the image at the junctions of D3/E3 and E3/E4. The obliteration of data between the areas of saturation (white) is an artifact that results from the saturation. Further geographic details of the Federal District are

Landsat Band 5

given in published maps (Refs. 21 and 22). Much of the residential area in Brasilia, Gama, and Taguatinga appears white on the Landsat image in the visible-red wavelength because of high reflectance at this wavelength. The Santa Maria reservoir (E1/E2) is equally perceptible on the radar and the Landsat images. The Lake of Rio Descoberto (C3, D3, and D4) on the radar image appears on the Landsat image in medium- to light-gray tones that suggest vegetation in the area. The lake apparently had not been constructed and filled at the time the Landsat image was acquired. Medium- to light-gray tones on the radar image in the area south of the Santa Maria reservoir (D2 to E2) come from the vegetation canopy of the Brasilia National Park. These correspond to the medium-gray tone on the Landsat image. Comparison of the bright-through-medium to dark-gray image tones on the radar image at C3/D3 and E3, F1, and G1 with the corresponding tones on the Landsat image suggests a varying pattern of land utilization that invites further investigation.

50. Villages and Cultivated Fields, Hebei-Shandong, China

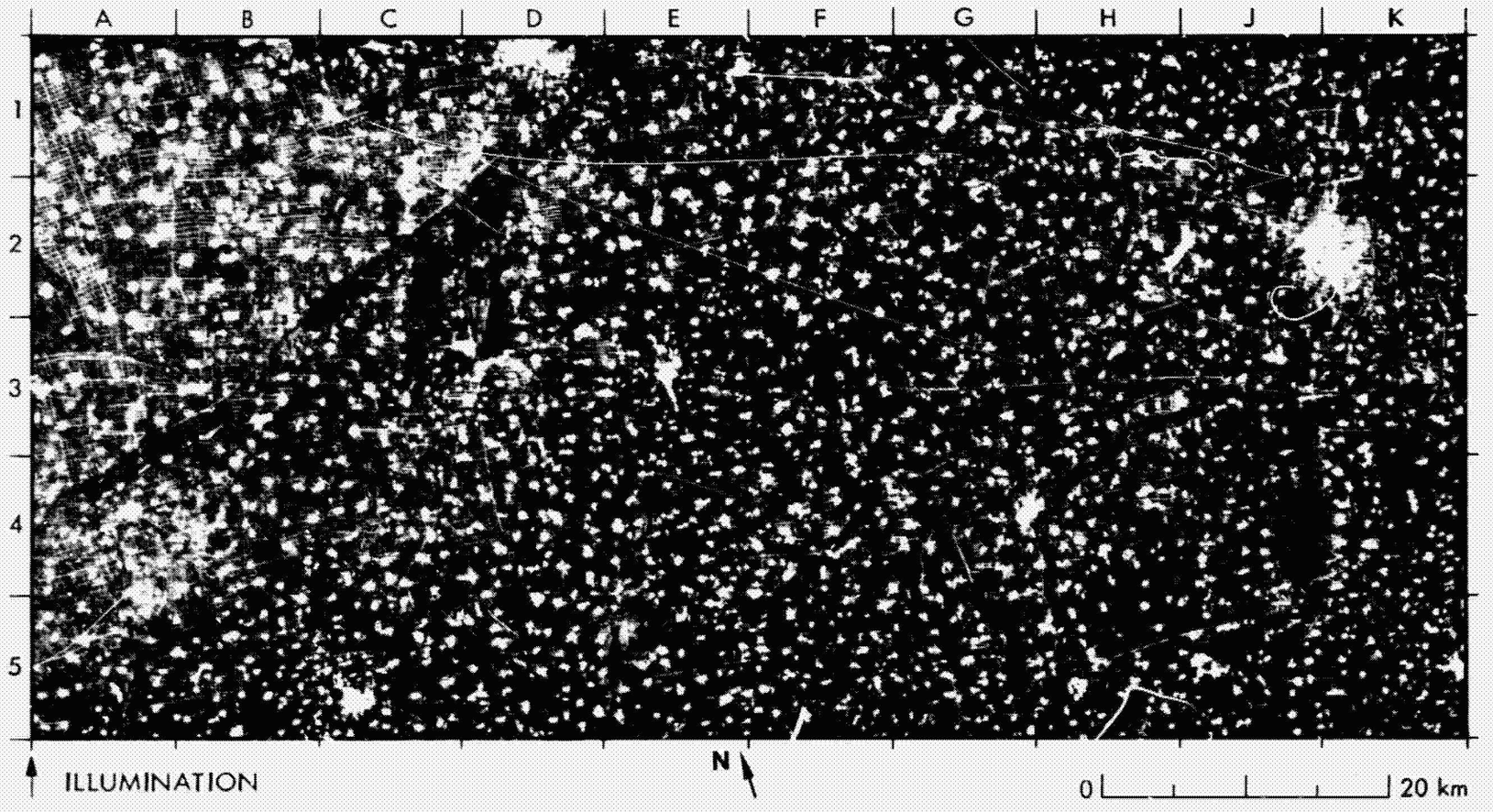

Intricate rectangular patterns and a multitude of bright spots on the SIR-A image indicate the cultivated fields and small villages of this area in eastern China, about 150 km north of the Huang He (river), China's largest river. Village density here is approximately one per km^2. The bright spots coalesce into the large cities of Dezhou (K2), Hengshui (D1/E1), and Nangong (C5).

The Grand Canal (K1 to H5) marks the provincial boundary between Hebei (west) and Shandong (east). It appears to be a double river on the radar image, but the Landsat image shows clearly that the channel itself runs between the two levees that produced the strong reflectance on the SIR-A image. The Fuyang He (E1 to A4/A5) also seems to be a double river, although the channel is the southernmost feature, and the levee the northernmost, as again seen more clearly on the Landsat image.

The two images are complementary in other ways as well. While the

Landsat Band 7

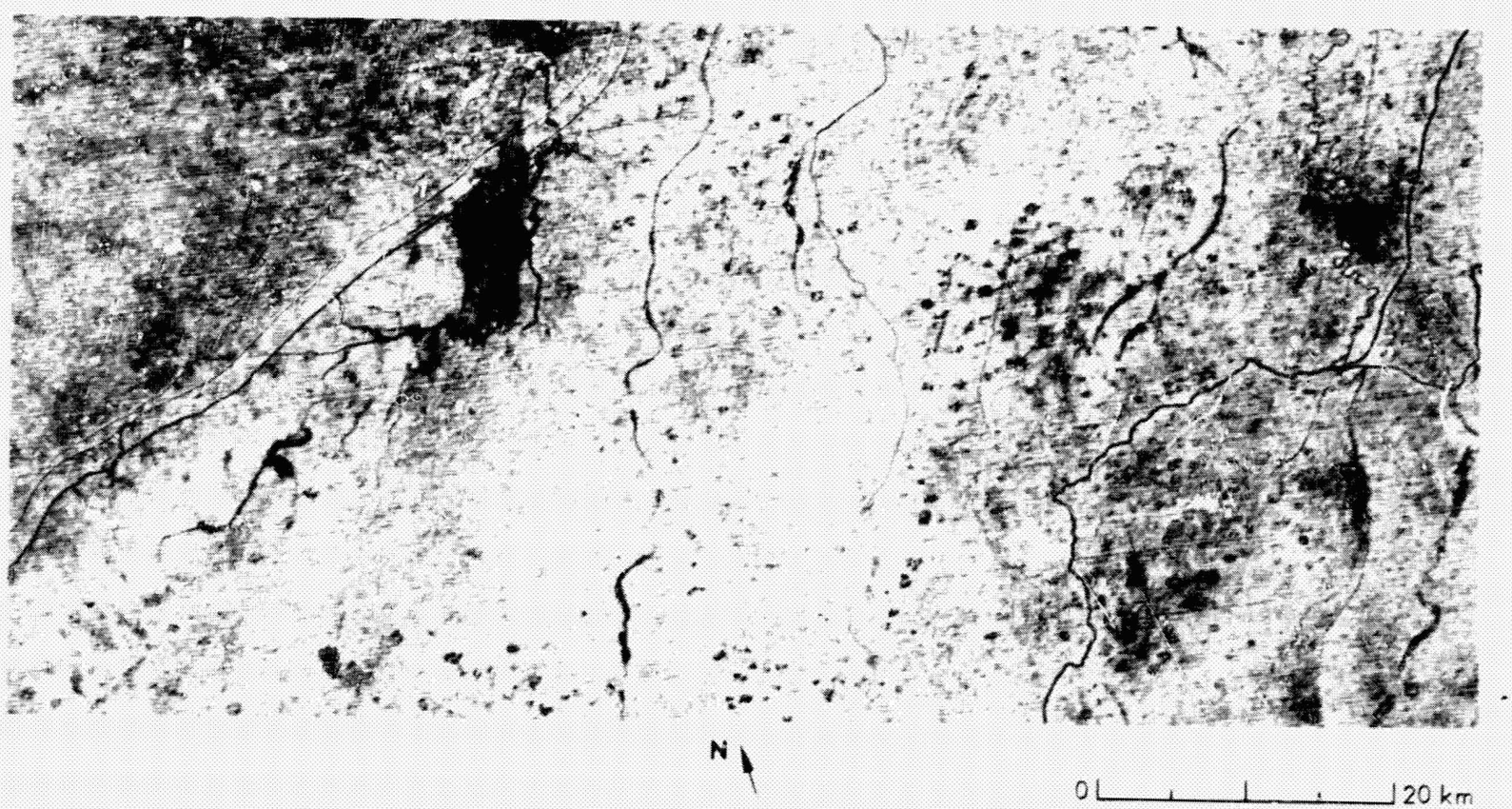

Chiang He (E1/F1 to E5) is nearly lost on the radar image, and its path is obvious on the Landsat image; the villages and fields are sharply displayed on the SIR-A image and almost invisible on the Landsat image. The small, dark patches on the Landsat image are probably ponds which are quite obscure on the SIR-A image.

Severe summer floods carry fine, fertile loess sediment from the provinces of Nei Monggol, Shanxi, Shaanxi, and Gansu to this area where it is captured by large catch basins along the Huang He. When the basins are filled, they are cultivated. An example of this reclamation is seen at C2/D2 and C3/D3, where cultivated fields exist on a filled, former lake basin. The basin appears as a lake on the 1976 Landsat image.

C. Oceanographic Features

Numerous oceanographic features were observed with SIR-A despite the high incidence angle and the generally low radar backscatter from the ocean surface. The types of ocean surface features imaged by SIR-A (Scene Nos. 51 through 57) corroborate previous observations of the oceans made by Seasat SAR. Surface waves and windrows are shown in Scene No. 51. A large internal wave train was imaged in Scene No. 52. Two successive orbital passes, separated by 1½ h, provide some information about the formation of surface disturbances due to local wind variations (Scene No. 54). Examples of other features observed include surface slicks, eddies, squall lines, and the dampening effect of rain cells. Vessels appear as very bright targets (Scene No. 53) as they do on Seasat SAR images. However, very few ships' wakes were observed. Because no ground-truth experiments were undertaken simultaneously with the SIR-A data collection, the interpretations are based on inferences from meteorological data, bathymetry, or documented observations.

51. Surface Waves, Western Mediterranean Sea

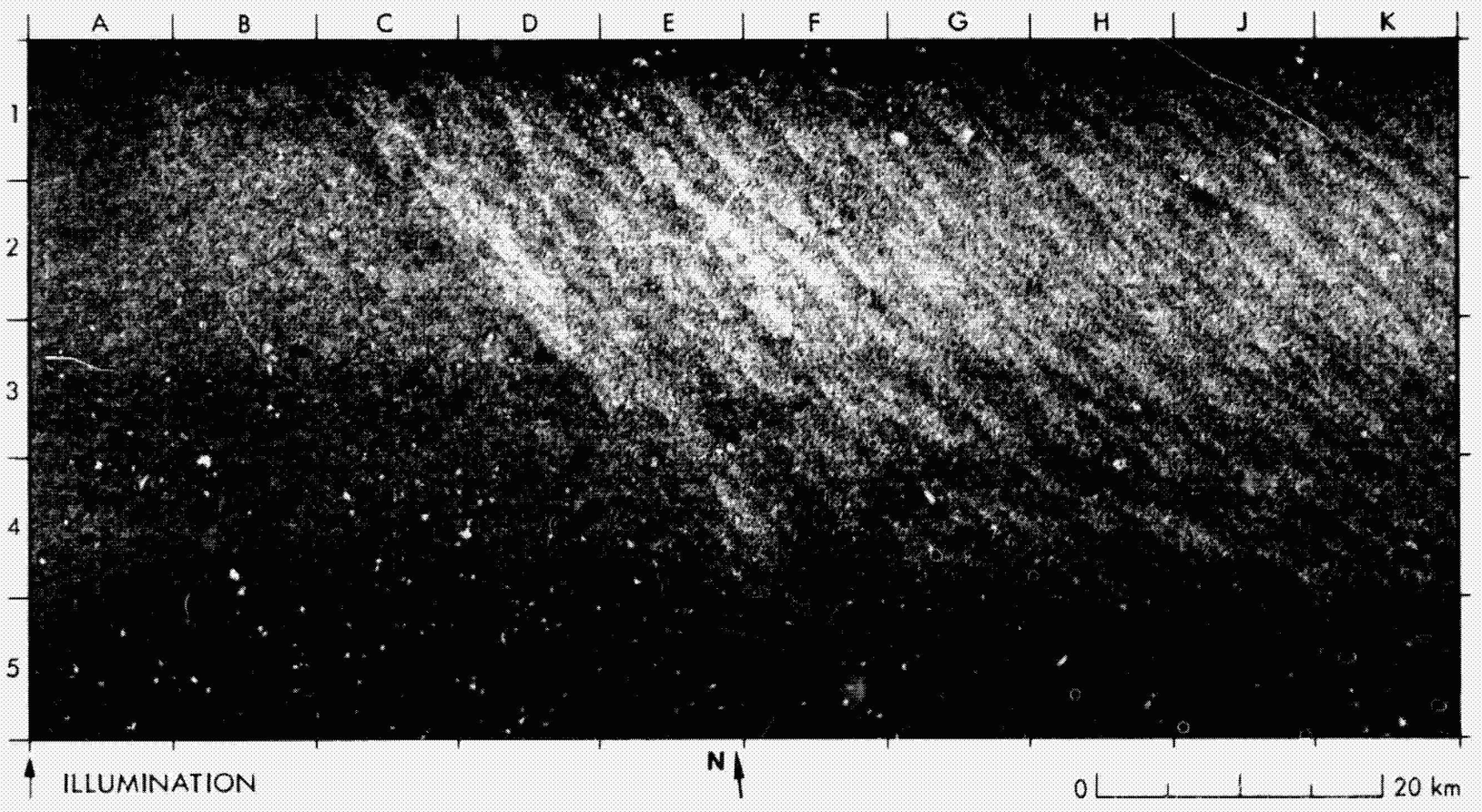

The surface waves and windrows in this image were in an area to the north of the Island of Minorca (Spain), in the western Mediterranean Sea. Swells with a wavelength of 150 m are visible as a periodic variation in the image brightness. This periodic variation results from modulation of the local surface slope by capillary waves. The capillary waves selectively backscatter the incident radar energy, reinforcing it where there is resonance with the radar wavelength (this is called the Bragg scattering effect).

Weather reports indicate that a steady 15-knot, north-northwesterly wind was blowing. This area is in the most windy region of the Mediter-

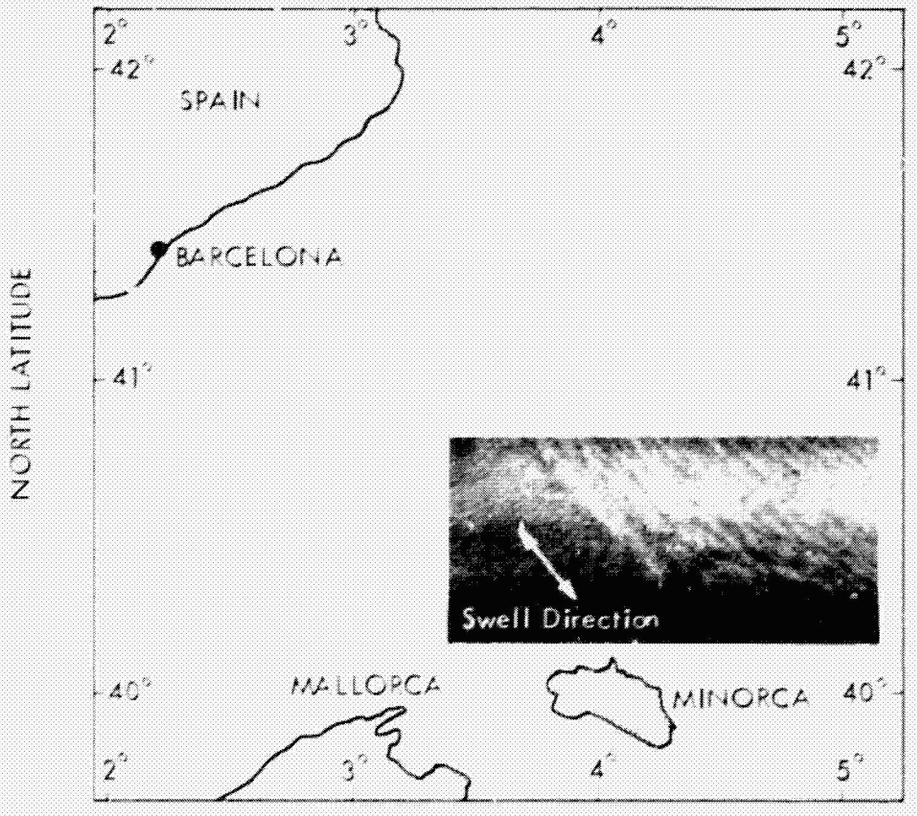

ranean Sea. The prevailing winds (the Mistral and the Tramontane) are strong and highly transient.

The large-scale linear striations are windrows. Windrows are cross-wind circulations that result from instability in the mean wind field. Their structure is periodic in the crosswind direction. Row axes are roughly parallel to the mean wind direction, which in this case was southeast. The wavelengths of these windrows—from 2.5 to 3 km—is within the range of typical windrows. The western boundary of the windrows shown here is approximately aligned with the easternmost of the Baleanic islands.

This image was acquired at 1030 GMT on November 14, 1981.

52. Internal Waves, Andaman Sea (Indian Ocean)

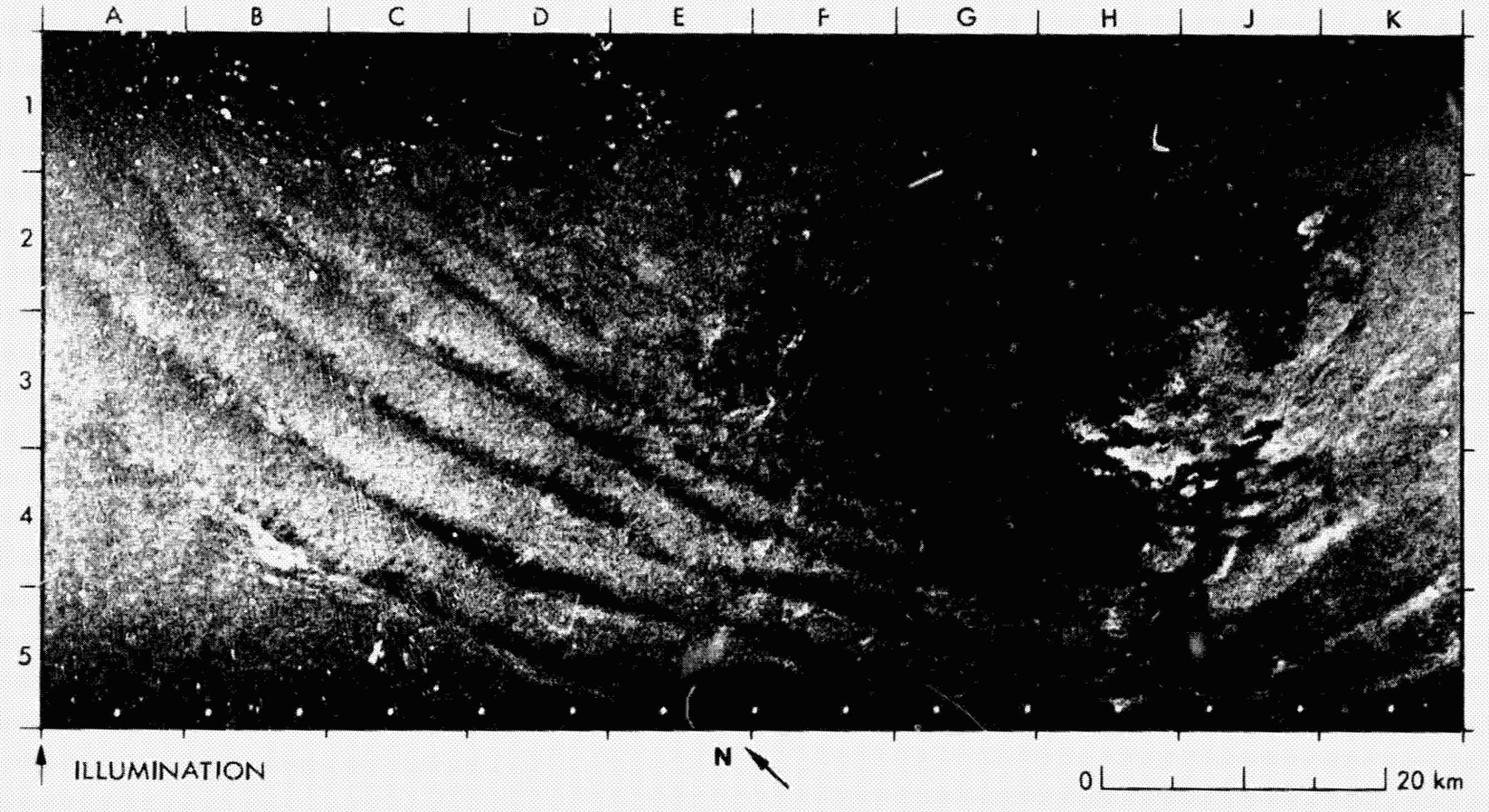

This large internal wave pack was about 150 km southeast of North Andaman Island (India) in the Andaman Sea. Presumably, internal waves are generated by the interaction of strong tidal currents with bottom topography. Internal waves can also be generated by shear-current flow and atmospheric disturbance. Once generated, the waves propagate along the boundary layer between waters of different density. Such boundary layers are associated with the oceanic thermocline and abrupt changes in density. An internal wave packet is geometrically characterized by a curvilinear front. The wavelength and amplitude decrease with distance from the front.

Internal waves are observed on radar images (many have been seen on Seasat SAR images) because of their effect on surface rough-

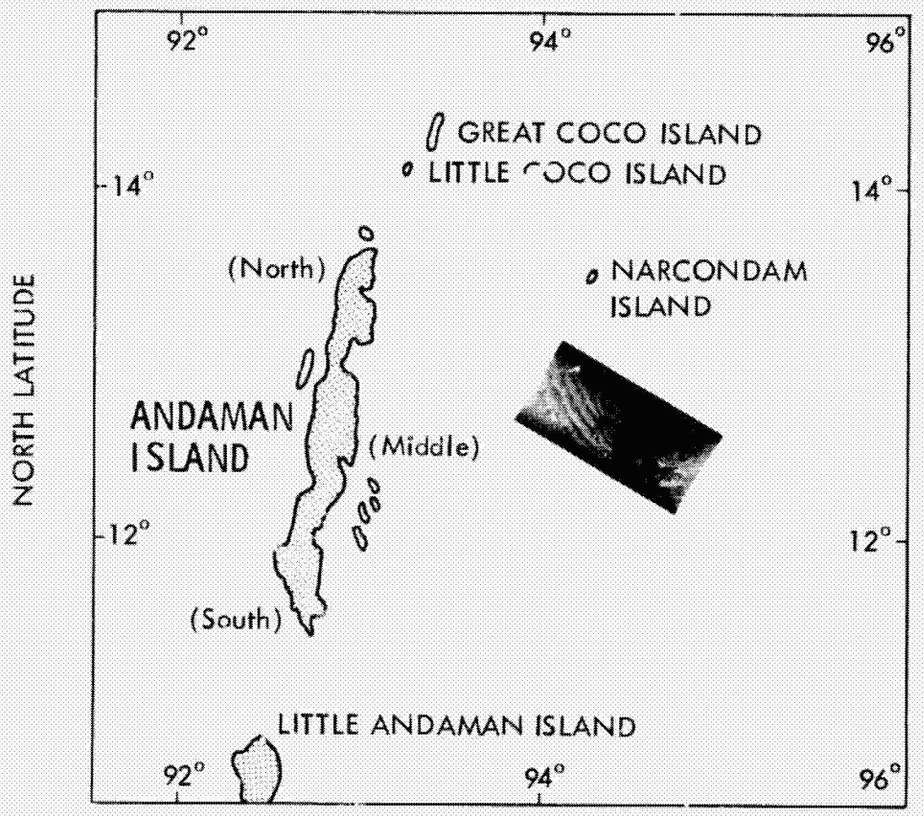

ness. Large currents associated with internal waves modify the capillary-ultragravity surface-wave spectrum that overlies the oscillations. These surface waves are the main scatterers of the radar signal; the radar image, then, shows the surface geometric pattern of the subsurface internal waves.

The wave train in this image had a 100-km-wide front and wavelengths from 2.5 to 6.5 km. Larger waves—up to 150 km long and with wavelengths of 15 km—have been observed in the Andaman Sea on Landsat images. They seem to be associated with the tidal cycle.

This image was acquired at 1056 GMT on November 14, 1981.

53. Surface Slicks and Ocean Vessels, Rio de Oro Coast, Atlantic Ocean

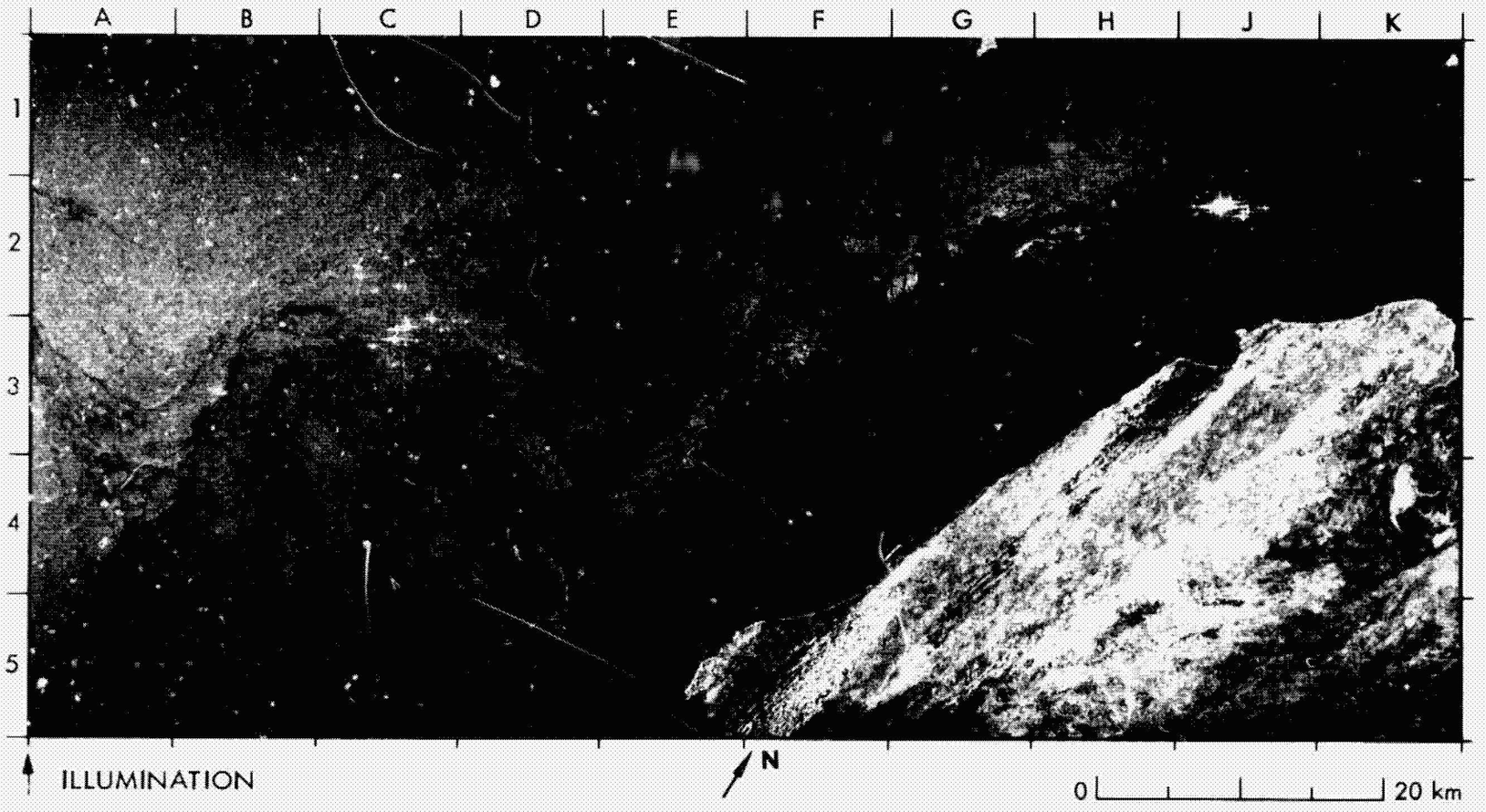

This region off the West-African coast is an area of known upwelling. The Oceanographic Monthly Summary (Ref. 23) shows a monthly anomaly of −1°C for the month of November, 1981, localized along the Rio de Oro Coast. Dark slicks on the ocean surface along the coast may be associated with the coastal upwelling. The weather report indicates a light wind with overcast for the period during which SIR-A acquired this coverage (0854 GMT, November 14, 1981). The filamentary pattern of the dark tones from smooth areas is probably a result of surface-water

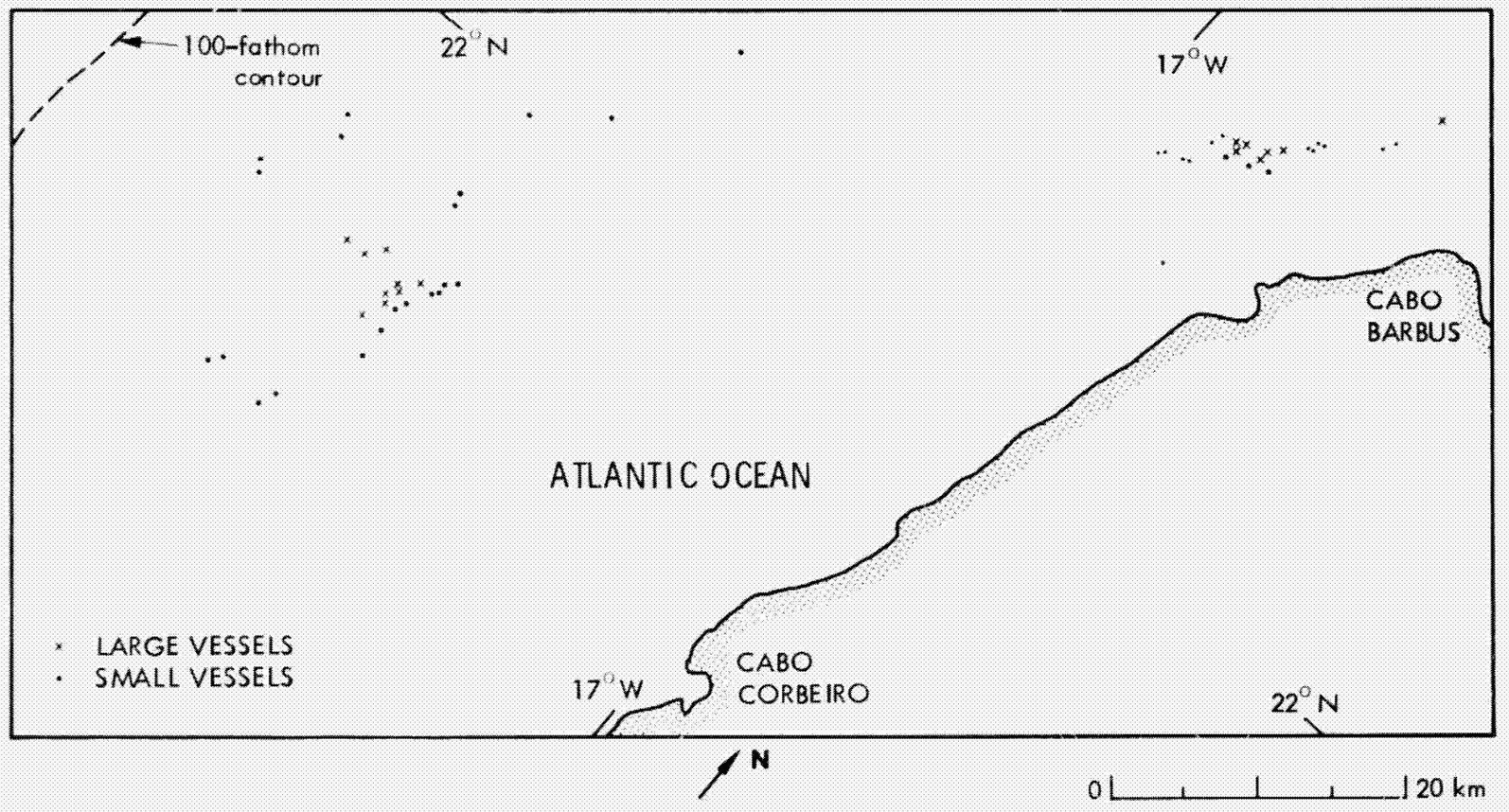

ORIGINAL PAGE IS OF POOR QUALITY

motion.

Large groups of fishing vessels are visible off the coast at J2 and C2/C3. Each group consists of a few large vessels and numerous smaller vessels. Returns from the large vessels were strong enough to saturate the radar sensor; this saturation created cross patterns on the image. Many of the small vessels travel in pairs with a fishing net extended between them (B2, B3, C1/C2, and C2/D2). The larger vessels are floating canneries that process the catches of the small vessels.

54. Wind Patterns Off Sardinia, Mediterranean Sea

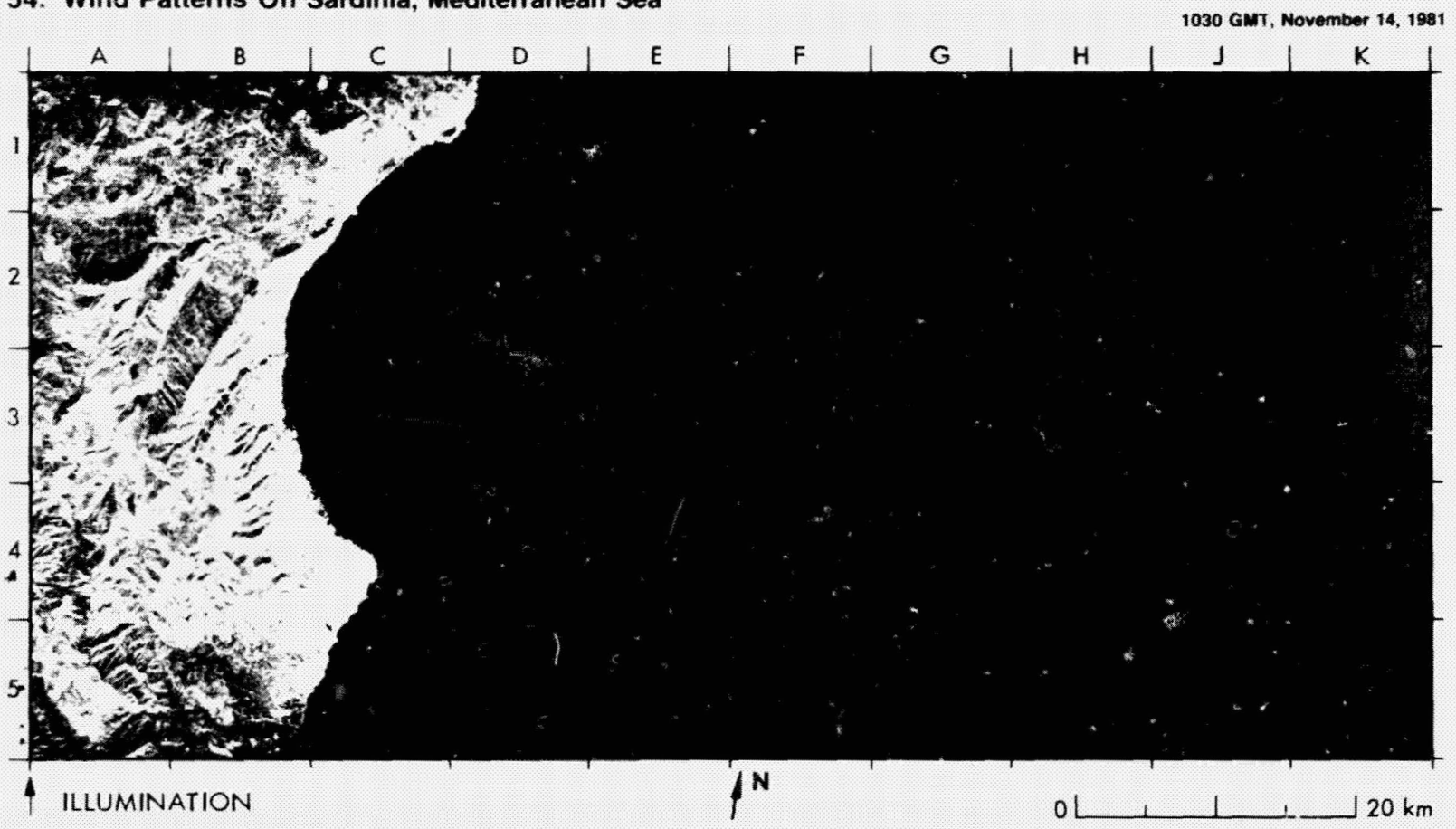

These two SIR-A images present a record of the temporal changes that occurred at this area of the sea surface over an interval of one hour and a half. The left image was acquired at 1030 GMT on November 14, 1981; the sea surface appears as a mostly homogenous gray tone, which suggests a somewhat uniform level of surface roughness. A small disturbance is evident from the pattern of light and dark tones in the Gulf of Orosei (C3/D3). The right image was acquired at 1200 GMT; the sea surface shows a wide range of gray tones, and a distinctly different texture in the area bounded by E1, K1, K3, and E3. These differences reflect changes in roughness due to capillary wave variations, most likely

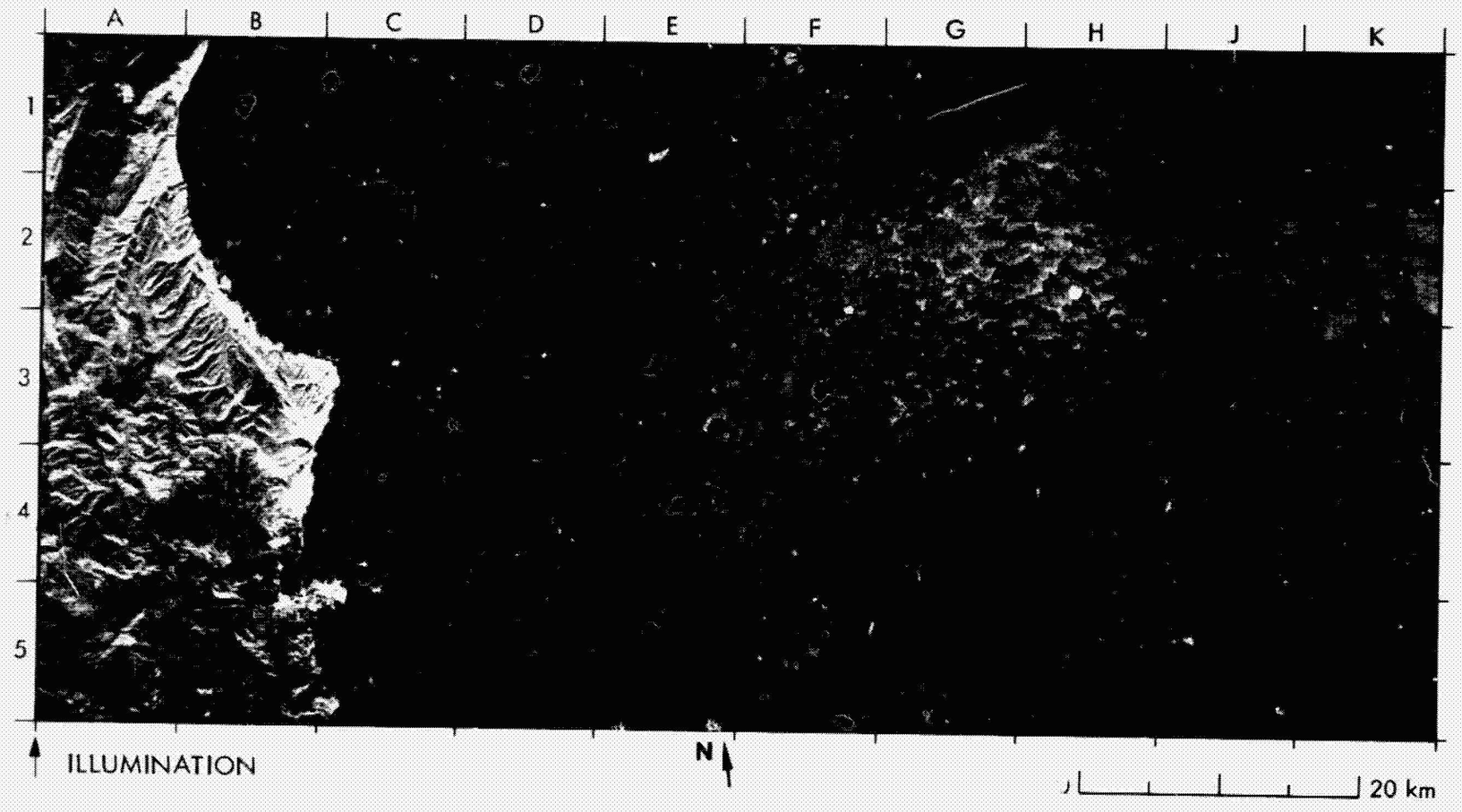

the result of local variation in the surface wind. A strong eddy from 10 to 15 km in diameter is clearly visible on the right image in the Gulf of Orosei at C1, C2, and D2. This eddy may be associated with the frontal system that separates two persistent cold eddies that occur off the coast of Eastern Sardinia in the months from summer to winter (Ref. 24). The bright point target on the right image in the lower left corner of C4 is a vessel. This vessel is not present on the earlier left image (B5, lower right).

55. Wind Slicks and Fronts, Moro Gulf, Celebes Sea

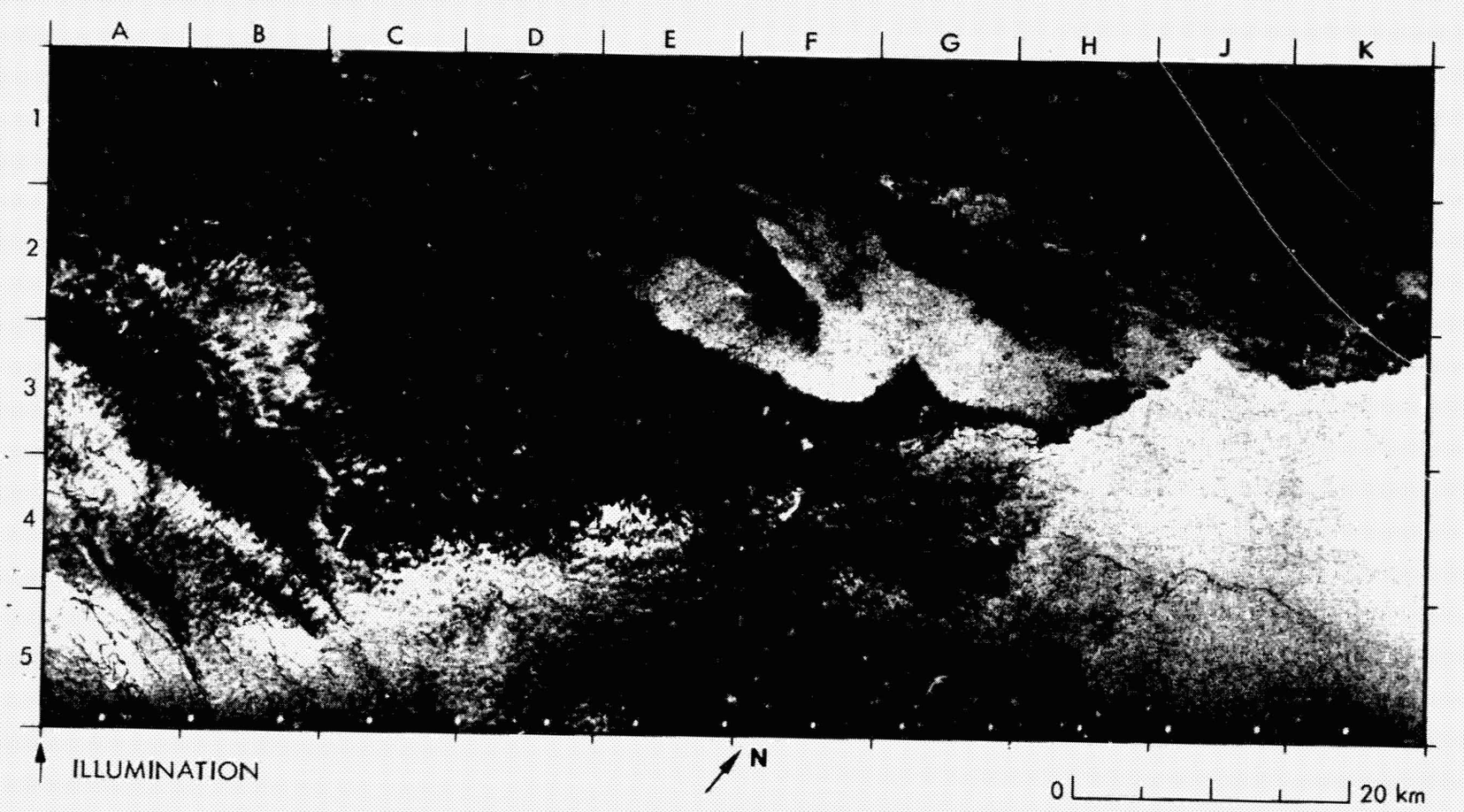

The sharp curvilinear boundaries on the image correspond to an abrupt local change in wind speed, as at E2 through G3 and J3 to K3. The local gusty winds create the rough seas that, in turn, produce strong radar returns. The bright areas on the image are regions of strong winds. The dark areas are either regions of low wind velocity or heavy rainfall, which tends to smooth the ocean surface by dampening the short gravity/capillary waves. The pattern of slicks at A4 and A5 is probably also related to wind activity.

The image was acquired at 2212 GMT on November 13, 1981.

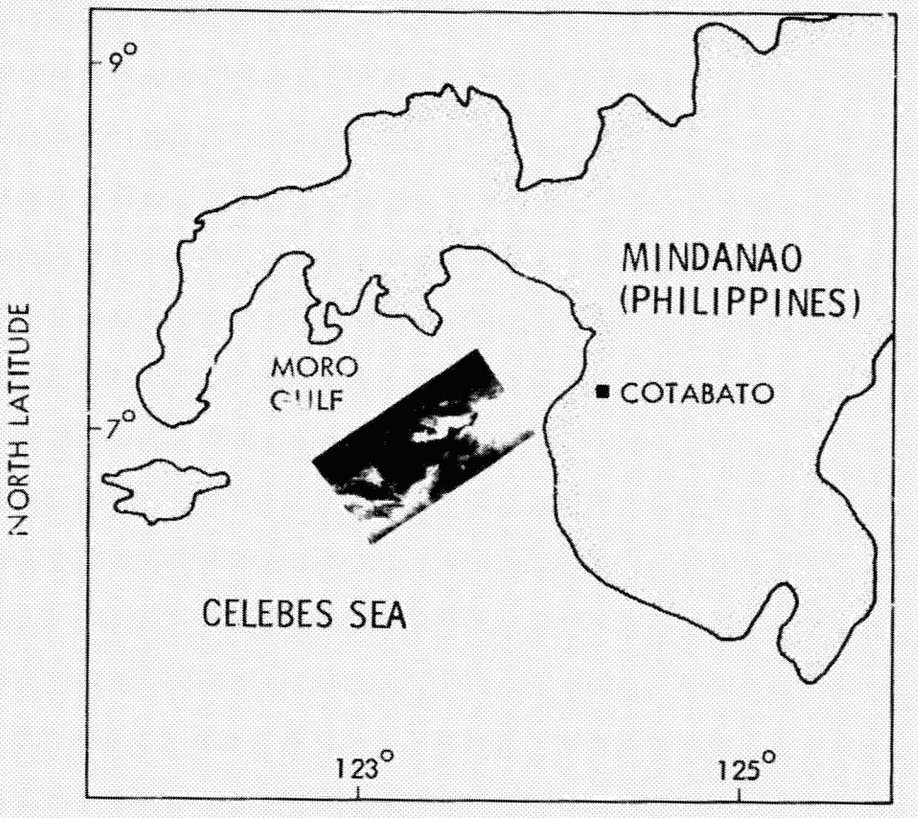

56. Ocean Eddy Off Dominican Republic, Atlantic Ocean

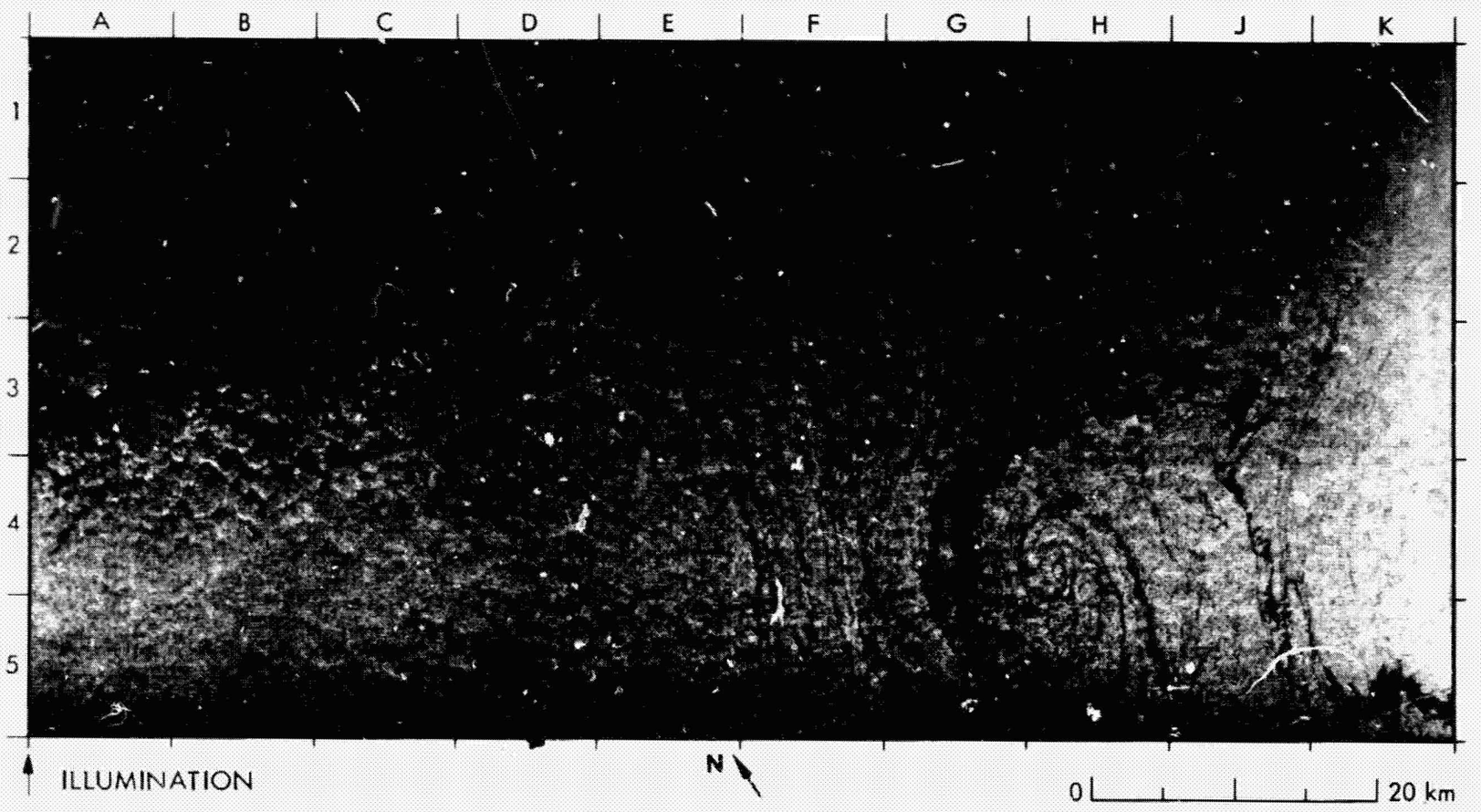

The ocean eddy from G3 through J3 to J5 and G5 was observed over the Silver Bank area of the Atlantic Ocean, about 40 km north of the Dominican Republic. The cyclonic eddy is visible because of the vortex shape of the dark surface slick. It is uncertain whether this eddy is due to oceanic currents or surface wind effects. The bright point target at the lower right of the eddy (H5) is a vessel. The mottled texture of the image at the center left from E2 to A3/A4 is likely due to local variations in the near-surface wind pattern (cf. SIR-A image of Scene No. 55).

This image was acquired at 2127 GMT on November 13, 1981.

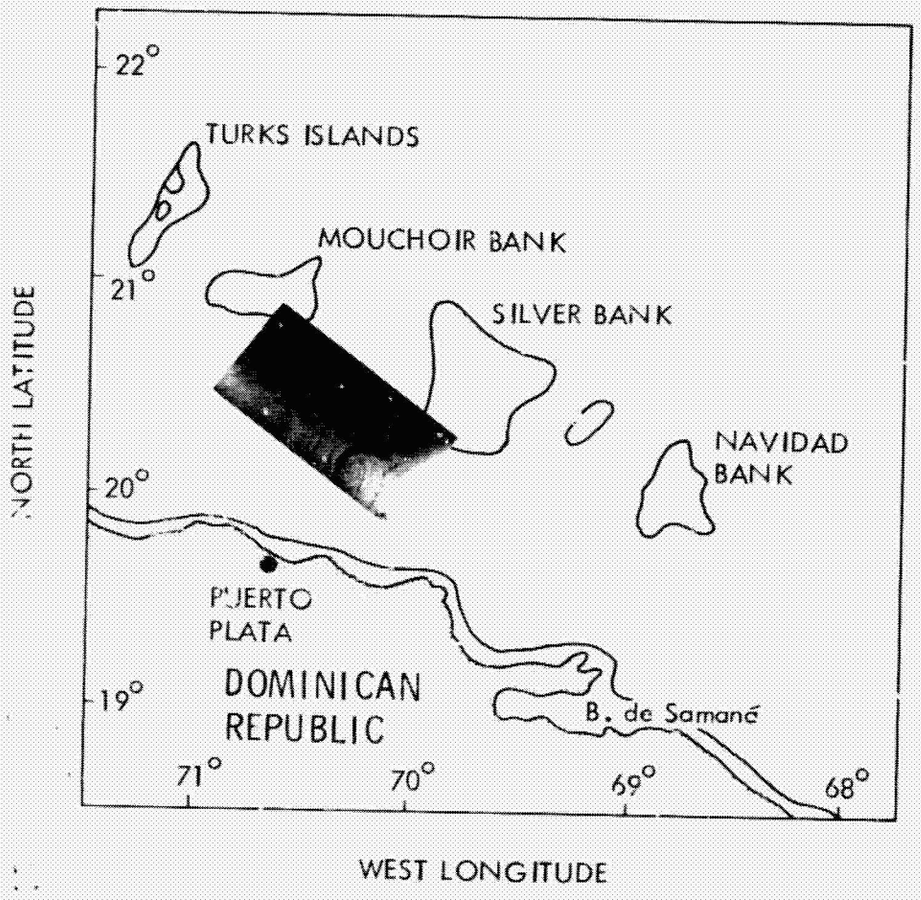

57. Ocean Surface Patterns Off Java, Indian Ocean

This surface signature of a tropical rain cell was taken about 100 km south of the coast of Java, Indonesia, in the Indian Ocean. The sharp boundary from A1 to F5 represents the associated squall line. The dark patches (e.g., C3 to D3) are heavy rainfall, which dampens the short capillary waves and consequently smooths the ocean surface (cf. SIR-A image of Scene No. 55). Similar ocean surface features have also been observed on Seasat SAR images.

This image was acquired at 2210 GMT on November 13, 1981.

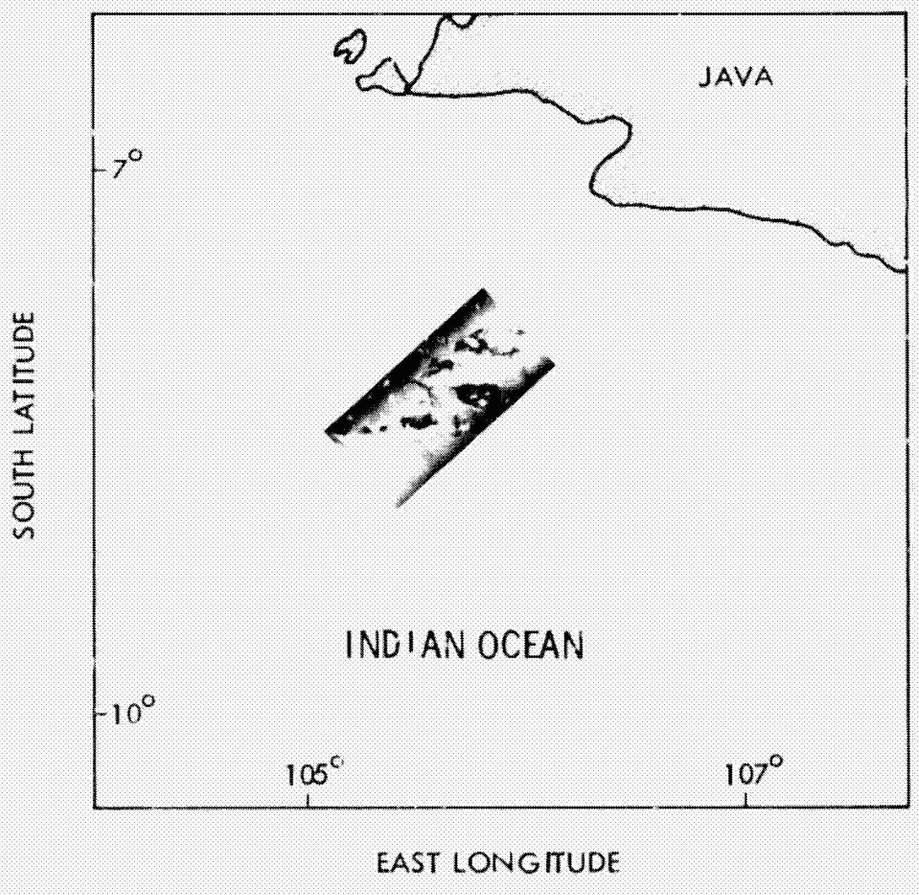

D. Man-Made Features

Evidences of human activity or occupation are widely represented in the SIR-A coverage. Structures such as routeways, transmission lines, canals, and bridges may appear bright or dark on SIR-A images depending on the orientation of the reflecting surfaces relative to the radar illumination. Platforms, vessels, and certain structures that behave as point-target reflectors appear very bright. Among the prominent man-made features recorded by SIR-A are the Corinth Canal (Scene No. 58), dams and large reservoirs (Scene No. 59), and offshore oil platforms (Scene No. 60).

58. Corinth Canal, Greece

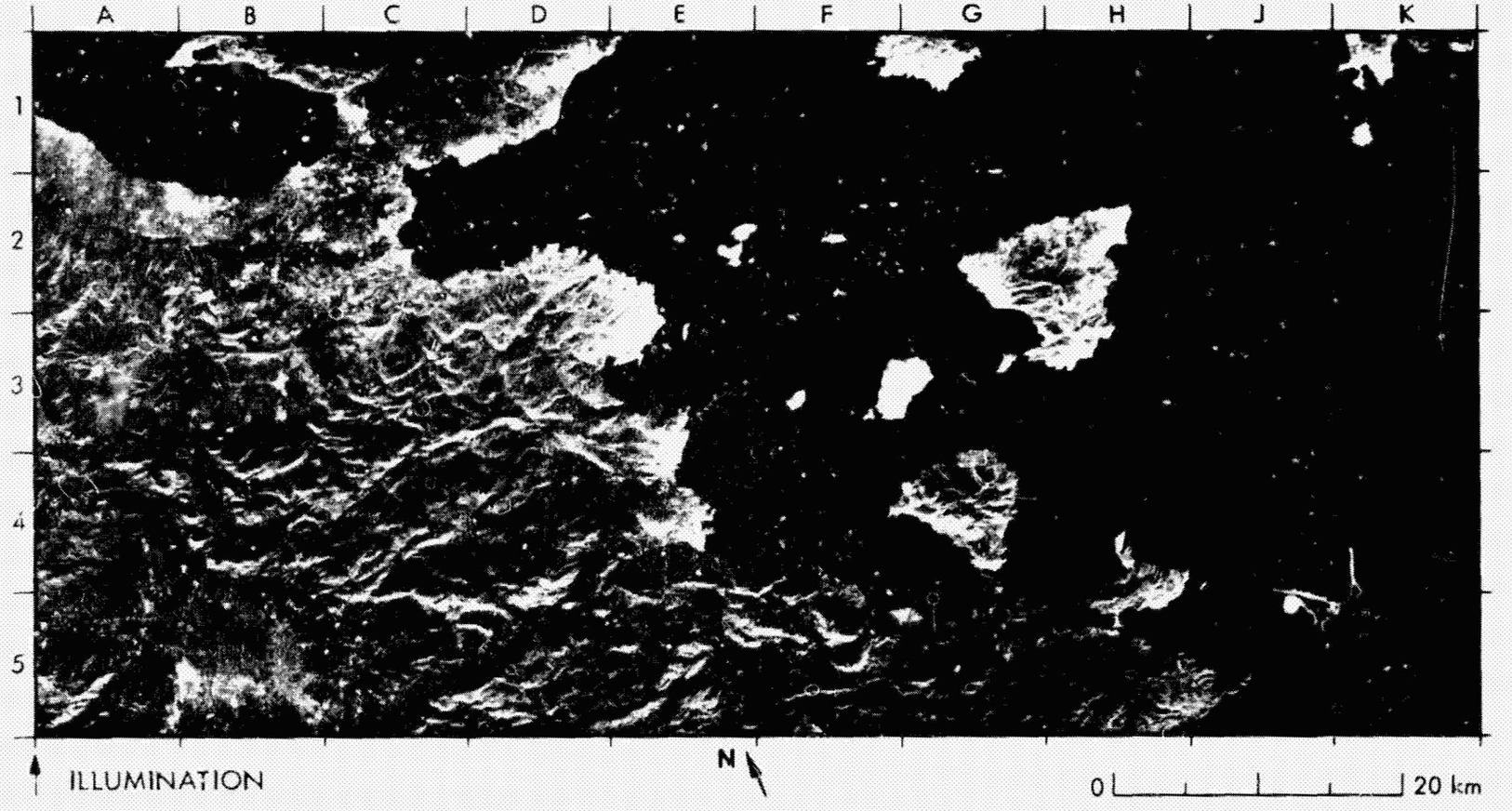

The narrow isthmus at C1/C2 joins the Peloponnesus (south) to the mainland of Greece (north). To the east lies the Gulf of Saronikos (C2) and to the west is the Gulf of Corinth (B1). The City of Corinth is at the lower right corner of B1. Athens and the Port of Piraeus are just outside the image margin at H1. The isthmus is flanked by bold rugged mountains to the north and south, which rise to elevations of 1200 to 2400 m.

In ancient Greece, this isthmus was used as a portage. Small vessels were hauled overland across the 6 km that separates the waters of the west and east. Agamemnon, Darius, and Xerxes dreamed of building a canal here to enable ships to pass freely from Corinth to Piraeus, and to circumvent the long circuitous route around the Peloponnesus peninsula. In AD 66, the Roman Emperor Nero proclaimed his intent to construct a canal here, and he sent legions of slaves to implement his command. Upon his death a few years later, the task was abandoned. In the late nineteenth century, canal construction was resumed. After an initial failure, the work was completed and the canal opened in 1893—following almost exactly the route that had been laid out by Nero 1800 years earlier. The canal is about 5 km long. Its sides at

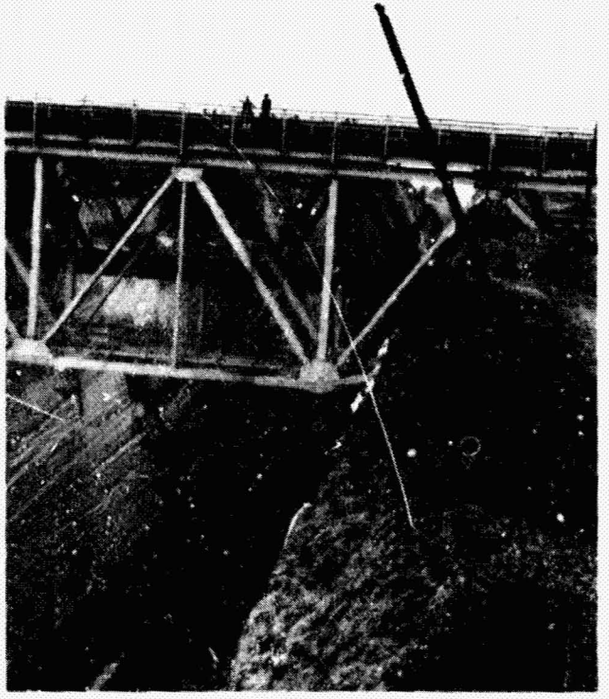

either end are formed by the sloping, natural contours, but the central two-thirds of its length are a deep cut in the land, the deepest part of which is just over 80 m. It is about 24 m wide at the base, increasing to widths of 80 to 90 m at the top.

A small section of the steep canal wall is shown in the accompanying photograph. On the radar image, the canal through the isthmus is represented by parallel dark and bright lines. The dark line on the image represents the radar shadow of the wall nearest to the direction of illumination. The bright line represents diffuse backscatter from the upper part of the distal wall.

Because the canal is linear and has no locks, it is regarded as one of the "cleanest" engineering cuts. Due to its small dimensions, however, it cannot accommodate ships with a beam of more than 18.2 m or a draft of more than 7.2 m. This limits its use to ships with a displacement of less than 10,000 tons.

59. Dams and Reservoirs, Rio Grande, Brazil

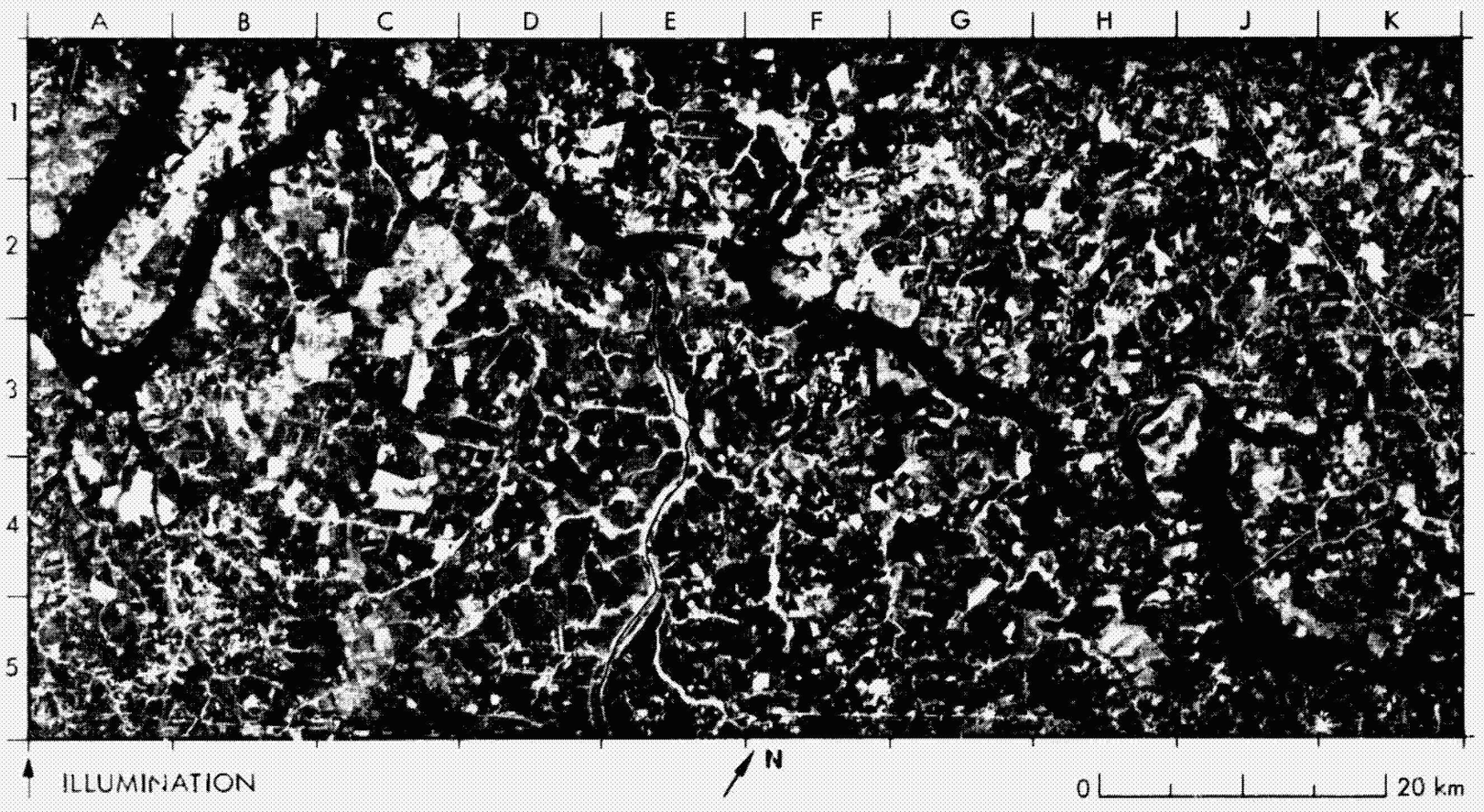

The Rio Grande follows a long, tortuous course through the Brazilian Highlands in a west-northwest direction toward the Paraná River. It is a major tributary of the Paraná, and has many cataracts and waterfalls along its length. At least eight major dams have been constructed along its course. This SIR-A image shows two: the Volta Grande Dam at J3, and the Porto Colombia Dam at E2. Evidence of a third major dam, the Marimbondo about 30 km downstream, north of the image margin at B1, is provided by the smooth outline and gradually increasing width of the water body from E2 to B1, and from the backed-up waters in tributary channels at A3 and A4. Backed-up waters are also prominent on the Sapucai River (F3 and G3), and at J3. Each of the three impoundments shown on the radar image provides a reservoir, flood control, waterworks, and hydroelectric generating potential for adjacent rural neighborhoods in the States of São Paulo to the south and Minas Gerais to the north. The middle of the river channel marks the boundary between the states in this area.

Marshland that formerly existed along the banks of the Rio Grande and numerous small islands in its channel have been covered by the waters in the reservoirs. The small island in the reservoir north of Miguelópolis (J5/K5)—about 3 km long—is all that remains above water of the

Landsat Band 5

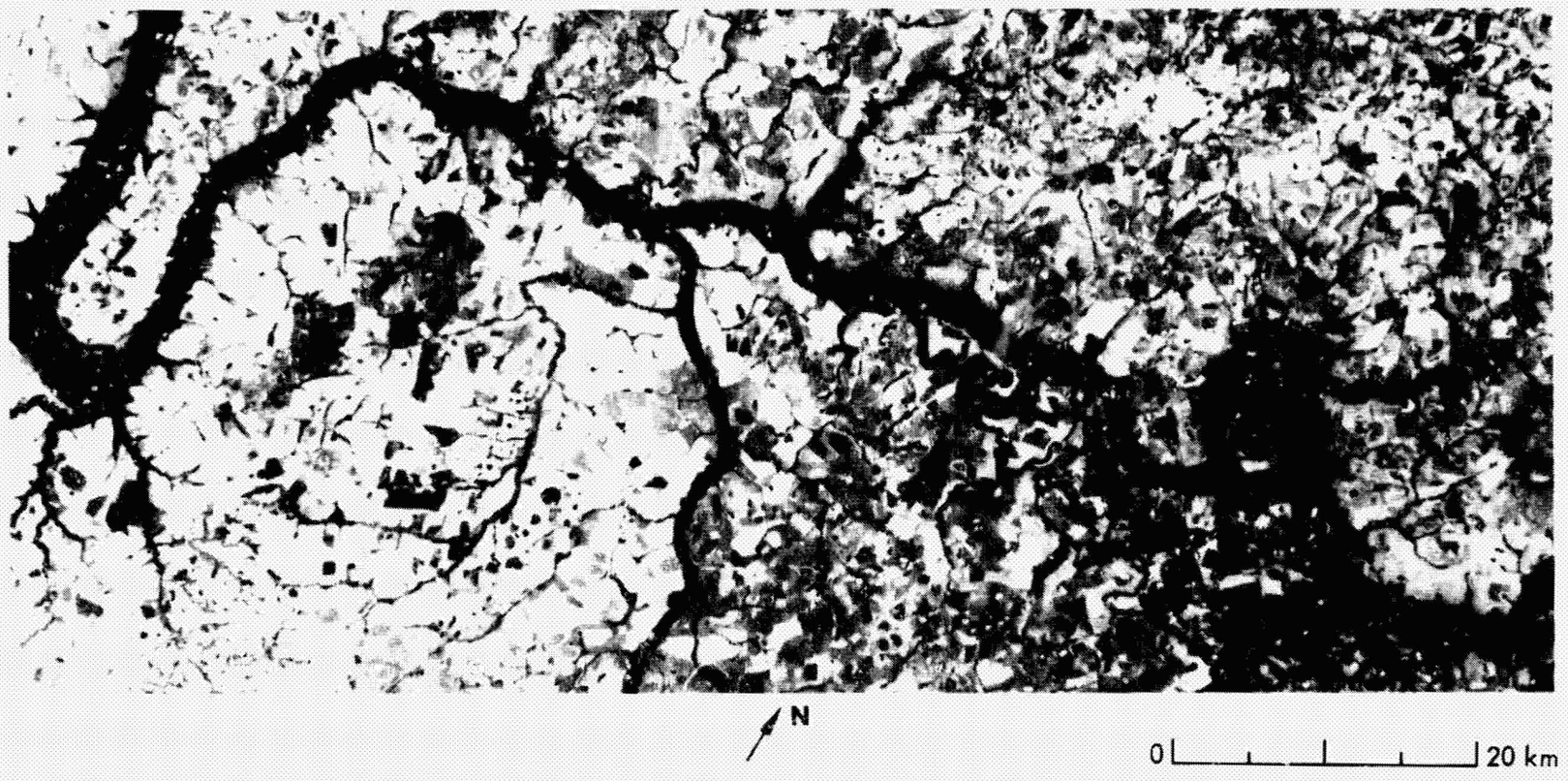

former Ilha Grande, which was approximately 6 km in length.

The clarity of the water in the reservoirs is indicated by the black tone on the Landsat image in the visible-red wavelength. At this wavelength, muddy water appears in shades of dark gray, but clear water is black. Near the center of D4, the small, nearly circular area about 700 m wide that is dark on both images is Lake Ouro Branco. Riparian vegetation along the stream channels that appears bright on the radar image is dark on the Landsat image. Forested areas with natural vegetation and pastures have a medium- to light-gray tone on the SIR-A image at C2 and C3 and a medium- to dark-gray tone on the Landsat image. The cultivated areas on either side of the Rio Pardo (from D2 and E2 through D5 and E5) show, in general, inverse image tones on the SIR-A and the Landsat images. Bare soil that had been plowed for planting was exposed in most of this area at the time the SIR-A image was acquired in mid-November.

The bright reflection of a transmission line from A5 to D5 and F5 to H5 that passes south of Guaira (F5/G5) is not visible on the Landsat image.

60. Offshore Oil Fields, Southern Persian Gulf

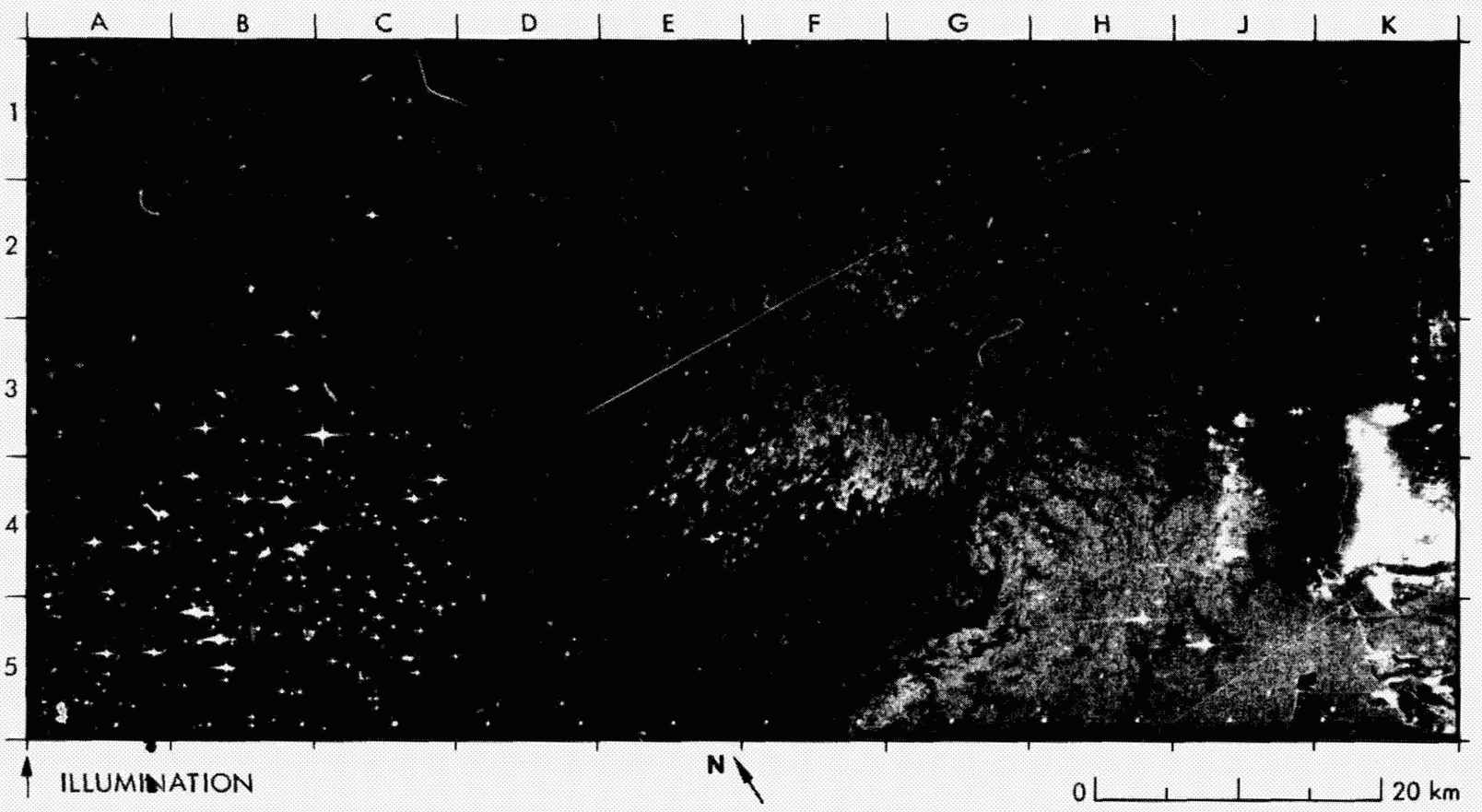

The bright point targets shown in the image are wellheads, oil rig platforms, or ships just off the west coast of the United Arab Emirates. Most of the bright features in the area bounded by A3, A5, C5, and C3 are wellhead towers in the Rugg az Zaqqum Field. Drilling platforms, buoys, and ships are also located in this region. The island in the lower right corner (K5) is Jazirat Fataisa. The larger very bright island at K4 is Abu Zahy. The accompanying sketch map (based on Ref. 25) shows that the water depth here is less than 6 fathoms.

More sparsely located point targets at G4 and H4 are wellheads and platforms in the Umm al Dalkh oil field, as shown on the sketch map. Other point targets shown on the image but not on the chart (e.g., C2 and E4/F4) may be wellheads or platforms built after publication of the chart on which the sketch map was based, or ships.

Medium- to light-gray tones in the right of the image indicate rough water surfaces; darker patterns throughout these waters are probably oil slicks.

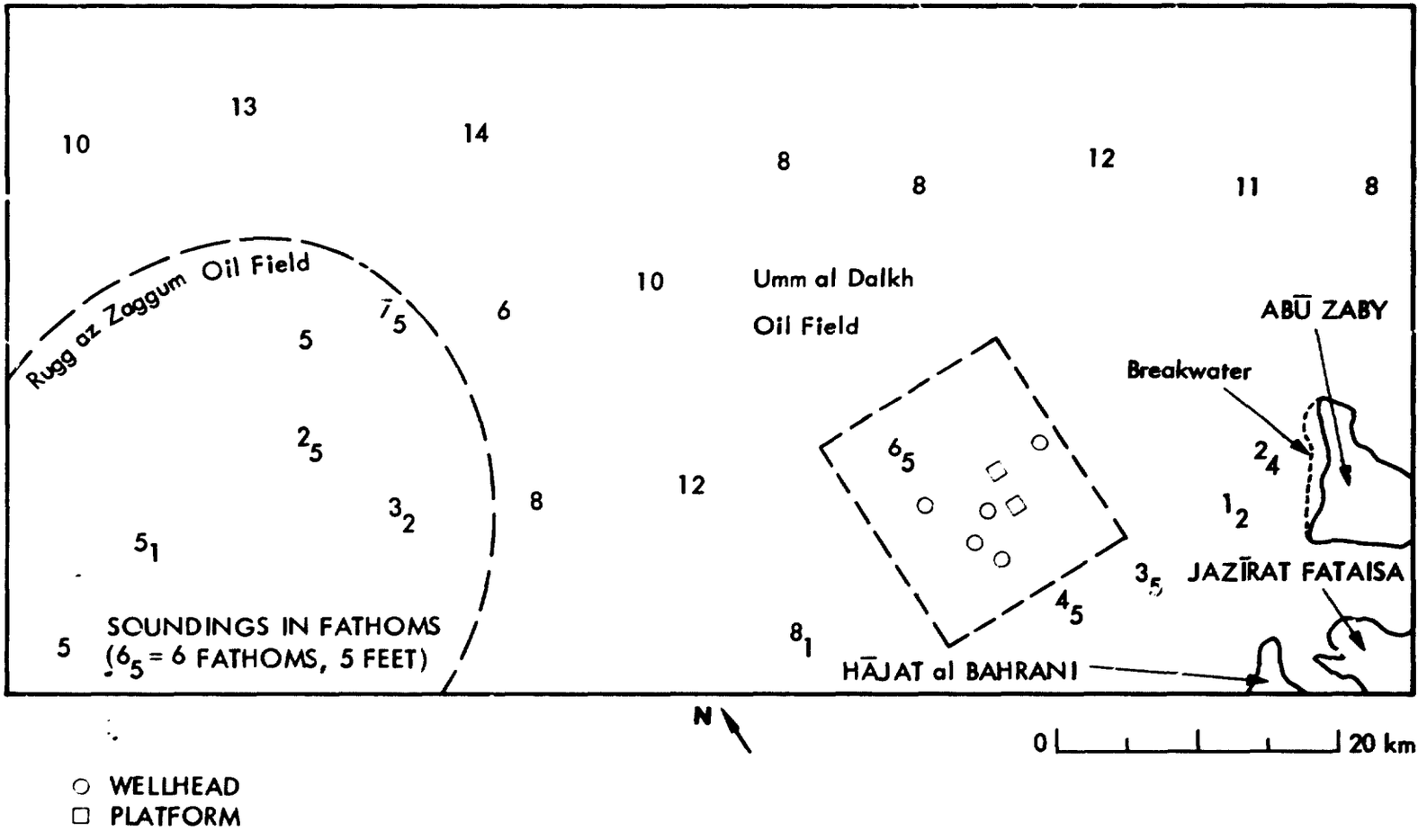

○ WELLHEAD
□ PLATFORM

ORIGINAL PAGE IS
OF POOR QUALITY

References

1. Elachi, C., et al., "Shuttle Imaging Radar Experiment," *Science*, Vol. 218, No. 4576, p. 996-1003, 1982.

2. Ford, J. P., et al., *Seasat Views North America, the Caribbean, and Western Europe With Imaging Radar*. Publication 80-67, Jet Propulsion Laboratory, Pasadena, California, Nov. 1, 1980.

3. Fu, L. L., and B. Holt, *Seasat Views Oceans and Sea Ice With Synthetic-Aperture Radar*. Publication 81-120, Jet Propulsion Laboratory, Pasadena, California, Feb. 15, 1982.

4. McCauley, J. F., et al., "Subsurface Valleys and Geoarchaeology of Egypt and Sudan Revealed by Shuttle Radar," *Science*, Vol. 218, No. 4576, p. 1004-1020.

5. Ford, J. P., "Geological Mapping From Spaceborne Imaging Radars: Kentucky Virginia, U.S.A." *IEEE - IGARSS '82*, Munich, Germany, Digest, p. FA6.6.1-FA6.6.6, 1982.

6. Dixon, T. H., and R. J. Stern, "Analysis of the Shuttle Imaging Radar (SIR-A) Data for the Egyptian Shield," submitted to *Geology*, 1982.

7. Kahle, A. B., et al., *Geologic Application of Thermal Inertia Imaging Using HCMM Data*. Publication 81-55, Jet Propulsion Laboratory, Pasadena, California, Sept. 15, 1981.

8. Ratman, N., *Geologic Map of the Manokwari Quadrangle, Irian Jaya*, scale 1:250,000. Geological Research and Development Centre of Indonesia, Bandung, Indonesia, 1981.

9. Pieters, P. E., U. Hartone, and Ch. Amri, *Preliminary Geologic Map of the Mar Quadrangle, Irian Jaya*, scale 1:250,000. Geological Research and Development Centre of Indonesia, Bandung, Indonesia, 1981.

10. Geological Survey of Western Australia, *Mount Bruce Sheet, Western Australia*, scale 1:250,000. SF 50-11, 1965.

11. Surveys and Mapping Branch, Dept. Mines and Technical Surveys, Canada, *Reconnaissance Geology of Part of West Pakistan; Geological Map No. 24, Sibi*, scale 1:253,440; *Geological Map No. 25, Lahri*, scale 1:253,440; *Geological Map No. 26, Quetta*, scale 1:253,440, 1958.

12. National Iranian Oil Company, *Geological Map of Iran, Sheet No. 2, North-Central Iran*, scale 1:1,000,000. Tehran, Iran, 1977.

13. Molnar, P., and P. Tapponnier, "Cenozoic Tectonics of Asia: Effects of a Continental Collision," *Science*, Vol. 189, No. 4201, p. 419-426, 1975.

14. Instituto Nacional de Investigaciones Geológico-mineras, Colombia, *Mapa Geológico de Colombia*, scale 1:1,500,000. 1976.

15. Ratman, N., and A. Yasin, *Geologic Map of the Komodo Quadrangle, Nusatenggara*, scale 1:250,000. Geological Survey of Indonesia, Bandung, Indonesia, 1977.

16. Instituto Geográfico Nacional, Guatemala, *Mapa Geológico de la Republica de Guatemala*, scale 1:500,000. 1970.

17. Bramkamp, R. A., et al., *Geology of the Jawf-Sakakah Quadrangle, Kingdom of Saudi Arabia*, scale 1:500,000. U.S. Geological Survey, Misc. Inv. Map I-201A, 1972.

18. U.S. Geological Survey, *Geologic Map of the Aswan Quadrangle, Egypt*, scale 1:500,000. Washington, D.C., 1978.

19. Said, R., *The Geology of Egypt*. Elsevier Publ. Co., New York, 1962.

20. Hall, N., "Adjustment in the Australian Wheat Growing Industry," *Quat. Review of the Rural Economy*, Vol. 3, No. 2 (May). Australian Bureau of Agricultural Economics, Canberra, Australia, 1981.

21. Tourist Dept., Federal District Government, Brasilia, *Brasilia – City Plan*, scale 1:41,000. c. 1975.

22. Departamento Nacional de Estradas de Rodagem, Brasil, *Mapa Rodoviário – Distrito Federal*, scale 1:130,000. 1980.

23. Auer, S., and Kundrat, J., "Atlantic Ocean Sea Surface Temperature," *Oceanographic Monthly Summary*, Vol. 1, No. 2, pp. 10-12. National Oceanic and Atmospheric Administration, Washington, D.C., November 1981.

24. Gallagher, J. J., M. Philippe, and B. Wanamaker, "Satellite Monitoring of Ocean Surface Temperature Variability in the Mediterranean Sea," in *Oceanography from Space*, J. F. R. Gower, ed., Plenum Press, New York, 1981.

25. DMA Hydrographic/Topographic Center, *Soundings Chart No. 62400, Ra's al Matbakh to ash Shariqah*, scale 1:350,000. Washington, D.C., 1981.

Appendix A
Glossary of Acronyms and Technical Terms

aa	basaltic lava flow with rough, splintery surfaces
acidic	containing over 66% SiO_2, as applied to igneous rock (cf. basic)
albedo	ratio of electromagnetic radiation reflected by a body to the amount incident upon it
alluvial fan	cone-shaped deposit formed where a stream issues from mountains onto lowlands
alluvium	stream deposits of comparatively recent time
andesitic	composed essentially of andesine and one or more mafic constituents, as applied to volcanic rocks
anticline	folded-rock structure whose limbs dip away from the fold axis
azimuth	bearing of a line measured clockwise from geographic north
azimuth (radar imaging)	along-track direction of image acquisition
backscatter (radar)	portion of transmitted microwave energy that is reflected back to the radar antenna to create a radar image
backslope	slope that is inclined away from an incident radar beam
band	an interval in the electromagnetic spectrum (qv) whose boundaries are marked by a lower and an upper limiting wavelength, or frequency
barrier bar	ridge composed of gravel deposits formed in a shallow-water offshore environment
barrier island	elongate ridges of beach sand that rise above the high-tide level, extend generally parallel to the coast, and are separated from the coast by a lagoon
basaltic	composed essentially of calcic plagioclase and pyroxene, as applied to fine- to medium-grain igneous rocks
basement	crustal rocks of deep-seated origin, generally igneous and metamorphic
basic	comparatively low in silica, as applied to igneous rocks (cf. acidic)
bedding	collective term for planes dividing sedimentary rock layers
blind valley	karst landform where a stream disappears underground and the valley has no outlet
Bragg scattering (radar)	reflections that are the result of radar waves superimposed on surface waves; the reflections reach a maximum when path-length differences between radar returns are an integral number of radar wavelengths
breccia	rock composed of highly-angular, coarse fragments
caldera	large circular depression in volcanic terrain that originates from collapse, or explosion, or erosion
carbonatite	intrusive carbonate rock
Carolina bay	oval-shaped depression, generally marshy, occurring extensively on the coastal plain from New Jersey to Florida, U.S.A.
cinder cone	accumulation of volcanic ash around a central vent, which is generally small (cf. lava dome)
correlation (radar)	processes by which the Doppler phase histories recorded on tape or radar signal film are converted into radar images, using optical or digital techniques
cutoff	short channel formed when a stream cuts through the neck of a horseshoe bend

dendritic	irregularly branching tributary streams in a drainage pattern
dielectric constant	ratio of the electric flux density to the electric field; identical with dielectric permittivity
dike	(1) tabular body of intrusive igneous rock that crosscuts the structure of the host rock (2) a wall built to prevent flooding
dip	angle at which a bed or other planar feature is inclined from the horizontal
dome	any structural deformation characterized by approximately circular local uplift (e.g., salt dome, rock dome)
Doppler history	record of frequency and phase change resulting from relative motion between observer and target
ejecta	fragmentary material thrown out by a volcano
electromagnetic spectrum	an ordered progression of radiations that includes cosmic, gamma, X, ultraviolet, visible, infrared, microwave, and radiowave energy
elevation (sun)	inclination of the sun to the horizontal
eolian	eroded or deposited by wind action
flatiron	pattern on remotely-sensed images and photographs from which dip and strike of layered rocks may be inferred
floodplain	the portion of a river valley built of sediment deposited by an existing river; the plain is covered with water when the river overflows its banks
foreslope	slope that is inclined toward an incident radar beam
gneissic	coarse grained with alternating bands of granular and schistose material, as applied to metamorphic rock
graben	elongated block that has been downthrown along faults that form its margins
granite	coarse-grained plutonic rock composed essentially of quartz and alkalic feldspar
HCMM	Heat Capacity Mapping Mission
hematite	principal ore of iron
holographic record	phase and amplitude information of radar return signals
igneous rock	rock solidified from a former molten state
illumination direction (radar)	direction in which pulses of microwave energy are transmitted from an imaging-radar antenna; normally at right angles to the line of flight of the imaging platform
image	visual reproduction of a scene acquired by SAR, MSS, HCMM, or photographic sensor
incidence angle (radar)	angle between the incident radar beam at the ground and the normal to the ground surface at the point of incidence
jaspilite	rock composed essentially of jasper and iron oxides in alternating bands
karst	an irregular hummocky terrain marked by subsurface drainage and numerous sinkholes interspersed with abrupt ridges. The subsurface is characterized by caverns and features formed by the solution and collapse of limestone
Landsat	any of a series of four orbital imaging satellites that have measured and recorded reflectance from the Earth's surface at visible and infrared wavelengths.
lava dome	accumulation of lava around a central vent, which is generally small (cf. cinder cone)

layover (radar)	geometric displacement of the top of a feature toward the near range on radar imagery
limonite	generic term for a brown hydrous iron oxide not specifically identified
look angle (radar)	angle between the vertical plane and the line that links an imaging-radar antenna to a feature on the ground
low-order stream	small tributary stream ranked by branching: the lowest-order streams are the smallest unbranched tributaries
meander	any of a series of C-shaped loops that form part of a sinuous stream channel
meander scar	outline of an erstwhile meander that has been cut off from a stream channel and filled with sediment that commonly supports a distinctive vegetation
metamorphic rock	rock altered from an original condition by elevated temperature and/or pressure that produces a change of texture and mineralogy
microwave	any electromagnetic wave having a wavelength in the interval between one millimeter and one meter
moraine	feature formed of unsorted, unstratified sediment transported and deposited by glacial ice
MSS	multispectral scanner (qv)
multispectral scanner	an airborne or spaceborne imaging system that acquires images by scanning a scene in several wavelengths simultaneously
oxbow	crescent-shaped lake in an abandoned stream bend
pahoehoe	basaltic lava flow with smooth, ropy surfaces
pisolitic	consisting of rounded grains like peas
planar array antenna	a two-dimensional planar collection of radiators or "elements" configured to produce a desired radiation pattern from the combined action of all the elements
pluton	igneous rock body formed and emplaced in the Earth's crust at depth below the surface
pyroclastic	formed by the accumulation of fragments scattered by volcanic explosions
radar	radio detection and ranging; radar is used in remote sensing for measuring and mapping the Earth and planetary surfaces
range (radar imaging)	across-track direction of image acquisition
resolution element	the minimum distance between two adjacent features on the ground, or the minimum size of a feature on the ground, that can be detected by an imaging system
returns (radar)	backscatter (qv)
SAR	synthetic-aperture radar (qv)
scarp	cliff or steep slope of some extent that may form a marked topographic boundary
scene	area covered by SAR, MSS, HCMM, or photographic image
Seasat	an Earth-orbiting satellite equipped with five instruments, including a side-looking synethic-aperture imaging radar system, for studying ocean dynamics
sedimentary rock	rock formed from the accumulation of particles of preexisting rock, or from chemical or biochemical precipitation
senescence	that phase of plant growth extending from full maturity to death

shadow (radar)	an area of no radar backscatter on an image caused by a ground feature that obstructs the radar beam and prevents illumination of the area behind it
shield volcano	a large broad volcanic cone with very gentle slopes built up of nonviscous basaltic flows
sinkhole	funnel-shaped depression, usually in a limestone region, that connects to a subterranean passage formed by solution
SIR-A	Shuttle Imaging Radar Experiment flown on Space Shuttle Columbia in November 1981
spectral reflectance	reflectance of electromagnetic energy at specified wavelength intervals
specular (reflections)	mirror-like returns of a radar signal
stratovolcano	cone composed of alternating layers of lava and pyroclastic materials, generally large and steep sided
strike	bearing of an inclined bed or structure on a level surface
strike-slip fault	fault in which the movement of the rocks on each side of the fault plane is predominantly horizontal. The displacement is either left-lateral or right-lateral depending on the direction of movement of the far block as viewed from either side of the fault
syncline	folded-rock structure whose limbs dip toward the fold axis
synthetic-aperture radar	a side-looking airborne or spaceborne imaging system that uses the Doppler principle to sharpen the effective beamwidth of the antenna.
tectonism	crustal instability
thermal inertia	measure of the response of a material to temperature change
thrust fault	low-angle dip-slip fault in which the block above the fault plane moves up and over the lower block
transcurrent fault	strike-slip fault (qv)
transform fault	a plate boundary along which strike-slip motion occurs, usually offsetting segments of a spreading ridge
tuff	rock formed of compacted volcanic fragments generally less than 4 mm in diameter
ultramafic	containing less than 45% silica, as applied to igneous rocks
volcanic rock	igneous rock formed by eruption at the Earth's surface
Yazoo-type stream	subsidiary drainage channel that runs parallel to a major stream in a floodplain for an extended distance, eventually joining the major stream

Appendix B
Index of Images

Scene No.	SIR-A Image	Data Take No.	Date, Nov. 1981	Center Coordinates		Correspondi Image and/ Diagram
				Latitude	Longitude	
1	Appalachian Mountains, Pennsylvania, U.S.A.	22	13	39°55′N	78°30′W	Landsat MS
2	San Rafael Swell, Utah, U.S.A.	24B	13	38°40′N	110°40′W	HCMM
3	Santa Ynez Mountains, California, U.S.A.	24C	13	34°28′N	119°45′W	Seasat SA
4	Lengguru Fold Belt, Irian Jaya, Indonesia	32–33	14	1°50′S	133°54′E	Landsat MS
5	West Pilbara Goldfield, Hamersley Range, Western Australia	38	14	22°52′S	117°28′E	Landsat MS
6	Sierra Madre Oriental, Coahuila, Mexico	24C	13	25°20′N	100°50′W	Landsat MS
7	Sibi District, Baluchistan Province, Pakistan	35–36	14	29°44′N	67°56′E	Landsat MS
8	Kalpir Chol and Chong Korum Mountains, Xinjiang, China	28	14	40°12′N	78°20′E	Landsat MS
9	Sierra Imeri, Amazonas, Venezuela	34	14	1°36′N	65°30′W	Landsat MS
10	Eastern Desert, Egypt	28	14	25°20′N	34°10′E	Landsat MS
11	Sahara Plateau, Mali (West Africa)	29–30	14	18°45′N	1°10′E	Landsat MS
12	Salt Domes, Great Kavir, Iran	28	14	34°55′N	55°00′E	Sketch ma
13	Altyn Tagh Fault System, Gansu, China	28	14	40°32′N	96°06′E	Landsat MS
14	Pakaraima Mountains, Guyana (South America)	3-	14	5°45′N	60°51′W	Sketch ma
15	Plains and Forest Lowlands, Meta, Colombia	24C	13	3°18′N	71°58′W	Landsat MS
16	Dunes Northeast of Ndjamena, Chad (Central Africa)	28	14	13°20′N	17°00′E	Landsat MS
17	Dunes, Oman, Arabia	37A	14	21°34′N	58°45′E	Landsat MS
18	Kara Kum Desert, Turkmen S.S.R.	28	14	37°32′N	62°50′E	Landsat MS
19	Badain Jaran Desert, Nei Monggol, China	28	14	39°57′N	102°55′E	Landsat MS
20	Pinacate Volcanic Field, Sonora, Mexico	24C	13	31°52′N	113°30′W	Landsat MS
21	Western Galápagos Islands, Ecuador	37	14	0°40′S	91°07′W	Landsat MS
22	Volcanic Field Northeast of Damascus, Syria	37A	14	33°22′N	36°58′E	Landsat MS
23	The Lesser Sunda Islands, Indonesia	35–36	14	8°30′S	119°15′E	Sketch ma
24	Central American Volcanic Belt, Guatemala	18	13	14°23′N	90°04′W	Landsat MS
25	Chott Merouane and Chott Melrhir, Algeria	32–33	14	34°10′N	6°20′E	Seasat SA Landsat MS
26	Northern Lop Nur, Xinjiang, China	28	14	40°49′N	90°10′E	Landsat MS

Center Coordinates		Corresponding Image and/or Diagram	Date	Scene ID	Sun Angle (Landsat)	
itude	Longitude				Elevation, deg	Azimuth, deg
55'N	78°30'W	Landsat MSS	Nov. 30, 1973	1495-15222-7	24	155
40'N	110°40'W	HCMM	Aug. 28, 1978	AA 0124204802	–	–
28'N	119°45'W	Seasat SAR	Jul. 18, 1978	Rev. 308	–	–
			Aug. 4, 1978	Rev. 552	–	–
50'S	133°54'E	Landsat MSS	Nov. 18, 1973	1483-00394-7	54	121
			Aug. 31, 1978	30179-00365-7	51	73
52'S	117°28'E	Landsat MSS	Nov. 13, 1972	1113-01343-5	57	87
			Oct. 4, 1973	1438-01381-5	50	66
20'N	100°50'W	Landsat MSS	Sept. 9, 1974	1778-16331-6	53	118
44'N	67°56'E	Landsat MSS	Nov. 3, 1972	1103-05312-7	38	148
12'N	78°20'E	Landsat MSS	Oct. 24, 1973	1458-04571-7	33	152
36'N	65°30'W	Landsat MSS	Sept. 5, 1978	21322-13401-7	48	81
			Sept. 21, 1973	1425-14030-7	57	91
20'N	34°10'E	Landsat MSS	Jan. 19, 1973	1180-07442-7	33	142
			Jan. 19, 1973	1180-07444-7	33	142
45'N	1°10'E	Landsat MSS	Nov. 25, 1973	1490-09501-7	41	143
55'N	55°00'E	Sketch map	–	–	–	–
32'N	96°06'E	Landsat MSS	Dec. 16, 1976	2694-03264-7	19	149
45'N	60°51'W	Sketch map	–	–	–	–
18'N	71°58'W	Landsat MSS	Oct. 19, 1972	1088-14323-7	57	113
20'N	17°00'E	Landsat MSS	Feb. 15, 1975	2024-08341-5	43	122
34'N	58°45'E	Landsat MSS	Nov. 26, 1972	1126-06024-7	39	145
32'N	62°50'E	Landsat MSS	Nov. 26, 1972	1126-05581-7	27	154
57'N	102°55'E	Landsat MSS	Oct. 7, 1973	1441-03201-5	39	148
52'N	113°30'W	Landsat MSS	Jun. 26, 1973	1338-17392-4, 5, 7	62	100
40'S	91°07'W	Landsat MSS	Mar. 24, 1980	30750-15310-5	49	87
			Mar. 24, 1980	30750-15312-5	49	85
22'N	36°58'E	Landsat MSS	Dec. 19, 1978	30289-07313-7	26	148
30'S	119°15'E	Sketch map	–	–	–	–
23'N	90°04'W	Landsat MSS	Dec. 31, 1978	30301-15385-7	39	136
			Jan. 28, 1979	21467-15311-7	37	127
10'N	6°20'E	Seasat SAR	Aug. 21, 1978	Rev. 791	–	–
		Landsat MSS	Oct. 1, 1973	10435-09404-4	45	144
49'N	90°10'E	Landsat MSS	Jul. 17, 1973	1359-04074-7	59	119

Scene No.	SIR-A Image	Data Take No.	Date, Nov. 1981	Center Coordinates		Corresponding Image and/or Diagram
				Latitude	Longitude	
27	The Great Kavir, Iran	28	14	35°40'N	55°25'E	Sketch map
28	Maya Mountains, Belize (Central America)	24C	13	17°02'N	88°31'W	Sketch map
29	Cotabato Province, Mindanao, Philippines	32-33	14	6°18'N	124°27'E	Landsat MSS
30	Mississippi River Deltaic Plain, Louisiana, U.S.A.	21	13	29°25'N	90°10'W	Landsat MSS
31	Red River Deltaic Plain, Viet Nam	32-33	14	20°33'N	106°10'E	Landsat MSS
32	Shatt al 'Arab, Persian Gulf	7	13	30°00'N	48°35'E	Landsat MSS
33	Mississippi, Missouri, and Illinois Rivers, U.S.A.	24A	13	39°08'N	90°30'W	Landsat MSS
34	Lüliang Shan, Shanxi, China	28	14	38°27'N	111°30'E	Landsat MSS
35	Rio Ucayali, Loreto, Peru	34	14	6°13'S	74°54'W	Landsat MSS
36	Ilhas Macuapanim, Amazonas, Brazil	24C	13	2°36'S	65°00'W	Landsat MSS
37	Al Widyan, Saudi Arabia and Iraq	37A	14	31°40'N	40°55'E	Landsat MSS
38	Mississippi River Floodplain, Louisiana, U.S.A.	24B	13	32°16'N	91°26'W	Seasat SAR Landsat MSS
39	Nile River, Egypt	28	14	24°20'N	32°35'E	Sketch map
40	Karakoram Mountain Glaciers, Pakistan	32-33	14	35°55'N	75°35'E	Landsat MSS
41	Highlands, Mato Grosso do Sul – Paraná, Brazil	29-30	14	23°12'S	53°40'W	Landsat MSS
42	Center-Pivot Irrigation, Southwest Nebraska, U.S.A.	24A	13	40°40'N	101°45'W	Landsat MSS
43	Circular Agricultural Fields, Libya	29-30	14	27°42'N	14°50'E	Sketch and enlargement
44	Wheat-Sheep Farms, New South Wales, Australia	38	14	33°38'S	146°23'E	Landsat MSS
45	Lower Coastal Plain, North Carolina, U.S.A.	21	13	34°55'N	76°59'W	Landsat MSS
46	Upper Coastal Plain, South Carolina – Georgia, U.S.A.	21	13	33°15'N	81°40'W	Landsat MSS
47	Southwest Coastal Swamp, Irian Jaya, Indonesia	32-33	14	5°17'S	138°00'E	Sketch map
48	Kapuas River and Deltaic Plain, West Kalimantan, Indonesia	35-36	14	0°23'S	109°25'E	Landsat MSS
49	Brasilia, D.F., Brazil	24C	13	15°52'S	47°57'W	Landsat MSS Sketch map
50	Villages and Cultivated Fields, Hebei-Shandong, China	28	14	37°30'N	115°42'E	Landsat MSS
51	Surface Waves, Western Mediterranean Sea	37A	14	40°35'N	4°25'E	Location map
52	Internal Waves, Andaman Sea (Indian Ocean)	35-36	14	12°28'N	94°00'E	Location map

ates ongitude	Corresponding Image and/or Diagram	Date	Scene ID	Sun Angle (Landsat)	
				Elevation, deg	Azimuth, deg
55°25'E	Sketch map	–	–	–	–
88°31'W	Sketch map	–	–	–	–
124°27'E	Landsat MSS	Jan. 21, 1979	21460-01071-7	41	123
		Dec. 19, 1972	1149-01261-7	47	133
90°10'W	Landsat MSS	Jan. 6, 1973	1177-16023-5	31	145
10°10'E	Landsat MSS	Dec. 29, 1975	2341-02393-7	34	130
		Apr. 20, 1975	2088-02360-7	56	100
48°35'E	Landsat MSS	Aug. 2, 1977	2923-06164-7	52	100
90°30'W	Landsat MSS	Oct. 17, 1976	5547-15154-7	30	136
111°30'E	Landsat MSS	Sept. 23, 1978	30202-02372-5	43	139
74°54'W	Landsat MSS	Oct. 2, 1972	1071-14402-6	57	88
65°00'W	Landsat MSS	Sept. 20, 1973	1424-13583-7	56	83
40°55'E	Landsat MSS	Jul. 14, 1973	1356-07193-7	61	103
91°26'W	Seasat SAR	Aug. 24, 1978	Rev. 838	–	–
	Landsat MSS	Oct. 2, 1972	1071-16125-7	46	140
32°35'E	Sketch map	–	–	–	–
75°35'E	Landsat MSS	Jun. 4, 1978	21229-04320-7	56	103
53°40'W	Landsat MSS	Apr. 21, 1981	22281-12483-5	36	52
			22281-12483-7	36	53
101°45'W	Landsat MSS	Aug. 18, 1972	1026-17015-5	53	131
14°50'E	Sketch and enlargement		–		
146°23'E	Landsat MSS	Jan. 1, 1973	1162-23310-7	52	84
76°59'W	Landsat MSS	Feb. 25, 1977	5678-14075-7	26	124
81°40'W	Landsat MSS	Jan. 17, 1977	2726-15072-7	25	141
138°00'E	Sketch map		–	–	
109°25'E	Landsat MSS	Aug. 12, 1978	30160-02134-7	49	66
47°57'W	Landsat MSS	Aug. 19, 1973	1392-12425-5	42	54
	Sketch map	–	–	–	–
115°42'E	Landsat MSS	Oct. 26, 1976	2643-02033-7	33	145
4°25'E	Location map		–		
94°00'E	Location map				

2 FOLDOUT FRAME

Scene No.	SIR-A Image	Data Take No.	Date, Nov. 1981	Center Coordinates		Corresponding Image and/or Diagram
				Latitude	Longitude	
53	Surface Slicks and Ocean Vessels, Rio de Oro Coast, Atlantic Ocean	32-33	14	22°02′N	17°05′W	Location map
54	Wind Patterns Off Sardinia, Mediterranean Sea	35-36	14	40°10′N	10°00′E	SIR-A
55	Wind Slicks and Fronts, Moro Gulf, Celebes Sea	24BB	13	6°35′N	123°30′E	Location map
56	Ocean Eddy Off Dominican Republic, Atlantic Ocean	24B	13	20°14′N	70°20′W	Location map
57	Ocean Surface Patterns Off Java, Indian Ocean	24BB	13	8°08′S	105°50′E	Location map
58	Corinth Canal, Greece	37A	14	37°43′N	23°20′E	Ground-based photograph
59	Dams and Reservoirs, Rio Grande, Brazil	29-30	14	20°15′S	48°28′W	Landsat MSS
60	Offshore Oilfields, Southern Persian Gulf	37A	14	24°10′N	54°10′E	Sketch map

NASA—JPL—Coml., L.A., Calif.

Center Coordinates		Corresponding Image and/or Diagram	Date	Scene ID	Sun Angle (Landsat)	
Latitude	Longitude				Elevation, deg	Azimuth, deg
22°02'N	17°05'W	Location map	–	–	–	–
40°10'N	10°00'E	SIR-A	Nov. 14, 1981	DT 37A, 1200 GMT 40°03'N; 10°07'E	–	–
6°35'N	123°30'E	Location map				
20°14'N	70°20'W	Location map				
8°08'S	105°50'E	Location map				
37°43'N	23°20'E	Ground-based photograph	1979	–	–	–
20°15'S	48°28'W	Landsat MSS	Sept. 9, 1981	22422-12282-5	42	62
24°10'N	54°10'E	Sketch map	–	–	–	–